JOURNAL OF RESEARCH

OF THE U.S. GEOLOGICAL SURVEY

SEPTEMBER–OCTOBER 1974
VOLUME 2, NUMBER 5

Scientific notes and summaries of investigations in geology, hydrology, and related fields

U.S. DEPARTMENT OF THE INTERIOR

UNITED STATES DEPARTMENT OF THE INTERIOR
ROGERS C. B. MORTON, Secretary
GEOLOGICAL SURVEY
V. E. McKelvey, Director

For sale by the Superintendent of Documents, U.S. Government Printing Office, Washington, DC 20402. Order by SD Catalog No. JRGS. Annual subscription rate $15.50 (plus $3.75 for foreign mailing). Single copy $2.75. Make checks or money orders payable to the Superintendent of Documents.

Send all subscription inquiries and address changes to the Superintendent of Documents at the above address.

Purchase orders should not be sent to the U.S. Geological Survey library.

Library of Congress Catalog-card No. 72-600241.

The Journal of Research is published every 2 months by the U.S. Geological Survey. It contains papers by members of the Geological Survey and their professional colleagues on geologic, hydrologic, topographic, and other scientific and technical subjects.

Correspondence and inquiries concerning the Journal (other than subscription inquiries and address changes) should be directed to the Journal of Research, Publications Division, U.S. Geological Survey, National Center 321, Reston, VA 22092.

Papers for the Journal should be submitted through regular Division publication channels.

The Secretary of the Interior has determined that the publication of this periodical is necessary in the transaction of the public business required by law of this Department. Use of funds for printing this periodical has been approved by the Director of the Office of Management and Budget through February 11, 1975.

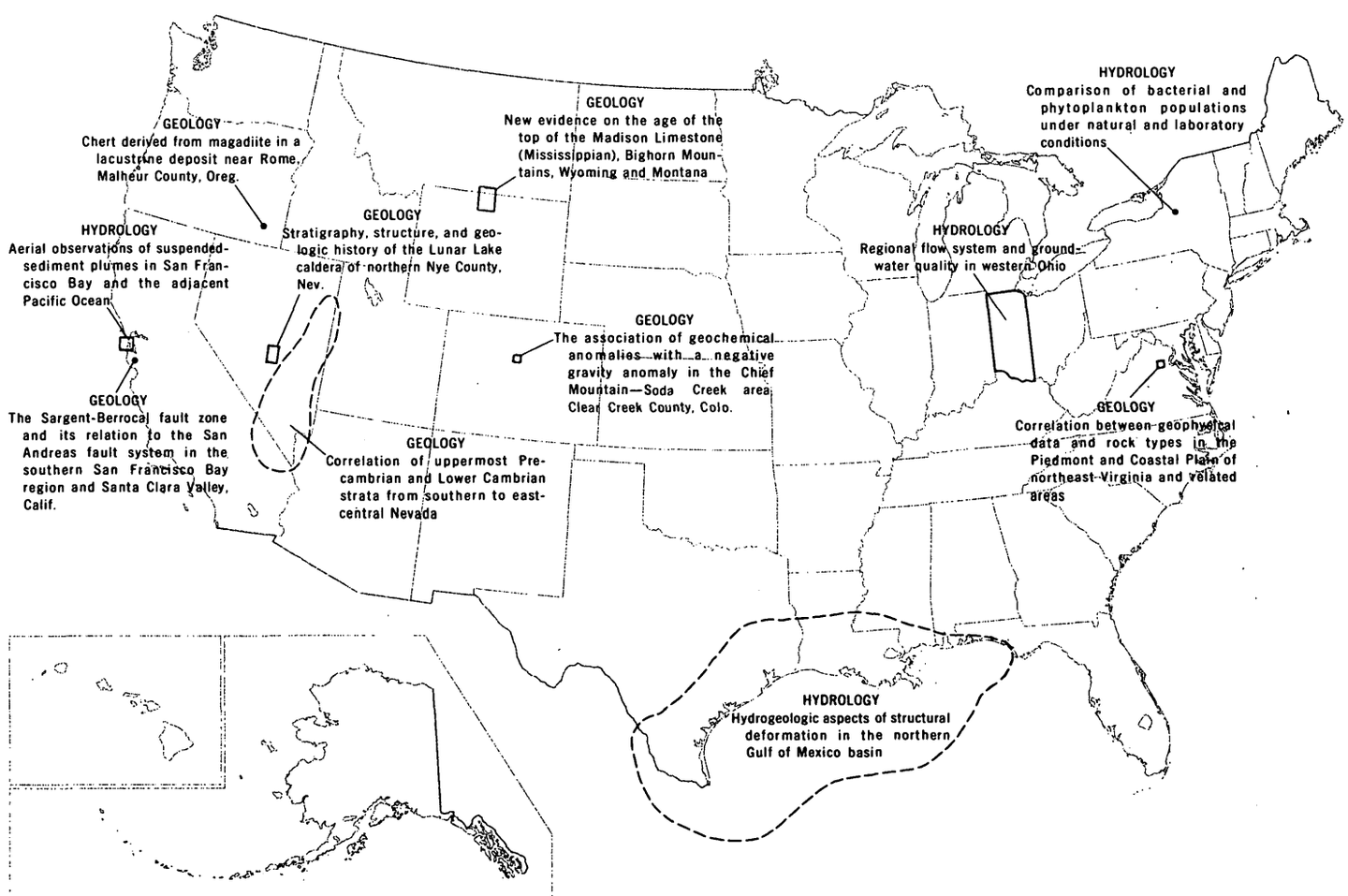

GEOGRAPHIC INDEX TO ARTICLES

See "Contents" for articles concerning areas outside the United States and articles without geographic orientation.

JOURNAL OF RESEARCH

of the

U.S. Geological Survey

Vol. 2 No. 5 Sept.-Oct. 1974

CONTENTS

ABBREVIATIONS

A . . . . . ampere
A . . . . . angstrom
abs . . . . . absolute
ADP . . . . . ammonium dihydrogen phosphate
atm . . . . . atmosphere
BOD . . . . . biochemical oxygen demand
Btu . . . . . British thermal unit
b.y. . . . . billion years
°C . . . . . degree Celsius
cal . . . . . calorie
C.I. . . . . color index
CIPW . . . . . Cross, Iddings, Pirsson, and Washington
cm . . . . . centimeter
cm^3 . . . . . cubic centimeter
concd . . . . . concentrated
d . . . . . day
DDD . . . . . dichloro-diphenyl-dichloro-ethane
DDE . . . . . dichloro-diphenyl-dichloro-ethylene
DDT . . . . . dichloro-diphenyl-trichloro-ethane
diam . . . . . diameter
DSDP . . . . . Deep Sea Drilling Project
Eh . . . . . oxidation-reduction potential
emf . . . . . electromotive force
emu . . . . . electromagnetic unit
eu . . . . . entropy unit
eV . . . . . electronvolt
F.D.&C. . . . . Food, Drug, and Cosmetic [dye]
ft . . . . . foot
ft^2 . . . . . square foot
ft^3 . . . . . cubic foot
g . . . . . gram
g . . . . . gravitational acceleration
γ . . . . . activity coefficient
gal . . . . . gallon
h . . . . . hour
ID . . . . . inside diameter
IDOE . . . . . International Decade of Ocean Exploration
in. . . . . inch
J . . . . . joule
K . . . . . Kelvin
keV . . . . . kiloelectronvolt
kg . . . . . kilogram
kHz . . . . . kilohertz
km . . . . . kilometer
km^2 . . . . . square kilometer
km^3 . . . . . cubic kilometer
kV . . . . . kilovolt
l . . . . . liter
lb . . . . . pound
lm . . . . . lumen
ln . . . . . logarithm (natural)
log . . . . . logarithm (common)
M . . . . . molarity; molar (concentration)
m . . . . . meter
m^2 . . . . . square meter
m^3 . . . . . cubic meter
m . . . . . molality; molal (concentration)
MA . . . . . megampere
mA . . . . . milliampere
mg . . . . . milligram
Mgal . . . . . million gallons
mGal . . . . . milligal
mi . . . . . mile
mi^2 . . . . . square mile
mi^3 . . . . . cubic mile
min . . . . . minute
ml . . . . . milliliter
mm . . . . . millimeter
mmol . . . . . millimole
mo . . . . . month
mol . . . . . mole
mol. wt . . . . . molecular weight
mV . . . . . millivolt
m.y. . . . . million years
μg . . . . . microgram
μm . . . . . micrometer
μmho . . . . . micromho
N . . . . . normality
nA . . . . . nanoampere
nm . . . . . nanometer
OD . . . . . outside diameter
PCB . . . . . polychlorinated biphenyls
PDB . . . . . Peedee belemnite
pH . . . . . measure of hydrogen ion activity
ppm . . . . . part per million
‰ . . . . . part per thousand
rad . . . . . radian
s . . . . . second
SMOW . . . . . standard mean ocean water
v . . . . . volt
v/v . . . . . volume per volume
W . . . . . watt
w/w . . . . . weight per weight
wt . . . . . weight
yd^3 . . . . . cubic yard
yr . . . . . year

Jour. Research U.S. Geol. Survey
Vol. 2, No. 5, Sept.-Oct. 1974, p. 511–517

HYDROGEOLOGIC ASPECTS OF STRUCTURAL DEFORMATION IN THE NORTHERN GULF OF MEXICO BASIN

By PAUL H. JONES and RAYMOND H. WALLACE, JR.,
Bay Saint Louis, Miss.

Abstract.—Resistance of unconsolidated clastic sediments to structural deformation, an inverse function of water content and pore pressure, has no uniform relation to depth of burial in the Gulf of Mexico basin. Deposited rapidly along the northwestern margin of the Gulf Coast geosyncline, sediments of younger deltas leapfrogged older deltas and spilled gulfward upon prodelta and marine clays of older deltas, burying them deeply before they could drain properly in response to compaction stress of overburden load. Contemporaneous gravity faults of major dimension occur along gulfward margins of delta-front sand bodies, reflecting the effect of sediment facies distribution on structure—sand bodies are more stable than shale masses. Such contemporaneous or growth faults are a most distinctive feature of the geology of the Gulf of Mexico basin; they are normal faults with progressive increase in throw with depth and, across which, from upthrown to downthrown block, correlative section thickens greatly. In plan and profile, faulted masses resemble land slides; fault planes are concave gulfward and upward, the dip decreasing with depth. Fault movement rotates the block, causing reversal of dip of beds in the block and sealing the landward ends of included aquifers to discharge of waters of compaction—producing geopressured conditions so common in the Gulf Coastal Plain and Continental Shelf. Early development of geopressure in the block reduces resistance to shear, and progressive landward side loading of the block sustains rotational stress. Geopressured water flowing into the fault zone—the easiest escape route—reduces drag and facilitates movement on the fault.

The northern Gulf of Mexico coastal segment of the North American continent is on no one's list of seismically active areas. In fact, there have been no more than six minor shocks recorded in the whole region, yet, it is laced with systems of contemporaneous gravity faults of regional dimension (fig. 1) marking the gulfward margin of each major depositional cycle since early Eocene time. Recent sparker seismic profiles of the continental shelf and slope area beneath the modern Gulf Continental Shelf (fig. 2) indicate that slump-type faulting—both glide plane and contemporaneous—is occurring even now.

Contemporaneous faults, known locally as growth faults (fig. 3), are the most distinctive structural feature of Gulf basin geology. They began forming at the inner margin of the Gulf Coastal Plain as Eocene deltas grew rapidly gulfward, their sediments being dumped upon a thick Jurassic salt layer which underlies much of the Gulf basin. With sedimentary loading the salt was deformed; it was squeezed out ahead of the advancing delta fronts (fig. 4). The basin floor then began to subside, and large masses of sediments slumped gulfward as deposition continued. The sediments of younger deltas leapfrogged older deltas and spilled sandy deposits gulfward upon prodelta and marine clay components of the older deltas, burying them deeply before they could drain properly in response to the compaction stress of the overburden load. These processes continue to the present time.

Growth faults are normal faults along which movement has occurred intermittently in geologic time—not as a single abrupt event. Maximum throw cannot be measured using offset of any one bed; it is cumulative, with concurrent movement and deposition on the downthrown block. However, as shown by Thorsen (1963, p. 103–110), fault activity as a function of time can be measured by comparing bed thicknesses on the upthrown and downthrown side of the fault plane. The greatest difference in bed thickness, downthrown versus upthrown, corresponds to the time of maximum movement. Displacements, measured in thousands of feet, die out downward in massive shales or along bedding planes (fig. 5); and they may die out upwards as movement ceases and deposition continues. Differential compaction or flowage of salt or shale has in some instances renewed movement, even extending fault planes to the land surface, producing faults with both growth and postdepositional normal faulting characteristics. In plan and profile the growth-faulted masses resemble landslides; fault planes are concave gulfward and upward, the dip decreasing with depth and with increasing geostatic ratio, until it parallels the bedding plane (fig. 6). Movement on the fault rotates the block, causing reversal of the dip of beds in the block and sealing the landward ends of included aquifers to discharge of water of compaction; thus producing the geopressured conditions so common in the Gulf Coastal Plain and Continental Shelf. Three types of contemporaneous fault systems are shown in figure 7.

Martin (1972, p. 54) states that large growth faults seem to be always associated with abnormally high fluid pressures. The occurrence of abnormally high fluid pressure, or geopressure, in Miocene deposits of the northern Gulf Coastal Plain coincides with the areas of down-dip deltaic sedimentation and growth faulting. Geopressured sands and clays of alternating deltaic, inner neritic and middle neritic depositional environ-

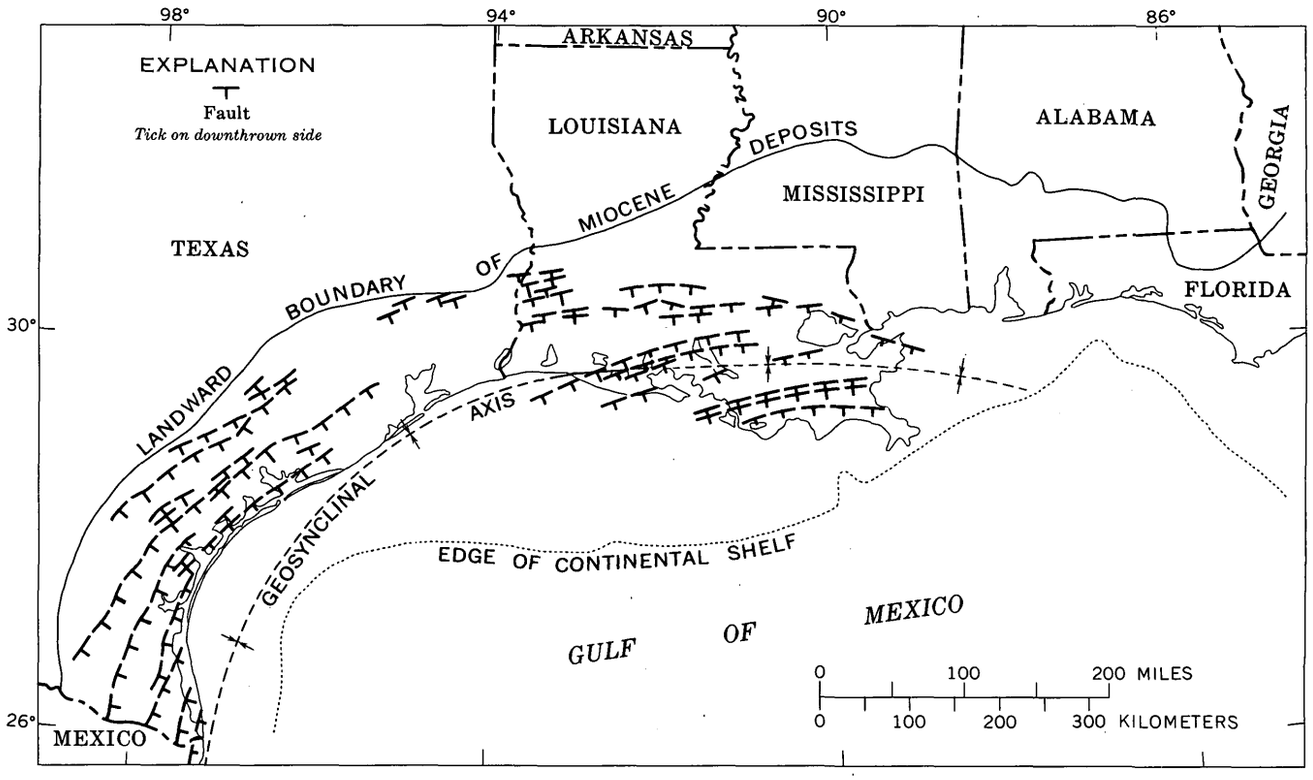

Figure 1.–Major regional fault zones in Neogene deposits, northern Gulf of Mexico basin (modified from Murray, 1961).

ment now occur at depths of about 1,500 m (5,000 ft) to depths in excess of 4,500 m (15,000 ft) below sea level (fig. 8). Geopressures are also present in beds of similar origin in older and younger deltaic deposits in the northern Gulf coastal area. Although the resistance of unconsolidated clastic sediments to structural deformation has no uniform relation to depth of burial in the Gulf basin, it can readily be seen that, in terms of basin evolution, resistance to deformation increases with time. Geopressured deposits gradually drain and compact into consolidated rocks.

A schematic north-south dip cross section (fig. 9) through deltaic and nearshore marine deposits shows the effect of faulting on normal up-dip release of fluids. In stage 1, before faulting, waters of deposition move upward and landward (up dip), as shown by the arrows, out of the rapidly buried sands and clays of the down-dip part by way of the sand beds. Newly deposited argillaceous sediments in the Gulf Coast contain 60 to 90 percent of pore space, which is water filled. The density of these shallow clays is about 1.8 g/cm^3, according to Dickinson (1953, p. 426). The "normal" fluid pressures which exist at this stage is due to the head of water filling the pores of the reservoir rock, the water being in communication with the land surface. Compaction and deposition proceed until faulting occurs in stage 2, offsetting aquifers and restricting further up-dip release of fluid. Thus compartmentalized, the sands and clays become increasingly "waterlogged" with deepening burial, and fluid-pressures rise accordingly. As expressed by Dickinson (1953, p. 425),

> Compression of argillaceous beds during the early stages of sedimentation and the concomitant expulsion of fluid give rise to progressive compaction as additional sediments are added to the overburden. As compaction proceeds, the expulsion of fluid becomes more difficult because of decreasing [porosity and] permeability, so that the pressure in the clay will be partly transmitted to the fluids, and thereby to the fluids in any sand body completely enclosed in the compacting mass, even through the sand body itself may not be compressible.

Figure 10 is a plot of compaction and porosity to depth, showing that under hydrostatic conditions, 75 percent of total clay compaction has occurred before 2,500 m (8,000 ft) of burial, and further compaction becomes exceedingly difficult. Average clay (or shale) densities in the Tertiary formations of the Gulf Coast range from 1.8 g/cm^3 at 300 m (1,000 ft) to about 2.35 g/cm^3 at 2,500 m (8,000 ft). It is interesting to note that even at depths of 4,500 m (15,000 ft), the average density is about 2.4 g/cm^3. Shale with little or no porosity has a density of approximately 2.65 g/cm^3; it is apparent, therefore, that large volumes of water remain to be expelled from shales buried to considerable depths in the Gulf basin, even under hydrostatic conditions.

The shale bulk-density profile for a typical Gulf Coast well (fig. 11) shows an increase in density with depth–as one

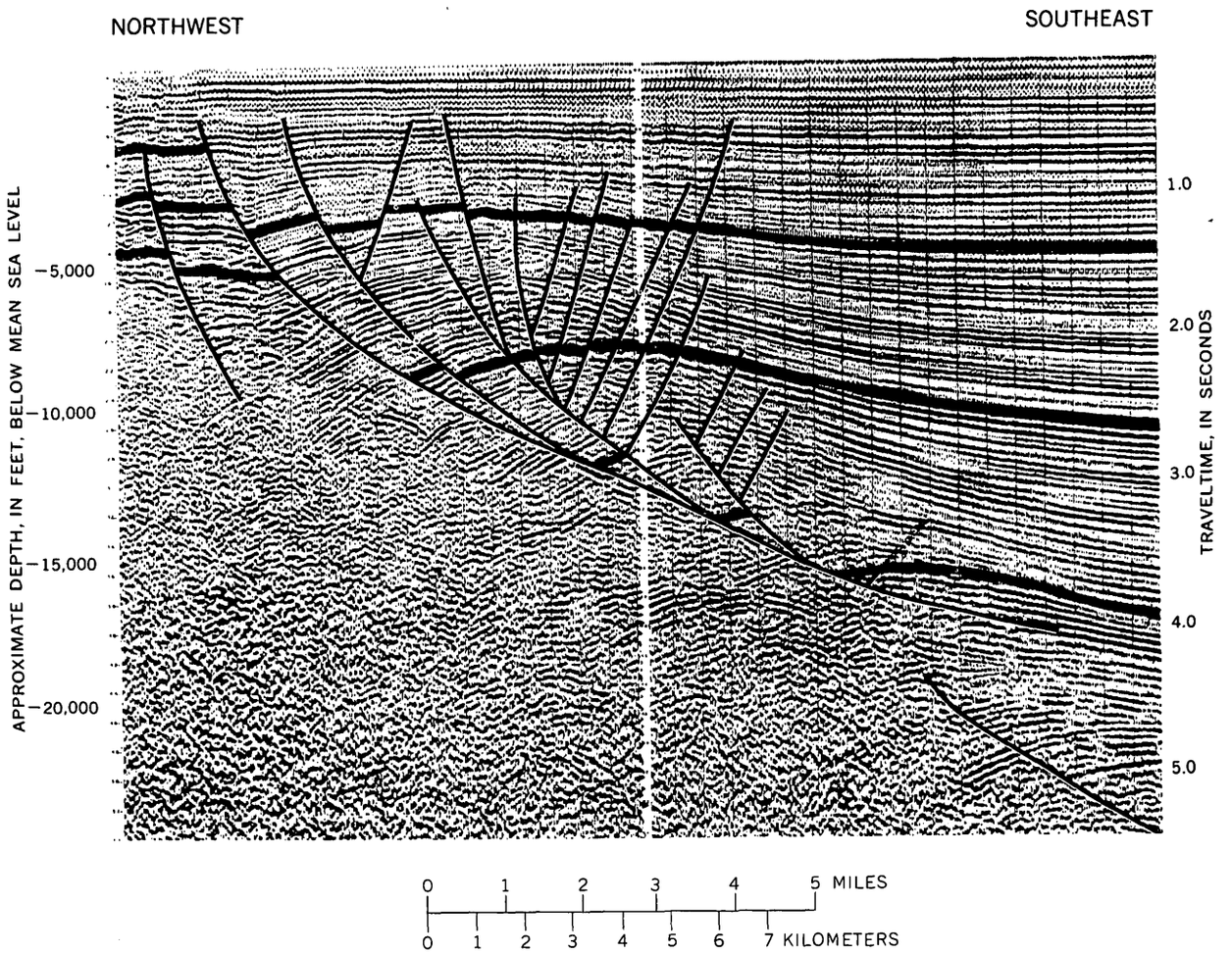

Figure 2.—Seismic profile showing flattening of growth fault angle with depth to the bedding plane, and collapse-fault complex above it (modified from Bruce, 1972).

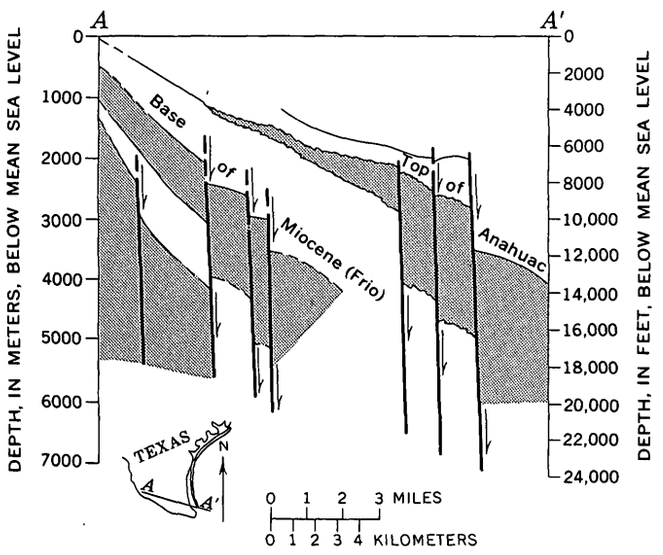

Figure 3.—Strata thickening across growth faults in the lower Rio Grande Embayment in Texas (Murray, 1961).

would expect. However, at a depth of about 2,750 m (9,000 ft) the trend temporarily reverses to about 3,000 m (9,800 ft) as geopressures are encountered. The density again increases to 2.3 g/cm^3 at 3,100 m (10,250 ft) and is maintained at about that value to the total depth of 3,965 m (13,000 ft). The high fluid pressures, plotted as geostatic ratio on the right side of this illustration, indicate that formation fluids support 50 to 75 percent of the overburden weight in this interval. Deposits that are not free to drain in direct response to pressure resulting from the overburden load remain undercompacted for millions of years.

Bornhauser (1958, p. 353) states that "the thickness of sedimentary overburden necessary to induce [diapiric] flow in an incompetent bed appears to vary with the degree of slope and the nature of the incompetent bed itself. Evaporites—mainly rock salt—and certain types of shale seem to require the least overburden and the smallest angle of slope." Three conditions must be met, according to Bornhauser (1958, p. 352–353), to initiate gravity flow: (1) Sediments must behave, during geologic time, like very viscous fluids, (2) a sloping surface

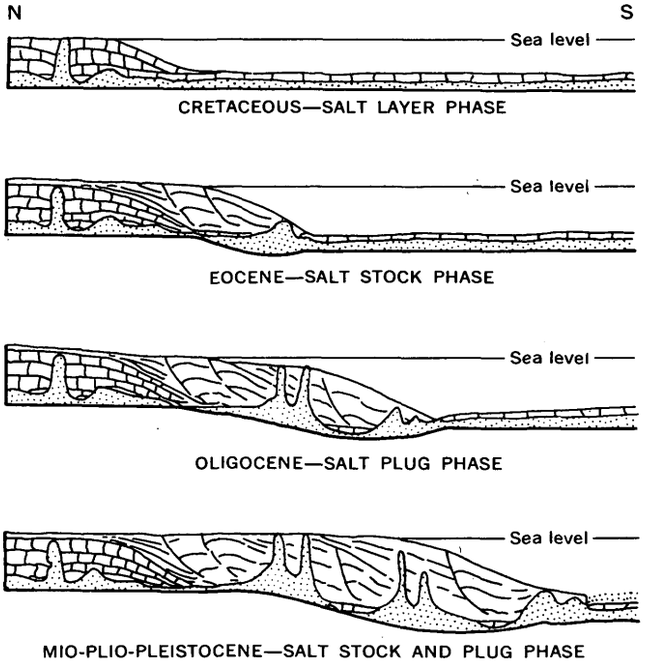

Figure 4.—Stages in the development of the Gulf Coast geosyncline, with salt flowage gulfward under progressive loading, growth of salt stocks and plugs with prograding sedimentation and contemporaneous faulting (modified from Wilhelm and Ewing, 1972).

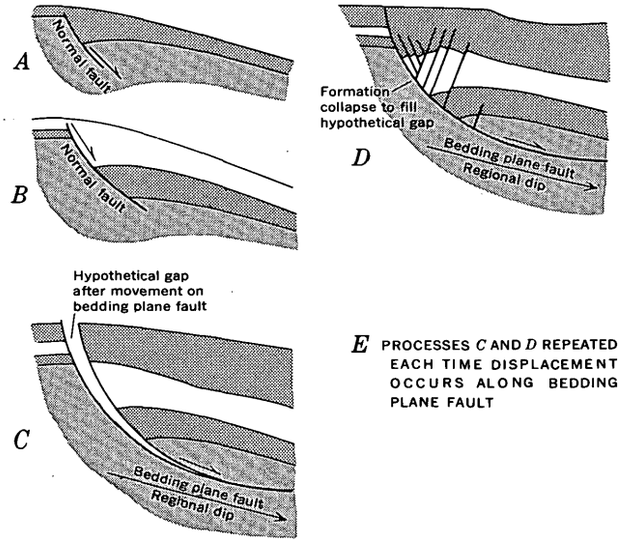

Figure 5.—Development of a bedding plane fault with collapse-fault system above it (from Bruce, 1972).

must be present—slope or dip angles as small as 2° to 3° are sufficiently large to induce gravity flow, and (3) sedimentary loading must take place. Bruce (1972, p. 23) states that "most regional contemporaneous fault systems in the Texas coastal area were formed during times of shoreline regression when periods of fault development were relatively short, and where comparatively simple down-to-the-basin fault patterns were formed."

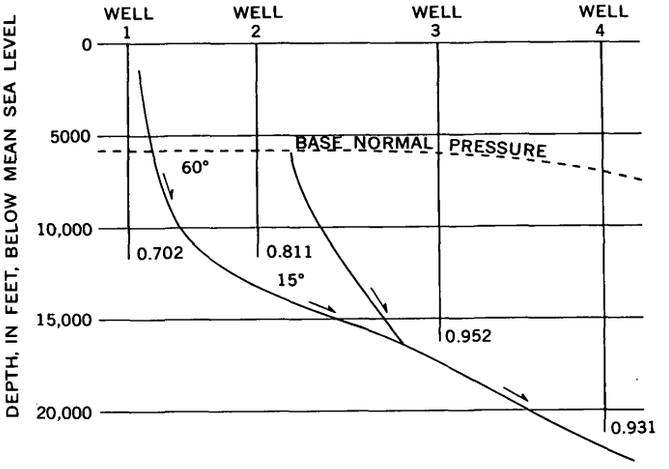

Figure 6.—Relation of the fault angle to the interstitial fluid pressure, expressed as the geostatic ratio observed at the total depth reached by each well. Vertical and horizontal scales are equal. (Modified from Bruce, 1972.)

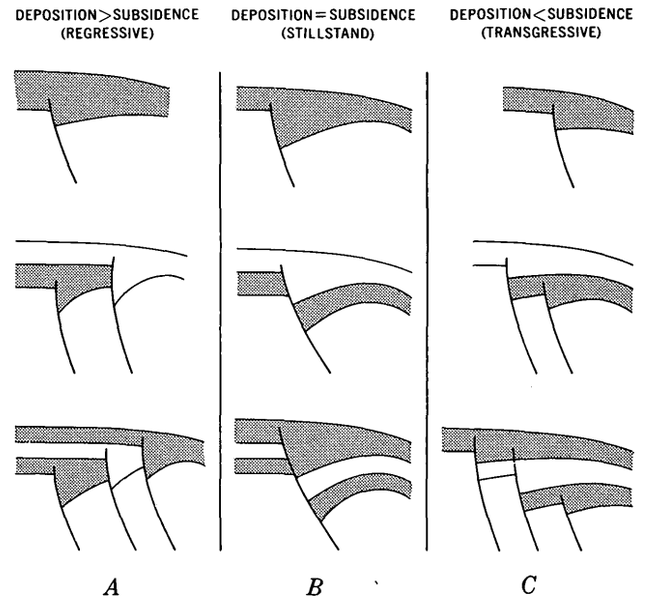

Figure 7.—Development of three types of growth fault systems (from Bruce, 1972).

Recent papers by Lehner (1969, p. 2431–2479), and Wilhelm and Ewing (1972, p. 575–600) show that growth faulting is occurring today at the margin of the Continental Shelf beneath the Gulf of Mexico. Growth fault movement should be expected to begin very early in the cycle of deltaic sedimentation, probably within the first few thousand feet of burial. Fine-grained sediments have their highest interstitial fluid content and least resistance to deformation at this time. Tensional shearing may initiate along the continental slope (fig. 5, stage C) as glide plane movement or submarine sliding

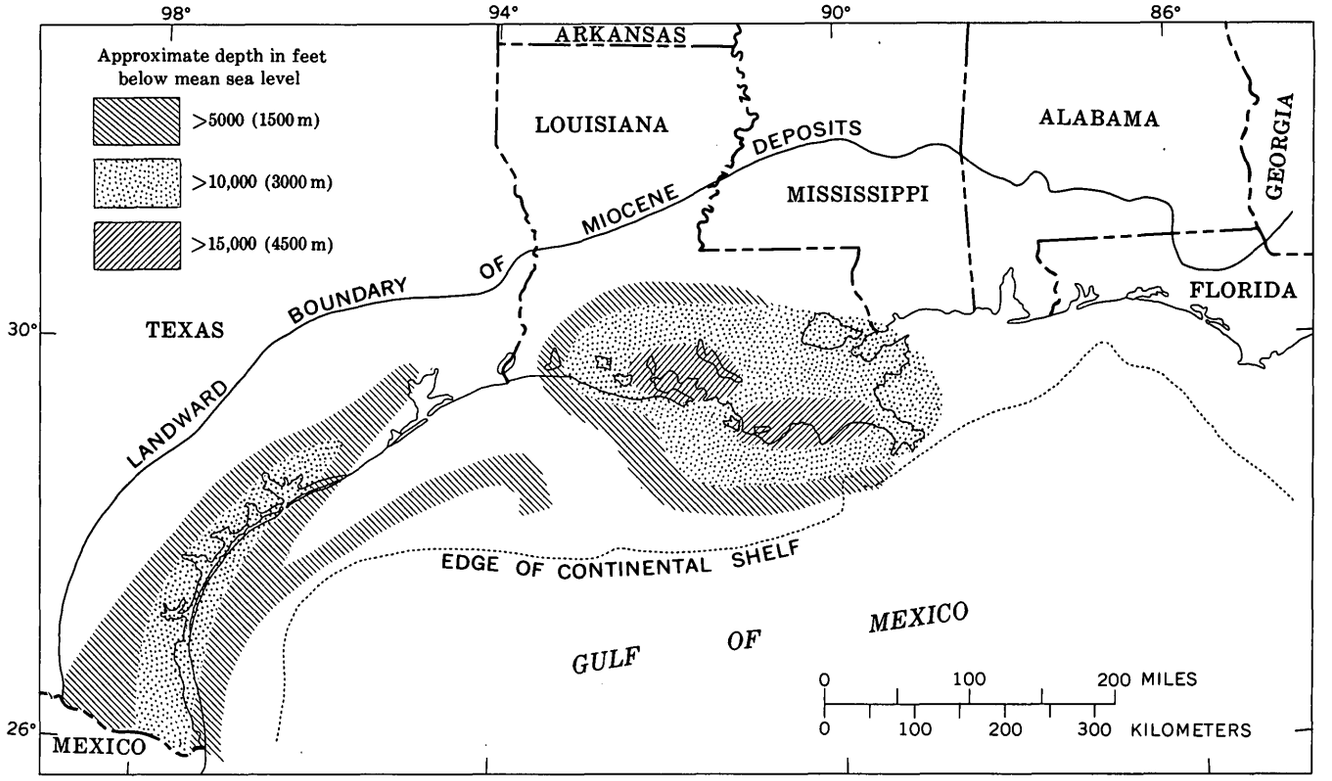

Figure 8.—Areal extent of geopressure zones in Neogene deposits of the northern Gulf of Mexico basin (modified from Jones, 1969b).

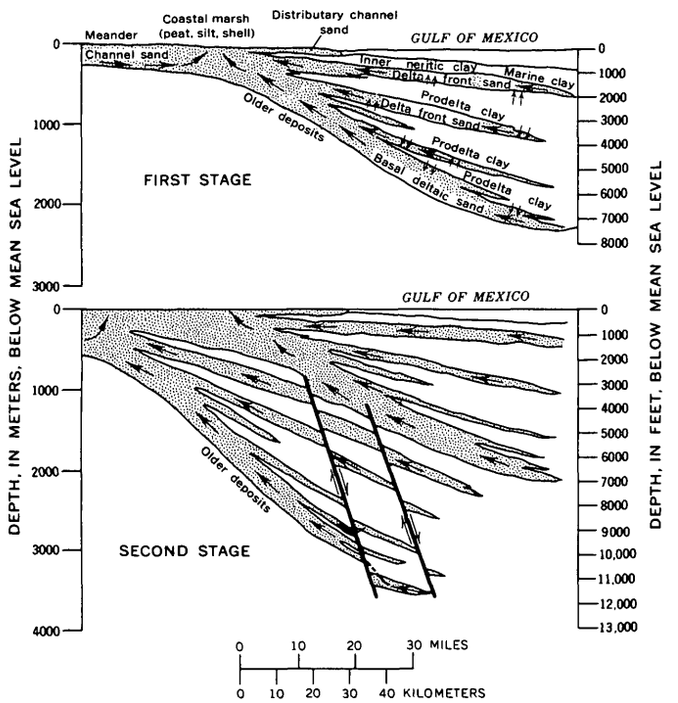

Figure 9.—Effect of growth faulting on the up-dip release of water from compacting deltaic sediments. Arrows indicate movement of water released by sediment compaction. (Modified from Jones, 1969b.)

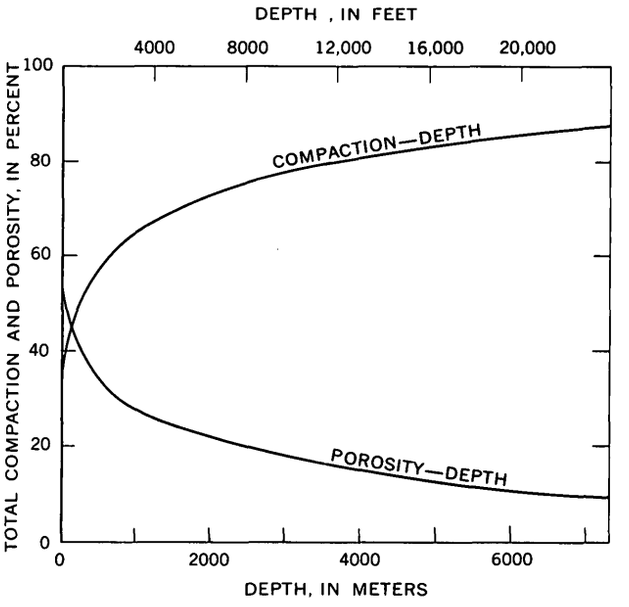

Figure 10.—Relation of compaction and porosity of clay to depth of burial under hydrostatic conditions (modified from Dickinson, 1953).

in response to sediments having exceeded their angle of repose. This is occurring today off the mouth of the South Pass of the Mississippi River.

Progressive loading on the gulfward side of the growth fault, coupled with differential compaction, would sustain the

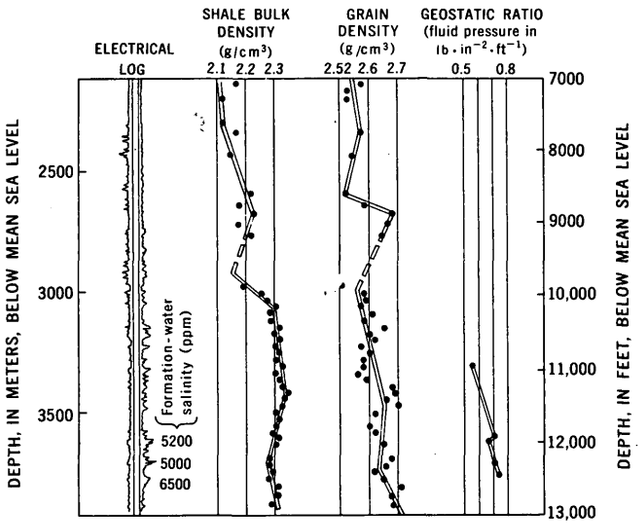

Figure 11.—Relation of shale bulk density, grain density, and geostatic ratio to depth of burial, Matagorda County, Tex. (modified from Myers and Van Siclen, 1964).

rotational stress, allowing progressive accumulation of sediment at the site. The thicknesses of individual beds in the downthrown block would then become greater than those of their up-dip correlatives. Flowage of salt at depth from beneath the advancing depositional mass toward the abyssal Gulf, as suggested by Lehner (1969, p. 2442), and Wilhelm and Ewing (1972, p. 593) (fig. 5), the compaction of underlying geopressured shale, and basinal subsidence combine to propagate the fault plane upward as deposition continues.

As fault movement proceeds and sand beds are rotated downward, their severed ends lie against shale beds across the fault plane; avenues of escape for expelled waters become progressively more restricted. Under these conditions the mashed sediments in the fault plane probably transmit fluids more readily than the compacting shale beds adjacent, and geopressured water flows from the shale beds into and upwards along the fault plane—the easiest route of escape. As pore pressure in the fault plane is increased, frictional drag is reduced, facilitating fault movement. Evidence that this avenue of escape has been much used is shown by isothermal profiles on structure sections, and by maps of the 70°C (158°F) isogeothermal surface, which show more than 1,800 m (6,000 ft) of relief in the vicinity of fault zones in south Texas. Upflux of high temperature water from the geopressured zone into the hydrostatic zone via the fault plane is a possible explanation of these features. Resistance to fluid movement increases and fault movement decreases as pore space is reduced with deepening burial, and escape routes become longer and more circuitous. Fault movement gradually becomes insignificant or ceases, and the locus of deposition and accompanying basinal subsidence shift gulfward. The potential for reactivation and movement, however, continues so long as undercompacted shales and salt remain buried beneath the thick sedimentary pile.

Sediments dilated by excess pore water, with pressures approaching geostatic, act as thermal insulating beds—resulting in high temperatures and large geothermal gradients within the zones where structural deformation is most effective in retarding the escape of fluids. Geothermal gradients show this effect as a "dog leg" at the top of the geopressure zone (fig. 12). The temperature-depth plots for wells in Cameron County, Tex., illustrate the temperature rise associated with a pressure gradient change under geopressured conditions. The geothermal gradient map of a six-county area in the south Texas Gulf Coast (fig. 13) shows gradients ranging from less than 25°C to 100°C per km (1.2°F to 10°F per 100 ft) in the depth interval between the 120°C and 150°C (250°F and 300°F) isogeothermal surfaces, both of which occur within the geopressured zone. Variations in the geothermal gradient reflect aquifer geometry and hydrology in the interval between the isogeothermal surfaces both of which are affected by structural deformation. Thermal gradients are highest in areas where fluid movement is most restricted by the geopressuring seal.

High temperatures decrease viscosity and increase plasticity in geopressured sediments, particularly rock salt and shale. The tendency of salt to flow increases directly with temperature—it becomes a perfect plastic at about 300°C (572°F)—and shale pore waters move more readily as their viscosity is decreased.

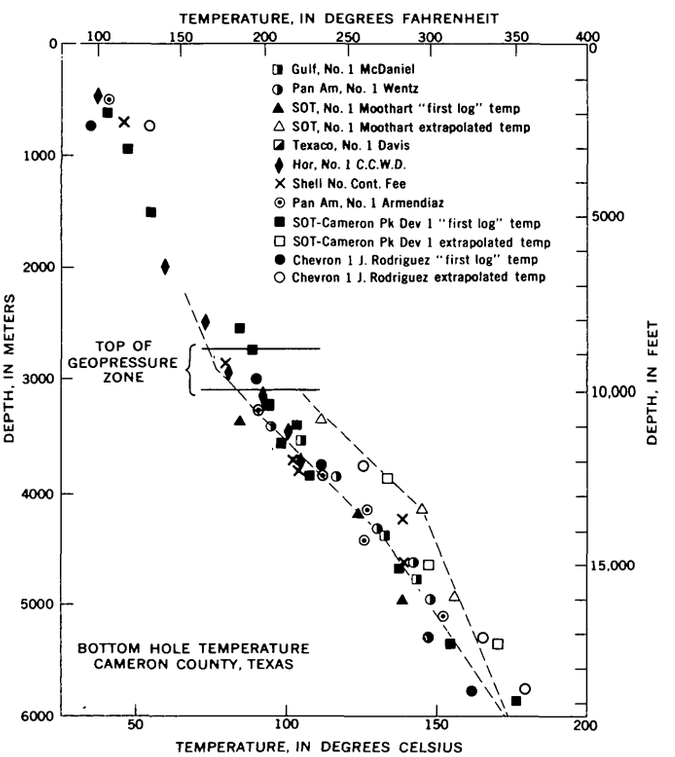

Figure 12.—Graphs showing changes in the geothermal gradient near the top of the geopressure zone, Cameron County, Tex.

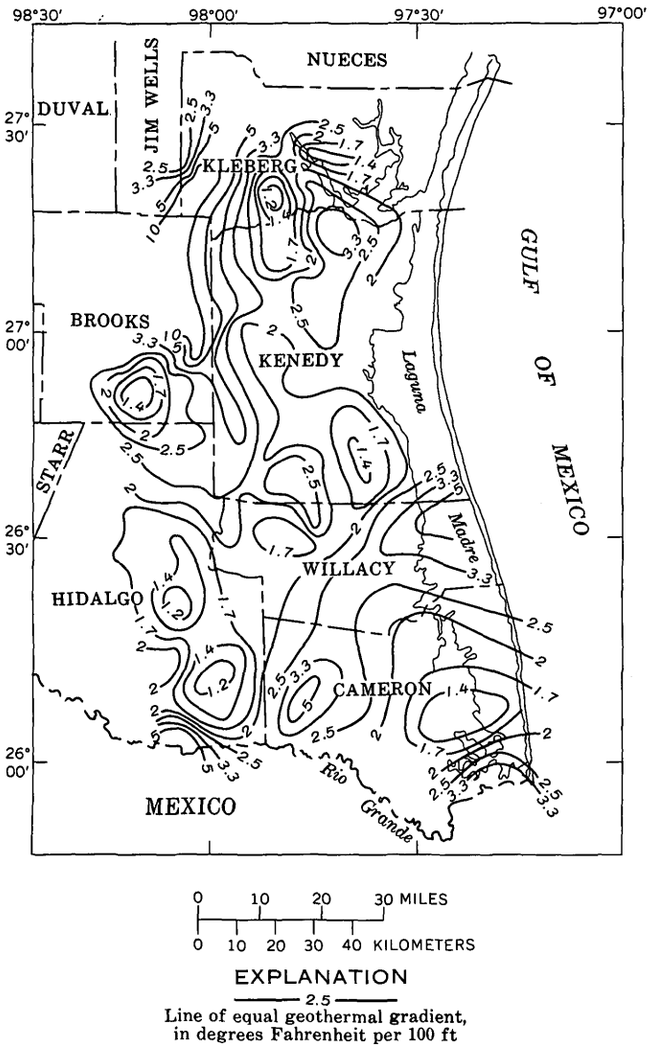

Figure 13.—Geothermal gradients between the 120°C and 150°C (250°F and 300°F) isogeothermal surfaces, south Texas Coastal Plain (from Wallace, 1970).

Shale minerals undergo diagenetic changes at elevated temperatures. Burst (1969, p. 79) states that the maximum rate of dehydration of clay occurs between about 80°C and 120°C (180°F and 250°F)—transforming montmorillonite to illite and mixed layer clays. Bound and intracrystalline water are released by the diagenetic process, in an amount equal to almost half the volume of clay mineral so altered—further reducing the load-bearing strength of the shales. Intracrystalline and bound water is fresh water, and it therefore readily drains from the clay beds to adjacent aquifers—unimpeded by resistive osmotic gradients.

The semipermeable property of clay beds is the factor that preserves geopressure for millions of years (Jones, 1969a, p. 803–810) thus providing the semiplastic substrate required for development of growth faults. Clay beds in this setting will pass water, but not the ionized dissolved solids. As some water loss occurs through the clay beds from the geopressured to the hydrostatic zone above, osmotic forces are generated between the salty water below and freshened water above. When flow has resulted in a concentration differential sufficient to generate osmotic forces downward equal to hydraulic forces upward, flow "leakage" from the geopressured zone stops. Only when structural movement abuts sand beds of the geopressured zone against sand beds of the hydrostatic zone can large scale leakage occur. Thus, the hydrology of clay is the dominant factor in the structural evolution of the Gulf Coast geosyncline.

REFERENCES CITED

Bornhauser, Max., 1958, Gulf Coast tectonics: Am. Assoc. Petroleum Geologists Bull., v. 42, p. 339–370.

Bruce, C. H., 1972, Pressured shale and related sediment deformation—a mechanism for development for regional contemporaneous faults: Gulf Coast Assoc. Geol. Socs. Trans., v. 22, p. 23–31.

Burst, J. F., 1969, Diagenesis of Gulf Coast clayey sediments and its possible relation to petroleum migration: Am. Assoc. Petroleum Geologists Bull., v. 53, p. 73–93.

Dickinson, George, 1953, Geological aspects of abnormal reservoir pressures in Gulf Coast Louisiana: Am. Assoc. Petroleum Geologists Bull., v. 37, p. 410–432.

Jones, P. H., 1969a, Hydrodynamics of geopressure in the northern Gulf of Mexico basin: Jour. Petroleum Technology, v. 21, p. 803–810.

——1969b, Hydrology of Neogene deposits in the northern Gulf of Mexico basin: Louisiana Water Resources Research Inst. Bull. GT-2, 105 p.

Lehner, Peter, 1969, Salt tectonics and Pleistocene stratigraphy on Continental Slope of northern Gulf of Mexico: Am. Assoc. Petroleum Geologists Bull., v. 53, p. 2431–2479.

Martin, G. B., 1972, Abnormal high pressure and environment of deposition, *in* Third symposium on abnormal subsurface pore pressure, Soc. Petroleum Engineers A.I.M.E. and Louisiana State Univ., Baton Rouge, La.: Soc. Petroleum Engineers A.I.M.E. Proc., p. 51–66.

Murray, G. E., 1961, Geology of Atlantic and Gulf coastal province of North America: New York, Harper Brothers, 692 p.

Myers, R. L., and Van Siclen, D. C., 1964, Dynamic phenomena of sediment compaction in Matagorda County, Texas: Gulf Coast Assoc. Geol. Socs. Trans., v. 14, p. 241–252.

Thorsen, C. E., 1963, Age of growth faulting in southeast Louisiana: Gulf Coast Assoc. Geol. Socs. Trans., v. 13, p. 103–110.

Wallace, R. H., 1970, Abnormal pressures and potential geothermal resources in the Rio Grande Embayment of Texas, *in* Second symposium on abnormal subsurface pressure, Baton Rouge, La.: Louisiana State Univ. Proc., p. 87–116.

Wilhelm, Oscar, and Ewing, Maurice, 1972, Geology and history of the Gulf of Mexico: Geol. Soc. America Bull., v. 83, p. 575–600.

Jour. Research U.S. Geol. Survey
Vol. 2, No. 5, Sept.-Oct. 1974, p. 519—526

AERIAL OBSERVATIONS OF SUSPENDED-SEDIMENT PLUMES IN SAN FRANCISCO BAY AND THE ADJACENT PACIFIC OCEAN

By PAUL R. CARLSON and DAVID S. McCULLOCH,
Menlo Park, Calif.

Work done in cooperation with the National Aeronautics and Space Administration

Abstract—Aerial observations of suspended-sediment patterns in the San Francisco Bay estuary system, together with shipboard water-property measurements, show that a plume of highly turbid, low-salinity water associated with the Sacramento-San Joaquin River system bifurcates in the central bay. During a winter storm period when Sacramento-San Joaquin discharge was about 7,800 m^3/s (275×10^3 ft^3/s), one lobe of the plume flowed 15 km (9.3 mi) south of the San Francisco—Oakland Bay Bridge while the main lobe flowed seaward 30 km (18.6 mi), covering an area of about 900 km^2 (347.5 mi^2). Salinity differences of 1—2 parts per thousand and light transmission differences of 15—20 percent were measured between the plume and the ambient waters. As the discharge from the Sacramento—San Joaquin River system decreased to 100 m^3/s (3.5×10^3 ft^3/s), the surface area of the plume in the Gulf of the Farallones decreased to about 100 km^2 (38.6 mi^2). In south San Francisco Bay, the plume characteristics are different during high and low river discharge. As the discharge decreased from 7,800 m^3/s (275×10^3 ft^3/s) in the winter to 100 m^3/s (3.5×10^3 ft^3/s) in the summer, the flow rate of the plume front into the south bay decreased from 113 cm/s (2.25 knots) to 65 cm/s (1.30 knots). These seasonal changes in flow rates and volumes of this critical water source must be considered when developing physical and (or) chemical models of the estuary.

Studies of discrete water masses in estuaries and coastal waters are hampered because on-the-water observations, made at single stations, are not sufficiently synoptic to describe water properties in dynamic systems where water masses move in response to winds, tides, and ocean currents. In San Francisco Bay and the adjacent Pacific Ocean, aerial photography provides a synoptic view of discrete water masses that can be differentiated by suspended-sediment load. The use of aerial photographs, together with in situ measurements, makes it possible not only to determine areal distribution of the sediment-laden water plumes but also to relate their movement to tide state and their areal extent and suspended-sediment load to seasonal variation in freshwater inflow.

The aerial photographs were taken with a 35-mm camera equipped with Kodachrome II film and a Honeywell UV filter.[1] The aircraft was flown at altitudes of 3,000 m (10,000 ft) or less. Variables measured on cruises coincident with aerial overflights were salinity (in parts per thousand), turbidity (in percentage of light transmission), and suspended-sediment concentration (in milligrams per liter). Salinity was measured with an electrodeless induction salinometer and turbidity, with a 10-cm beam path transmissometer (alpha meter). Suspended-sediment samples were collected with a Van Doren bottle from a depth of 1—2 m, then vacuum filtered through 0.45-μm silver filters.

Two plumes of low-salinity, near-surface water were observed: one flowing into south San Francisco Bay, the other through the Golden Gate Strait into the Gulf of the Farallones (fig. 1). A total of 39 observations were made between November 1967 and June 1973, directly from: (1) light aircraft and helicopter at altitudes of less than 3,000 m (10,000 ft), (2) Telegraph Hill in San Francisco, which provides a good view of the central bay, and (3) cruising ships, and indirectly from: (1) high-altitude aerial photographs from altitudes up to 20,000 m (≈65,000 ft), and (2) satellite imagery from an altitude of about 915 km (570 mi). The high-altitude photographs and images were taken by the U.S. Air Force and the National Aeronautics and Space Administration. Gross concepts of the history of these two plumes and the factors that control their size may be developed from a series of aerial photographs taken throughout the year during conditions of high and low runoff (fig. 2).

SOUTH SAN FRANCISCO BAY

High-discharge conditions

During high discharge of the Sacramento—San Joaquin River system, a pronounced plume of low-salinity, high-turbidity

[1] Use of these terms in this paper is for descriptive purposes only and does not constitute an endorsement of the products by the U.S. Geological Survey.

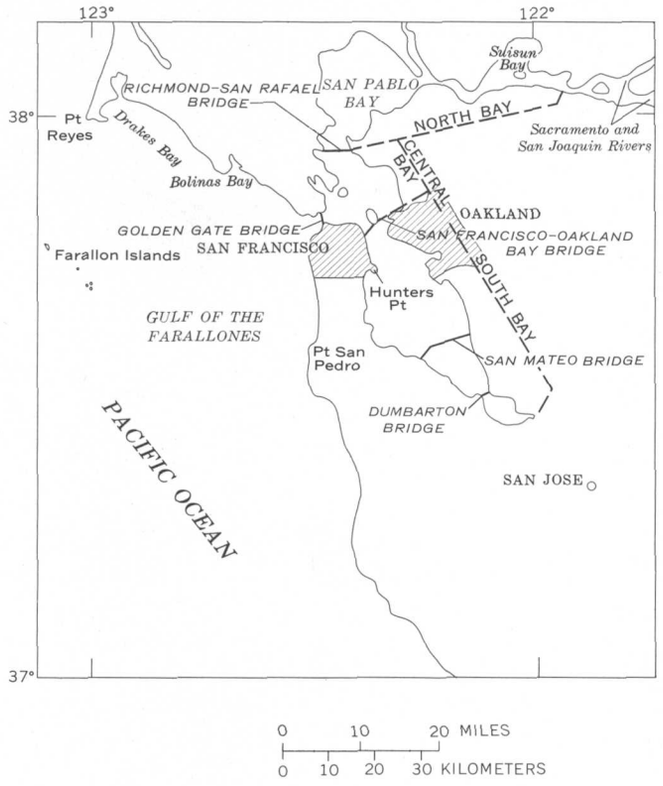

Figure 1.—San Francisco Bay estuary and the Gulf of the Farallones.

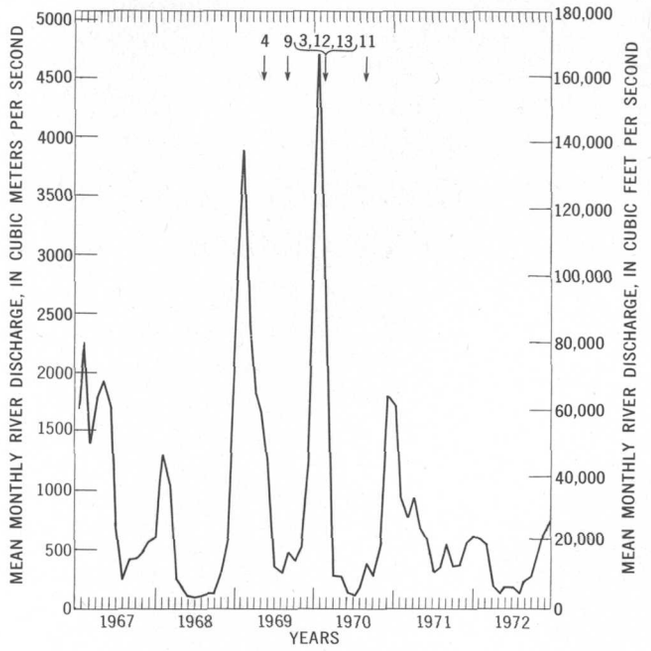

Figure 2.—Discharge from the Sacramento–San Joaquin River system (includes Yolo Bypass) into San Francisco Bay estuary, January 1967–December 1972. Discharge data from U.S. Bureau Reclamation (Norman Beck, oral commun., 1973) and U.S. Geological Survey (Sally Walker, written and oral commun., 1973). Numbers at top indicate when the photographs included in this report (figs. 3,4,9,11,12,13) were taken.

brown water can be observed flowing into south San Francisco Bay at certain times of the tidal cycle. This plume starts to move across the central bay about 3 h after maximum ebb at the Golden Gate, at a time when water from the north bay is in the last stages of ebb tide, but owing to the tidal-phase difference, the flood stage is just beginning in the south bay (Smith, 1966).

The lack of rainfall and high rate of evaporation prior to this high-discharge period produce salinities in the south bay that in many years approach or exceed the salinity of the ocean water (33–34 parts per thousand) adjacent to San Francisco Bay.

It is into this high-salinity, low-turbidity blue-green water in south San Francisco Bay that the plume of turbid brown water flows. The higher concentrations of suspended sediment (30–40 mg/l over ambient concentrations) in the incoming plume of flood water make it easily visible (fig. 3). The turbid brown water assumes a lobate front that maintains its integrity as it moves to approximately 15 km (9.3 mi) south of the Bay Bridge. Turbulence and debris concentrated at the leading edge of the plume (fig. 4) create sufficient relief to make the front of the plume visible on a ship's radar more than a mile away. A comparison of turbidity, salinity, and suspended-sediment concentrations within the plume and the adjacent south bay water during January 1970 (fig. 5) shows that in any one tidal cycle the observed salinities of the browner low-salinity water and more blue-green ambient bay water differ by only 1 or 2 parts per thousand, whereas light transmissivity (a measure of turbidity) readings often differ by 15 percent, and the amount of suspended sediment in the plume may be four times greater than in the ambient south bay water.

Figure 3.—Plume of low-salinity, high-turbidity water (lighter color) that has moved approximately 15 km (9.3 mi) into south San Francisco Bay. San Francisco (left) and Oakland (right), connected by the San Francisco–Oakland Bay Bridge. View northwest, from an altitude of 1,800 m (5,800 ft), January 28, 1970.

Figure 4.—Turbulent front of low-salinity water (lighter color) advancing into south San Francisco Bay. The dark elongate patch (center) is rhodamine WT dye dropped from a helicopter about 20 min earlier. View from a helicopter at an altitude of 150 m (500 ft), May 6, 1969, looking west toward Army Street Pier, San Francisco. Photograph by G. E. Stoertz. (See Stoertz and others, 1970, for locations of dye drops.)

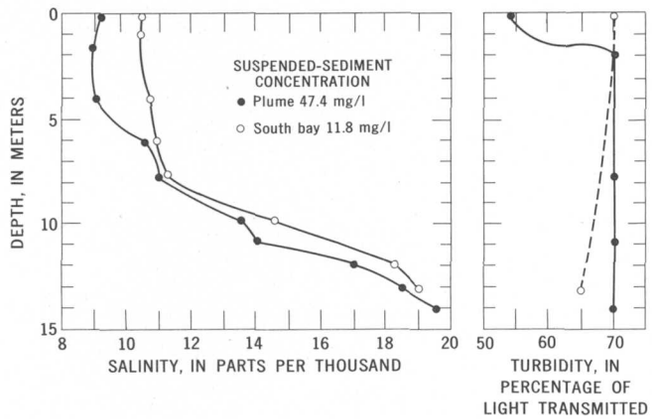

Figure 5.—Salinity, turbidity, and suspended-sediment concentration in front of and just behind the leading edge of the low-salinity, high-turbidity water plume shown in figure 3. Concentration of suspended sediment was measured from samples collected approximately 1 m below the water surface. Samples and measurements were taken January 27, 1970, at the same time in the tidal cycle as the aerial photograph (fig. 3).

Aerial observations (fig. 3) provide a basis for estimating the surface area covered by this turbid plume: the length was approximately 15 km (9.3 mi) and the width approximately 4 km (2.5 mi), a surface area of 60 km^2 (23.2 mi^2). If it is assumed that the in situ measurements (fig. 5), which indicate a minimum thickness of about 2 m (6.6 ft), are representative throughout the area covered by the plume, the calculated volume is 12×10^7 m^3 (424×10^7 ft^3).

Intermediate discharge conditions.

Discharge from the Sacramento—San Joaquin River system is high during the winter storm season and often remains relatively high during the spring snowmelt (March-June) (fig. 2). In May of 1969, the plume was tracked into the south bay to approximately 15 km (9.3 mi) south of the Bay Bridge (fig. 6). Also during May 1969, Rhodamine WT dye was dropped from a helicopter just behind the leading edge of the plume of low-salinity, high-turbidity water as it advanced into the south bay (Stoertz and others, 1970). Dye movement, monitored over a period of 2 h by a radar-tracked helicopter, showed that the plume front moved south at a rate of 125 cm/s (2.5 knots). The dye formed a circular patch upon impact with the water and quickly became elongate parallel to the flow of water toward the front of the plume (fig. 4), suggesting a flow of water within the plume toward the plume front. The water must then roll under as the plume overrides the south bay water.

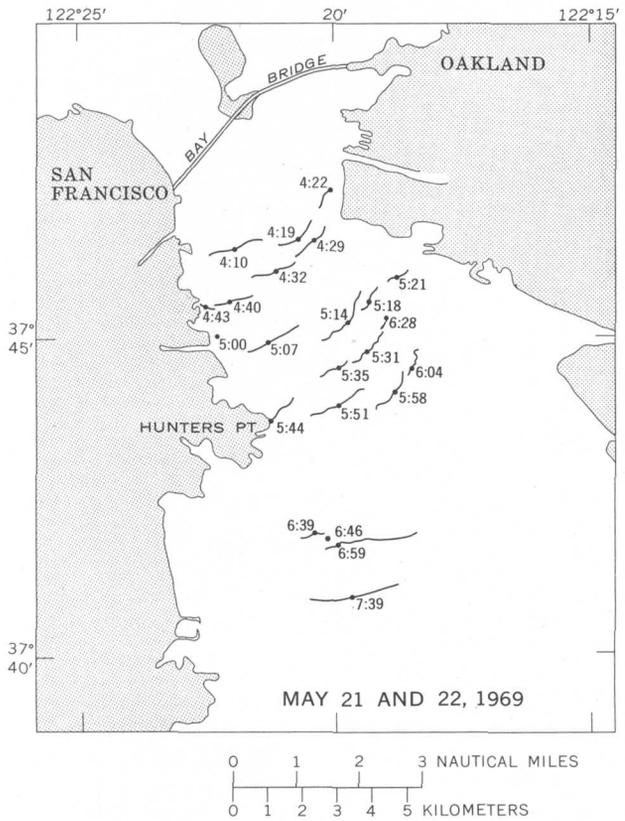

Figure 6.—Advance of low-salinity, high-turbidity water into south San Francisco Bay (average speed 100 cm/s or 2 knots). Dots, actual locations occupied by the vessel; positions determined by radar. *Lines extending from dots, front of plume visible from* bridge of vessel. Times for each location, hours and minutes after maximum ebb at the Golden Gate. Positions marked 4:10 through 6:59 occupied May 21, 1969, and position marked 7:39 occupied May 22, 1969.

Low-discharge conditions

The low-discharge stage of the Sacramento–San Joaquin River system begins in the summer after the decrease in snowmelt discharge (fig. 2) and lasts until the first major flood of the next rainy season. As the river discharge decreased from 7,800 m^3/s ($275X10^3$ ft^3/s) in the winter to 100 m^3/s ($3.5X10^3$ ft^3/s) in the summer, the flow rate of water from the north to the south bay also decreased. The arrival times of the plume front at the Bay Bridge and at Hunters Point (fig. 7) indicate a difference of 2 and 3 h, respectively, in periods of high- and low-discharge conditions, a decrease in flow rate from 116 cm/s to 67 cm/s (2.25 to 1.30 knots).

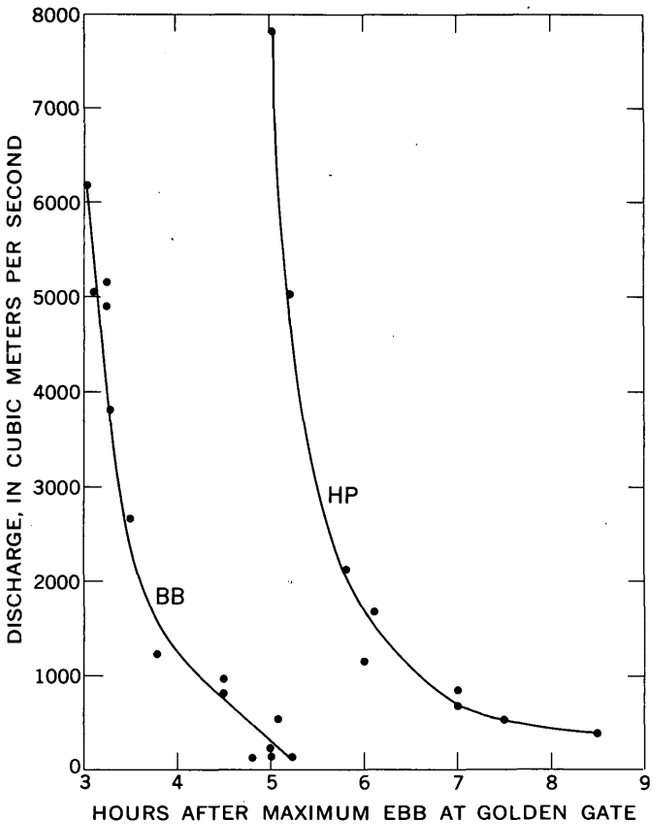

Figure 7.–Arrival time of suspended-sediment plume at the San Francisco–Oakland Bay Bridge (BB) and at Hunters Point (HP) relative to the Sacramento–San Joaquin River system discharge for January 1969–July 1973. Discharge data from U.S. Bureau Reclamation (Norman Beck, oral commun., 1973) and U.S. Geological Survey (Sally Walker, oral and written commun., 1973).

The colors of the two water bodies (plume and south bay) during the summer-fall season are the reverse of what they are during the winter-spring season. As river discharge is lowered and the amount of suspended sediment is reduced (fig. 8), the plume becomes greener, whereas the south bay water maintains its brown color because of (1) the presence of blooming phytoplankton that proliferate during the months of high solar radiation, and (2) wind-induced resuspension of bottom sediment in the shallower waters.

The visual effect of the low-turbidity, low-salinity water on the south bay is not as great during this period of low river

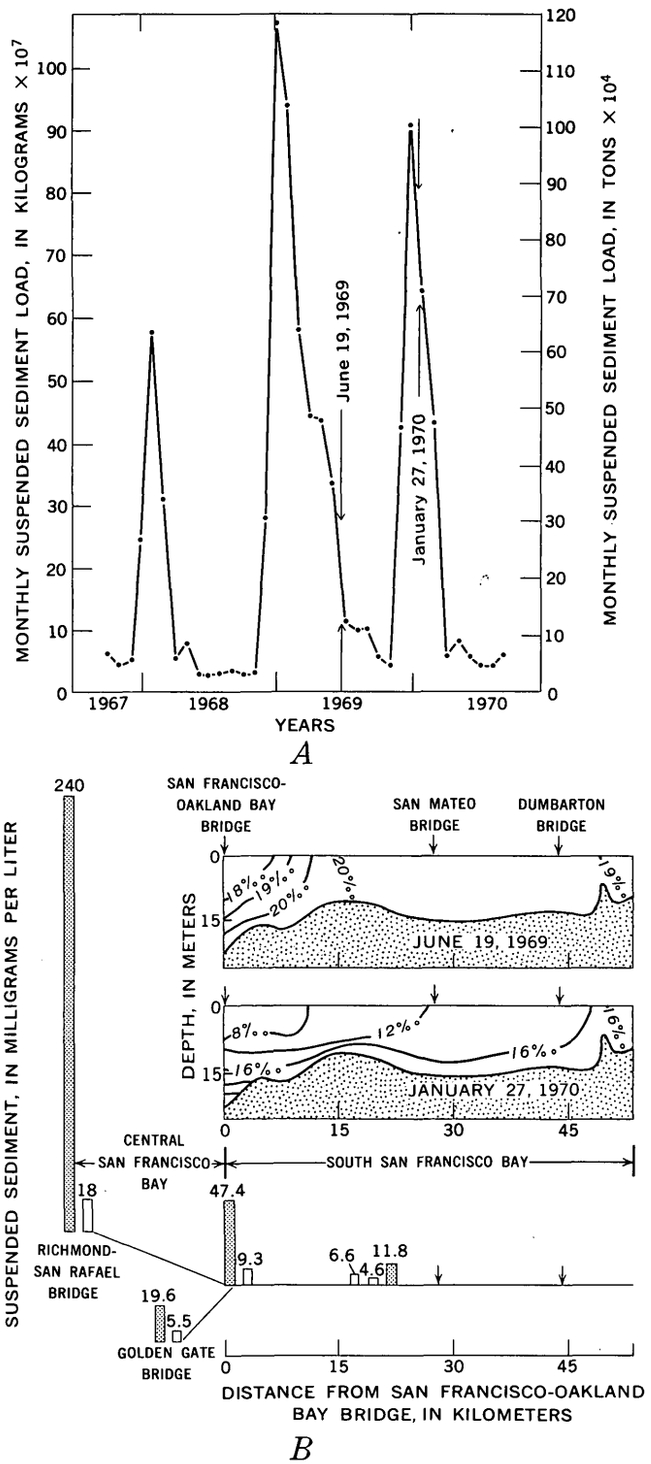

discharge as during the time of higher river discharge. For example, during August 1969 (total monthly river discharge of 1.6×10^9 m^3 (56.5×10^9 ft^3); see fig. 2), the visual difference in water characteristics could be detected only faintly from an aircraft (fig. 9) and not at all from a boat. And the front of the southward-flowing water becomes more digitate at times of low discharge than at times of high discharge (compare figs. 3 and 9). The intricacy of the water pattern along the digitate contact between the plume and the south bay water points up the importance of an aerial synoptic view in evaluating the individual water measurements.

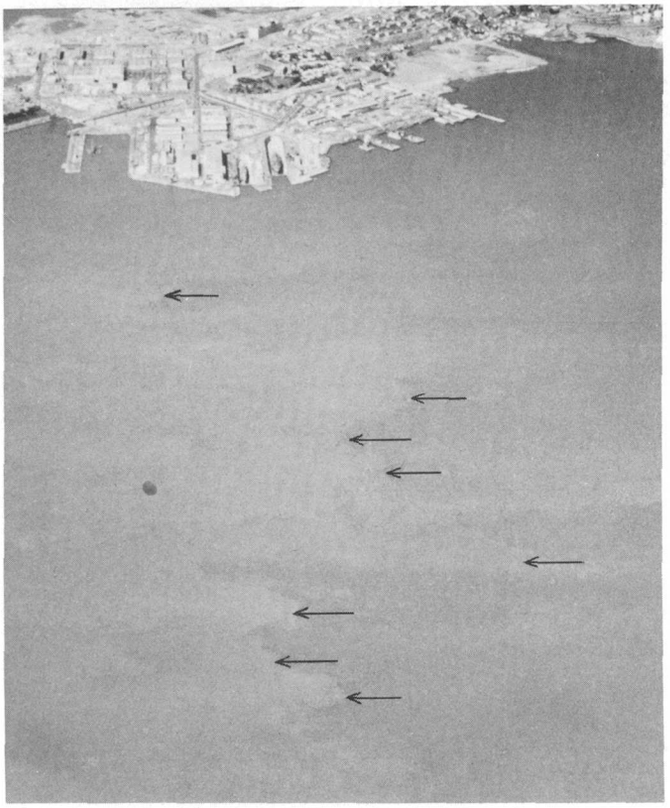

Figure 9.—Poorly defined front (shown by arrows) of low-salinity water off Hunters Point characterized by a digitate contact typical of low-discharge conditions. Lighter colored water to the left (south) is browner than the incoming water. Salinities measured in this part of the bay on the following day were approximately 28 parts per thousand. Taken from an altitude of ≈1500 m (5,000 ft), August 27, 1969.

Figure 8.—Hydrologic data from the San Francisco Bay estuary system. *A*, Suspended-sediment load carried into the estuary by the Sacramento–San Joaquin River system (Oct. 1967–Sept. 1970). Data from U.S. Geological Survey (1968-1970). *B*, Suspended-sediment concentration in San Francisco Bay and corresponding salinity in south San Francisco Bay during high- and low-discharge conditions. Bar graphs represent suspended-sediment concentrations (milligrams per liter) as measured at the Richmond–San Rafael Bridge, the Golden Gate Bridge, and south San Francisco Bay. Salinity contours, in parts per thousand. Solid bars, high-discharge conditions, January 27, 1970; open bars, low-discharge conditions, June 19, 1969.

GULF OF THE FARALLONES

The second plume of turbid, low-salinity water described in this paper flows through the Golden Gate into the Gulf of the Farallones, which occupies a large indentation in the central California coast between Point Reyes on the north and Point San Pedro on the south (fig. 1). The western limit of this gulf is the partly submerged granitic ridge of the Farallon Islands, about 40 km (25 mi) west of the Golden Gate.

Throughout the year the direction of net nontidal drift of low-salinity surface and higher salinity bottom water remains the same through the Golden Gate; surface water from the bay has a net nontidal drift out and bottom water has a net nontidal drift in through the strait (Conomos and others, 1971). The size of the sediment-laden plume that enters the gulf increases with increase in discharge into the bay from the Sacramento–San Joaquin River system. A comparison of plume surface area and discharge (fig. 10) indicates that as the discharge increases from 100 m^3/s (3.5×10^3 ft^3/s) to 7,800 m^3/s ($>275 \times 10^3$ ft^3/s), there is a corresponding increase in the area of the plume from about 100 km^2 (38.6 mi^2) to 900 km^2 (347.5 mi^2).

The location of the seaward edge of the plume shows a corresponding change. In time of low or intermediate discharge characteristic of most of the year, the turbid, low-salinity surface water can be observed only a few kilometers seaward of the Golden Gate (fig. 11). During the winter high-discharge period when monthly discharges of several hundred million cubic meters (several million acre feet) are common (fig. 2), the plume extends many kilometers seaward of the Golden Gate.

In January 1970, a year of particularly high discharge, the well-defined edge of the plume was observed 30 km (18.6 mi) seaward (fig. 12), and the plume had a maximum width of approximately 30 km (18.6 mi). The northwestern edge extended about 25 km (15.5 mi) north of the Golden Gate Strait, halfway between Point Reyes and Bolinas Bay. The southeastern edge of the turbid, low-salinity water flowed about 5 km (3.1 mi) south of the Golden Gate, suggesting a northwestward surface drift of the water very near shore. This direction of flow is consistent with the winter season's northward flow of the near-shore water along the California coast in response to the winter winds, which are primarily from the south (Schwartzlose and Reid, 1972). The plume was brownish gray green and had a pronounced foam line at its leading edge (see fig. 13). This turbid water advanced as a relatively smooth convex front across the bluer, less turbid, more oceanic water.

Two weeks after aerial observations were made (figs. 12, 13), near-surface measurements (1–2 m depth) in the plume and Gulf of the Farallones showed differences in salinity of 1.5

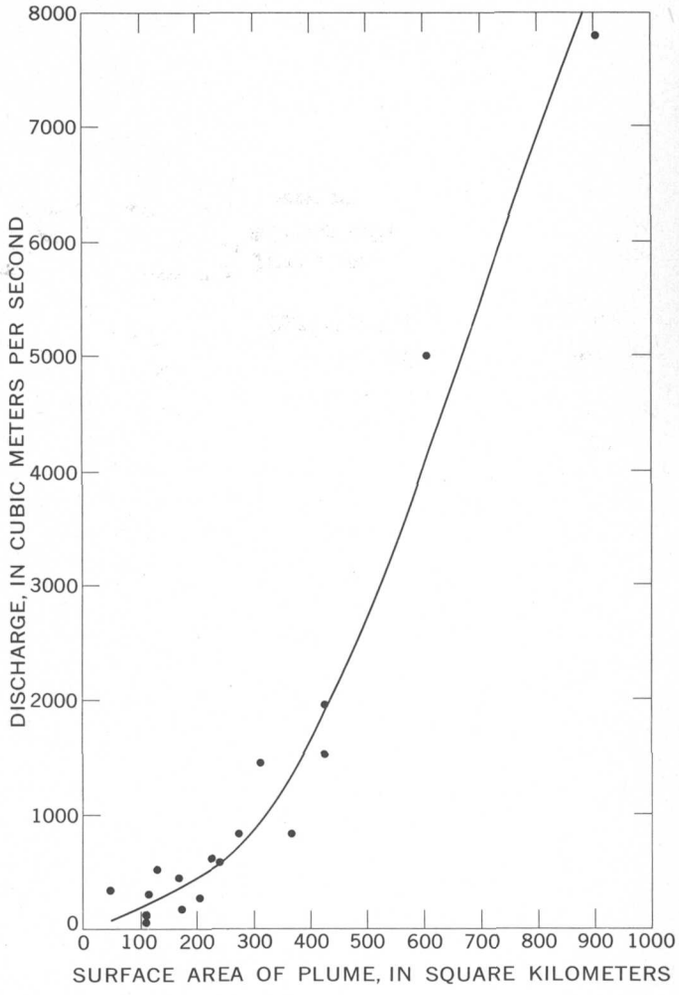

Figure 10.—Surface areas of suspended-sediment plumes in the Gulf of the Farallones relative to discharge from the Sacramento–San Joaquin River system (includes Yolo Bypass). Surface areas of plumes measured from aerial photographs and satellite images taken from November 1967 through May 1973. Discharge data from U.S. Bureau Reclamation (Norman Beck, oral commun., 1973), and U.S. Geological Survey (Sally Walker, oral and written commun., 1973).

Figure 11.—Plume of San Francisco Bay water during the dry season extending approximately 8 km (5 mi) into the Gulf of the Farallones. Area of plume, 108 km² (41.7 mi²). San Francisco at right center, Bolinas Bay upper left. Taken from an altitude of 2,865 m (9,400 ft), July 28, 1970.

Figure 12.—Plume of low-salinity, high-turbidity water from the San Francisco Bay system during a period of high freshwater discharge. The front of the lobe is about 30 km (18.6 mi) from the Golden Gate, or two-thirds of the distance to the Farallon Islands in foreground. Total surface area of plume, 900 km² (347.5 mi²). Some internal structure is visible within the plume. San Francisco at extreme right of coastline, coast north of Bolinas Bay at extreme left. Taken from an altitude of 2,090 m (6,000 ft), January 28, 1970.

parts per thousand and differences in light transmission of 20 percent, quite similar to those obtained for the south bay water and plume (figs. 3, 5).

Multiple plume fronts have often been observed in the Gulf of the Farallones (fig. 13). These fronts probably represent tidally modulated outflows of San Francisco Bay water into the Gulf of the Farallones. Relative ages of the fronts can be determined on aerial photographs by examining the overlapping relations of plumes with differing sediment concentrations; the older, less turbid plumes probably have lower sediment concentrations.

Additional observations on the areal extent of the San Francisco Bay affluent were made with an airborne radiometer. Continuous sea-surface radiation data collected from aircraft by the U.S. Coast Guard (1970) on the same day as the aerial observations of figure 12 over the Gulf of the Farallones indicated a large, low-temperature plume. This plume (defined by the 12.8°C isotherm) extended 90 km (55 mi) southwest of the Golden Gate, covering an area of about 6,300 km² (2,400 mi²) (fig. 14). The plume defined by the isotherms suggests that surface water in the central gulf and beyond was being carried south. The seaward edge of the most prominent plume of turbid water seen on the aerial photographs (fig. 12) did not coincide with the isotherms, except along the southern boundary, where the edge of the turbid water plume coincided with the 12.2°C isotherm. A much less

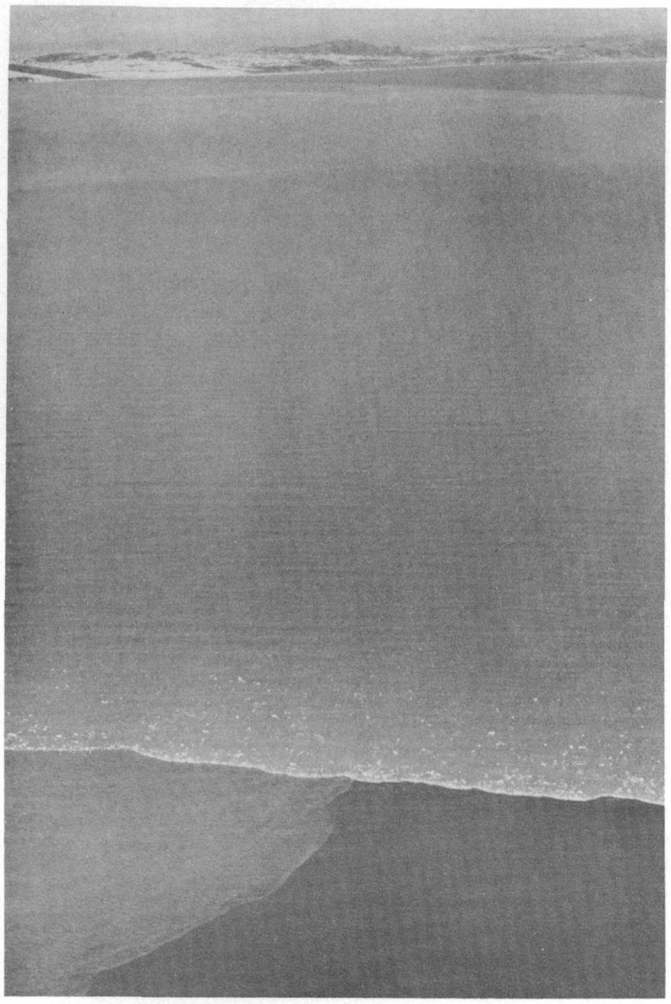

Figure 13.—Three discrete water bodies in the Gulf of the Farallones. Dark-colored water at lower right is ambient Farallon water; light-colored water with prominent foam line is a body of recently discharged low-salinity San Francisco Bay water; water of intermediate shade at lower left apparently is a remnant of an older plume of bay water carried into the gulf during a previous tidal cycle or storm discharge peak. Line extending from land to right edge of upper part of photograph is the southern edge of the plume. Note also line of internal structure within the plume. Shoreline extends south from San Francisco, extreme left, nearly to Point San Pedro, extreme right. Taken from an altitude of 2,090 m (6,000 ft), January 28, 1970.

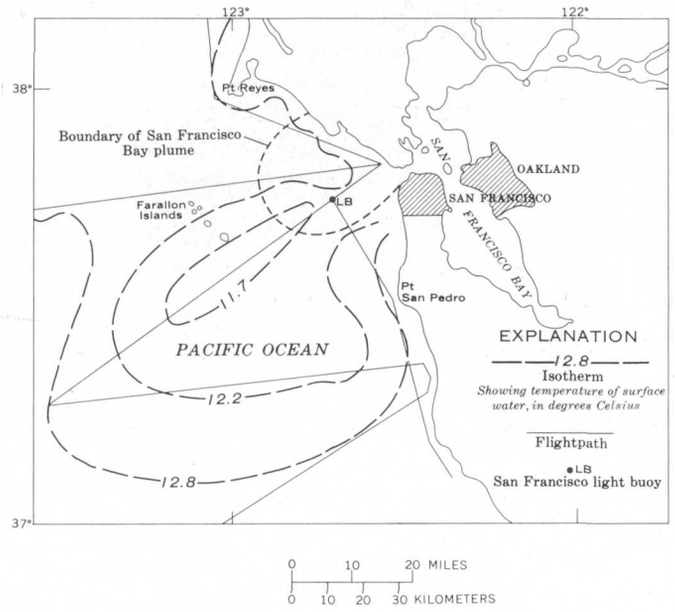

Figure 14—Surface isotherms in the Gulf of the Farallones on January 28, 1970, measured with an airborne infrared-radiation thermometer. Modified from U.S. Coast Guard (1970). Approximate limit of visually distinct San Francisco Bay plume observed January 28, 1970 (see fig. 12) is superimposed on the isotherms.

distinct northeast-southwest-trending water-color boundary that extended from the outer boundary of the plume to beyond the Farallon Islands coincided approximately with the 11.7°C isotherm located immediately south of the Farallon Islands.

The difference in the location of the plume determined by photographs and by radiometer data is probably due to the fact that the aerial photographs record a short-term history of the turbid-water plume of only a few tidal cycles, whereas the temperature data represent a longer, more integrated record of the thermal plume. Wind effects probably account for the different directions indicated by the two plumes. A storm passed through the area the day before the overflights. The resulting northwesterly winds of 55 to 65 km/h (30–35 knots) (weather data from Gulf of Farallones Lightship, U.S. Weather Bureau, San Francisco, Calif., John Stiltz, oral commun., 1972) would tend to push the surface water in a southerly direction—hence, the southwest orientation of the temperature plume. The next day, after the storm had passed, the wind shifted and began to blow from an easterly direction (18–37 km/h; 10–20 knots). This wind blowing from the bay through the Golden Gate Strait would tend to move the water in a more westerly direction. The net effect of wind, tide, and high freshwater discharge combined with a clockwise, rotary tidal current, as measured near the San Francisco light buoy (Marmer, 1926), would be to push the visible plume of turbid water to the northwest.

CONCLUSIONS

1. Light aircraft are effective observation platforms for synoptic views of suspended-sediment patterns that can be used as indicators of circulation of coastal and estuarine surface waters.
2. In the San Francisco Bay system, two plumes of turbid water become clearly visible during periods of high freshwater discharge from the Sacramento–San Joaquin

River system, one flowing out to sea into the Gulf of the Farallones, the other into south San Francisco Bay.

3. The surface area of the turbid-water plume in the Gulf of the Farallones reflects changes in the discharge of the Sacramento–San Joaquin River system. During summer-fall flow conditions, observed when the discharge was 500 m^3/s (17,660 ft^3/s) or less, the plume had an area less than 200 km^2 (77 mi^2). During winter flood conditions, when the discharge reached 7,800 m^3/s (275,400 ft^3/s the area of the plume increased to about 900 km^2 (347.5 mi^2).
4. The turbid-water plume that flows into south San Francisco Bay during a short period of the tidal cycle also reflects changes in the discharge of the Sacramento–San Joaquin system. As the discharge changed from less than 500 m^3/s (17,660 ft^3/s) to more than 5,000 m^3/s (176,600 ft^3/s), the rate of flow of the plume front into the south bay increased from 67 cm/s to 116 cm/s (1.30–2.25 knots).

REFERENCES CITED

Conomos, T. J., McCulloch, D. S., Peterson, D. H., and Carlson, P. R., 1971, Drift of surface and near-bottom waters of the San Francisco Bay system, California–March 1970 through April 1971: U.S. Geol. Survey open-file rept.

Marmer, H. A., 1926, Coastal currents along the Pacific Coast of the United States: U.S. Coast and Geodetic Survey Spec. Pub. 121, 80 p.

Schwartzlose, R. A., and Reid, J. L., 1972, Near-shore circulation in the California Current: California Coop. Oceanic Fisheries Inv. Repts., v. 16, p. 57–65.

Smith, Bernard, 1966, The tides of San Francisco Bay: San Francisco Bay Conserv. Devel. Comm. Rept., 42 p.

Stoertz, G. E., Hemphill, W. R., and Markle, D. A., 1970, Remote analysis of fluorescence by a Fraunhofer line discriminator: Marine Technology Soc., 6th Ann. Mtg., Preprints, v. 2, 24 p.

U.S. Coast Guard, 1970, Pacific Coast continental shelf temperature survey, central area, January 1970: San Francisco, Calif., 1 p.

U.S. Geological Survey, 1968-1970, Water resources data for California, Pt. 2: U.S. Geol. Survey, Water Quality Records, 416 p., 378 p., and 450 p.

Jour. Research U.S. Geol. Survey
Vol. 2, No. 5, Sept.-Oct. 1974, p. 527—531

REGIONAL FLOW SYSTEM AND GROUND-WATER QUALITY IN WESTERN OHIO

By STANLEY E. NORRIS, Columbus, Ohio

Work done in cooperation with the Ohio Department of Natural Resources, Division of Water

Abstract.—Most relatively deep wells drilled in the carbonate aquifers in western Ohio tap a recognizable regional flow system encompassing all or parts of several major basins. The principal recharge area includes the higher, central part of the region, where much of the terrane is hummocky to hilly glacial moraine. The principal discharge areas are the valleys of the major streams and lowlands along Lake Erie. Ground water moving through this system undergoes a progressive change in chemical quality, from a calcium bicarbonate type in recharge areas to a calcium sulfate type in discharge areas. Changes in selected chemical constituents are orderly and, within the observed parameters, predictable.

Limestone and dolomite beds constitute important aquifers in the western half of Ohio, where they crop out or lie beneath a covering of glacial drift that varies widely in thickness. Yielding about 56 *M*gal/d (212,000 m^3/d) of water, or about 5 percent of the State pumpage, they are not the best aquifers in western Ohio; they rank far below the sand and gravel watercourse aquifers. Their importance lies in their capacity to provide a dependable supply over a large area, approximately 16,500 mi^2 (42,735 km^2), or about 40 percent of the State's total land area.

Dependable yields of 5 to 10 gal/min (0.32–0.63 l/s) from individual wells, sufficient for farm and domestic use, can be obtained from the carbonate rocks at virtually any site within their area of occurrence, at depths ranging from 50 to 200 ft (15.2–61 m). Municipal and industrial wells yield 50 to 500 gal/min (3.2–32 l/s) at depths of 150 to 400 ft (46–122 m).

Water from the carbonate rocks is hard and high in mineral content, typical of water from a limestone region. Generally, the water becomes more mineralized the deeper the well is drilled and may change with depth from a calcium bicarbonate to a calcium sulfate type, with an accompanying increase in hydrogen sulfide.

Early concepts (Stout and others, 1943, p. 108) implied that water of good or acceptable quality floated in these rocks as a discrete layer on a base of mineralized water. The purpose of this paper is to show that the chemical quality of water in the carbonate aquifers is not the result of a static system, but of a dynamic interchange between the water and all other elements of the hydrologic system and that chemical quality is intimately related to the regional flow system. Progressive changes in chemical properties occur as the water moves through the aquifers from recharge to discharge areas in response to the natural circulatory system.

This paper draws largely upon results of recent investigations of the Ohio Department of Natural Resources, Division of Water, made in cooperation with the U.S. Geological Survey. In 1968–70 the State drilled and tested 77 wells in the carbonate rocks in a 20-county area of northwest Ohio. The investigation was expanded in 1971 by drilling and testing 53 additional wells in the southwest and central parts of the State. The Geological Survey analyzed the water from the test wells and other selected wells in the study area. Results of these regional investigations are described in reports by Walker and others (1970) and Norris and Fidler (1969, 1971a, b, 1973).

THE AQUIFER FRAMEWORK

The sedimentary beds that principally constitute the carbonate aquifer are units of the Bass Islands Group of Late Silurian age, in combination in much of the area with the underlying Lockport Dolomite of Middle Silurian age. These beds lie on and near the crest of the Cincinnati arch, a slightly north-plunging regional anticline whose long axis extends from north to south across western Ohio from Cincinnati to the vicinity of Toledo. (See fig. 1, "Hydrogeology.") The carbonate beds are nearly flat lying on the crest of the arch and dip away from the crest on both sides at low angles. As the arch was uplifted, the surface was eroded to a generally even plain, exposing progressively older rocks toward the crest. The Lockport Dolomite is exposed on the crest in much of southwestern Ohio, where the Bass Islands Group has been removed by erosion. In the extreme southwestern part of the State the

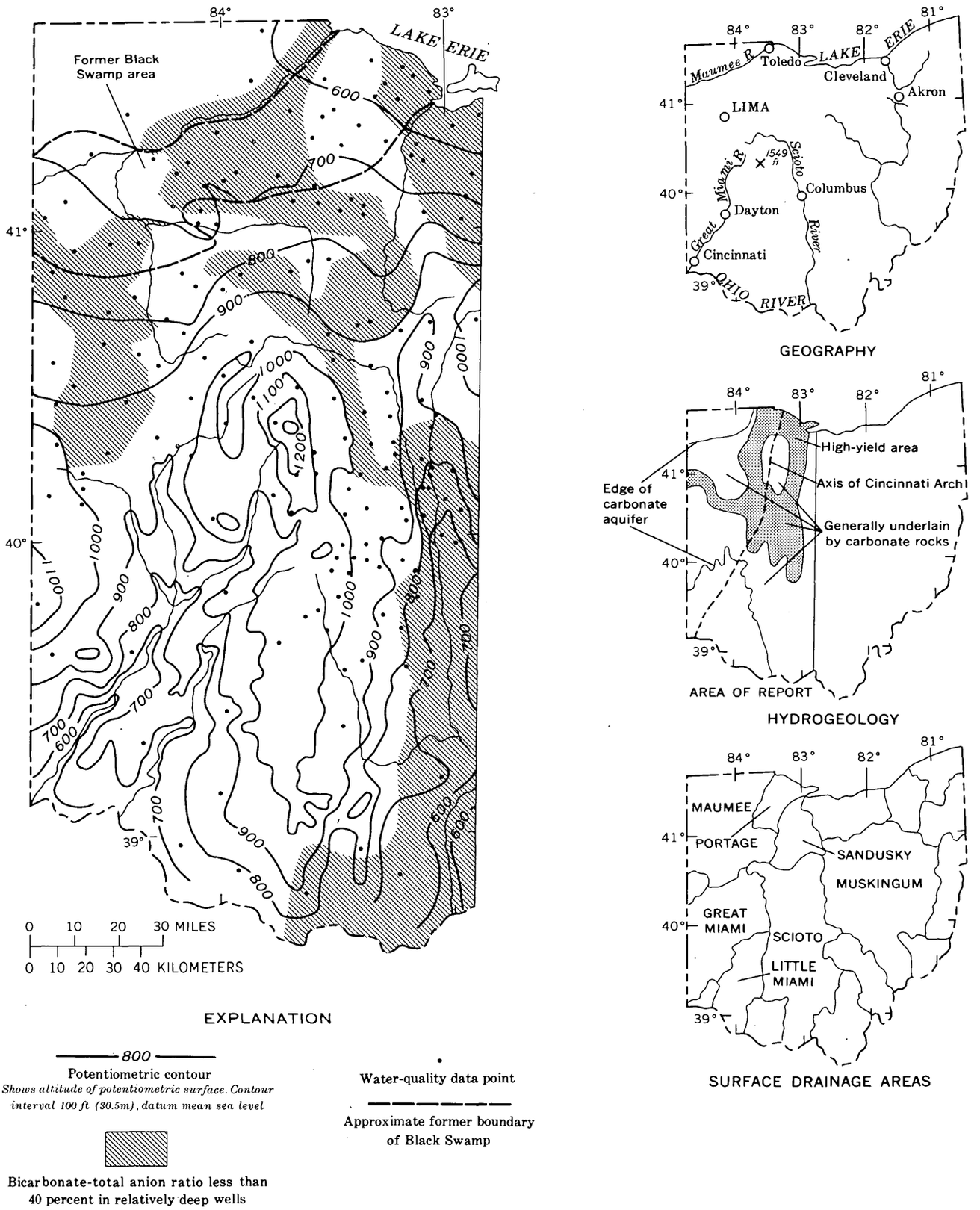

Figure 1.—Index maps and map of western Ohio showing relation of ground-water quality in the consolidated-rock aquifers to to the regional flow system.

carbonate beds have been entirely removed, and the bedrock consists of poorly permeable shale and shaly limestone of Ordovician age. Likewise, in the northwest corner of the State, the carbonate rocks are not a source of water because they are too deeply buried by younger rocks (shale of Devonian age) to be readily accessible to drilling. Figure 1, "Hydrogeology," shows the approximate limits of the carbonate aquifer in the study area.

The carbonate rocks thicken, in the aggregate, on both sides of the arch downdip. On the east side, the thickness ranges from zero at the edge of the outcrop in western Ohio to about 600 ft (183 m) near the eastern boundary of the study area, where locally, as at Columbus, the carbonate sequence includes as much as 130 ft (40 m) of Devonian-age Columbus and Delaware Limestones. Typically, the carbonate aquifer is from 150 to 450 ft (46–137 m) thick in most of the area in which it is a principal source of ground water.

Constituting the thickest and most productive part of the carbonate aquifer, the Bass Islands Group (typically 350 ft (107 m) thick in much of the study area) consists generally of a thinly bedded brown to drab crystalline to granular slightly shaly dolomite. The underlying Lockport Dolomite is much purer, consisting of light-gray to white finely to coarsely crystalline dolomite, typically occurring in beds ranging in thickness from a foot to about 5 ft (1.5 m). Locally, the Lockport grades into reeflike masses, with little or no discernible bedding. The change from normal bedding to the reef phase is accompanied by much thickening; it is estimated that reefs characterize the unit wherever it is more than about 100 ft (30.5 m) thick.

Permeability in the carbonate rocks is chiefly the result of solution by water moving through joints and other openings. Most permeability developed during erosion of the rising Cincinnati arch. For long intervals the upper part of the arch lay at or slightly above sea level, with only the structurally and topographically higher beds subject to ground-water circulation. The beds that underwent most solution and, consequently, those now most permeable underlie an area of relatively high ground-water yield, in which specific capacities of wells generally exceed 5 gal/min per foot (1 l/s per meter) of drawdown (Norris and Fidler, 1971a, 1973). The high-yield area rings the arch in the northern part of the study area and extends across the crest and partly down the flanks in the central part (fig. 1, "Hydrogeology"). Also, in the central part of the area, the permeability of the lower part of the Bass Islands Group, called the Newburg zone, has been increased by ground-water circulation and solution (Norris and Fidler, 1973).

Water in the carbonate aquifer occurs under both confined and unconfined conditions. The confined condition is the more common, owing to the poorly permeable glacial till that generally overlies the bedrock. Also, the dip of the carbonate beds away from major recharge areas along the crest of the Cincinnati arch results in progressive deepening of the zones of highest permeability away from the crest. As the water moves through the carbonate rocks toward points of discharge, it becomes increasingly confined beneath a thickening cover of less permeable rock. The water level in relatively deep wells drilled in topographically low areas typically rises above the water table. In some areas the regional potentiometric head is sufficient to raise the water from the deeper beds to the surface.

GROUND-WATER FLOW SYSTEM

Toth (1962) defined three types of ground-water flow systems—local, intermediate, and regional—that can occur in a typical small drainage basin. A local system, according to Toth, has its recharge area at a topographic high and its discharge area in an adjacent low. Local flow systems originate only where relief is well defined; the higher the relief, the deeper the local systems. An intermediate system is one in which one or more topographic highs intervene between recharge and discharge areas, and these areas do not correspond to the highest and lowest places, respectively, in the basin. A regional system will develop where local relief is small and there is a general slope only. Ground water in a regional system moves in long, arcuate paths from the highest to lowest parts of the basin; generally from the principal drainage divides, which function as recharge areas, to discharge areas in and along major streams and lakes.

Ground-water flow is generally downward in recharge areas, upward in discharge areas, and lateral in intervening areas. In recharge areas the potentiometric head at greater depths in the saturated zone is typically lower than the potentiometric head at the water table, indicating the movement of water downward into the principal flow system. The water level in a well being drilled becomes progressively lower as the well is deepened, reflecting a decline in head with depth. In discharge areas, the reverse is true; the potentiometric surface is generally higher than the water table, and the water level in a relatively deep well progressively rises as the well is deepened, indicating upward flow in response to the prevailing gradient.

Chemical properties of the water yielded largely depend on the location of wells with respect to recharge and discharge areas. Chemical changes in water from well to well typically reflect differences in traveltime of water along flow paths of different lengths.

Toth's concept of flow systems is useful in describing the principal ground-water system in western Ohio and the effects of this system on ground-water quality. The principal or regional flow system in western Ohio is assumed by the author to be consequent upon the configuration of the regional potentiometric surface and may be defined, in part, by topographic and terrane features. Recharge areas may be assumed to coincide generally with areas of high potentiometric levels, and discharge areas with areas of low levels.

Figure 1 shows approximate contours on the regional potentiometric surface in western Ohio, based on the altitude of ground-water levels reported or measured in selected deep wells drilled in the consolidated-rock aquifers. Data are derived principally from the test wells drilled by the State, supplemented by data from municipal, industrial, or domestic wells—including wells drilled in the Ordovician shale in the southwest part of the study area—for which records are available in the files of the Ohio Division of Water.

The potentiometric contours are highly generalized. In some areas data were sparse; and, in many, head varies with depth, so that the water level measured in a well represents an integration of head values along the vertical section tapped by the well.

In western Ohio, water enters the regional flow system in the higher parts of the basins and moves toward the principal discharge areas in bottom lands along and beneath the major streams and in the lowlands along and adjacent to Lake Erie. Head decreases with depth in the upland recharge areas and increases with depth in the discharge areas. Much recharge to the regional flow system occurs in the central part of the study area, in the northern parts of the Great Miami and Scioto basins, where much of the terrane is composed of hummocky to hilly glacial moraine, consisting of deposits 200 to 300 ft (61–92 m) thick of till interbedded or associated with extensive beds of permeable sand and gravel. This morainal complex, where it overlies a prominent outlier centering in Logan County, about 30 mi (48 km) southeast of Lima, includes the highest point (1,549 ft or 472 m above mean sea level) in the State. Water moves downgradient from this area to discharge areas principally along the upper reaches of the Great Miami and Scioto River systems.

The topographic divides between surface drainage areas, as shown in figure 1, coincide with the divides for shallow ground-water circulation, but not necessarily with divides in the regional ground-water flow. For example, there is evidence of deep ground-water movement from the Great Miami and Scioto River basins into the Maumee and Sandusky basins, beneath the topographic divide separating these basins. Some deep wells in the upper reaches of the Maumee River basin exhibit water levels at or near land surface; these water levels appear to be derived from higher terrain in the adjoining basins and indicate flow from these basins toward lower areas to the north. Orton (1888) indicated that this condition existed in the hydrologic system several decades ago, prior to any appreciable human intervention in the hydrologic system.

The ground-water flow system in northwestern Ohio meets the criteria given by Toth (1962) as defining a regional flow system. The relief is low, and the general slope is toward Lake Erie. Before Ohio was settled and the land drained for agriculture, an area of about 2,500 mi^2 (6,475 km^2), including the central part of the Maumee Basin and virtually all of the Portage basin, consisted of an extensive swamp, called the Black Swamp (fig. 1). The land in much of the former swamp area is flat; slopes of 2 to 4 ft/mi (1–2 m/km) are common. Drainage posed a difficult problem for settlers, and Kaatz (1955) reported that about half the Black Swamp was in its origianl state as late as 1870. The Black Swamp resulted from a combination of poor drainage and ground-water discharge from the regional ground-water flow system into this stagnant area. The potentiometric surface in relatively deep wells in much of the former swamp area is presently close to the land surface; flowing wells are common. The Black Swamp was sharply bounded on the north by the Maumee River along most of the river's lower course, part of which also roughly coincides with a change in the underlying bedrock from limestone and dolomite on the south side of the river to shale on the north side. Soils and topography are similar on both sides of the river. The situation suggests that the Maumee River essentially forms the northern boundary of the western Ohio regional flow system in the carbonate aquifer.

The present regional flow system is generally similar to that which must have prevailed over much of past geologic time in western Ohio. The relatively high terrain in the central part of the study area, situated on and near the crest of the Cincinnati arch, existed throughout much of geologic time. The regional flow system, then as now, derived its energy from water entering this higher ground, whence the water began its slow movement toward the principal discharge areas. An important consequence of the regional movement of ground water in western Ohio is indicated by changes in the chemical quality of water in the carbonate aquifers.

GROUND-WATER QUALITY

Maclay and Winter (1967) made a geochemical study of a small drainage basin in Minnesota and identified five basic water types that were related both to the ground-water flow systems and the character of the rocks within the basin. They found, for example, that calcium bicarbonate type water occurred in recharge areas and that concentrations of all ions except bicarbonate increased in the direction of ground-water flow. They concluded that changes in water chemistry indicate the direction of ground-water movement in the basin, and these changes agree with the direction of flow, as determined by the slope of the potentiometric surface.

Geochemical evidence in western Ohio is in agreement with certain of the conditions described by Maclay and Winter. Wells drilled in the consolidated-rock aquifers, tapping the regional flow system, yield calcium bicarbonate type water in and near areas of recharge. The water becomes progressively more mineralized as it moves down the potentiometric gradient, and it changes to a calcium sulfate type in the principal discharge areas. This regional change in water chemistry is illustrated by the map (fig. 1), which shows areas where the ratio of the bicarbonate ion to the total anions in representative samples from the deeper wells is relatively low. The

location of these areas with respect to the potentiometric contours shows that the bicarbonate ratio is low, indicating a corresponding increase in the sulfate ion, in areas where the potentiometric surface is also low. The bicarbonate ratio exceeds 80 percent in much of the central part of the study area, which includes the principal areas of recharge; it drops below 40 percent in the major discharge areas of the carbonate aquifers. The bicarbonate ratio is also relatively high in water from wells drilled in recharge areas underlain by the Ordovician shale in the northern part of its outcrop area. Data are lacking, but the ratio probably falls below 40 percent in the southern part of the shale area, in discharge areas along the Ohio River.

The bicarbonate ratio, as shown in figure 1, is low in much of the former Black Swamp area, as would be expected for a major discharge area. However, in sizeable areas of the former swamp, including that part underlain by the high-yield area, the ratio is relatively high. The local occurrence of relatively high bicarbonate may indicate that not all the former swamp was a discharge area—it may reflect inaccuracies in the rather meager data upon which the map is based, perhaps resulting from the mixing of waters from different zones within the aquifer.

For the high-yield area as a whole, including areas outside the study area, the bicarbonate ratio data indicate that both recharge and discharge occur within the region of high yield, depending on topographic control. This is at variance with an earlier hypothesis (Norris and Fidler, 1971b) which theorized that the high-yield area was a major recharge area for the carbonate aquifer.

Norris and Fidler (1973), investigating the relation between ground-water quality and the regional flow system in southwest Ohio, compared chemical constituents in 15 samples of water from selected State-drilled test wells. Five of these wells were in recharge areas, five were in discharge areas, and five were in intermediate areas. Comparison of the three groups of analyses showed that a general change in chemical properties occurred as the water moved from areas of recharge through intermediate areas to areas of discharge. Calcium averaged 88 mg/l for the five wells in recharge areas, 125 mg/l for the five wells in intermediate areas, and 323 mg/l for the wells in discharge areas. Dissolved solids averaged 435, 715, and 1,826 mg/l for the respective areas; chloride averaged 5, 9, and 28 mg/l, and sulfate averaged 69, 256, and 981 mg/l, respectively. The increases in these constituents reflect the progressive mineralization of the water in moving through the regional flow system. Interestingly, the total bicarbonate content declines slightly as the water moves through the system; the five-well average declined from 425 mg/l in recharge areas to 375 mg/l in intermediate areas and to 360 mg/l in discharge areas.

CONCLUSIONS

Evidence shows that the chemical characteristics of water in the carbonate aquifers in western Ohio are intimately related to the regional flow system. The general change in chemical quality and increases in selected constituents that occur as the water moves from recharge to discharge areas are orderly and, in a measure, predictable. This knowledge represents an important step forward in defining the water-quality characteristics in a large area of the State; it will be highly significant in future problems involving site selection and development of ground-water supplies and perhaps also in the consideration of underground waste-injection projects.

REFERENCES CITED

Kaatz, M. R., 1955, The Black Swamp: A study in historical geography: Annals Assoc. American Geogrs., v. 45, no. 1, p. 1–35.

Maclay, R.W., and Winter, T.C., 1967, Geochemistry and ground-water movement in northwestern Minnesota: Ground Water, v. 5, no. 1, p. 11–19.

Norris, S.E., and Fidler, R.E., 1969, Correlation of carbonate rock units in northwest Ohio by natural gamma logging, *in* Geological Survey research 1969: U.S. Geol. Survey Prof. Paper 650-B, p. B158–B161.

——1971a, Availability of ground water from limestone and dolomite aquifers in northwest Ohio and its relation to geologic structure, *in* Geological Survey research 1971: U.S. Geol. Survey Prof. Paper 750-B, p. B229–B235.

——1971b, Carbonate equilibria distribution and its relation to an area of high ground-water yield in northwest Ohio, *in* Geological Survey research 1971: U.S. Geol. Survey Prof. Paper 750-C, p. C202–C206.

——1973, Availability of ground water from limestone and dolomite aquifers in southwest Ohio and the relation of water quality to regional flow system: U.S. Geol. Survey Water Resources Invest. 17–73.

Orton, Edward, 1888, The Trenton limestone as a source of oil and gas in Ohio: Ohio Geol. Survey, v. 6, p. 101–310.

Stout, Wilber, Ver Steeg, Karl, and Lamb, G.F., 1943, Geology of water in Ohio: Ohio Geol. Survey, 4th ser. Bull. 44, 694 p.

Toth, J., 1962, A theoretical analysis of ground-water flow in small drainage basins, *in* Proceedings of Hydrology Symposium No. 3, Ground Water: Queens Printer, Ottawa, Canada, p. 75–96.

Walker, A.C., Schmidt, J.J., Eagon, H.B., Jr., Johe, D.E., and Stein, R.B., 1970, Ground water for planning in northwest Ohio, a study of the carbonate-rock aquifers, *with sections by* Janssens, A.E., and *by* Norris, S.E., and Fidler, R.E.: Ohio Dept. Nat. Resources, Div. Water, Ohio Water Plan Inventory Rept. 22, 63 p.

Jour. Research U.S. Geol. Survey
Vol. 2, No. 5, Sept.-Oct. 1974, p. 533—539

COMPARISON OF BACTERIAL AND PHYTOPLANKTON POPULATIONS UNDER NATURAL AND LABORATORY CONDITIONS

By THEODORE A. EHLKE, Albany, N.Y.

Abstract.—Bacteria and blue-green algae were isolated from Oneida Lake, N.Y., and other sources. The blue-green algae *Anabaena flos-aquae, Anabaena spiroides, Gloeotrichia echinulata,* and *Microcystis aeruginosa* were grown under laboratory conditions and were separated into unialgal cultures. The bacterial population living in association with the unialgal blue-green algae differed significantly from the bacterial flora of Oneida Lake. *Bacillus, Pseudomonas, Aeromonas,* and *Zoogloea* were the most frequently occurring genera of bacteria from the lake, whereas *Flavobacterium, Achromobacter,* and *Pseudomonas* were the most common bacteria isolated from laboratory blue-green cultures. Nutritional and physiological characteristics of bacteria isolated in the laboratory were more uniform than those isolated from the lake.

Oneida Lake, a large, shallow, eutrophic lake in central New York, was the site of this study. The lake, with an area of 79.8 mi^2 (206.7 km^2), is the largest lake wholly within New York. It is used almost exclusively for recreational purposes. During summer, Oneida Lake characteristically exhibits a tremendous growth of planktonic blue-green algae. Production of these organisms is so great that the recreational uses of the lake are hindered, and the decomposition of algae along the shore becomes esthetically unpleasant for lakeside residents (Greeson and Meyers, 1969).

Acknowledgments.—For their help and encouragement in the study, the author acknowledges his appreciation to Phillip E. Greeson, project supervisor, and Tamara Psasoglu, who aided in bacterial identifications. Water samples were analyzed by the U.S. Geological Survey laboratory, Albany, N.Y.

OBJECTIVES OF STUDY

Some species of blue-green algae are known for their bloom-forming capabilities in eutrophic lakes and are the principal cause of economic and esthetic deterioration of bodies of water affected by the algae. Blue-green algae are probably the cause of taste and odor problems in some public water supplies. Kuentzel (1969), in an extensive review of the literature, stated that blue-green algae live in a symbiotic association with certain bacteria. Symbiosis includes mutualism, commensalism, and parasitism. In mutualism, both sides benefit from the association; in commensalism, one side benefits, and the other is unaffected; and in parasitism, one side is adversely affected. Objectives of the current study were to identify members of algal and bacterial populations under natural conditions and to develop methods for study of algal and bacterial isolates in the laboratory.

PREVIOUS STUDIES

The literature on planktonic freshwater algae is voluminous; however, little information is available on the symbiotic association between blue-green algae and bacteria. Gerloff, Fitzgerald, and Skoog (1950) suggested that bacteria normally penetrate and live in the gelatinous mucilage that surrounds the cells and filaments of blue-green algae; but, because of the difficulty in culturing algae under controlled conditions, they were unable to prove conclusively that symbiosis exists.

In a study of algal-bacterial symbiosis, Lange (1967) concluded that planktonic blue-green algae are always associated with bacteria and that rapid algal growth results "from a symbiotic relationship within their systems." Lange made no attempt to isolate and identify the bacterial symbionts nor to define the mechanisms of the symbiosis. He suggested, however, that the bacteria assimilated carbonaceous material to produce carbon dioxide, which accelerated algal photosynthesis.

Bunt (1961) observed symbiotic association of bacteria with certain algae and found that an unidentified species of *Nostoc* grows in symbiosis with the stalked bacterium *Caulobacter.* Growth of the alga in axenic culture was slow, whereas growth in cultures containing *Caulobacter* was rapid. Addition of indole-3-acetic acid, a growth hormone, affected recovery of the axenic *Nostoc.* Later studies indicated that normal development of the *Nostoc* does not depend entirely on the contribution of a growth hormone.

Soli (1963) reported that bacteria antagonize diatom populations. The bacteria that he studied were all gram-negative rods belonging to the families Pseudomonadaceae and Achromobacteraceae. Bacteria-free cultures of diatoms grew faster, attained greater numbers, and lived longer than those

cultures that were bacterized. The author concluded that the bacteria probably thrived at the expense of the sugars that the diatoms produced during photosynthesis.

Lanskaya (1963) found that rapidly growing marine diatom cultures depressed bacterial development and that, as the diatom population senesced, the bacterial population increased greatly. Lanskaya found no correlation between particular species of algae and bacteria.

Endosymbiotic bacteria have been reported in marine dinoflagellates. Gold and Pollingher (1971) found a brown pigmented bacterium within the cells of *Gymnodinium splendens* and *Cryptothecodinium cohnii*. The fact that bacteria grow only within the algae, and not in ordinary culture media, indicates strict growth requirements.

Berland, Bianchi, and Maestrini (1969) identified bacteria associated with a mixed population of marine algae. The bacterial genera *Pseudomonas*, *Flavobacterium*, and *Achromobacter* seemed to be the most common, and their metabolic requirements were similar.

Jones (1971) attempted to correlate natural algal and bacterial populations. Bacterial numbers in samples from the epilimnion and in mud samples were not related to fluctuations in algal populations. The bacterial population in a eutrophic lake correlated with temperature, pH, and dissolved-oxygen content and in an oligotrophic lake with particulate matter, pH, and rainfall.

Litchfield, Colwell, and Prescott (1969) identified 29 bacterial isolates from nonaxenic growths of *Chlorella sorokiniana*, a green alga. The bacteria were included in the genera *Pseudomonas*, *Acinetobacter*, *Flavobacterium*, and *Bacillus*. The rather uniform metabolic requirements of these organisms included the ability to utilize free amino acids in the culture medium. In related studies, Chan and McManus (1969) identified the epiphytic bacterial flora of the marine algae *Polysiphonia lanosa* and *Ascophyllum nodosum*. The bacterial genera *Vibrio* and *Flavobacterium* were the most frequent isolates; six other genera formed the other isolates. The authors stated that the bacteria required amino acids for growth and that the amino acids were probably obtained from the algae. Many of the marine bacterial isolates utilized glucose, galactose, and mannitol, which are the carbohydrates most often found in the marine environment. Fogg (1962) found that glucose, xylose, galactose, and arabinose were the basic constituents of extracellular polysaccharides secreted by many different algae.

SAMPLING AND ANALYTICAL PROCEDURES

Samples of algae from Oneida Lake were collected at the inlet near Sylvan Beach, the outlet near Brewerton, and Shackelton Point. Other sites (Godefrey Point and a pier near Brewerton) were sampled under bloom conditions (fig. 1). Samples were collected on the following dates: August 11, September 10, and October 28, 1970; and April 22 and August 26, 1971.

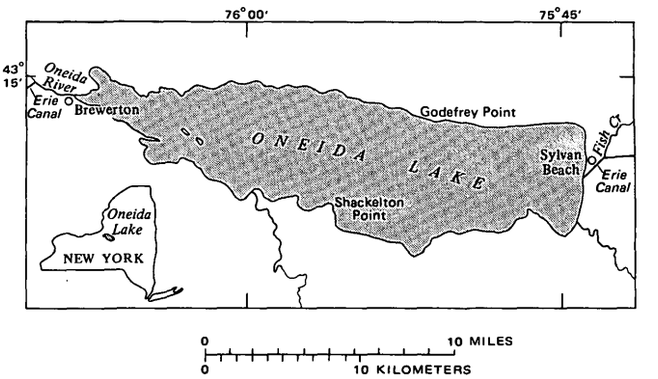

Figure 1.—Oneida Lake (modified from Greeson and Meyers, 1969).

Samples of water were collected for identification of phytoplankton and bacteria and for chemical analysis. Samples for identification of phytoplankton consisted of 1-liter preserved aliquots for quantitative evaluation and net or concentrated preserved samples for qualitative identification. A live net sample was collected for culturing in the laboratory. Samples were preserved by treating with 40-percent formaldehyde solution, saturated cupric sulfate solution, and a 20-percent detergent solution. The resulting volume of the three preservatives had a formaldehyde concentration of 4 percent.

Samples for identification of bacteria were collected in sterile 160-ml milk dilution bottles by technique described in American Public Health Association and others (1971, p. 678–685). Plates from which to count the bacterial population of the lake water were prepared by spreading a 0.1-ml aliquot onto the surface of TGY (Difco Tryptone Glucose Yeast[1] extract) agar. The plates were incubated in an inverted position at ambient temperature of 25° to 28°C (Celsius) for shipment to the laboratory. At the laboratory, the plates were incubated for 48 h at 30°C and were then counted. Aliquots of net live phytoplankton samples were also spread-plated by the same procedure to evaluate the bacterial flora of the algae. Bacteria from laboratory cultures were later isolated by the same technique.

Analysis of the lake water consisted of onsite measurements of dissolved-oxygen content, water temperature, pH, and specific conductance. In addition to onsite measurements, a series of samples were collected in 1-liter polyethylene bottles for analysis in the laboratory. All samples for analysis in the laboratory were filtered through a 0.45-μm mean pore size membrane filter. Analytical methods described in American Public Health Association and others (1971) and Brown, Skougstad, and Fishman (1970) were used. Samples for determination of nitrogen species were preserved with

[1] Use of product names in this report is for identification only and does not imply endorsement by the U.S. Geological Survey.

mercuric chloride; samples for determination of phosphorus were stored in glass citrate bottles. The following parameters were determined: silica, calcium, magnesium, sodium, potassium, mercury, carbonate, bicarbonate, sulfate, chloride, fluoride, nitrate, nitrite, ammonia (as NH_4), organic nitrogen (as N), total nitrogen (as N), total phosphorus (as P), dissolved-solids content, hardness (as $CaCO_3$), specific conductance, and pH.

Laboratory handling of the various samples was divided into five distinct phases:

1. Qualitative and quantitative identification of phytoplankton in preserved cultures.
2. Counting of bacterial colonies on the TGY spread plates.
3. Identification of the bacterial colonies.
4. Culturing of phytoplankton on laboratory media.
5. Isolation and identification of bacteria growing in algal cultures in the laboratory.

Phytoplankton were identified and were counted at X 200 magnification using a Sedgwick Rafter cell and a Whipple ocular grid. Algae were identified to species where possible. After 48 h, growth on the TGY spread plates was adequate to permit counting. After the counting, approximately 100 colonies were selected at random for subcultures and identification by the following procedure:

Subcultures were restreaked a minimum of three times from isolated colonies until staining and colonial morphology indicated purity. Cultures were then transferred to TGY slants and were maintained by biweekly transfer. The bacterial identification schemes of Skerman (1967) and Breed, Murray, and Smith (1957) were used to identify genus. Identification of most cultures to species was not possible because of incomplete agreement with recognized keys. Later, the bacterial flora of algal cultures grown in the laboratory was identified in virtually the same way that the Oneida Lake bacteria were identified. A dilution of the algal culture was spread-plated on the surface of TGY plates. After incubation at 30°C for approximately 48 h, some of the colonies were subcultured for identification.

Blue-green algae were cultured from water samples collected near Sylvan Beach, Shackelton Point, Brewerton, and Godefrey Point. Mixed-algal cultures were also developed from samples collected from Lake Okeechobee, Fla. Unialgal cultures of *Anabaena spiroides* (I.U. 1552) were obtained from the Indiana University collection. *Gloeotrichia echinulata* and *Anabaena flos-aquae* were supplied by Robert Safferman, Environmental Protection Agency, Cincinnati, Ohio. Not all blue-green algae will grow well on laboratory media, so that many different techniques were tried before the algae could be routinely cultivated. Laboratory culturing of algae was done in two steps: First, the algae were permitted to grow in mixed culture; and, second, they were separated into pure or unialgal cultures.

Initial culturing of algae was done in liquid (broth) and on solid (agar) media. Solid media differed from broth only by the addition of 1.5 percent (wt/volume) Difco agar. All the culture media are listed in table 1. Liquid media were dispensed as 20 ml in 18- by 150-mm screwcap test tubes or 100 ml in 250-ml Erlenmeyer flasks. One milliliter of inoculum was added to the culture vessels before they were placed under 75 ft-c (foot-candles) or 807 lm/m^2 (lumens per square meter) of constant grow-lux illumination at room temperature (25° to 27°C). Some of the Erlenmeyer flasks were placed on a reciprocal shaker operating at 50 to 60 c/m (cycles per minute) under constant illumination, but growth of cultures in flasks that were shaken was not appreciably different from cultures not shaken; therefore, use of the shaker was discontinued. Solid media were dispensed in 15- by 100-mm and 12- by 50-mm petri dishes. The resulting plates were inoculated by spreading 0.1-ml sample on the surface. After inoculation, the plates were taped to prevent moisture loss and were incubated under 75 ft-c (807 lm/m^2) of constant grow-lux illumination at room temperature (25°–27°C).

Table 1.—*Media for cultivation of blue-green algae*

Ingredient	Amount
1. Inorganic medium (modified from Starr, 1964)	
KNO_3 ..... grams ..	5.0
K_2HPO_4 ..... do....	0.1
$MgSO_4 \cdot 7H_2O$ ..... do....	0.05
Citric acid ..... do....	0.003
$Fe(NH_4SO_4)_2 \cdot 12H_2O$ ..... do....	0.003
Distilled water ..... milliliters ..	1,000
2. Cyanophycean agar (Starr, 1964)	
Medium 1 ..... milliliters ..	1,000
Agar ..... grams ..	12
3. Soil-water tube	
$CaCO_3$ ..... grams ..	0.01
Oats ..... do....	0.01
Humified soil ..... do....	3
Tap water ..... 18X150-mm test tube ..	To fill
4. Soil-water tube with inorganic supplement	
Medium 1 ..... milliliter ..	1
Medium 3 ..... 18X150-mm test tube ..	To fill
5. Soil-water medium	
Medium 1 ..... milliliters ..	900
Soil-water extract[1] ..... do....	100
6. Difco algae broth	
$NaNO_3$ ..... grams ..	1.0
NH_4Cl ..... do....	0.05
$CaCl_2 \cdot 6H_2O$ ..... do....	0.058
$MgSO_4$ ..... do....	0.513
K_2HPO_4 ..... do....	0.25
$FeCl_3$ ..... do....	0.003
Distilled water ..... milliliters ..	1,000

Table 1.—*Media for cultivation of blue-green algae*—Continued

Ingredient	Amount
7. TRIS buffered inorganic medium (Smith and Wiedeman, 1964)	
KNO_3 (0.1 *M*) ..... milliliters ..	20
Na_2HPO_4 (0.1 *M*) ..... do....	10
$MgSO_4 \cdot 7H_2O$ (0.1 *M*) ..... do....	3
$CaCl_2 \cdot 2H_2O$ (0.1 *M*) ..... do....	1
$H_2NC(CH_2OH)_3$ (TRIS) (0.2 *M*) ..... do....	25
Solution I[2] ..... do....	1
Solution II[3] ..... do....	1
Solution III[4] ..... do....	1
Solution IV[5] ..... do....	1
Distilled water ..... do....	To 1,000
8. Gerloff medium (Gerloff and others, 1950)	
$CaCl_2 \cdot 2H_2O$ ..... grams ..	0.0359
Citric acid ..... do....	0.003
Ferric citrate ..... do....	0.003
KCl ..... do....	0.0086
$MgCl_2 \cdot 6H_2O$ ..... do....	0.0209
Na_2CO_3 ..... do....	0.020
$NaNO_3$ ..... do....	0.413
Na_2HPO_4 ..... do....	0.0082
Na_2SiO_3 ..... do....	0.250
Na_2SO_4 ..... do....	0.0146
Lake water ..... milliliters ..	To 1,000
9. Algal assay procedure medium (PAAP) (Joint Industry-Government Task Force on Eutrophication, 1969)	
$NaNO_3$ ..... grams ..	0.085
K_2HPO_4 ..... do....	0.00348
$MgCl_2$ ..... do....	0.019
$MgSO_4 \cdot 7H_2O$ ..... do....	0.049
$CaCl_2 \cdot 2H_2O$ ..... do....	0.0147
Na_2CO_3 ..... do....	0.050
$FeCl_3$ ..... do....	0.00032
Trace-metal solution[6] ..... milliliters ..	1
Distilled water ..... do....	1,000
10. Chu No. 10 with trace elements (modified from Starr, 1964)	
$Ca(NO_3)_2 \cdot 4H_2O$ ..... grams ..	0.232
K_2HPO_4 ..... do....	0.01
$MgSO_4 \cdot 7H_2O$ ..... do....	0.025
Na_2CO_3 ..... do....	0.02
$Na_2SiO_3 \cdot 5H_2O$ ..... do....	0.044
Ferric citrate ..... do....	0.0035
Citric acid ..... do....	0.0035
Trace elements:	
H_3BO_3 ..... do....	2.4×10^{-3}
$MnCl_2 \cdot 4H_2O$ ..... do....	1.4×10^{-3}
$ZnCl_2$ ..... do....	4.0×10^{-4}
$CaCl_2 \cdot 6H_2O$ ..... do....	2.0×10^{-5}
$CuCl_2 \cdot 2H_2O$ ..... do....	1.0×10^{-7}
Distilled water ..... milliliters ..	To 1,000

[1] Prepare soil water extract as follows:

$CaCO_3$	grams ..	2.0
Humified soil	do....	200
Distilled water	milliliters ..	1,000

Autoclave 1 h and retain supernatant.

[2] Solution I consists of the following:

EDTA	grams ..	50
KOH	do....	31
Distilled water	milliliters ..	1,000

Table 1.—*Media for cultivation of blue-green algae*—Continued

[3] Solution II consists of the following:

H_3BO_3	grams ..	11.42
Distilled water	milliliters ..	1,000

[4] Solution III consists of the following:

$FeSO_4 \cdot 7H_2O$	grams ..	4.98
H_2SO_4 (concd)	milliliters ..	1
Distilled water	do....	1,000

[5] Solution IV consists of the following:

$ZnSO_4 \cdot 7H_2O$	grams ..	8.82
$MnCl_2 \cdot 4H_2O$	do....	1.44
MoO_3	do....	0.71
$CuSO_4 \cdot 5H_2O$	do....	1.57
$Co(NO_3)_2 \cdot 6H_2O$	do....	0.49
Distilled water	milliliters ..	1,000

[6] Trace-metal solution consists of the following:

H_3BO_3	grams ..	0.618
$MnCl_2$	do....	0.881
$ZnCl_2$	do....	0.109
$CaCl_2$	do....	0.0026
$CuCl_2$	do....	0.00003
$Na_2MoO_4 \cdot 2H_2O$	do....	0.024
$Na_2EDTA \cdot 2H_2O$	do....	7.44
Distilled water	milliliters ..	1,000

Cultures in the liquid media grew much faster than those on solid media and could be subcultured after 3 to 4 weeks. At this time, the mixed (impure) liquid cultures were separated into pure or unialgal cultures by spread-plating 0.1 ml of different dilutions onto the surface of an agar plate. In sufficiently high dilution, the algae formed separate and distinct colonial types that could be removed and aseptically transferred to fresh media as pure cultures. The algae grew differently on one medium than on another, but for a given medium the growth on agar was usually similar to that in broth. Best growth was sustained with Chu No. 10. The other media, in order of decreasing effectiveness, were: PAAP (algal assay procedure medium), TRIS ($H_2NC(CH_2OH)_3$), inorganic modified, Difco, Gerloffs, and soil water with or without modifications. Therefore, Chu No. 10 medium was used for all later work. Although initial plating of sample on agar resulted in very slow algal growth (2–3 mo) compared with growth in broth (4–6 weeks), the agar allowed visible growth of the less numerous algal types. In many of the broth cultures, only the dominant types survived.

RESULTS AND DISCUSSION

A summary of the phytoplankton identified in Oneida Lake during this study is shown in table 2. The 19 species identified include 8 blue-green algae. *Microcystis aeruginosa*, *Aphanizomenon holsaticum*, and *Lyngbya Birgei* were very common. The greatest variety of algal types was observed at Shackelton Point and at Brewerton (fig. 1). Many of the small embayments contained blooms differing greatly from the populations of nearby areas. On one day, a nearly unialgal bloom of *Gloeotrichia echinulata* was observed near Godefrey Point. On this same day, *Microcystis aeruginosa* was the dominant alga at Shackelton Point; and *Aphanizomenon* and

Table 2.—*Phytoplankton observed in Oneida Lake samples collected during 1970*

Alga	Shackelton Point	Brewerton	Sylvan Beach
Anabaena circinalis[1]	X	X	
flos-aquae[1]	X	X	
spiroides[1]		X	
Aphanizomenon holsaticum[1]	X	X	X
Asterionella formosa		X	
Closterium sp.	X		
Eudorina elegans		X	
Fragilaria brevistriata	X	X	
crotonensis	X		
Gloeotrichia echinulata[1]	X	X	
Lyngbya Birgei[1]	X	X	
Melosira sp.	X	X	X
Microcystis aeruginosa[1]	X	X	
incerta[1]	X		
Pandorina morum	X	X	
Pediastrum Boryanum	X		
duplex	X	X	
Pleodorina californica		X	
Volvox aureus		X	

[1] Blue-green alga.

Melosira were dominant at Brewerton and Sylvan Beach, respectively. In summer, blue-green algae nearly always dominated the population; in fall, diatoms dominated. A given alga seldom dominated during successive samplings at the same site on different days. Greeson (1971, p. 117–120) reported similar results in his studies of Oneida Lake.

Classifications of organisms isolated from Oneida Lake samples and from laboratory cultures during 1970 are listed in table 3. *Aeromonas*, *Bacillus*, *Pseudomonas*, and *Zoogloea* were the most frequently occurring bacteria. White and pink pigmented yeasts were regularly isolated but were never present in high numbers. All the bacteria isolated except one, the gram-positive *Bacillus*, were gram negative. One sample collected near Godefrey Point was a nearly unialgal bloom of *Gloeotrichia echinulata*. The bacterial flora of this sample consisted almost entirely of *Bacillus* and fewer numbers of the gram-negative rod, *Aeromonas*. According to Bennett (1969), gram-negative organisms usually dominate in natural water. Gram-negative organisms dominated in this study, except for the bloom of *Gloeotrichia*. This anomaly cannot be explained on the basis of previous work or on other findings of this study. The conditions that caused abundant growth of *Bacillus* were never reproduced, for the laboratory culture of *Gloeotrichia* did not contain any gram-positive bacteria. Certain algae produce antibiotic substances that inhibit growth of certain bacteria (Bennett, 1969). This may have been a factor in the anomaly.

Usually (but not in the *Gloeotrichia* bloom) the bacterial flora was much more diverse in the natural state than in laboratory cultures. The natural flora comprised nine genera, including gram-positive and gram-negative bacteria as well as yeasts. *Aeromonas*, *Bacillus*, *Cytophaga*, *Erwinia*, *Zoogloea*, and one yeast were found in lake samples but not in laboratory cultures.

Table 3.—*Classification of organisms isolated from Oneida Lake and from laboratory cultures*

	Samples from Oneida Lake					Laboratory cultures			
	1	2	3	4	5	6	7	8	9
Achromobacter sp.		X				X	X	X	X
Acinetobacter sp.							X		
Aeromonas sp.	X	X	X	X					
Alcaligenes sp.								X	
Bacillus sp.	X	X	X	X	X				
Cytophaga sp.				X					
Erwinia sp.				X	X				
Flavobacterium sp.						X	X		X
Pseudomonas sp. (no differentiation)			X	X	X				
Pseudomonas aeruginosa							X		
Pseudomonas (alcaligenes group)						X	X	X	
Pseudomonas (fluorescent group)							X		X
Pseudomonas maltophilia							X		
Pseudomonas putida								X	
Serratia sp.						X	X		
Vibrio sp.		X							
Yeast				X	X				
Zoogloea sp.				X	X				

1. Bloom of *Gloeotrichia echinulata* collected near Godefrey Point, August 11, 1970.
2. Water sample collected near Brewerton, August 11, 1970.
3. Water sample collected near Sylvan Beach, September 11, 1970.
4. Water sample collected near Shackelton Point September 14, 1970.
5. Water sample collected near Brewerton, September 14, 1970.
6. Unialgal culture of *Gloeotrichia echinulata*.
7. Unialgal culture of *Microcystis aeruginosa*.
8. Unialgal culture of *Anabaena flos-aquae*.
9. Unialgal culture of *Anabaena spiroides*.

Types of bacteria isolated from laboratory cultures of blue-green algae are shown in table 3. The data indicate great differences between the laboratory and the natural populations; for example, the laboratory population consists entirely of gram-negative bacteria, whereas the natural population contains both gram-negative and gram-positive bacteria and has greater species diversity. Six genera of bacteria in laboratory cultures and nine genera from Oneida Lake were isolated. More importantly, only minute morphological and physiological differences separated certain genera isolated from laboratory cultures. The lack of correlation between particular species of algae and bacteria that were observed in this study agrees with results of studies on the bacterial flora of diatoms by Lanskaya (1963).

The bacterial floras of the four unialgal cultures had many similarities but were not identical. To summarize the characteristics of all laboratory-bacterial isolates, the data in table 3 indicate that the genera *Flavobacterium*, *Achromobacter*, and *Pseudomonas* were isolated from all or nearly all algal cultures. *Acinetobacter*, *Alcaligenes*, and *Serratia* were found in one or more algal cultures but never in great numbers. All six genera are reported to be very common in freshwater. *Flavobacterium* was usually the dominant bacterial type in *Gloeotrichia echinulata*, *Microcystis aeruginosa*, and *Anabaena spiroides* cultures but was not isolated from Oneida Lake samples. Other genera not isolated from Oneida Lake samples include *Acinetobacter*, *Alcaligenes*, and *Serratia*. Except for *Serratia*, which may be a contaminant from the laboratory surroundings, these genera have been reported by Bennett (1969) and others to be a part of the diverse bacterial

flora of natural water. Perhaps they were in the Oneida Lake samples but were overlooked because of low initial numbers, slow growth, or for other reasons. *Pseudomonas* was isolated from *Gloeotrichia echinulata*, *Microcystis aeruginosa*, *Anabaena flos-aquae*, and *Anabaena spiroides* and also from most Oneida Lake samples. The *Pseudomonas* group, a diverse and widely distributed form, is one of the most common genera of aquatic bacteria.

As indicated by the data in table 3, similar *Pseudomonas* and *Achromobacter* types were found in many laboratory algal cultures. *Pseudomonas* isolates of the alcaligenes group were found in *Gloeotrichia*, *Microcystis*, and *Anabaena* cultures. *Achromobacter* isolates having similar physiological and morphological characteristics were isolated from all laboratory algal cultures. Results similar to these were reported by Berland, Bianchi, and Maestrini (1969) and by Chan and McManus (1969) in studies of the bacterial flora of marine algae.

Litchfield, Colwell, and Prescott (1969) found that the bacterial flora of the green alga, *Chlorella sorokiniana* was uniform in metabolic activity and growth requirements. The flora consisted of the genera *Pseudomonas*, *Acinetobacter*, *Flavobacterium*, and *Bacillus*. The same genera, except for *Bacillus*, were observed in the laboratory cultures in this study.

Oneida Lake is a shallow eutrophic lake in which the water quality does not seem to have changed appreciably, at least since 1888 when the earliest known investigation of the water quality of the lake was published by the New York State Board of Health. The present study indicates that concentrations of certain chemical parameters and properties, such as chloride content and hardness, have increased slightly since that time. Later reports (New York State Department of Health, 1957; Greeson, 1971) indicate no change in alkalinity during the period 1927–69. Chemical analyses during this study (table 4) indicate that the water in Oneida Lake is primarily a calcium bicarbonate type. Concentrations of the major inorganic ions (calcuim, magnesium, sodium, potassium, bicarbonate, carbonate, sulfate, and chloride) indicate the enriched condition of the lake. Dissolved-oxygen content of most samples was above saturation value, which is an indication of the high algal population. Concentrations of chemical constituents were not noticeably different from those in a previous investigation (Greeson, 1971).

Table 4.—*Mean specific conductance, water temperature, and concentrations of dissolved chemical constituents in Oneida Lake; and median pH*

[Chemical constituents, hardness, and dissolved-solids contents, in milligrams per liter]

Constituent	Dates of sample collection		Range (1970)
	1967–69[1]	1970[2]	
Silica (SiO_2)	2.1	4.1	1.6 – 5.4
Calcium (Ca)	38	41	35 – 45
Magnesium (Mg)	8.6	7.5	6.8 – 8.3
Sodium (Na)	4.9	5.4	5.2 – 5.9
Potassium (K)	.9	1.0	.8 – 1.1
Ammonia (as NH_4)	.12	.23	.12– .30
Mercury (Hg)	.0001	<.1	<.1
Bicarbonate (HCO_3)	99	99	86 –108
Carbonate (CO_3)	1	1.5	0 – 8
Sulfate (SO_4)	48	50	39 – 55
Chloride (Cl)	9.0	11	9.2 – 13
Fluoride (F)	<.1	.1	.1 – .2
Organic nitrogen (as N)	.16	.20	.12– .45
Nitrite (NO_2)	.01	.07	.02– .15
Nitrate (NO_3)	.4	.6	.1 – 2.2
Total nitrogen (N)	.34	.54	.28– .94
Total phosphorus (as P)	.12	.31	.06– .48
Dissolved oxygen	[3]9.69	[4]8.8	6.9 – 11.8
Dissolved-solids content (sum)	163	175	149 –188
Hardness (as $CaCO_3$)	124	112	34 –142
pH	[5]8.1	[5]8.3	7.1 – 9.2
Specific conductance μmhos/cm at 25°C	275	317	268 –320
Water temperature °C	19.1	21.2	10.5 – 25.9

[1] Greeson (1971, p. 92).
[2] 10 samples. <10 sites
[3] 102 percent saturation.
[4] 98 percent saturation.
[5] Median value.

SUMMARY AND CONCLUSIONS

The relationship between blue-green algae and bacteria is very difficult to study under natural conditions because many uncontrolled events, such as currents, winds, and temperature, affect population numbers. Therefore, in the initial phase of the study, blue-green algae were obtained from a variety of sources and were grown in the laboratory. Conclusions based on the study follow:

1. The chemistry of Oneida Lake indicates eutrophic conditions that have increased slightly since 1888.
2. As in other eutrophic lakes, a great variety of algae occur in Oneida Lake. Usually, blue-green algae are dominant in summer.
3. Most blue-green algae can be routinely cultured from lake samples by inoculation into Chu No. 10 broth and agar.
4. Unialgal cultures can usually be obtained from mixed-algal cultures by streaking dilutions of the mixed-algal cultures onto agar.
5. The genera *Bacillus*, *Pseudomonas*, *Aeromonas*, and *Zoogloea* were the bacteria most frequently isolated from Oneida Lake.
6. Bacterial floras of blue-green algal cultures grown in the laboratory were much less diverse than the natural population. In this study, *Flavobacterium*, *Achromobacter*, and *Pseudomonas* were the most common organisms. Similar types of bacteria were found in many laboratory blue-green algal cultures. There was no correlation between particular species of algae and bacteria.

REFERENCES CITED

American Public Health Association, American Water Works Association, and Water Pollution Control Federation, 1971, Standard

methods for the examination of water and wastewater [13th ed.]: New York, Am. Public Health Assoc., 874 p.

Bennett, E. A., 1969, A study of the distribution of heterotrophic bacteria in the Great Lakes. 1. The heterotrophs in lake water: Toronto, Ontario Water Resources Comm., 32 p.

Berland, B. R., Bianchi, M. G., and Maestrini, S. Y., 1969, Etude des bactéries associées aux Algues marines en culture: Marine Biology, v. 2, p. 350–355.

Breed, R. S., Murray, E. G. D., and Smith, N. R., eds, 1957, Bergey's manual of determinative bacteriology, 7th ed.: Baltimore, Williams and Wilkins, 1094 p.

Brown, Eugene, Skougstad, M. W., and Fishman, M. J., 1970, Methods for collection and analysis of water samples for dissolved minerals and gases: U.S. Geol. Survey Techniques Water-Resources Inv., book 5, chap. A1, 160 p.

Bunt, J. S., 1961, Blue green algae: Nature, v. 192, p. 1274–1275.

Chan, E. C. S., and McManus, E. A., 1969, Distribution, characterization, and nutrition of marine microorganisms from the algae *Polysiphonia lanosa* and *Ascophyllum nodosum*: Canadian Jour. Microbiology v. 15, p. 409–418.

Fogg, G. E., 1962, Extracellular products, *in* Lewin, R. A., ed., Physiology and biochemistry of algae,: New York, Academic Press, p. 475–489.

Gerloff, G. C., Fitzgerald, G. P., and Skoog, Frank, 1950, The isolation, purification, and culture of blue-green algae: Am. Jour. Botany, v. 37, p. 216–218.

Gold, Kenneth, and Pollingher, Utsa, 1971, Occurence of endosymbiotic bacteria in marine dinoflagellates: Jour. Phycology, v. 7, p. 264–265.

Greeson, P. E., and Meyers, G. S., 1969, The limnology of Oneida Lake. An interim report: New York Water Resources Comm. Rept. Inv. R1-8, 64 p.

Greeson, P. E., 1971, Limnology of Oneida Lake with emphasis on factors contributing to algal blooms: U.S. Geol. Survey open-file rept., 185 p.

Joint Industry-Government Task Force on Eutrophication, 1969, Provisional algal assay procedure: New York, U.S. Environmental Protection Agency, 62 p.

Jones, J. G., 1971, Studies on freshwater bacteria: Factors which influence the population and its activity: Jour. Ecology, v. 59, p. 593–613.

Kuentzel, L. E., 1969, Bacteria, carbon dioxide, and algal blooms: Jour. Water Pollution Control Federation, v. 41, p. 1737–1747.

Lange, Willy, 1967, Effect of carbohydrates on the symbiotic growth of planktonic blue-green algae with bacteria: Nature, v. 215, p. 1277–1278.

Lanskaya, L. A., 1963, Fission rate of plankton algae of the Black Sea in cultures, *in* Oppenheimer, C. H., ed., Marine microbiology: Springfield, Ill., Charles C. Thomas, p. 127–132.

Litchfield, C. D., Colwell, R. R., and Prescott, J. M., 1969, Numerical taxonomy of heterotrophic bacteria growing in association with continuous-culture *Chlorella sorokiniana*: Appl. Microbiology, v. 18, p. 1044–1049.

New York State Board of Health, 1888, Annual report of the New York State Board of Health: Albany, N.Y., p. 194–202 and 233–235.

New York State Department of Health, 1957, Oneida River drainage area: New York State Dept. Health, Oswego River Drainage Basin Survey Rept. 5, 173 p.

Skerman, V. B. D., 1967, A guide to the identification of the genera of bacteria: Baltimore, Williams and Wilkins, 303 p.

Smith, R. L. and Wiedeman, V. E., 1964, A new alkaline growth medium for algae: Canadian Jour. Botany, v. 42, p. 1582–1586.

Soli, George, 1963, Axenic cultivation of a pelagic diatom, *in* Openheimer, C. H., ed., Marine microbiology: Springfield, Ill. Charles C. Thomas, p. 122–126.

Starr, R. C., 1964, The culture collection of algae at Indiana University: Am. Jour. Botany, v. 51, p. 1013–1044.

Jour. Research U.S. Geol. Survey
Vol. 2, No. 5, Sept.-Oct. 1974, p. 541–543

DISTRIBUTION OF CHLORINATED HYDROCARBONS IN STREAM-BOTTOM MATERIAL

By DONALD F. GOERLITZ and LEROY M. LAW, Menlo Park, Calif.

Abstract.—Six stream-bottom samples, contaminated in situ with high levels of chlorinated hydrocarbons, were size graded and the separates were analyzed. The contaminants were found distributed throughout the sample. The complexity of bottom-material samples is such that the distribution of chlorinated hydrocarbons may be controlled to a major extent by the organic matter and associated organisms. All particle-size fractions must be considered if representative samples are to be taken and quantitatively related to a stream.

Chlorinated hydrocarbon insecticides reported in surface water, are usually found in concentrations of less than 1 μg/l (Brown and Nishioka, 1967; Manigold and Schulze, 1969; and Lichtenberg and others, 1970). The significance of low levels of chlorinated hydrocarbons in aquatic ecosystems and their effects on animals of different trophic levels in food chains is well recognized (Cope, 1965; Newsom, 1967; and U.S. Department of Health, Education, and Welfare, 1969). The grab sampling methods and analytical techniques used indicate that sorbed compounds were not emphasized when in fact chlorinated hydrocarbon insecticides are associated primarily with the sediment. For example, the distribution ratio of concentrations of pesticides in suspended sediment and in water is as great as 1,000:1 for *p*, *p*′-DDT and dieldrin (Caro and Taylor, 1971, and Haan, 1971). Pesticides from agricultural lands most likely are transported to surface water during runoff events and enter in association with suspended sediment (Bradley and others, 1972). In studies of suspended sediments carried by the Sacramento River, Calif., we found that the amounts of chlorinated hydrocarbon insecticides in transport were directly proportional to the suspended sediment concentration. "Insoluble" chlorinated hydrocarbons are reported to be transported in surface water associated with organic soil colloids and with aquatic microbes and adsorbed on suspended clay (Leshniowsky and others, 1970; Poirrier and others, 1972). Eventually, the suspended particles in the aquatic system are redeposited. If it is not possible to collect suspended sediment samples, analysis of bottom material may be useful for reconnaissance studies. The purpose of this paper is to show the distribution of some chlorinated hydrocarbons in bed material samples from selected surface streams.

METHOD

Samples were collected by scooping submerged bottom material from the stream into glass jars. The jars were capped with Teflon-lined lids and stored at 0°C until processed. After preliminary analysis of a subsample, the remaining sample was separated by diameter size into gravel (>2.0 mm), sand (2.0–0.062 mm), silt (0.062–0.004 mm) and clay (<0.004 mm). Techniques detailed by Guy (1969) were followed for fractionation. Glassware, sieves, and water were specially prepared to minimize analytical interference (Goerlitz and Brown, 1972).

In order to separate the samples into size fractions, the wet bottom material first was tumbled with two volumes of distilled water. The mixture was sieved through 2.0- and 0.062-mm screens and the liquid passing through the sieves was collected in a glass cake dish. The tumbling and sieving process was repeated three times with addition of fresh distilled water each time. The silt-clay-water mixture was collected in 4-liter bottles. The sand and gravel fractions were more thoroughly rinsed of fines under the distilled water tap until the washings were clear. The silt and clay were separated by first dispersing in distilled water and then siphoning the clay-water suspension after the silt settling time was satisfied (Guy 1969). The clay was separated from the water by centrifugation at a relative centrifugal force of 25,500 *g* for 45 min using a refrigerated centrifuge. After centrifugation, the water was decanted from the clay and returned for resuspension of the silt. The silt-clay separation procedure was repeated two more times to ensure adequate separation. Finally, the silt was also centrifuged to remove water. The oven-dry weight was determined on a subsample of each fraction prior to chlorinated hydrocarbon analysis. The method of Goerlitz and Brown (1972) for the determination of chlorinated hydrocarbon insecticides in stream-bottom material was used. Both electron-capture gas chromatography and gas chromatography-mass spectometry were used in the determinative step.

RESULTS AND DISCUSSION

Six stream-bottom samples, contaminated in situ with high levels of chlorinated hydrocarbon were selected for this study.

Results of analyses of the separate fractions of each sample are given in tables 1–6. Analysis of the water used for fractionation showed less than 1 percent loss of the chlorinated hydrocarbon to the aqueous phase. Identities of the individual chlorinated hydrocarbons found in each fraction of each sample were confirmed by use of a computerized mass spectrometer coupled to a gas chromatograph.

The occurrence of chlorinated hydrocarbons in the various fractions of each sample is given in table 7. The expectation that the greatest concentration of these compounds would be related to the surface area, that is on the finer material, was not always correct. Note that in sample 2, St. Francis River, Ark., the gravel fraction contained the highest concentration of chlorinated insecticides; however, the gravel fraction was mostly clam shells. The distribution of the total pesticides occurring in each sample is summarized in table 8. The greatest amounts of the subject compounds were found in the coarser fractions of four of the samples.

In using bottom-material samples for reconnaissance studies, we conclude that one must exercise caution in applying time-honored generalizations to interpretation. Although surface area was generally related to sorption, notable exceptions were observed. The sand fractions from each of the samples appeared as clean mineral grains. A hand lens revealed an occasional crustacean or mollusk. Further, the sand fraction

Table 1.—*Sample 1, Bayou Bartholomew near McGehee, Ark.*

		Particle class			
		Clay	Silt	Sand	Gravel
Composition	percent	4.8	20.4	62.3	12.6
Distribution of total pesticides	percent	8.1	10.3	72.4	9.2
Concentration of total pesticides	10^{-6} g/kg	1800	538	1230	774
Concentration of individual pesticides:					
DDD	10^{-6} g/kg	556	208	528	256
DDE	10^{-6} g/kg	451	119	238	105
DDT	10^{-6} g/kg	788	211	465	413

Table 2.—*Sample 2, St. Francis River at Marked Tree, Ark.*

		Particle class			
		Clay	Silt	Sand[1]	Gravel[2]
Composition	percent	9.0	11.6	67.0	12.3
Distribution of total pesticides	percent	11.1	13.3	36.4	39.2
Concentration of total pesticide	10^{-6} g/kg	60.3	56.5	27.0	156
Concentration of individual pesticides:					
DDD	10^{-6} g/kg	33.0	24.9	14.6	104
DDE	10^{-6} g/kg	9.07	13.4	4.61	24.3
DDT	10^{-6} g/kg	18.2	18.3	7.78	27.9

[1] Small amount of woody material.
[2] Mostly clam shells.

Table 3.—*Sample 3, Calaveras River near Waterloo, Calif.*

		Particle class			
		Clay	Silt	Sand	Gravel
Composition	percent	7.4	41.2	48.6	2.9
Distribution of total pesticides	percent	14.5	37.9	43.7	3.9
Concentration of total pesticides	10^{-6} g/kg	628	354	287	419
Concentration of individual pesticides:					
DDD	10^{-6} g/kg	191	100	78.1	144
DDE	10^{-6} g/kg	110	59.1	38.2	73.8
DDT	10^{-6} g/kg	327	195	171	201

Table 4.—*Sample 4, Kings River near Kingsburg, Calif.*

		Particle class			
		Clay	Silt	Sand	Gravel
Composition	percent	1.6	9.9	88.5	0
Distribution of total pesticides	percent	22.2	42.0	35.8	0
Concentration of total pesticides	10^{-6} g/kg	260	77.6	7.62	0
Concentration of individual pesticides:					
DDD	10^{-6} g/kg	122	33.8	3.45	0
DDE	10^{-6} g/kg	81.5	22.7	2.03	0
DDT	10^{-6} g/kg	56.4	21.1	2.14	0

Table 5.—*Sample 5, Molino Creek near Davenport, Calif.*

		Particle class			
		Clay	Silt	Sand	Gravel[1]
Composition	percent	22.2	59.3	13.9	4.5
Distribution of total pesticides	percent	34.4	57.6	6.8	1.2
Concentration of total pesticides	10^{-6} g/kg	10,000	6280	3160	1800
Concentration of individual pesticides:					
DDD	10^{-6} g/kg	3390	2250	1400	307
DDE	10^{-6} g/kg	1380	935	574	137
DDT	10^{-6} g/kg	5020	2970	1140	1330
Lindane	10^{-6} g/kg	221	126	41.1	22.4

[1] Mostly floating woody material.

Table 6.—*Sample 6, Sacramento River near Anderson, Calif.*

		Particle class			
		Clay	Silt	Sand	Gravel
Composition	percent	0.2	0.9	94.1	4.8
Distribution of total PCB	percent	3.2	4.6	92.0	0.2
Concentration of total PCB	10^{-6} g/kg	3210	942	172	7.97

Table 7.—*Occurrence of chlorinated hydrocarbons in order of decreasing concentrations in six samples*

1	2	3	4	5	6
Clay	Gravel	Clay	Clay	Clay	Clay
Sand	Clay	Gravel	Silt	Silt	Silt
Gravel	Silt	Silt	Sand	Sand	Sand
Silt	Sand	Sand		Gravel	Gravel

Table 8.—*Distribution of chlorinated hydrocarbon in order of decreasing relative amounts in six samples*

1	2	3	4	5	6
Sand	Gravel	Sand	Silt	Silt	Sand
Silt	Sand	Silt	Sand	Clay	Silt
Gravel	Silt	Clay	Clay	Sand	Clay
Clay	Clay	Gravel		Gravel	Gravel

contained a considerable number of plant seeds which germinated in the glass storage containers during a period when the fractions were out of the refrigerator. The complexity of bottom-material samples is such that the distribution of chlorinated hydrocarbons may be controlled to a major extent by the organic matter and associated organisms. Physical and mineralogical considerations may be of less importance. This investigation shows that all particle-size fractions must be considered if a representative bed-material sample is to be collected and quantitatively related to the stream.

REFERENCES CITED

Bradley, Jr., J. R., Sheets, T. J., and Jackson, M. D., 1972, DDT and toxaphene movement in surface water from cotton plots: Jour. Environmental Quality, v. 1, no. 1, p. 102–105.

Brown, Eugene, and Nishioka, Y. A., 1967, Pesticides in selected western streams–A contribution to the national program: Pesticides Monitoring Jour., v. 1, no. 2, p. 38–46.

Caro, J. H., and Taylor, A. W., 1971, Pathways of loss of dieldrin from soils under field conditions: Jour. Agr. Food Chemistry, v. 19, no. 2, p. 379–384.

Cope, O. B., 1965, Agricultural chemicals and fresh-water ecological systems, *in* Research in pesticides: New York, Academic Press, p. 115–117.

Goerlitz, D. F., and Brown, Eugene, 1972, Methods for analysis of organic substances in water: U.S. Geol. Survey Techniques Water-Resources Inv., book 5, chap. A3, 40 p.

Guy, H. P., 1969, Laboratory theory and methods for sediment analysis: U.S. Geol. Survey Techniques Water-Resources Inv., book 5, chap. C1, 58 p.

Haan, C. T., 1971, Movement of pesticides by runoff and erosion: Am. Soc. Agr. Engineers, Trans., v. 14, no. 3, p. 445–449.

Leskniowsky, W. O., Dugan, P. R., Pfister, R. M., Frea, J. I., and Randles, C. I., 1970, Adsorption of chlorinated hydrocarbon pesticides by microbial floc and lake sediment and its ecological implications: Internat. Assoc. Great Lakes Research, 13th Conf., Proc., p. 611–618.

Lichtenberg, J. J., Eichelberger, J. W., Dressman, R. C., and Longbottom, J. E., 1970, Pesticides in surface waters of the United States–a 5-year summary, 1964–1968: Pesticides Monitoring Jour., v. 4, no. 2, p. 71–86.

Manigold, D. B., and Schulze, J. A., 1969, Pesticides in selected western streams–a progress report: Pesticides Monitoring Jour. v. 3, No. 2, p. 124–135.

Newsom, L. D., 1967, Consequences of insecticide use on nontarget organisms: Ann. Rev. Entomology, v. 12, p. 257–286.

Poirrier, M. A., Bordelon, B. R., and Laseter, J. L., 1972, Adsorption and concentration of dissolved carbon-14 DDT by coloring colloids in surface waters: Environmental Sci. and Technology, v. 6, no. 12, p. 1033–1035.

U.S. Department of Health, Education, and Welfare, 1969, Report of the Secretary's Commission on pesticides and their relationship to environmental health. Parts I and II: Washington, U.S. Govt. Printing Office, 677 p.

Jour. Research U.S. Geol. Survey
Vol. 2, No. 5, Sept.-Oct. 1974, p. 545–550

CALCULATED VOLUMES OF INDIVIDUAL SHIELD VOLCANOES ALONG THE HAWAIIAN-EMPEROR CHAIN

By KEITH E. BARGAR and EVERETT D. JACKSON
Menlo Park, Calif.

Abstract.—Volume was calculated for the 107 individual volcanic shields along the Hawaiian Ridge–Emperor Seamounts chain to help fulfill the need for volume data essential to determining eruption rates, fraction of mantle melted, and other parameters. Boundaries used were based principally upon location of rift zones related to each shield. Volcanic loci shown are modified from an earlier map to accommodate changes in bathymetry. Total volumes calculated for the Emperor and Hawaiian chains are 336.3×10^3 km^3 and 744.9×10^3 km^3

Prevalent hypotheses regarding the origin of the Hawaiian Ridge–Emperor Seamounts chain stem from Wilson's hypothesis (1963) attributing the linearity and age sequence of the Hawaiian Ridge to movement of the Pacific plate over a fixed hot spot in the mantle. Morgan (1971, 1972a, 1972b), in a modified and expanded version of Wilson's hypothesis, explained the locus of active volcanism in the Hawaiian and Emperor chains as resulting from a stationary convection plume of lower mantle origin. Jackson, Silver, and Dalrymple (1972) showed that Hawaiian and Emperor volcanic vents were confined to short sigmoidal loci and that volcanism along such loci was episodic. More recently, Shaw and Jackson (1973) proposed that the chain was localized by a gravitational anchor, not a thermal plume.

Little detailed information is available for the northwest, Emperor part of the Hawaiian-Emperor chain, Kanmu Seamount to Meiji Seamount; most ideas concerning its origin are derived from work on the younger, southeast part of the chain, the Hawaiian ridge. Studies of rift zones in conjunction with gravity and age data for the Hawaiian Islands suggest that the orientation of rifts on individual volcanic shields is related to both regional structure and gravitational forces (Fiske and Jackson, 1972). Positive Bouguer gravity anomalies in the Hawaiian Islands have been shown by a number of workers (see Malahoff and Woollard, 1971, and Fiske and Jackson, 1972, for detailed references) to be nearly coincident with the central vent area of the shield volcanoes, and to a lesser extent, the rift zones. Using this relation, Jackson, Silver, and Dalrymple (1972) located probable central vent positions, and hence individual shields for the entire Hawaiian-Emperor chain.

Time-distance-volume relations along the Hawaiian Ridge were recently examined by Shaw (1973) in working out his shear-melting hypothesis. Shaw's volume data were confined to the Hawaiian Ridge and were calculated for several segments of the ridge rather than for individual volcanoes. Recognizing the limitations of these volume data, Shaw pointed out the need for more detailed volume data essential for calculating eruption rates, fraction of mantle melted, and other parameters. We hoped to fulfill this need by calculating the volume of each volcanic shield in the Hawaiian-Emperor chain.

IDENTIFICATION OF INDIVIDUAL SHIELDS IN THE HAWAIIAN-EMPEROR CHAIN

Boundaries of the individual volcanic shields used in this study were based principally upon location of rift zones. Fiske and Jackson (1972) showed the location of rift zones radiating from the volcanic centers of the southeastern Hawaiian Islands. The rifts were located partly by direct observation (as for Mauna Loa, Kilauea, Koolau, Niihau), partly by Bouguer gravity data of several workers (summarized in Malahoff and Woollard, 1971, table 1; Fiske and Jackson, 1972), and partly on the configuration (bathymetry) of the rift systems. Unfortunately, gravity investigations for most of the Hawaiian-Emperor chain are limited and lack detail needed to delineate rift zones. The topography was used to supplement gravity data in delineating rift systems for the rest of the chain. The rift zones are mapped in figure 1*A* with the volcanic centers, marked by rift intersections, located at the highest elevation on the shields consistent with rift geometry. The criteria used to locate rift zones and central vents were based upon the conclusions of Fiske and Jackson (1972) that (1) the intersection of rift systems occurs at the central vent areas of shield volcanoes, (2) isolated seamounts have rift systems nearly parallel to the loci of Jackson, Silver, and Dalrymple (1972) because of regional forces, and (3) orientation of the rift systems of coalesced seamounts is determined by the gravitational forces imposed by neighboring preexisting shields. (These rift systems were originally drawn by E.D. Jackson in

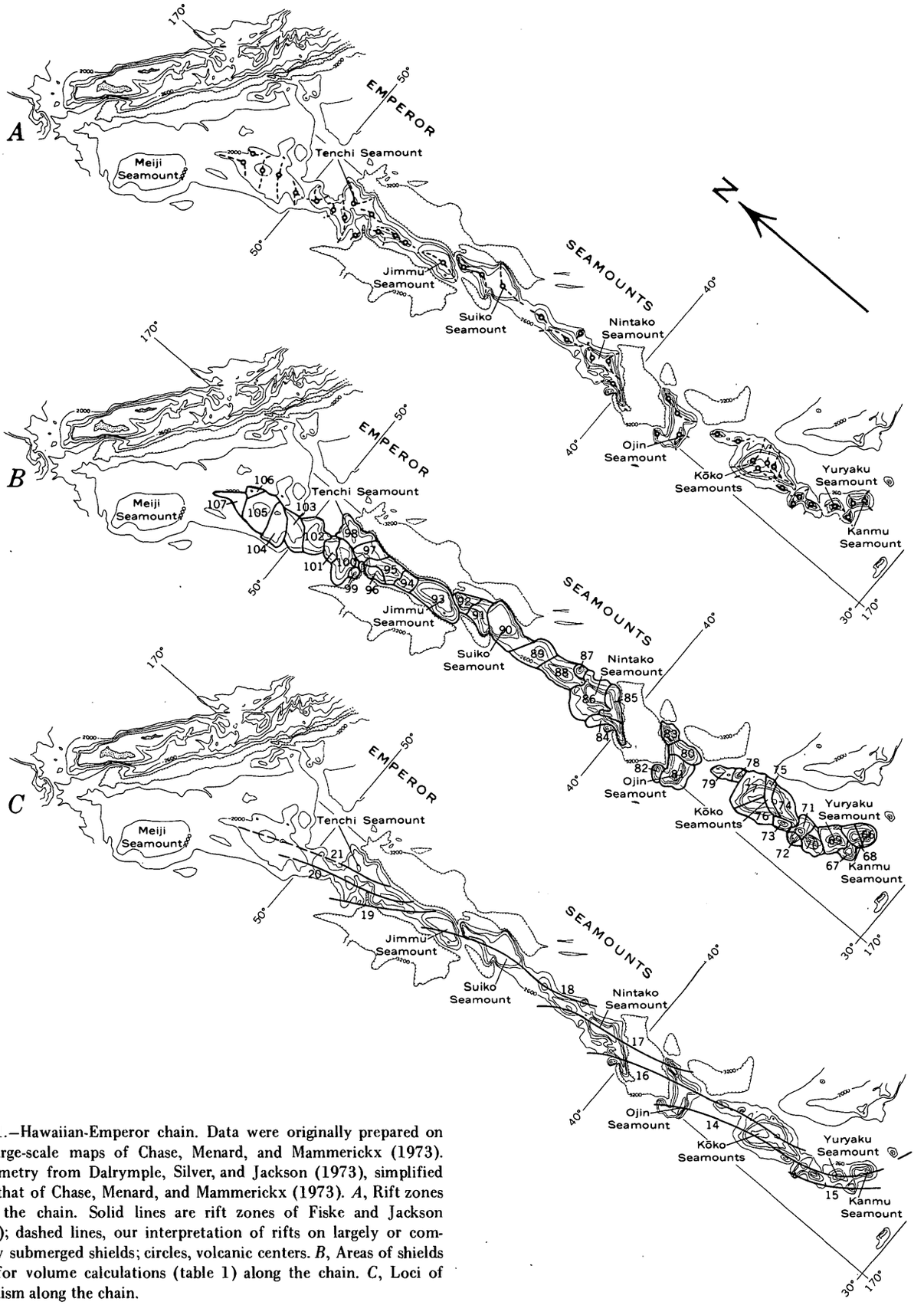

Figure 1.—Hawaiian-Emperor chain. Data were originally prepared on the large-scale maps of Chase, Menard, and Mammerickx (1973). Bathymetry from Dalrymple, Silver, and Jackson (1973), simplified from that of Chase, Menard, and Mammerickx (1973). *A*, Rift zones along the chain. Solid lines are rift zones of Fiske and Jackson (1972); dashed lines, our interpretation of rifts on largely or completely submerged shields; circles, volcanic centers. *B*, Areas of shields used for volume calculations (table 1) along the chain. *C*, Loci of volcanism along the chain.

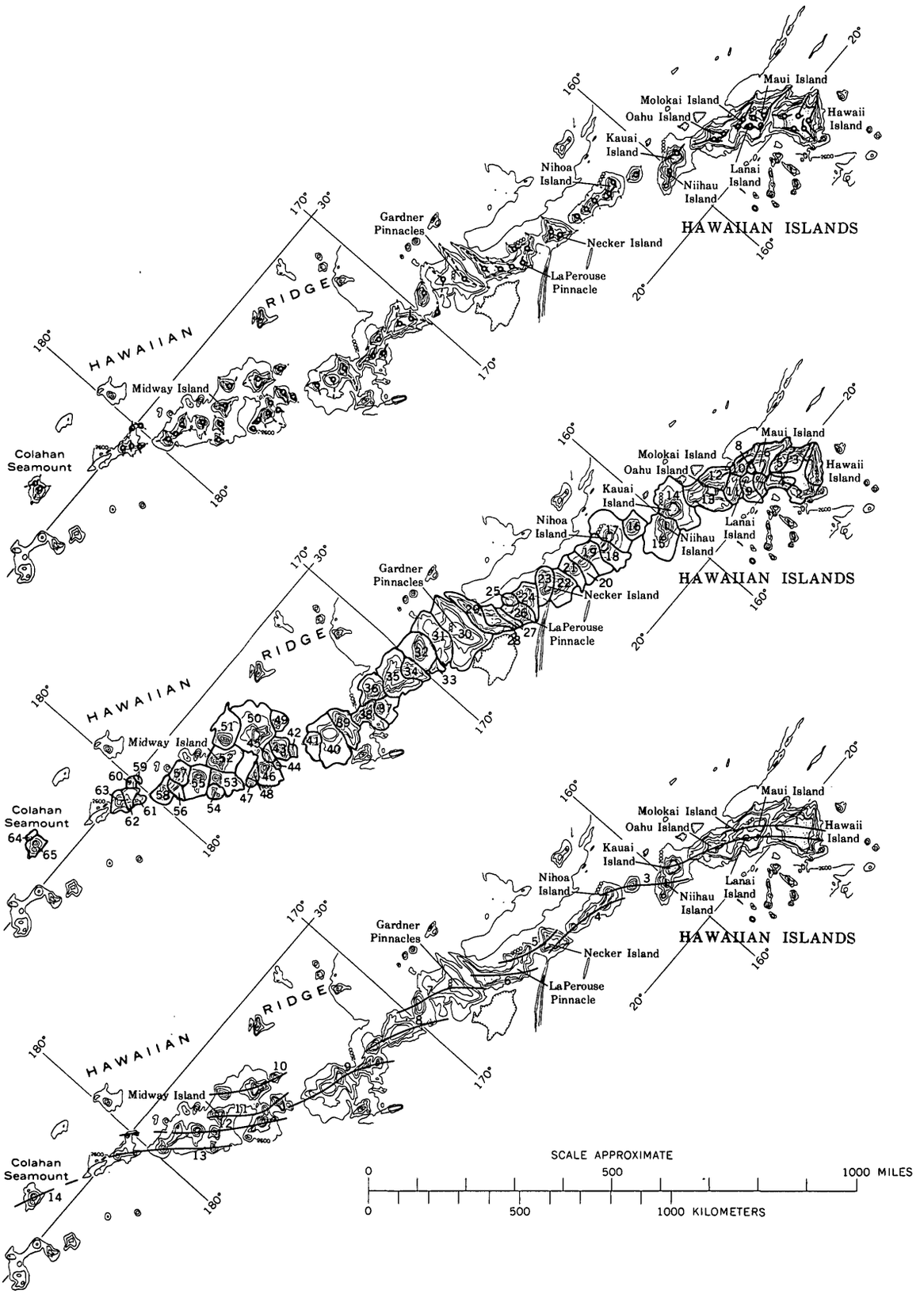
HAWAIIAN RIDGE
HAWAIIAN ISLANDS
Midway Island
Colahan Seamount
Gardner Pinnacles
Necker Island
LaPerouse Pinnacle
Nihoa Island
Kauai Island
Oahu Island
Molokai Island
Maui Island
Hawaii Island
Niihau Island
Lanai Island
180°
170°
160°
30°
20°
SCALE APPROXIMATE
0
500
1000 MILES
0
500
1000 KILOMETERS

attempting to locate the centers of individual shields as given in Jackson, Silver, and Dalrymple (1972); they have been reexamined and partly redrawn by us.)

CRITERIA FOR DEFINING THE SHAPE OF EACH SHIELD

Seamounts in the Hawaiian-Emperor chain occur either as isolated or as clustered volcanic shields. The criteria used to delineate the area of the isolated shields, and hence the area within which a volume was calculated, were that (1) the rift zones, as shown in figure 1, must lie completely within the shield, (2) the base of the shield was arbitrarily determined to be one bathymetric contour above a moat or depression, such as the Hawaiian Deep, (3) where no moat occurs, the base was chosen as the lowest contour reflecting the overall shape of the seamount, and (4) for a few shields, the margin was drawn between bathymetric contours so as to exclude an unrelated feature (for example, Necker Ridge).

Criteria for delineation of individual shields in coalesced seamounts include conditions 1 and 2 above. Further, the contacts separating shields on the Island of Hawaii were observed to lie in saddles between adjacent shields; this was utilized to differentiate shields where saddles occur between volcanic centers. Where coalesced seamounts occur without definitive bathymetry, the shields were defined by criterion 1 alone.

For areas of the shields employed in the volume calculations along the chain as delineated in figure 1*B*, all contacts between shields are assumed to be vertical. Most shields, however, grow downchain and are overlapped in time by younger shields such that their actual contacts are interdigitated, as can be observed between Mauna Loa and both Kilauea and Mauna Kea. The assumption of vertical contacts is therefore not accurate in detail, but it is convenient to assume that, for any individual shield, its upchain deficit in volume under a vertical contact assumption will be balanced by its downchain excess.

VOLUME CALCULATIONS FOR INDIVIDUAL SHIELDS

The revised bathymetric charts of Chase, Menard, and Mammerickx (1973) were utilized as base maps for the submarine part of the chain. A 1-mm plastic overlay grid (½- or 2-mm grids were used for a few shields) was placed over each shield, and the bathymetry read or interpolated for every grid intersection lying within the area of the shield. To correct for the Mercator projection of the bathymetric data, the grid interval (in kilometers) was computed individually for each seamount after applying a latitude correction based upon the approximation that 1° latitude is equal to 111 km.

For the subaerial volume calculations, a U.S. Geological Survey topographic State map of Hawaii (scale 1:500,000) was utilized as a base. Three overlay grids (equaling 1½, 3, and 6 km) were used to obtain a sufficient number of points per shield. The rest of the computation was the same as that for submarine calculations. The shield volumes of table 1 were calculated by computer using a modification of a program written by Doherty (1970) based on Simpson's rule. Computer

Table 1.—*Calculated volumes of shields in the Hawaiian-Emperor Chain*

Shield No.	Shield	Volume (10^3 km^3)		
		Subaerial	Submarine	Total
1	Kilauea	0.7	18.7	19.4
2	Mauna Loa	7.5	35.0	42.5
3	Mauna Kea	3.1	21.7	24.8
4	Hualalai	.6	11.8	12.4
5	Kohala	.4	13.6	14.0
6	Haleakala	1.1	28.2	29.3
7	Kahoolawe	.02	8.8	8.8
8	West Maui	.2	6.2	6.4
9	Lanai	.1	11.9	12.0
10	East Molokai	.2	16.4	16.6
11	West Molokai	.04	17.0	17.0
12	Koolau	.2	20.7	20.9
13	Waianae	.1	24.9	25.0
14	Kauai	.6	28.8	29.4
15	Niihau	.02	17.0	17.0
16	Unnamed seamount	....	....	6.7
17	Nihoa Island	<.01	....	13.1
18	Unnamed seamount	....	....	9.3
19	....do	....	....	9.2
20	....do	....	....	5.2
21	....do	....	....	4.7
22	....do	....	....	12.5
23	Necker Island	<.01	....	13.4
24	French Frigate Shoals	<.01	....	10.9
25	Unnamed seamount	....	....	2.8
26	La Perouse Pinnacle	<.01	....	13.8
27	Unnamed seamount	....	....	5.5
28	....do	....	....	13.9
29	....do	....	....	17.4
30	Gardner Pinnacles	<.01	....	54.1
31	Unnamed seamount	....	....	20.8
32	Raita Bank	....	....	15.0
33	Unnamed seamount	....	....	1.7
34	....do	....	....	12.1
35	Maro Reef	....	....	25.2
36	Laysan Island	....	....	11.3
37	Northampton Bank	....	....	6.8
38	Unnamed seamount	....	....	12.8
39	Pioneer Bank	....	....	15.3
40	Lisianski Island	<.01	....	19.8
41	Unnamed seamount	....	....	4.1
42	....do	....	....	1.1
43	....do	....	....	5.7
44	....do	....	....	1.0
45	....do	....	....	2.9
46	Salmon Bank	....	....	7.6
47	Unnamed seamount	....	....	0.9
48	....do	....	....	1.8
49	....do	....	....	2.2
50	Pearl and Hermes Reef	....	....	22.4
51	Unnamed seamount	....	....	9.0
52	Midway Island	<.01	....	10.8
53	Nero Bank	....	....	5.3
54	Unnamed seamount	....	....	2.2
55	Kure Island	<.01	....	11.3
56	Unnamed seamount	....	....	2.3
57	....do	....	....	8.2
58	....do	....	....	4.6

Table 1.—*Calculated volumes of shields in the Hawaiian–Emperor Chain*—Continued

Shield No.	Shield	Volume (10^3 km^3) Subaerial	Submarine	Total
59	Unnamed seamount	....	....	0.5
60	....do	....	....	0.9
61	....do	....	....	0.9
62	....do	....	....	2.9
63	....do	....	....	3.3
64	....do	....	....	0.3
65	Colahan Seamount	....	....	4.1
66	Kanmu Seamount	....	....	6.9
67	Unnamed seamount	....	....	3.3
68	....do	....	....	6.7
69	Yuryaku Seamount	....	....	9.8
70	Unnamed seamount	....	....	5.8
71	....do	....	....	2.5
72	Kinmei Seamount	....	....	5.9
73	Unnamed seamount	....	....	2.5
74	....do	....	....	15.2
75	Kōko Seamount	....	....	11.2
76	Unnamed seamount	....	....	15.1
77	....do	....	....	18.6
78	....do	....	....	1.5
79	....do	....	....	2.4
80	....do	....	....	10.7
81	Ojin Seamount	....	....	14.4
82	Unnamed seamount	....	....	2.5
83	Jingu Seamount	....	....	5.7
84	Unnamed seamount	....	....	6.6
85	....do	....	....	13.3
86	Nintoku Seamount	....	....	23.7
87	Unnamed seamount	....	....	2.3
88	....do	....	....	13.4
89	....do	....	....	7.0
90	Suiko Seamount	....	....	23.9
91	Unnamed seamount	....	....	8.2
92	....do	....	....	4.4
93	Jimmu Seamount	....	....	21.6
94	Unnamed seamount	....	....	3.3
95	....do	....	....	9.0
96	....do	....	....	3.2
97	....do	....	....	6.5
98	....do	....	....	9.9
99	....do	....	....	0.7
100	Tenchi Seamount	....	....	10.0
101	Unnamed seamount	....	....	2.8
102	....do	....	....	6.6
103	....do	....	....	6.2
104	....do	....	....	6.1
105	....do	....	....	5.1
106	....do	....	....	0.3
107	....do	....	....	1.4
Total				1,081.1

input consisted of the grid interval (kilometers), the bathymetric values for each grid intersection, and the bathymetric value of the shield base.

A problem occurred in calculating the volume of some clustered shields where the base is lower on one side of the shield than on the opposite side. For example, in cross section, the base of shields 4 and 5 of figure 1*B*, being 200 fathoms lower on one side, is an inclined plane. For practical reasons, we calculated the volumes of the two shields as though the change in base were a step, using a separate base for each shield.

Another problem involved how to account for the volume of coral caps and the volume of basalt eroded from the shields. Accurate representation of these two factors would require considerably more sparker-profile or drill-hole information than is available at the present time. Approximations can be made, however; Janda (1970) estimated the rate of denudation for Oahu as 2 to 30 cm/10^3 yr. Easton (1973) has reported the rate of vertical coral growth for Oahu to be about 600 cm/10^3 yr, which lies at the lower range of the rate given by Stearns (1946). At favorable latitudes, the rate of vertical growth of reefs is therefore considerably greater than the denudation rate. At these latitudes, however, the total volume of eroding basalt is much larger than the volume of fringing reefs. Moreover, if the entire chain is moving northward, as suggested by the plate tectonic theory and the paleolatitude data of Grommé and Vine (1972), coral growth must become inhibited and cease and the corals become subject to erosion. Indeed, profiles of Kōko Seamount given by Davies, Wilde, and Clague (1972) show the volume of coral caps to be very small compared with the volume of the seamount itself. As we assumed, for practical purposes, that the volume of coral growth over the entire chain equals the volume of eroded materials, although the volume of eroded materials may be somewhat greater, the calculated volumes are probably minima for the original shields themselves.

Although we have no precise method for assessing the errors involved in the volume calculations, it is probable that the volume calculations are accurate to one or two significant figures for the volcanoes from Kilauea through Molokai, and that, disregarding assumptions on coral growth relative to denudation, the accuracy of the volume calculations should be of roughly the same significance upchain as far as Niihau Island. Beyond that, errors may be somewhat greater owing to uncertainty in locating rift zones and shield areas, but we have nonetheless given the same significant figures in table 1.

VOLUME CALCULATIONS FOR LOCI

A comparison of volumes presented in this paper with those of Shaw (1973) indicates that his volume calculations for the Hawaiian part of the chain are slightly higher (total 8.5×10^5 km^3 as compared with 7.4×10^5 km^3). The difference, if significant, can be accounted for by a combination of several factors: (1) Bathymetry of his division I was revised subsequent to his volume calculations (Chase and others, 1973), (2) four of the seamounts in his division II were omitted in this paper, as we decided that they are unrelated to the Hawaiian Ridge, (3) Shaw's volumes were calculated for large groups of shields using a constant base level for each group, whereas our computations are for individual shields and take into account different base levels from shield to shield, and (4) Shaw's calculations were based on a standard 12-km grid inter-

val, whereas our grid size was, for most of the chain, half as large and our grid interval in the Hawaiian part of the chain varied from 6.1 to 5.3 km.

A modified version of the loci map of Jackson, Silver, and Dalrymple (1972), figure 1*C*, takes into account recent changes in bathymetry (Chase and others, 1973). The total volume of shields along each of the loci lines of figure 1*C* is listed in table 2. These volume data appear to be generally consistent with the hypotheses of Shaw (1973) and Shaw and Jackson (1973), but further discussion of the detailed effects of the revised loci map and calculated volumes on these hypotheses seems premature without additional data on radiometric ages along the loci.

Table 2.—*Volume of shields along loci lines shown in figure 1C*

Loci No.	Volume (10^3 km^3)	Loci No.	Volume (10^3 km^3)
1	110.4	12	36.5
2	168.0	13	16.2
3	36.8	14	70.3
4	40.9	15	9.2
5	27.1	16	66.3
6	50.5	17	56.1
7	89.9	18	67.3
8	50.3	19	7.2
9	60.0	20	34.6
10	33.5	21	29.0
11	19.4	Total	1,079.5

In addition to grouping volumes along loci lines, one can look at the volumes in terms of the two chains, Emperor and Hawaiian. Recent estimates of Clague and Dalrymple (1973) place the age of the Hawaiian-Emperor bend at about 42 to 44 m.y. The age of Meiji Seamount, which we interpret as part of the northern end of the Emperor chain, is about 70 m.y. from fossil evidence (Scholl and others, 1971). Average eruption rates based upon these ages and the volumes of shields in the two chains are 0.012 km^3/yr (336.3×10^3 km$^3 \div 28$ m.y.) and 0.018 km^3/yr (744.9×10^3 km$^3 \div 42$ m.y.) for the Emperor and Hawaiian chains, respectively. These average rates are considerably lower than those reported by Moore (1970) and Decker (1971) (0.05 km^3/yr) for the Island of Hawaii and by Swanson (1972) (0.11 km^3/yr) for Kilauea Volcano during the past 20 yr. They are lower than the rates calculated by Shaw (1973) except for the islands of Kauai and Oahu. Our average rates support the contentions of Jackson, Silver, and Dalrymple (1972), Shaw (1973), and Shaw and Jackson (1973) that present rates of eruption in Hawaii far exceed average rates, and that volcanism along the Hawaiian-Emperor chain, in particular along the loci, has been episodic.

ACKNOWLEDGMENTS

We thank our colleagues G. Brent Dalrymple and D.A. Swanson for critically reviewing the manuscript. We particularly thank Swanson, who made the volume calculations used in Shaw's paper (1973), for consulting with us on methods of volume computation.

REFERENCES CITED

Chase, T.E., Menard, H.W., and Mammerickx, Jacqueline, 1973, Bathymetry of the north Pacific [revision of 1970 charts]: La Jolla, Scripps Inst. Oceanography Charts 2, 7, 8.

Clague, D.A., and Dalrymple, G.B., 1973, Age of Kōko seamount, Emperor Seamount chain: Earth and Planetary Sci. Letters, v. 17, no. 2, p. 411–415.

Dalrymple, G.B., Silver, E.A., and Jackson, E.D., 1973, Origin of the Hawaiian Islands: Am. Scientist, v. 61, p. 294–308.

Davies, T.A., Wilde, P., and Clague, D.A., 1972, Kōko Seamount—a major guyot at the southern end of the Emperor Seamounts: Marine Geology, v. 13, no. 5, p. 311–321.

Decker R.W., 1971, Icelandic versus Hawaiian volcanoes [abs.]: Am. Geophys. Union Trans., v. 52, p. 371.

Doherty, P.C., 1970, Volume of ground swelling: U.S. Geol. Survey Computer Contr. C-628, 9 p.

Easton, W.H., 1973, Submarine bench at 5 m, Oahu, Hawaii: Geol. Soc. America Bull., v. 84, p. 2275–2280.

Fiske, R.S., and Jackson, E.D., 1972, Orientation and growth of Hawaiian volcanic rifts—the effect of regional structure and gravitation stresses: Royal Soc. [London] Proc. A., v. 329, p. 299–326.

Grommé, Sherman, and Vine, F.J., 1972, Paleomagnetism of Midway Atoll lavas and northward movement of the Pacific plate: Earth and Planetary Sci. Letters, v. 17, p. 159–168.

Jackson, E.D., Silver, E.A., and Dalrymple, G.B., 1972, Hawaiian-Emperor chain and its relation to Cenozoic circumpacific tectonics: Geol. Soc. America Bull., v. 83, p. 601–618.

Janda, R.J., 1970, Multiple approaches to computing denudation rates for the Waianae and Koolau volcanoes, Island of Oahu, Hawaii: Geol. Soc. America Abstracts with Programs, v. 2, no. 2, p. 105–106.

Malahoff, Alexander, and Woollard, G.P., 1971, Geophysical studies of the Hawaiian Ridge and Murray Fracture Zone: Hawaii Inst. Geophysics Contr. 312, p. 27–85.

Moore, J.G., 1970, Relationship between subsidence and volcanic load, Hawaii: Bull. Volcanology, v. 34, p. 562–576.

Morgan, W.J., 1971, Convection plumes in the lower mantle: Nature v. 230, no. 5288, p. 42–43.

——1972a, Deep mantle convection plumes and plate motions: Am. Assoc. Petroleum Geologists, v. 56, no. 2, p. 203–213.

——1972b, Plate motions and deep mantle convection, *in* Studies in earth and space sciences (Hess volume): Geol. Soc. America Mem. 132, p. 7–22.

Scholl, D.W., Creager, J.S., Boyce, R.E., Echols, R.J., Fullam, T.J., Grow, J.A., Koizumi, I., Lee, H., Ling, H.-Y., Supko, P.R., Stewart, R.J., and Worsley, T.R., 1971, Deep Sea Drilling Project Leg 19: Geotimes, v. 16, no. 11, p. 12–15.

Shaw, H.R., 1973, Mantle convection and volcanic periodicity in the Pacific; evidence from Hawaii: Geol. Soc. America Bull., v. 84, no. 5, p. 1505–1526.

Shaw, H.R., and Jackson, E.D., 1973, Linear island chains in the Pacific—result of thermal plumes or gravitational anchors?: Jour. Geophys. Research, v. 78, no. 35, p. 8634–8652.

Stearns, H.T., 1946, An integration of coral-reef hypotheses: Am. Jour. Sci., v. 244, p. 245–262.

Swanson, D.A., 1972, Magma supply rate at Kilauea volcano 1952–1971: Science, v. 175, p. 169–170.

Wilson, J.T., 1963, A possible origin of the Hawaiian Islands: Canadian Jour. Physics, v. 41, no. 6, p. 863–870.

Jour. Research U.S. Geol. Survey
Vol. 2, No. 5, Sept.-Oct. 1974, p. 551—562

STRATIFORM CHROMITITE AT CAMPO FORMOSO BAHIA, BRAZIL

By DAVID C. HEDLUND; JAIRO FERNANDES DE COUTO MOREIRA,[1] ANTÔNIO CARLOS FERRAZ PINTO,[1] JOSÉ CARLOS GONÇALVES DA SILVA,[1] and GERALDO VIANNEY V. SOUZA,[1]
Denver, Colo.; Rio de Janeiro, Brazil

Work done in cooperation with the Departamento Nacional da Produção Mineral and the Companhia de Pesquisa de Recursos Minerais, under the sponsorship of the Agency for International Development, U.S. Department of State

Abstract.—Serpentinized ultramafic rocks of pre-Minas age (Precambrian) crop out in an elongate belt 1 km wide and 15 km long on the west side of the Serra de Jacobina near Campo Formoso, Brazil. The original stratiform ultramafic body has been so metamorphosed, faulted, and eroded that only narrow dismembered segments occur along the thrust-faulted west side of the Serra de Jacobina. The most economically important segment is that near Campo Formoso where chromitite layers can be followed for about 8 km near the base of the intrusion. Three to five chromitite layers of minable thicknesses have been mapped, the thickest being 1.4 to 1.8 m. The aggregate thickness of chromitite is about 5 m and the average grade is about 43.5 percent Cr_2O_3. The Cr:Fe ratio ranges from 1.6:1 in weathered friable chromite to 3:1 in massive unweathered chromitite; in cleaned chromite concentrates the ratio is as much as 3.3:1. Estimates of indicated chromite ore reserves range from 16 to 20 million metric tons, of which only an estimated 6 million tons can profitably be mined. Factors preventing full exploitation of the chromite include (1) the local presence of as much as 7 m of overlying colluvium, (2) the extremely faulted character of the chromitite layers, (3) the presence of an overlying quartzite thrust plate very near the line of chromitite outcrops, and (4) the steep dips of the chromitite layers, 15° to 40° along the Pedrinhas-Limoeiro trends and 50° to 65° along the Cascabulhos trend.

The Campo Formoso chromite district is in north-central Bahia, Brazil, approximately 420 km by road northwest of Salvador (fig. 1). Geologic mapping of this district by the Departamento Nacional da Produção Mineral (DNPM) and Companhia de Pesquisa de Recursos Minerais (CPRM) began in July 1969 and continued through June 1971. The purpose of this work was to determine more accurately the chromitite reserves of the district and to map the existing mine workings. The U.S. Geological Survey (USGS) cooperated in the study under the sponsorship of the Agency for International Development, U.S. Department of State.

[1] Companhia de Pesquisa de Recursos Minerais.

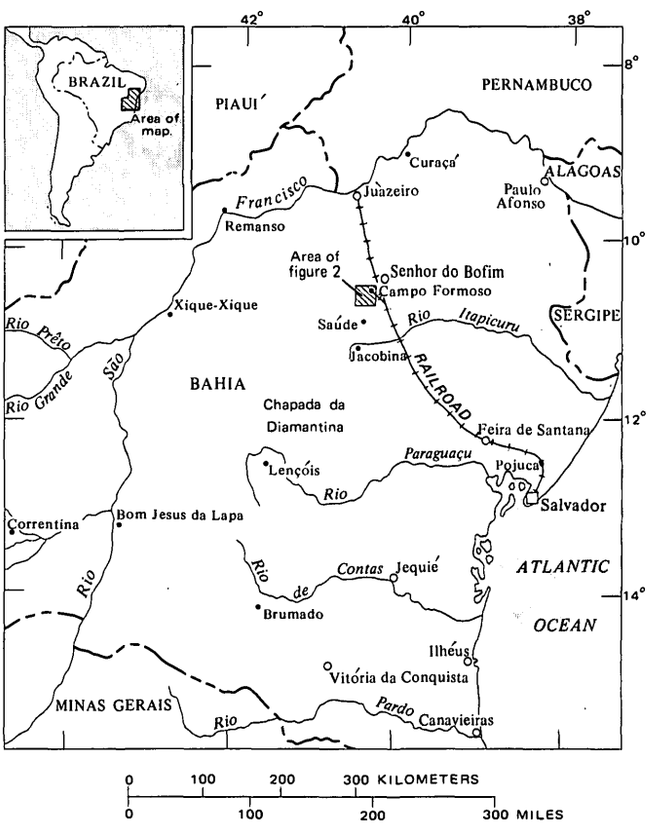

Figure 1.—Index map showing the location of the Campo Formoso district in the State of Bahia, Brazil.

The chromite deposits of the Campo Formoso district were discovered in 1908 by M. M. Monte Flores in the vicinity of the Cascabulhos mine (de Oliveira, 1936). Before 1962 chromite ore production was small and erratic, but with the beginning of chromite smelter operations near Pojuca in 1962

and the purchase of the Pedrinhas, Cascabulhos, and other small mines by Ferro Ligas da Brasil, S.A. (FERBASA), mining activity in the district increased. Greater emphasis was placed on extracting metallurgical-grade chromite, and exploratory drilling for chromitite lump ore below the zone of intensive weathering began. It is estimated that during 1965-69 the amount of chemical- and refractory-grade chromite shipped was three to six times the amount of metallurgical-grade ore.

Refractory, chemical, and metallurgical grades of chromite are being mined by FERBASA and Coitezeiros Mineraços, S. A. (COMISA), in the Campo Formoso district. The largest tonnages of high-grade chromitite come from the Pedrinhas, Coitezeiros, Campinhos, and Cascabulhos mines; all the chromitite workings are open pits or trenches located along a 1-km-wide outcrop belt of serpentinized peridotite that extends approximately 15 km along the west side of the Serra de Jacobina (fig. 2). Because chromite is the only primary mineral left, and the original olivine and pyroxene have been altered to mixtures of serpentine minerals, chrome-chlorite, talc, and amphibole, the chromite-bearing rocks are herein referred to collectively as metaperidotite. The metaperidotite and included chromitite layers are largely concealed by a thrust plate of quartzite and phyllite of the Jacobina Group and by a cover of colluvium or lateritic soil. Consequently, most of the geologic information about the chromitite and metaperidotite has been obtained from mapping of open pits and trenches and from logs of 200 core holes that were drilled in the Pedrinhas, Coitezeiros, Campinhos, Cascabulhos, Limoeiro, and Jatobá mining areas (fig. 3).

The climate of the Campo Formoso region is strongly influenced by the Serra de Jacobina and can vary from semitropical to semiarid within short distances from the range. The Limoeiro, Coitezeiros, Pedrinhas, and Campinhos mines are along a topographic bench at the north-facing foot of the range and are in a semitropical zone that receives about 1,000 mm of rainfall per year. The morning hours are almost invariably overcast, and rainfall is seasonal; maximum rains are in April, May, and June. In the vicinity of the Pedrinhas and Coitezeiros mines, the water table fluctuates widely, and weathering has penetrated the metaperidotite to depths of 40 to 50 m. In the vicinity of the Cascabulhos mine and Santo Antônio, the range front faces westward, and the metaperidotite is slightly farther from the range crest. There the climate is more arid and weathering effects have penetrated only to depths of 10 to 20 m.

The climate is an important economic factor because great tonnages of friable chromite of refractory grade can readily be mined from the chromitite layers in the saprolite zone by power shovel. However, this advantage is offset by the greater thickness of colluvium overlying friable ores in areas of higher rainfall near the fault scarp.

Acknowledgments.—Both FERBASA and COMISA permitted access to their properties, and Dr. Julio Franco da Silva, mining engineer for FERBASA, made drill cores available for study and sampling. We have benefited from field discussions with T. P. Thayer, D. B. Hoover, and W. J. Dempsey, of the USGS, and Juracy Mascarenhas of CPRM. L. V. Blade, USGS, gave valuable assistance in the study of thin and polished sections of chromite-bearing rocks, and J. J. Matzko, USGS, provided the X-ray identification of kammererite. Many chemical and spectrographic analyses were provided by the USGS analytical laboratories in Washington, D.C., and Denver, Colo. Electron microprobe analyses of the chromite grains by G. A. Desborough, USGS, furnished an insight into zoning of chromite-ferritchromit composites. Various maps and unpublished data prepared by J. C. Griffon, Fausto Soares de Andrade, T. P. Thayer, C. A. Wendell, and others provided very useful background information on the geology and mineral economics of chromite at Campo Formoso.

The stratiform character of the chromitite at Campo Formoso was clearly demonstrated by Johnston and de Souza (1943). However, as good rock exposures were not then available, they did not recognize the continuity of the metaperidotite and chromitite layers over a distance of at least 15 km. They assumed that many of the ore bodies were fault slices or blocks within the underlying gneiss. T. P. Thayer (unpub. data, 1970) verified the presence of stratiform chromitite and suggested that the ultramafic rocks were part of a metamorphosed, faulted, and highly eroded peridotite complex that originally had considerable thickness. Poeschl (1966) described the ultramafic rocks as a dike or sill 500 to 700 m thick that was intruded along the contact between the gneiss and the quartzite of the Jacobina Group. The regional geology of the Campo Formoso quadrangle was mapped by Griffon (1967). Griffon (1965, 1966), Mascarenhas (1969), and Leo, Cox, and Carvalho (1964) studied the Jacobina Group and the regional structure of the Serra de Jacobina. One of the earliest maps of the chromite deposits (Elisio Gondim, unpub. map, 1931) shows topography and mine locations near Santo Antônio. An excellent summary report with maps was prepared by de Souza (1942). Fausto Soares de Andrade (unpub. data, 1960) of DNPM described the geology of the Coitezeiros mine and presented many analyses of chromite concentrates. C. A. Wendell, USGS, and Celso Pinto Ferraz, DNPM (unpub. data, 1969), made an economic evaluation of the chromitite deposits and briefly described the geology. Other papers have been of a more specific nature, such as Leonardos' (1935) description of the occurrence of garnierite, and Trajano's (1943) study on the problems of beneficiating the chromite.

GEOLOGIC SETTING

Metasedimentary rocks and structure

The Serra de Jacobina is a north-northeast-trending range in north-central Bahia that consists of a section approximately 8,000 m thick of tightly folded and faulted quartzite and

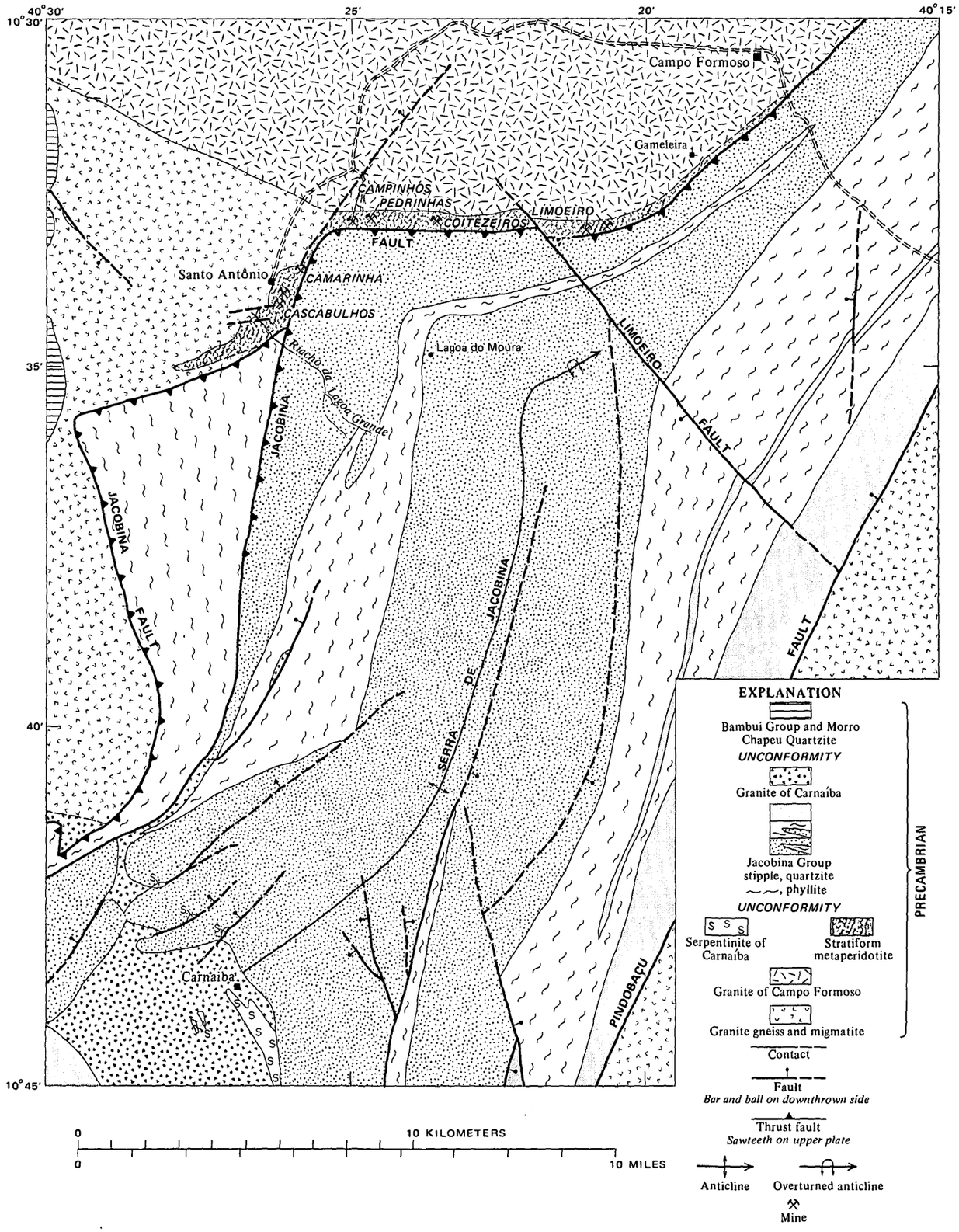

Figure 2.–Regional geology of the Campo Formoso area. UTM grid, 4-km increments, origin at the equator and long. 45° W.

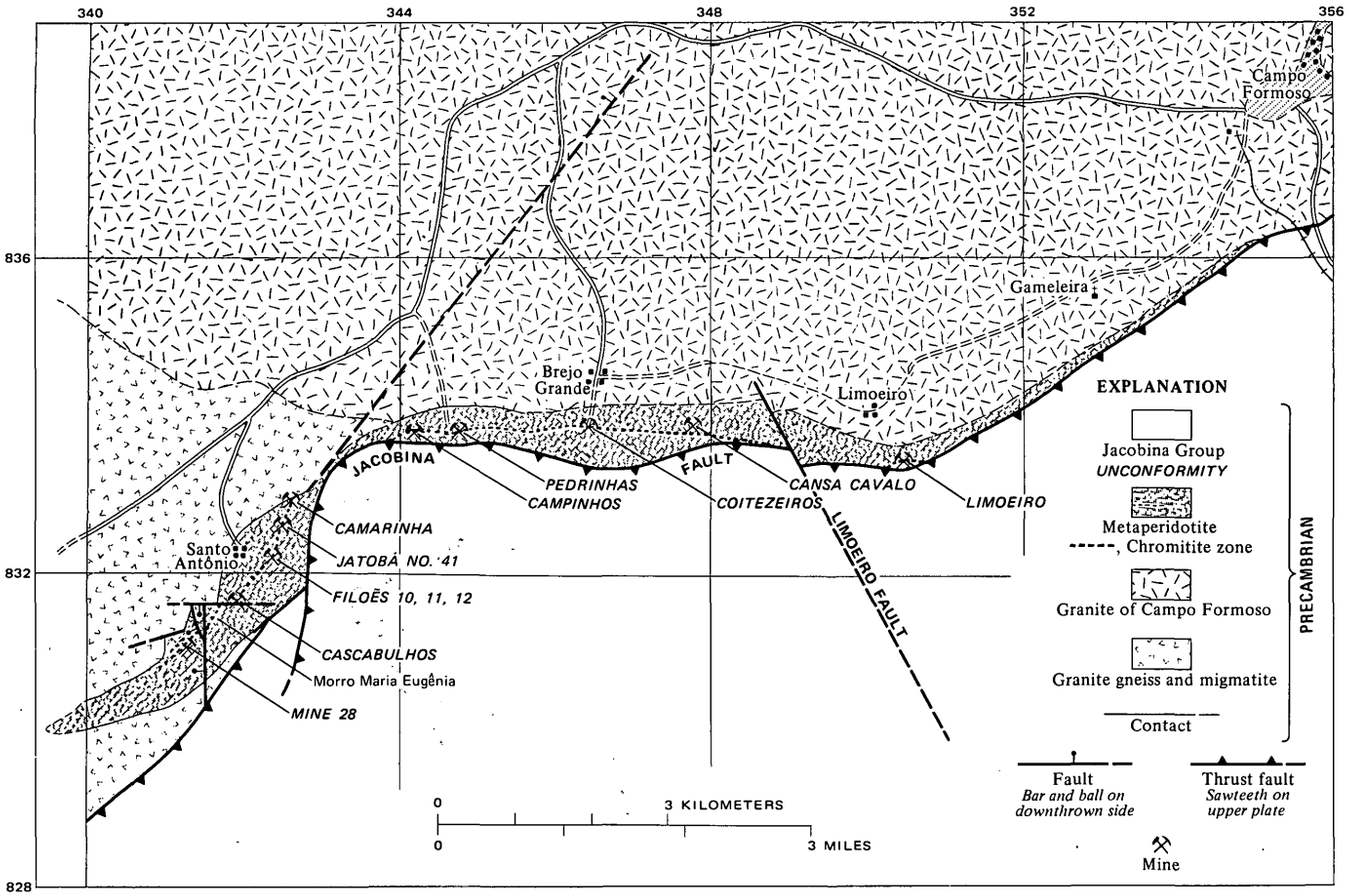

Figure 3.—Generalized geologic map of the Campo Formoso chromite district.

phyllite. The quartzite forms prominent strike ridges that reach altitudes of 900 to 1,100 m. The phyllite is far less resistant to weathering and forms strike valleys within the range and low rounded hills reaching altitudes of 500 to 700 m along the flanks of the range.

The quartzite, phyllite, and sedimentary iron-formation that make up the Jacobina Group have been regionally metamorphosed to the lower amphibolite facies; locally andalusite, kyanite, and garnet have been identified within the phyllite layers, and chrome-muscovite and green tourmaline have been identified within the quartzites. Although the Jacobina Group is in fault contact with older granite gneiss and migmatite and the metaperidotite of Campo Formoso, the presence of detrital chromite in the Jacobina quartzite indicates that the Jacobina Group is younger than the metaperidotite. Because the Jacobina Group has an age of about 1,800 m.y. (Precambrian), as shown by the recent geologic map of Brazil (Departamento Nacional da Produção Mineral, 1971), the metaperidotite at Campo Formoso is older than 1,800 m.y. This is in accord with a Precambrian age for stratiform chromitites throughout the world (Thayer, 1970).

In the Campo Formoso area, the quartzite and phyllite of the Jacobina Group are folded into a tight anticline that trends N. 40° E., and plunges 35° to 45° NE. The west limb of the anticline is locally overturned and buckled in the area from Lagoa do Moura to the Limoeiro fault (fig. 2) as the result of post-anticlinal folding. As a consequence of this cross-folding, the range front trends N. 70° E. from near the Camarinha mine to Campo Formoso. Near Campo Formoso and to the north, the west limb of the anticline is absent, having been faulted and removed by subsequent erosion. The east limb of the anticline is not overturned, as indicated by the normal stratigraphic sequence and the fracture cleavage within phyllite.

The east side of the range is bounded by a high-angle normal fault that strikes N. 35° E. and dips about 80° WNW. This fault is termed the Pindobaçu fault, although its continuation farther south in the Jacobina area outside the mapped area may be part of the Itaitu fault system.

The thrust along the west and northwest margin of the range is termed the Jacobina fault. This fault is locally imbricate, and near Riacho da Lagoa Grande, 2 km south of Santo

Antônio, the phyllite is thrust over quartzofeldspathic gneiss, and quartzite is thrust over phyllite. Only near Campo Formoso does it appear that competent quartzite beds have been thrust over equally competent granite.

Granite

Two granite stocks crop out within the area mapped (fig. 2). The granite of Carnaíba is clearly younger than the sedimentary rocks of the Jacobina Group, as shown by the presence of quartzite inclusions in the granite and the comagmatic pegmatites that cut quartzite and older serpentinite. The granite of Campo Formoso is of uncertain age; it cuts older granite gneiss and migmatite, but intrusive contacts with quartzite and the metaperidotite were not observed. The metaperidotite cuts the inferred projection of the granite-gneiss contact near the Campinhos mine, which strongly suggests that the metaperidotite is younger than the granite.

Ultramafic rocks

The original ultramafic complex near Campo Formoso was a stratiform body consisting chiefly of peridotite and chromitite, and probably minor pyroxenite and gabbro layers. Only eroded remnants of the original faulted and metamorphosed complex remain and include (1) the serpentinite, chromitite, and actinolite gneiss complex in the Campo Formoso area, which is at least 15 km long and slightly less than 1 km wide, (2) the small occurrence of chromitite and serpentinite to the north of Campo Formoso near Fazenda Sacaiba outside the mapped area, and (3) probably the serpentinite at Carnaíba. The metamorphosed remnant at Campo Formoso may extend for an appreciable distance beneath the Jacobina thrust plate, as suggested by a strong gravity gradient over the Serra de Jacobina near Campo Formoso (D. B. Hoover, USGS, written commun., 1970). Although serpentinite has relatively low density (2.6 g/cm^3), the presence of included chromitite layers with a density of 3.3 g/cm^3 contributes to the total density contrast with the surrounding granite, migmatite, and quartzite. Only one drill hole has penetrated the quartzite thrust plate, and this was insufficient to test the continuity of the ultramafic rocks beneath the thrust plate, which dips 40° S. at the drill site.

The attitude of the granite of the granite-metaperidotite contact is of significance to the exploration of chromitite in the vicinity of the Pedrinhas-Coitezeiros-Limoeiro mining areas. If the granite of Campo Formoso is older than the metaperidotite, then along strike the chromitite zone should be the same distance from the granite-metaperidotite contact, and this contact should be tilted in accordance with the dip of the chromitite layers in this area, that is, 15° to 40°. Generally the chromitite zone is not greatly divergent from the granite-metaperidotite contact (fig. 3), and the slight divergence from this contact can be explained by reverse or thrust faulting nearly parallel to the strike of the layering. In contrast, if the granite of Campo Formoso were younger than the metaperidotite, then significant variations in attitude and distance of the chromitite zone from the intrusive contact would be expected.

Serpentinite and serpentine-rich rocks of the greenschist facies of metamorphism are the dominant types within the metaperidotite of Campo Formoso. The fresh serpentinite ranges from dark-greenish black to dark olive to dark-greenish gray and is locally translucent in various shades of light green. In some samples disseminated chromite grains having mantles of kammererite impart a purple speckled pattern to the rock when wet. Serpentinite from some drill cores has abundant anastomosing veinlets of kammererite and shows partial replacement by pale-purple chrome-chlorite. Sparse chrysotile veinlets tend to follow microfractures in the more translucent serpentinite. The dominant serpentine mineral is antigorite, which has a very low birefringence and n_γ=1.565±0.005. In some massive varieties of serpentinite the flaky or fibrolamellar antigorite is commonly intergrown with talc, and the chrome-chlorite is pseudomorphic after pyroxene or olivine. In other types the antigorite is pseudomorphic after olivine, and the chrome-chlorite forms mantles about disseminated and resorbed chromite grains.

In the vicinity of the Cascabulhos mine and to the south near Morro Maria Eugênia, minor amounts of chlorite and tremolite are intergrown with serpentine. The rock in this area is commonly light-greenish gray and has a brown patchy mottling that is attributable to the partial oxidation of ferrian dolomite and magnetite. At Mine 28, fibrous needles of tremolite as long as 1 cm are intergrown with antigorite and talc. Carbonate is not abundant but where present is commonly in the form of clotted aggregates of dolomite containing disseminated chromite grains. Minor calcite veinlets cut the more schistose and talcose serpentinite.

Talc schist is most common along shear zones, where it partially or completely replaces the serpentinite. Pale-greenish-gray talc pods, as much as 0.3 m across, locally fill former tensional fractures between chromitite boudins at the Cascabulhos mine.

Highly foliated actinolite gneiss and amphibolite have been cut by drill holes at the Pedrinhas mine and locally crop out at the Campinhos and Cascabulhos mines. At many places the actinolite gneiss grades into amphibolite that consists of 20 to 30 percent sodic andesine (An_{38-42}), 60 percent actinolite, and about 5 percent secondary quartz. Cumulate textures are rare, but in a drill core taken from the Pedrinhas mine, hole F-92-2-S (at depth 121–123 m, coordinates–N:8833.674, E:344.982), the alternation of centimeter-thick layers of greenish-brown biotite with actinolite-rich layers suggests an original rhythmic cumulate deposition. Elsewhere, metamorphism, shearing, and faulting have made interpretation of origin doubtful. At most localities the amphibolite and actinolite gneiss are in fault contact with chromitite-bearing metaperidotite, and late-stage hydrothermal alteration has resulted in the replacement of actinolite by talc along fault

boundaries. Quartz veins locally cut the amphibolite, and minor amounts of pyrite and pyrrhotite are present as fracture fillings and as disseminated grains. As a working hypothesis, the actinolite gneiss and amphibolite are considered to be metamorphosed, sheared, and faulted gabbro and pyroxenite layers within the stratiform complex.

The paragenetic sequence from early to late for the metamorphic mineral assemblage is as follows: antigorite, actinolite-tremolite, biotite → kammererite, ferritchromit → talc and chrysotile → carbonate, chiefly ferrian dolomite. The assemblage suggests that the peridotite was metamorphosed to antigorite and the pyroxenite-gabbro to actinolite, chlorite, and biotite. Late-stage reactions involved the mobilization of chromium, iron, and aluminum to form kammererite and ferritchromit, and of silica and CO_2 to form talc and the carbonates.

A sample of light-greenish-gray serpentine-chlorite-talc schist containing minor amounts of disseminated chromite and magnetite was chemically and spectrographically analyzed. This sample was taken from the bottom of the Cascabulhos trench and appeared to be only slightly weathered. The analytical results and calculated normative mineral values (table 1) suggest that the original rock was a peridotite of about 52 percent enstatite, 36 percent forsterite, and 7 percent disseminated chromite and magnetite.

Quaternary surficial deposits

Quaternary colluvium is as much as 7 m thick in the vicinity of the Campinhos, Pedrinhas, Coitezeiros, and Limoeiro mines. It consists of light-brown to reddish-brown sandy soil 1 to 3 m thick, and underlying coarse colluvium, generally about 3 m thick, that contains angular quartzite and chromitite fragments. Most of the chromitite float ore (rolado) is obtained from the lower part of the coarse colluvium. Inasmuch as most of the chromitite float ore moves downslope by soil creep, concealed chromitite layers are most easily found by trenching upslope.

Below the lower colluvial interval is a saprolitic or lateritic zone formed from serpentinitic rocks. In the Pedrinhas area this zone is as much as 40 m thick. Dusky-green chromiferous nontronite, containing as much as 1.5 percent nickel and 7.5 percent Cr_2O_3, is commonly concentrated along the contact between the coarse colluvium and the underlying laterite. Within the saprolite, the massive chromitite layers show varying degrees of fracturing, slumping, and even slight flexuring. In places the dusky-green nontronite is concentrated along faults or along fractures in the massive chromitite layers. Chromiferous clays also preferentially mantle the individual chromite grains in the net-textured chromite-serpentinite rock; they probably formed by the weathering of kammererite and ferritchromit. X-ray diffraction patterns of the dusky-green clay indicate that garnierite is not present in detectable amounts. The presence of trace amounts of La, Y, and Yb (0.0015–0.015 percent) in the clay suggests that the rare earths are not mobile under intensive tropical weathering conditions.

CHROMITITE DEPOSITS

Serpentinite containing more than 20 percent chromite is considered to be a segregated rock, and that containing more than 75 percent chromite is a high-grade ore, whereas that

Table 1.—*Chemical and semiquantitative spectrographic analyses, in weight percent, and norm of serpentine-chlorite-talc schist from the metaperidotite, Cascabulhos mine*

Chemical analysis and norm

[Analyses by P. L. D. Elmore, Gillison Chloe, James Kelsey, H. C. Smith, and J. L. Glenn, U.S. Geological Survey, 1970]

SiO_2	40.8	C	4.0
Al_2O_3	4.0	or	0.6
Fe_2O_3	2.0	ab	0.2
FeO	1.8	an	0.2
MgO	36.2	en	51.8
CaO	0.11	fo	35.6
Na_2O	0.05	mt	3.3
K_2O	0.10	cr	4.3
TiO_2	0.05		
P_2O_5	0.05	Total	100
MnO	0.10		
CO_2	0.05		
H_2O+	12.0		
H_2O-	0.59		
Total	98		

Semiquantitative spectrographic analysis

[Results are reported in percent to the nearest number in the series 1, 0.7, 0.5, 0.3, 0.2, 0.015, and so forth; about 30 percent of the assigned groups for semiquantitative spectrographic results include the quantitative values. G, greater than 10 percent; N, not detected at limit of detection. Analyses by J. L. Harris, U.S. Geological Survey, 1970]

Si	G	Cu	N
Al	2	Ga	N
Na	.01	La	N
K	N	Y	N
Fe	5	Yb	N
Mg	G	Mo	N
Ca	.003	Ni	.3
Ti	.01	Pt	N
P	N	Pd	N
Mn	.1	Sc	.0015
Ba	.002	V	.005
Co	.005	Zr	N
Cr	3		

containing 20 to 75 percent chromite is a low-grade ore (Thayer, 1970). At Campo Formoso low-grade ores commonly include net-textured and rhythmically laminated chromite-serpentinite rock, whereas the massive and occluded-textured chromitites commonly are high-grade ores. Massive chromitite layers commonly have a sharp footwall and grade upward into occluded-textured chromitite and then into rhythmically laminated or net-textured chromite-serpentinite rock. The net-textured and rhythmically laminated types of chromite-bearing serpentinite are generally economically mined only where weathering has been intense enough to yield friable ore.

Areal distribution

The chromitite deposits can be traced for about 8 km, although they are broken into three segments by major faults. The most economically important segment—the Pedrinhas trend—is about 5,500 m long and includes the Pedrinhas, Campinhos, Coitezeiros, and Cansa Cavalo mines (fig. 3). This segment is bounded on the east by the Limoeiro fault and on the south and west by the overlying Jacobina thrust fault. The Cascabulhos trend is about 2,500 m long and includes the Cascabulhos mine, the trenches at Morro Maria Eugênia, Filões 10, 11, and 12, the Jatobá No. 41, and the Camarinha mines. The north end and east side of this segment are concealed by the overlying Jacobina thrust plate and the south end is terminated by faults that have displaced the metaperidotite. The Limoerio trend is at least 300 m long and includes small pits and trenches near the base of the Jacobina fault scarp near the village of Limoeiro. Reconnaissance surveys indicate that the chromitite along the Limoeiro trend is largely concealed by the Jacobina thrust plate. Within each segment or trend, numerous smaller faults have disrupted the continuity of the chromitite layers. Many of these faults predate the Jacobina thrust fault and caused shearing and development of boudinage in the chromitite layers. For this reason, correlation of the various chromitite layers between the different faulted segments is difficult.

Tentative correlation of the layers can be made by comparing sections compiled from drill-core data with sections measured at the mines (fig. 4). Owing to the abundance of small faults, measured sections within the mines are more reliable than the drill core data; probably the best nonfaulted section is in the Coitezeiros "A" mine where five chromitite layers, each 0.3 to 1.4 m thick, are exposed in an interval of 10 m (fig. 5).

The presence of such a thick section of chromitite near the base of the original stratiform complex suggests that the intrusion was of considerable thickness in order to account for the large volumes of cumulate chromite. Pre-Jacobina erosion probably extended into the chromitite zone within the lower

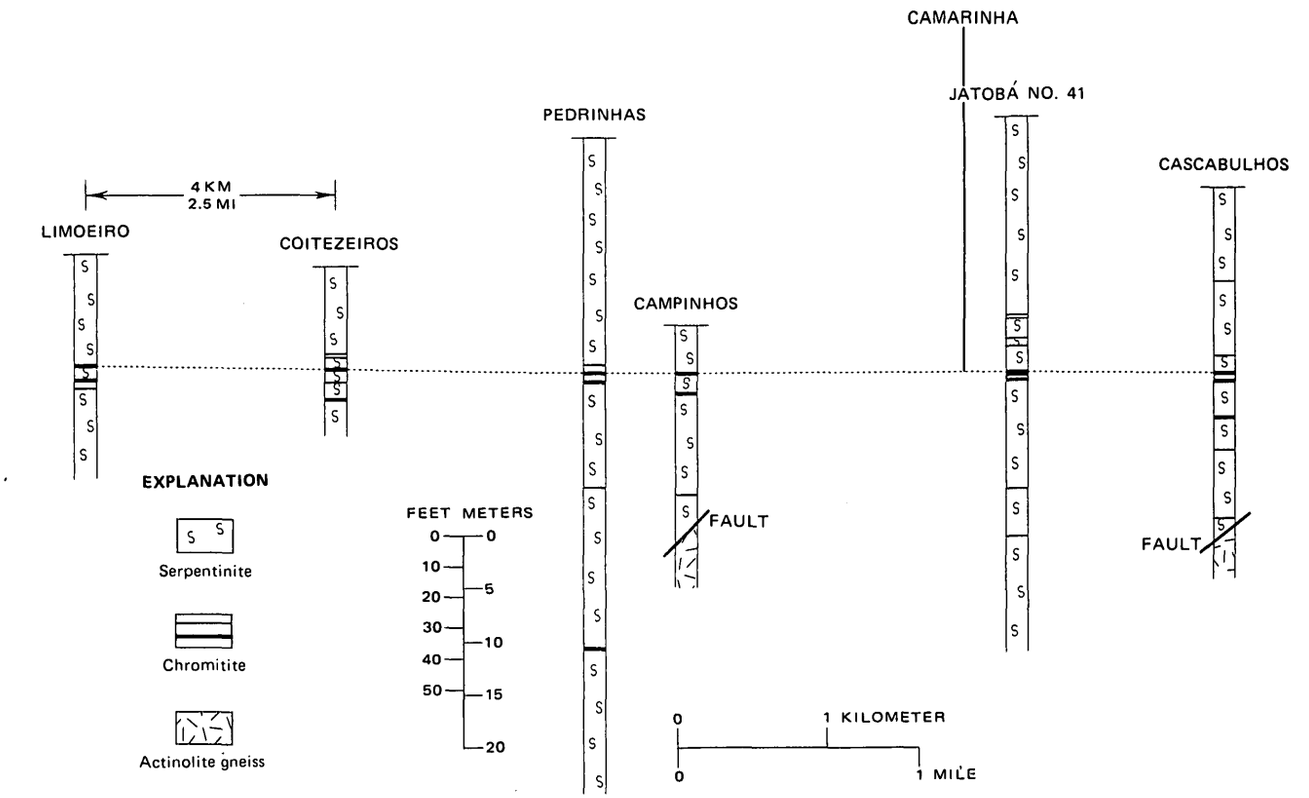

Figure 4.—Tentative correlation of the chromitite zones as indicated by drill-hole information from the various mining areas. Thrust plate and colluvium cover from Camarinha to Campinhos mines.

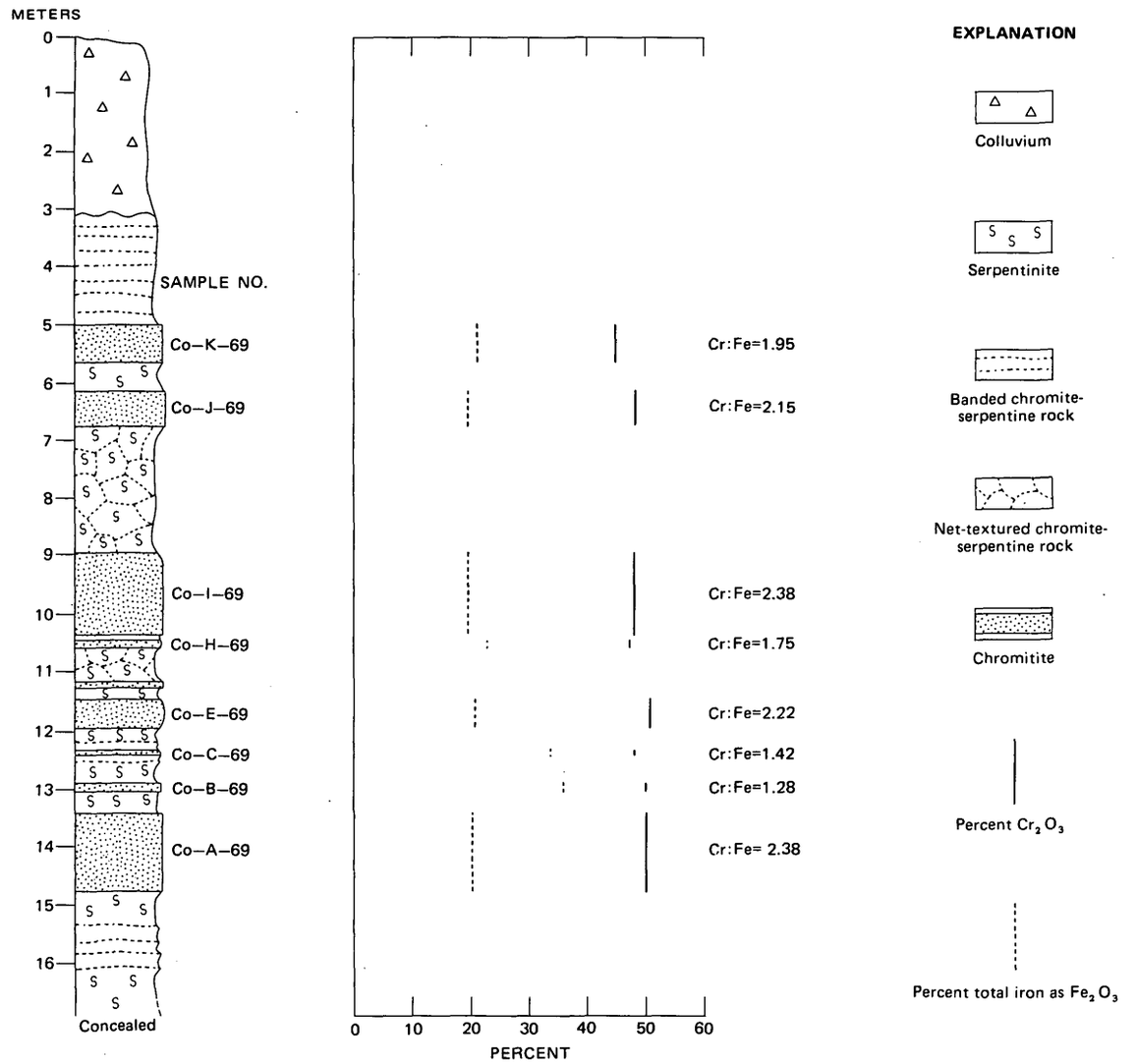

Figure 5.—Measured section within the Coitezeiros "A" mine.

part of the complex, as shown by the local presence of detrital chromite in the quartzite of the Rio do Ouro Formation. Because most of the complex is concealed by the overlying thrust plate of quartzite and phyllite of the Jacobina Group, it is uncertain how much of the complex was removed by pre-quartzite erosion.

Structure and magnetic properties

The metaperidotite has been faulted and tilted in such a manner that along the Pedrinhas-Limoeiro trends the stratiform rocks strike N. 60° to 75° E., dip 15° to 40° S., and thus project under the quartzite fault scarp. In contrast, along the Cascabulhos trend the layering strikes N. 20° to 30° E., and dips 50° to 65° SE. These two contrasting strikes and attitudes are the result of a strong west-northwest-directed stress that caused greater tilting of the layering along the Cascabulhos trend. The resultant strain was relieved by thrusting along the Pedrinhas-Limoeiro trends, where tilting was less. Probably this same stress also deformed the anticlinal structure of the Serra de Jacobina and caused cross-folding, thrusting, and local overturning of the quartzite and phyllite.

Although core drilling has not been sufficient to establish details of the fault pattern along the Pedrinhas-Limoeiro trends, preliminary core data suggest that in the vicinity of the Pedrinhas mine large faults have brought amphibolite and actinolite gneiss into contact with the chromitite zone. Field evidence suggests that the larger faults are essentially parallel to the strike of the layering in the metaperidotite.

About 1 km south of Santo Antônio the fault pattern is more obvious because of better exposures. In this area a strong east-striking fault has displaced the chromitite belt about 150 m to the west of the Cascabulhos trend (fig. 3).

The mapping of concealed faults has been aided by a series of magnetic ground traverses across the strike of steeply to moderately dipping chromitite layers. Generally the more steeply dipping chromitite layers produce strong magnetic anomalies that can be related to the high magnetic susceptibility of chromite-ferritchromit composite and zoned grains. Ground magnetic surveys have been especially useful along the Cascabulhos trend where the steep dips and thin colluvial cover have enhanced the magnetic profiles (Roberto A. V. de Moraes and D. B. Hoover, written commun., 1970).

Magnetic susceptibility measurements were made on 17 specimens of serpentinite, chromitite, friable chromite, and actinolite gneiss with a magnetic-susceptibility bridge (table 2). These results indicate that massive to occluded-textured chromitite layers generally have a high magnetic susceptibility in the zone of intensive weathering where K values may be as much as 0.1198 emu/cm^3. This high magnetic susceptibility is closely related to the presence of ferritchromit replacement of the chromite along fractures and along the margins of the individual grains.

Table 2.—*Magnetic susceptibility data for serpentinite, chromitite, and actinolite gneiss from Campo Formoso, Bahia*

[Measurements by W. C. Rivers, U.S. Geological Survey]

Rock type	Number of samples	K-values (emu/cm^3)
Serpentinite-serpentine-talc schist	7	0.00064 – 0.003595
Actinolite gneiss	1	.000141
Net-textured chromite-serpentine rock	2	.000079 – .007495
Banded chromite-serpentine rock	1	.0525
Massive to occluded-textured chromitite	5	.000108 – .1198
Friable chromite	1	.0171

Mineralogy

At Campo Formoso the massive chromitite is characterized by 75 to 90 percent of closely packed, even-textured, subhedral to euhedral chromite octahedra and 10 to 25 percent interstitial antigorite, talc, and chrome-chlorite. Many of the chromite grains in the low-grade ore show slight marginal rounding and etching which are attributable in part to boundary resorption effects during metamorphism and in part to weathering. A size analysis of the disaggregated chromite grains shows most to range in diameter from 0.250 to 0.500 mm. This uniformity of size is characteristic of all the textural types of chromite-bearing serpentinite. Within the massive chromitite there may be occluded clots of antigorite-talc-chlorite pseudmorphs after olivine or pyroxene. Some of the occluded silicates are alined within the massive chromitite and provide evidence for the amount of tilting or deformation of the cumulate layer. Within the massive chromitite the silicates are interstitial to the chromite grains, and most commonly a marginal selvage of talc or chrome-chlorite is present around the chromite. Owing to this silicate fraction, most of the massive chromitite layers have a bulk density of about 3.85 g/cm^3.

In thin section most chromite grains show some zoning of dusky reddish-brown cores of chromite and opaque rims of ferritchromit. This zoning of the chromite grains is present in both nonweathered and weathered chromitites but is more extensive in the weathered chromitite where the replacement of chromite by ferritchromit is also fracture controlled, and some grains are completely replaced by ferritchromit. The zoning in the nonweathered chromite is attributable to the migration of iron and chromium during metamorphism. Generally the ferritchromit shell is less than 0.1 mm thick and can be measured under reflected light, inasmuch as the ferritchromit margins have a higher reflectivity than the chromite core (fig. 6). Rutile and ilmenite have been identified in some drill cores of chromitite but generally are not abundant and do not display any crystallographic control within the chromite grains.

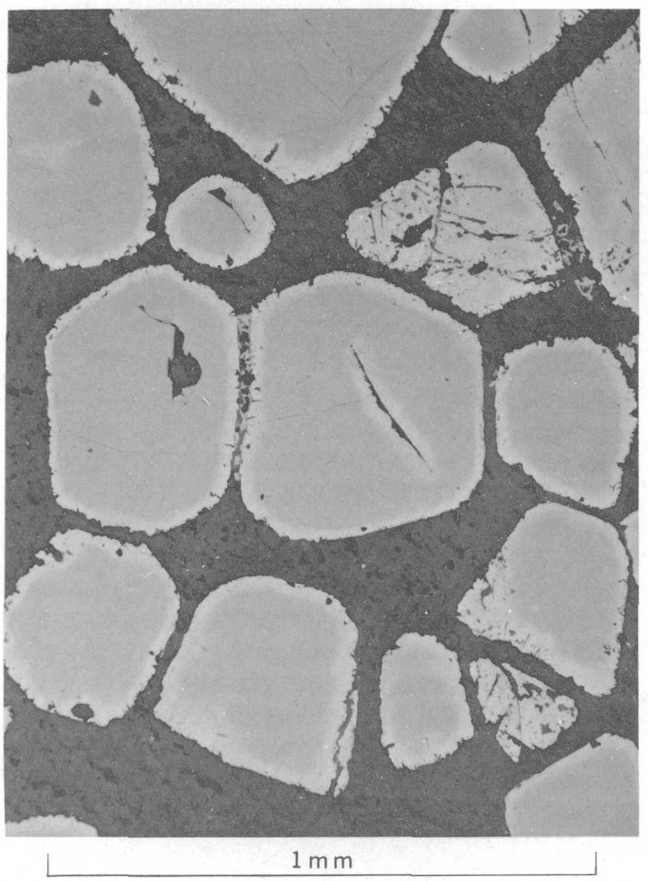

Figure 6.—Photomicrograph of massive chromitite in reflected light showing ferritchromit along the grain margins and along fractures within the chromite. The subhedral chromite grains are fractured and have slightly subrounded outlines. Dark-gray areas are serpentine minerals and chrome-chlorite; medium-gray, chromite; light-gray rims, ferritchromit.

Although no step-scan electron microprobe analyses were made across the individual chromite-ferritchromit grains, petrographic studies provide good evidence for the migration of Al^{+3}, Cr^{+3}, Mg^{+2}, and Fe^{+2} across the chromite-antigorite boundary during metamorphism. The formation of ferritchromit is due to the replacement of Mg^{+2} and Al^{+3} by Fe^{+2} and Fe^{+3}, respectively. This increase in iron would result in a higher magnetic susceptibility for the chromite-ferritchromit zoned grains. With the formation of chrome-chlorite mantles about the individual chromite grains, Al^{+3} and Cr^{+3} have also been transferred out of the chromite to form kammererite, which contains 5.05 percent Cr_2O_3 and 11.5 percent Al_2O_3. This alteration resulted in slight rounding and etching of the chromite. The formation of ferritchromit about chromite cores has also been observed and studied in the serpentinized chromitites from the Stillwater Complex of Montana (Beeson and Jackson, 1969).

The chrome-chlorite, kammererite (table 3), is very closely associated with chromite and forms marginal films about individual chromite grains and fills fractures within the chromitite layers. The kammererite is pale red-purple (5*RP* 6/2), biaxial positive with very small $2V$, $\alpha \cong \beta = 1.585 \pm 0.004$ and X-ray diffraction patterns are identical with standard samples. The calculated formula based on the chemical analysis of kammererite (Cp-1-S-70) (table 3) is $(Mg^{+2}_{5.0}\ Fe^{+2}_{0.1}\ Fe^{+3}_{0.04}\ Cr^{+3}_{0.4}\ Al_{0.3})_{5.84}\ (Si_{3.2}Al_{1.0})_{4.2}O_{18}\ H_{8.1}$ and is calculated on the basis of 18 oxygens per half cell.

Chemistry and minor elements

Chemically the serpentinite is characterized by low SiO_2 content (40.8) and high MgO content (36.2), giving a $MgO:SiO_2$ ratio of 0.887. As the average $MgO:SiO_2$ ratio of harzburgite is approximately 1.02, and of dunite is about 1.23, the chemical data strongly suggest that the serpentinitic rocks of Campo Formoso were originally pyroxene-bearing peridotite containing about 52 percent enstatite (table 1).

The fixed water content of the serpentinite is as much as 12 percent and indicates that large volumes of water in the range of stability for antigorite (300°–500° C) were involved in the metamorphism of peridotite to serpentinite. It is suggested that this water was of meteoric origin and postdated deposition of the quartzite of the Jacobina Group. Chrome muscovite and green chromiferous tourmaline are commonly present in the lower part of the quartzite of the Rio do Ouro Formation, and this chromium doubtless had its source in the ultramafic rocks. The thermal waters that dissolved and transported the chromium necessarily postdate the ultramafic rocks and the quartzite, and either were contemporaneous with the metamorphism or preceded it.

Two analyses of chromite concentrates extracted from massive chromitite, one analysis of weathered friable chromite, and one published analysis of cleaned chromite from banded ore (Stevens, 1944) are presented in table 4. Except in the highly weathered friable chromite, the Cr_2O_3 content ranges from 56.30 to 58.60 percent, and the Cr:Fe ratio ranges from 2.2:1 to 3.3:1 (table 4). All the samples were taken from depths of 23 m or less, and the Campinhos sample is probably most representative of nonoxidized and weakly weathered chromitite. Normative spinels (table 4) were calculated to 100 percent on a silicate-free basis, and of the four spinels calculated for relatively unweathered chromite, hercynite ($FeAl_2O_4$) is the most invariant and ranges from 15 to 19 percent; magnesiochromite ($MgCr_2O_4$) ranges from 54 to 64 percent; chromite ($FeCr_2O_4$) ranges from 12 to 21 percent; and magnetite ($FeFe_2O_4$) ranges from 5 to 10 percent. The oxidation ratio $Fe^{+3}:(Fe^{+2} + Fe^{+3})$ ranges from 0.227 to 0.988, with the unoxidized chromites having values of 0.227 and 0.259.

The minor elements in the chromite concentrates are as follows (in weight percent): Mn, 0.5; Co, 0.02; Ni, 0.07; V, 0.05; and Ti, 0.07. The nickel content in samples of chromitite ranges from 0.07 to 0.15 percent, depending on the amount and kind of silicate present. Two samples of massive chromi-

Table 3.—*Chemical and semiquantitative spectrographic analyses of kammererite from the Campinhos mine*

Chemical analysis

[Results in weight percent. Analysis by J. J. Warr, Jr., 1972, U.S. Geological Survey]

Cr_2O_3	5.05
SiO_2	33.7
Al_2O_3	11.5
Fe_2O_3 (calc)	.59
FeO	1.09
Total iron as FeO	1.22
MgO	35.0
H_2O+	12.8
Total	99.1

Semiquantitative spectrographic analysis

[Results are reported in weight percent to the nearest number in the series 1, 0.7, 0.5, 0.3, 0.2, 0.015, 0.1, and so forth; about 30 percent of the assigned groups for semiquantitative spectrographic results include the quantitative values. G, greater than 10 percent; N, not detected at limit of detection. Analysis by J. L. Harris, 1970, U.S. Geological Survey]

Si	G	P	N	Y	N
Al	7	Mn	.03	Yb	N
Na	.01	Ba	.0003	Mo	N
K	N	Co	.01	Ni	.3
Fe	1.5	Cr	G	Pt	N
Mg	G	Cu	.0002	Pd	N
Ca	.003	Ga	N	Sc	.0015
Ti	.007	La	N	V	.003
				Zr	N

Table 4.—*Chemical analyses and norms of friable chromite and cleaned chromite concentrates from disaggregated chromitite, Pedrinhas and Campinhos mines*

Rock type	(1) Friable chromite, weathered (Pedrinhas)	(2) Chromitite (Pedrinhas)	(3) Chromitite (Campinhos)	(4) Chromitite (Pedrinhas)
	Chemical analyses, in weight percent			
[Analyses 1–3 by J. J. Warr, Jr., and J. I. Dinnin, U.S. Geological Survey, 1970-71; analysis 4 from Stevens (1944). Except for analysis 4, Al, Mg, and Mn were determined by atomic absorption spectometry. Other determinations were performed by modifications of the procedures described by Dinnin (1958, 1960)]				
Cr_2O_3	50.3	[1]57.34	56.30	58.60
Al_2O_3	10.8	11.2	8.7	11.08
Total iron as Fe_2O_3	30.1	[2]16.95	22.13	------
Fe_2O_3	26.2	17.2	6.40	3.94
FeO	3.55	1.51	16.4	12.06
MgO	6.5	11.8	11.4	13.57
MnO	------	0.15	0.21	0.13
CaO	------	------	------	0.04
TiO_2	------	------	------	0.19
SiO_2	1.11	0.17	0.21	0.22
H_2O	------	------	------	0.26
Total	98.46	99.4	99.6	100.11
	Norms			
$3\,MgO \cdot 2\,SiO_2$	2.21	0.341	0.422	0.442
$MgCr_2O_4$	25.7	55.4	53.5	63.9
$FeCr_2O_4$	44.2	20.0	20.9	11.9
$FeAl_2O_4$	18.4	19.1	14.8	18.9
$FeFe_2O_4$	9.5	5.2	10.4	4.9
Total	100	100	100	100
Excess Fe_2O_3	19.6	13.6	-0.79	0.56
Cr:Fe	1.62	2.97	2.24	3.30
$Fe^{+3}:(Fe^{+2}+Fe^{+3})$	.870	.988	.259	.227

[1] Analysis of bulk ore before cleaning: Cr_2O_3=43.1 percent.
[2] Total iron as FeO.

tite (Ca-39 and F-3A-P-55) were analyzed by the fire-assay and solution spectrographic method for Pt, Pd, and Rh (analysts: W. D. Goss, V. C. Haubert, and Joseph Haffty, U.S. Geological Survey, 1972). Both samples were of massive unoxidized chromitite with less than 10 percent silicates and were untreated by hydrofluoric acid. They contain less than 0.010 p/m Pt, 0.004 to 0.044 p/m Pd, and 0.027 to 0.037 p/m Rh.

ECONOMIC GEOLOGY

Within the district, the principal active mines are the Pedrinhas, Campinhos, Cascabulhos, Jatobá No. 41, Filões 10, 11, and 12, and the Cansa Cavalo controlled by FERBASA; and the Coitezeiros mine, operated by COMISA, chiefly a producer of chemical-grade chromite. All are open-pit mines, and no underground mining is being done. The Pedrinhas mine is by far the largest producing mine; as of June 1971 the open pit measured approximately 465 by 180 m and had a depth of 25 m. Both low-grade friable chromite and lump metallurgical-grade chromitite were extracted. In 1968–71 an estimated 18,000 metric tons of metallurgical-grade chromitite was shipped yearly from the Coitezeiros, Pedrinhas, and other mines controlled by FERBASA. This production was expected to increase to 75,000 metric tons in 1973, and possibly to 125,000 metric tons in future years. Most of the lump metallurgical-grade ore has an average Cr_2O_3 content of about 44 percent, and a Cr:Fe ratio of about 2.8:1. Unknown quantities of friable refractory-grade chromite are sized and packaged in 28-kilogram bags for shipment as foundry sand.

The stratiform nature of the chromitite deposits suggests that relatively large reserves are available over a length of 8 km in a belt slightly less than 1 km wide. Indicated reserves are 16 million to 20 million metric tons, of which only about 6 million metric tons now can be profitably mined. About half of this 6 million tons of chromite consists of friable low-grade ore that is readily mined by power shovel. Most of the friable ore is extracted along the Pedrinhas trend where weathering has been intense and the layers dip from 15° to 40°.

Many factors have inhibited the full exploitation of the chromite: (1) Colluvial overburden as thick as 7 m, (2) discontinuity of the chromitite layers due to faulting, (3) an overlying thrust plate of quartzite very near the line of chromitite outcrops, and (4) the attitude of the chromitite layers, which ranges from 15° to 40° along the Pedrinhas-Limoeiro trends and 50° to 65° along the Cascabulhos trend.

REFERENCES CITED

Beeson, M. H., Jackson, E. D., 1969, Chemical composition of altered chromites from the Stillwater Complex, Montana: Am. Mineralogist, v. 54, nos. 7–8, p. 1084–1100.

Departamento Nacional da Produção Mineral, 1971, Mapa Geológico do Brasil: Brazil Dept. Nac. Prod. Mineral Map, scale 1:5,000,000.

Dinnin, J. I., 1958, Rapid analysis of chromite and chrome ore: U.S. Geol. Survey Bull. 1084-A, p. 31–68.

——1960, Determination of total iron in chromite and chrome ore, *in* Short papers in the geological sciences: U.S. Geol. Survey Prof. Paper 400-B, p. B476–B477.

Griffon, J. C., 1965, A tectônica da Serra de Jacobina ao Norte do Rio Itapicurú Mirim: Resumo da Exposição no. I° de Geologia do Nordeste-Maceio.

——1966, Tectônica da parte central da Serra de Jacobina: Resumo da Exposição no. XX Congresso Brasileiro de Geologia-Vitória, Espírito Santo.

——1967, Mapa geológico da parte central da Serra de Jacobina (Bahia, Brasil): Folha Pindobaçú, scale 1:100,000.

Johnston, W. D., Jr., and de Souza, H. Capper A., 1943, Layered or banded chromite at Campo Formoso, Baía, Brasil: Econ. Geology, v. 38, p. 287–297.

Leo, G. W., Cox, D. P., and Carvalho, J. P. P., 1964, Geologia da parte Sul da Serra de Jacobina, Bahia, Brasil: Brazil Dept. Nac. Prod. Mineral Bol. 209, 97 p.

Leonardos, O. H., 1935, Ocurrência de garnierita associada à cromita em Cascabulhos municipio de Campo Formoso, Bahia: Brazil Dept. Nac. Prod. Mineral Bol. 9, p. 57–61.

Mascarenhas, Juracy de Freitas, 1969, Estudo geológico de parte norte da Serra de Jacobina-Bahia-Brasil: Soc. Brasileira de Geologia Bull., v. 18, no. 1, p. 1–22.

Oliveira, A. I. de, 1936, Depositos de chromita do estado da Baía: Brazil Dept. Nac. da Produção Mineral Avulso 12, p. 1–8.

Poeschl, A., 1966, Sôbre geologia e formação da jazida de cromita de Campo Formoso, Bahia: Eng. Mining and Metallurgical Jour., v. XLIV, no. 262, Outubro 1966, p. 173–178.

Souza, H. C. A. de, 1942, Cromo na Baía: Brazil Dept. Nac. Prod. Mineral Bol. 54.

Stevens, R. E., 1944, Composition of some chromites of the western hemisphere: Am. Mineralogist, v. 29, nos. 1 and 2, p. 1–34.

Thayer, T. P., 1970, Chromite segregations as petrogenetic indicators: Geol. Soc. South Africa Spec. Pub. 1, p. 380–390.

Trajano, R. B., 1943, Estudo sôbre o beneficiamento da cromita de Santo Antônio, Estado da Bahia: Brazil Dept. Nac. Prod. Mineral Bol. 7, p. 9–26.

Jour. Research U.S. Geol. Survey
Vol. 2, No. 5, Sept.-Oct. 1974, p. 563–567

DETAILED NEAR-BOTTOM GEOPHYSICAL PROFILE ACROSS THE CONTINENTAL SLOPE OFF NORTHERN CALIFORNIA

By ELI A. SILVER, Menlo Park, Calif.

Abstract.—A geophysical profile was run across the continental slope off the California-Oregon border by use of a deeply submerged instrument package, approximately 50 m above the sea floor, containing a proton magnetometer and a 3.5-kHz transducer for shallow seismic penetration. Surface-towed seismic reflection equipment was operated concurrently. The deep-tow data show that the slope is relatively smooth; this agrees with interpretation of surface seismic profiles. Features smaller than 1 km in length can be resolved with the deep profiles but not with the surface profiles. The deep profiles show small-scale undulations less than 0.5 km long that are especially well formed on the steeper parts of the slope. These undulations may be caused by minor downslope movement of surface sediment or by depositional processes. The deep-tow and surface seismic profiles can be combined to give a more accurate structural picture of the continental slope than can be obtained with surface data alone.

Late Cenozoic subduction of oceanic crust beneath the continental margin off northernmost California and the resulting pattern of deformation of the margin was interpreted from seismic and magnetic evidence (Silver, 1969a; 1971) using sensors towed at the ocean surface. These earlier studies utilized conventional wide-beam echo sounding and reflection profiling, which are unable to reflect the true morphology and finer scale structural details over areas of steep slopes and (or) deep water (see Krause, 1962). Previous studies of the deep sea floor using the deep-tow instrument package developed by the Marine Physical Laboratory of Scripps Institution of Oceanography (Spiess and Mudie, 1970) have revealed much detail not possible to obtain by surface techniques (Spiess and others, 1969; Luyendyk, 1970; Normark, 1970; Larson, 1971). The deep-tow instrument had not been used previously in continental margin studies but had been found to be most useful in geologic studies at scales of hundreds of meters to a kilometer in horizontal dimension and of tens of meters in local vertical relief. It was anticipated that the use of the deep tow would resolve surface configuration and shallow subbottom structure of the continental slope, and that these findings, in turn, would enhance our ability to interpret standard seismic records in this region and improve our understanding of this tectonic environment.

METHODS

In September 1970 a deep-tow profile was run over the continental slope off northern California (fig. 1) across a region previously studied in detail by conventional surface-ship techniques (Silver, 1969a; 1971). The deep tow (hereafter referred to as the fish) is a 1.5-m-long pressure housing for electronic gear and appended transducers; the fish is towed at an average height of 50 m above the sea floor. An armored tow cable containing a coaxial conductor relays information to recorders on board the towing ship. Three of the available geophysical sensing systems were important to this study: (1) A narrow-beam (0.05 rad) downward-looking echo sounder (40 kHz) used in conjunction with a wide-beam upward-looking echo sounder (23 kHz) to provide precision (within 2 m) bathymetry, and to establish the vertical position of the fish, (2) a relatively wide-beam 3.5-kHz subbottom reflection profiling system, and (3) a proton magnetometer. Side-looking sonar data and bottom photography from the fish were of limited use because of equipment malfunctions.

The towing vessel, R/V *Thomas Washington* of Scripps Institution, was positioned by satellite navigation. Under normal operating conditions (Spiess and Mudie, 1970), bottom-sitting transponders are used to position the fish acoustically, but as this single profile was intended to be about 10 times the maximum transponder range, they were not used. In deep water the fish tows as much as several kilometers behind the ship (fig. 1), moving at a survey speed of 1.5 to 2 knots. If the path of the ship is curved, the fish tends to cut inside the ship's path on the corners; on the lower continental slope, the fish's track may have been as much as several hundred meters to the side of the ship's track.

RESULTS AND DISCUSSION

The precision bathymetry and 3.5-kHz reflection data have been combined in figure 2 (produced by digitizing deep-tow records); figure 3 shows the accompanying surface air-gun profile for the west end of the area of figure 2. These profiles, when plotted to the same vertical exaggeration and scale and superimposed, show close correspondence of the larger

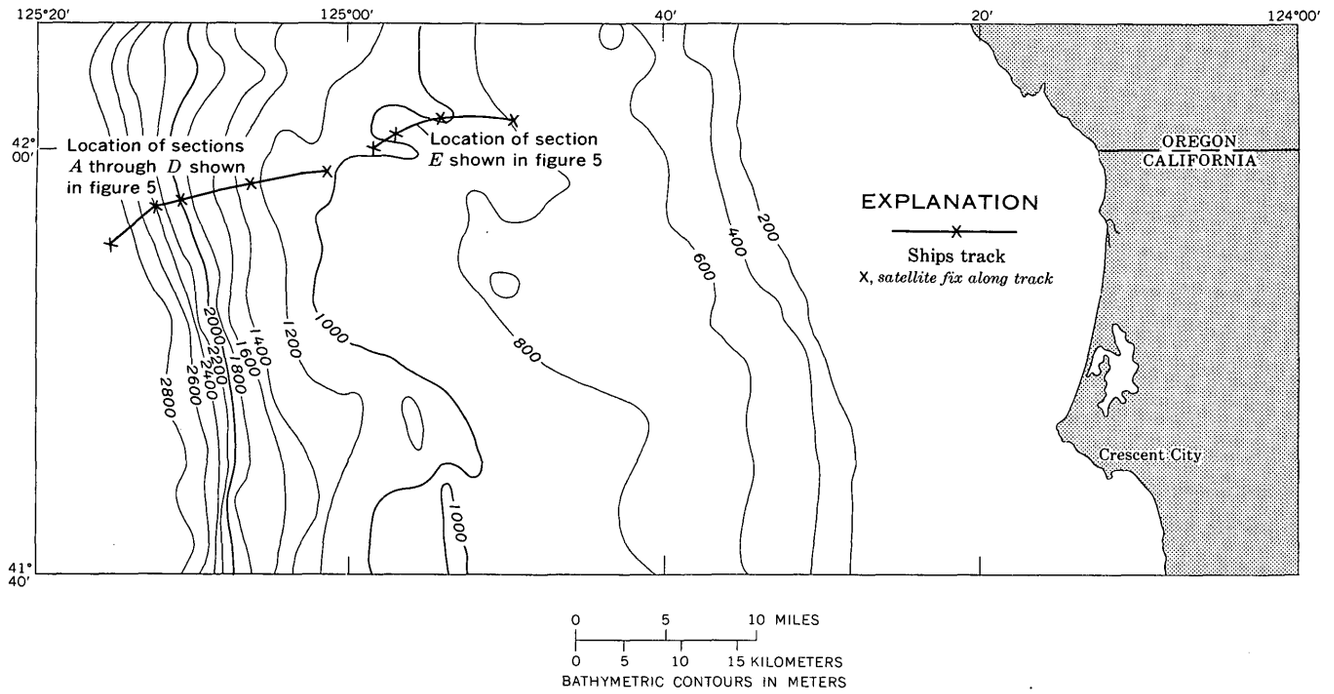

Figure 1.—Bathymetric map showing ship's track during deep-tow run off the coast of northern California.

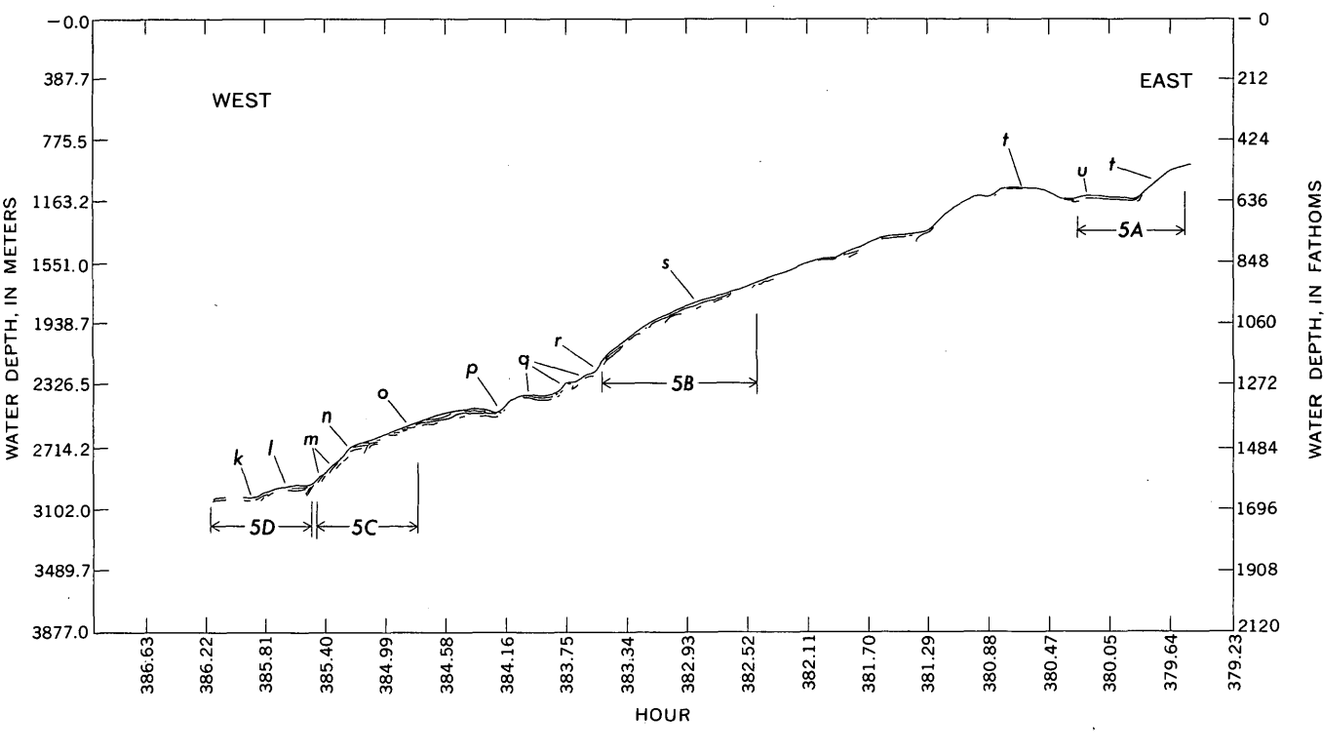

Figure 2.—Digitized reflectors from 3.5-kHz system on deep tow. Vertical exaggeration, X 3.5. Letters *k*–*u* refer to localities discussed in text; detailed sections shown in figure 5 are labeled 5*A*–5*D*.

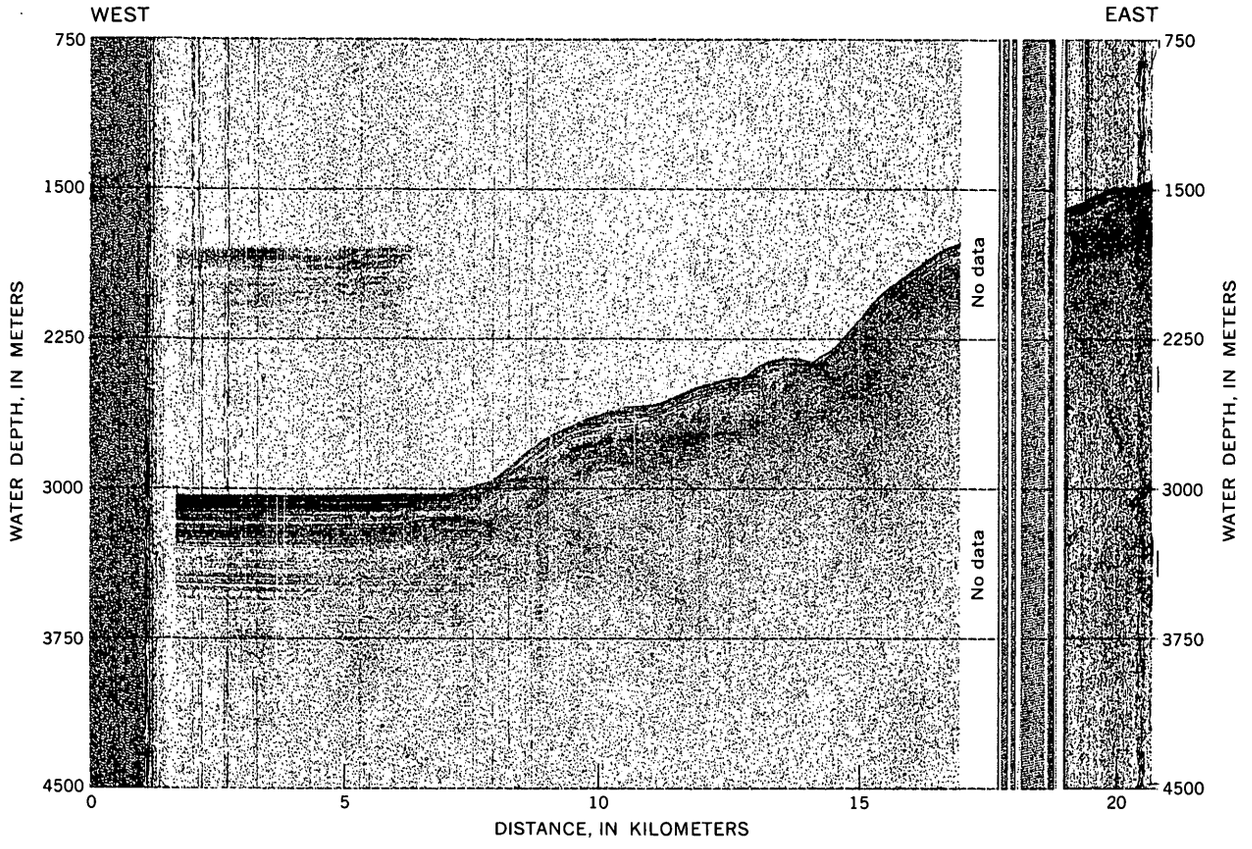

Figure 3.—Air-gun profile of west end of area shown in figure 2. Full sweep, 10 s. Vertical exaggeration, × 3.5.

features, 1 km or greater in length. From a composite line drawing of the data, figure 4, with surface topography controlled by the deep tow (fig. 2) and deep penetration (fig. 3) by the air gun and assuming the deep-tow profile as a standard for comparison, it is clear that in water as deep as 3,000 m, the air-gun record correctly portrays the structure of features greater than 1 km in length. A critical difference between the two records is the effect of hyperbolic echoes on the air-gun profile. Just above the base of the continental slope is a low bench, 1 km wide, labeled *l* in figure 2 and shown in figure 5*D*. The bench is seen on the air-gun record (fig. 3) also but a set of reflectors from the slope above is superimposed over the bench. These hyperbolic echoes can be removed (migrated) from the record to obtain a truer measure of the narrow slope just above the bench. Several features revealed by the profile (fig. 2) are not clearly discernible on the air-gun record. Surficial lumps, possible slide masses revealed by the deep tow upslope of the bench (*m*, fig. 2), cannot be identified on the air-gun record (fig. 3). Near-surface reflectors that clearly crop out at *n* (see fig. 5*C*) are only vaguely suggested in figure 3. Similarly several well-defined blocks, again possible slide masses, occur in figure 2 (at *q*) but only the larger block shows up on the air-gun record (fig. 3). A small erosional channel at *p* in figure 2 cannot be identified as such in figure 3.

In general, the deep-tow record across the lower slope shows minor undulations with crests ⅓ to ½ km apart (see fig. 5*B*, *C*). Most of these undulations do not appear to be related to erosional channeling because the bottom surface gradients do not reverse at the broad troughs, as expected from channels such as *p* in figure 2. The undulations may be caused by surficial movement of the upper sediment layers on the slope, even on the gentle slopes at *o* and *s* (fig. 2). As the layers are not internally deformed, the sediment must have moved as coherent masses. The amount of movement would be only a few tens of meters, except on the steeper parts of the slope (fig. 2; *m*, *r*) where a few hundred meters of lateral movement may have occurred. Alternatively, the undulations may be effects of depositional processes acting on the slope.

The deep-tow crossing of a ridge in figure 5*E* shows gently upturned layers on its east flank. Successively older layers crop out as one approaches the ridge from the east. The ridge has a relatively smooth surface on the 3.5-kHz record, although dredge hauls from this and other nearby ridges yielded dolomite and limestone concretions 25 to 50 cm across containing late Cenozoic Foraminifera (Silver, 1969b).

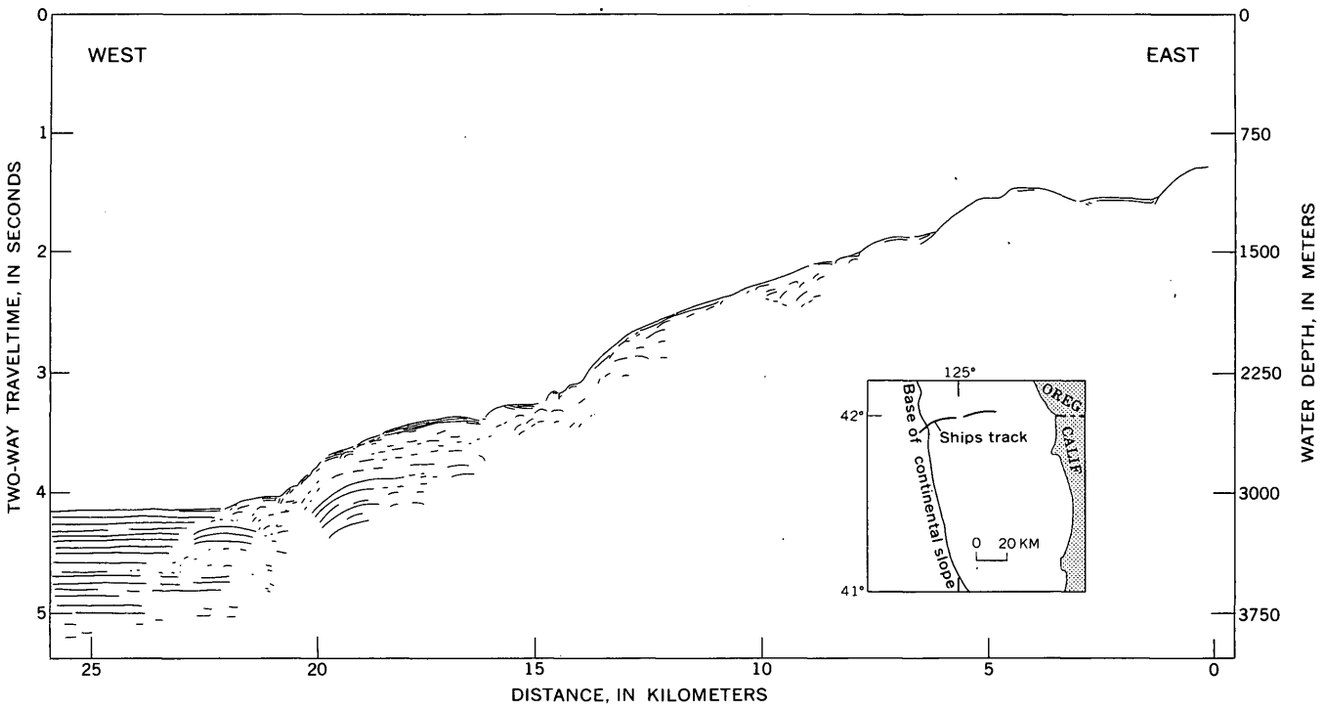

Figure 4.—Composite line drawing of data from figures 2 and 3.

A gently arched surface (*u*) occurs between two ridges (*t*) on the deep-tow profile (figs. 2, 5*A*). Approximately 0.02 s (15–20 m) below the surface is a subbottom reflector. The thickness of sediment between the surface and the subbottom reflector is greatest in the central part of the arch, thinning toward the flanks. Differential deposition controlled by bottom currents (accelerated around the ridges) could contribute to this kind of geometry. The fact that the subbottom reflector is arched suggests possible gentle warping, but the structure may be depositional in origin.

Just beyond the base of the slope the air-gun profile (fig. 3; fig. 4, 22.5 km) shows a buried fault with a small offset and gently warped sediments. As faulting here does not affect the surface layers, it is not discerned in the deep-tow profile (fig. 2). Figure 5*D* shows a gently undulating surface just beyond the base of the low bench, but the microrelief is probably unrelated to the deeper structure.

CONCLUSIONS

For continental margin studies at water depths at least as great as 3 km, seismic reflection profiling is a useful tool for determining the structure of features greater than 1 km in length. Smaller features are not adequately resolved, especially on slopes exceeding about 5°, where hyperbolic echoes obliterate the finer details.

The combined deep-tow and air-gun record shows the surface of the lower continental slope to be formed of several large (approx 5 km) benches sloping gently seaward. Small-scale undulations (approx 0.5 km) on these benches are possibly caused by minor downslope movement of sediment masses or by depositional processes. Between benches are steeper slopes (approx 20°) along which more pronounced sliding is suggested. Faulting at depth may be responsible for the stepped appearance of the slope (Silver, 1971). The remarkably smooth appearance of the slope in the detailed deep-tow record probably means that the slope is underlain by relatively "soft," low-strength, broadly folded sediment.

The near-surface deposits on the benches are not deformed, but the air-gun record across the lower bench suggests gentle folding at depth. Any compressional strain on the continental slope affecting the surface layers associated with subduction is concentrated along zones of reverse faulting that crop out between the benches. Evidence for minor tectonic warping of near-surface deposits is seen on the flanks of low ridges on the upper part of the slope.

ACKNOWLEDGMENTS

Use of the deep-tow instrument package and associated computer software required the expertise of many people. Colleagues from the Scripps Institution, F. N. Spiess, Tony Boegeman, Martin Benson, and W. R. Normark, were chiefly responsible for operating the equipment while at sea; Gordon Miller provided computer plots of the deep-tow data. Spiess and Normark gave advice and encouragement in interpreting

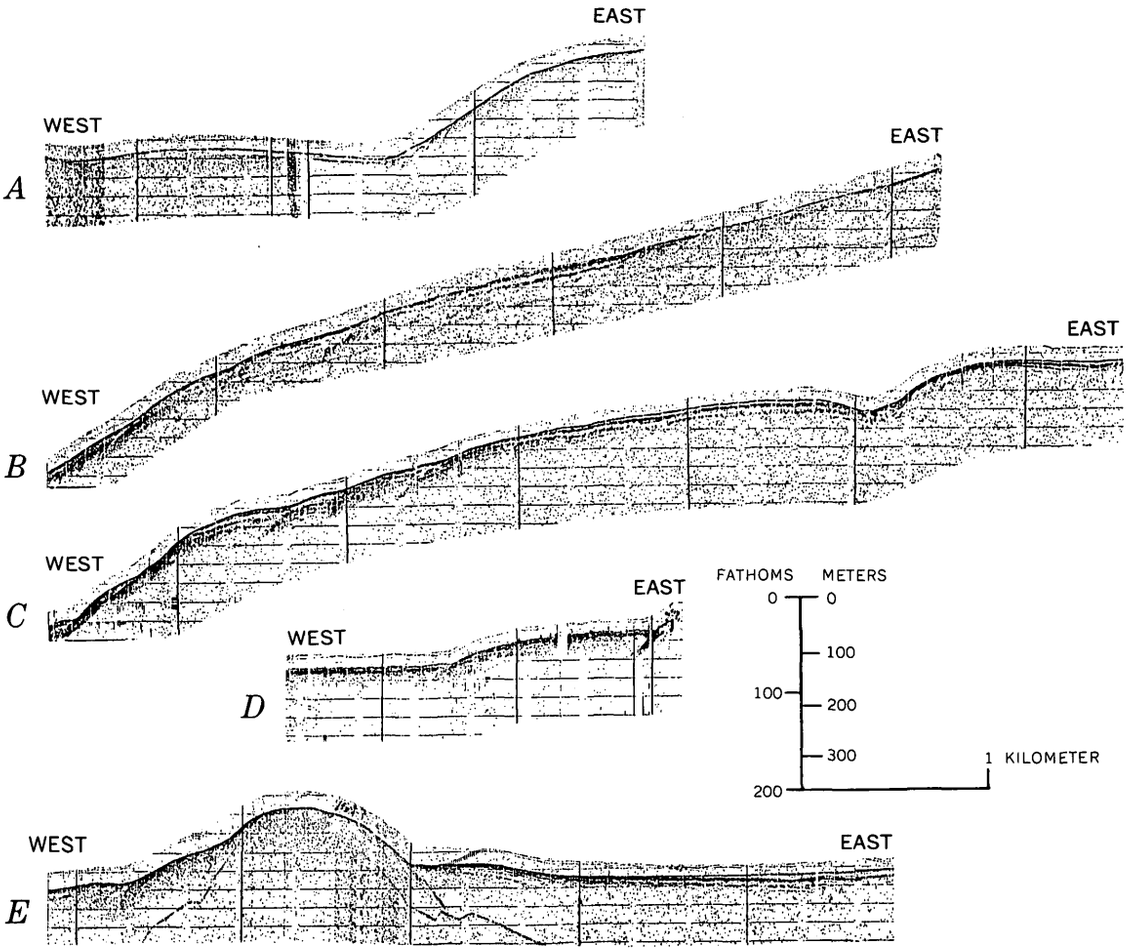

Figure 5.—Detailed sections of deep-tow profile. *A–D*, Sections located in figure 2. *E*, Crossing of ridge at top of continental slope (not shown in fig. 2).

the deep-tow data, and the manuscript was improved by review of W. R. Normark and U.S. Geological Survey colleagues, D. W. Scholl and G. W. Moore.

REFERENCES CITED

Krause, D. C., 1962, Interpretation of echo sounding profiles: Internat. Hydrog. Rev., v. 39, p. 65–122.

Larson, R. L., 1971, Near-bottom geological studies of the East Pacific Rise crest: Geol. Soc. America Bull., v. 82, p. 823–842.

Luyendyk, B. P., 1970, Origin and history of abyssal hills in the northeast Pacific Ocean: Geol. Soc. America Bull., v. 81, p. 2237–2260.

Normark, W. R., 1970, Growth patterns of deep-sea fans: Am. Assoc. Petroleum Geologists Bull., v. 54, p. 2170–2195.

Silver, E. A., 1969a, Late Cenozoic underthrusting of the continental margin off northernmost California: Science, v. 166, p. 1265–1266.

———1969b, Structure of the continental margin off northern California, north of the Gorda Escarpment: San Diego, Univ. California, Ph. D. dissert., 123 p.

———1971, Transitional tectonics and late Cenozoic structure of the continental margin off northernmost California: Geol. Soc. America Bull., v. 82, p. 1–22.

Spiess, F. N., Luyendyk, B. P., Larson, R. L., and others, 1969, Detailed geophysical studies on the northern Hawaiian Arch using a deeply towed instrument package: Marine Geology, v. 7, p. 501–527.

Spiess, F. N., and Mudie, J. D., 1970, Small scale topographic and magnetic features, *in* Maxwell, A. E., ed., The sea—V. 4, New concepts of sea floor evolution, Pt. 1, General observations: New York and London, Wiley-Interscience, p. 205–250.

Jour. Research U.S. Geol. Survey
Vol. 2, No. 5, Sept.-Oct. 1974, p. 569—580

CORRELATION BETWEEN GEOPHYSICAL DATA AND ROCK TYPES IN THE PIEDMONT AND COASTAL PLAIN OF NORTHEAST VIRGINIA AND RELATED AREAS

By LOUIS PAVLIDES, KENNETH A. SYLVESTER;[1] DAVID L. DANIELS; and ROBERT G. BATES;[2] Beltsville, Md.; Silver Spring, Md.; Washington, D.C.

Abstract.—Physical, chemical, and mineralogic characteristics of rock units in parts of the northeast Virginia Piedmont are reflected in the aeromagnetic, aeroradioactivity, and gravity data for this area. Magnetic anomalies show the areal distribution of rocks containing magnetite. Aeroradiometric anomalies in the Piedmont and Coastal Plain provinces are directly related to the K_2O content of the formations. In the crystalline rocks of the Piedmont this is reflected in their muscovite and microcline content, whereas in the Coastal Plain province it is related to the glauconite content of the Aquia Formation. Locally, in the crystalline rocks of the Piedmont, uranium- and thorium-bearing mineral content is of greater importance than K_2O-bearing mineral content in producing aeroradiometric anomalies. The region also is characterized by (1) a northern gravity high, (2) a southern gravity high presumed to be caused by mafic rocks, and (3) an intervening zone characterized by low gravity relief and underlain by schist and gneiss. Geologic and geophysical extrapolation southward toward the Arvonia area show that the Chopawamsic Formation and the volcanic rocks of the Evington group are coeval. Also, on the northwest side of these volcanic rocks is a belt of small rootless mafic and ultramafic rocks diapirically emplaced in folded rocks of Early Cambrian (?) age.

Geologic mapping now in progress in southern Stafford County, Va. (figs. 1, 8), has delineated rock units whose mineralogic and physical properties are strikingly reflected in aeromagnetic, aeroradioactivity, and Bouguer gravity maps. The geologic maps accompanying this report show only generalized and simplified lithologic units for comparison with the geophysical data.

The airborne geophysical surveys discussed in this report were made by the U.S. Geological Survey in 1960 in an aircraft that flew 1-mi-spaced, east-west traverses at a nominal altitude of 500 ft. above the ground as measured by a continuously recording radar altimeter. The instrumentation and general information concerning the aeroradiometric and aeromagnetic surveys of this region have been summarized elsewhere by Neuschel (1965; 1970, p. 3575–3577). The gravity survey conducted by our late colleague, R. G. Bates, with the assistance of S. K. Neuschel and J. W. Allingham of the U.S. Geological Survey, used a Worden Explorer I gravimeter that was calibrated at the Fredericksburg, Va., base station. The Bouguer values were calculated by using a density of 2.67.

GENERAL GEOLOGY

The region discussed in this report is within the Piedmont and Coastal Plain provinces. Pervasive weathering has modified many of the rocks to saprolite or clay residuum; fresh bedrock in the Piedmont is generally confined to stream or river courses.

The Piedmont rocks, characterized by poorly preserved bedding but generally with a well-developed compositional layering, have steep to vertical dips. A north- to northeast-trending foliation also with steep to vertical attitudes is common in almost all rocks of the area. However, in parts of the Fredericksburg complex, foliation dips less steeply and locally defines north- to northeast-trending fold patterns. The Coastal Plain sediments are unmetamorphosed and are essentially flat lying or have a gentle regional dip eastward.

The Piedmont rocks within the area have been progressively metamorphosed and include mineral assemblages of both the greenschist and amphibolite facies. Retrogressive metamorphism has locally affected some of these regionally metamorphosed rocks.

A preliminary generalized stratigraphic sequence of the rock units referred to in this report is given in figure 2. In general, there are two distinct terranes of Piedmont rocks—that of the informally designated Fredericksburg complex and that to the northwest.

Fredericksburg complex.—This unit is a tectonic rather than a stratigraphic complex that consists chiefly of schist and gneiss that have been extensively invaded by felsic plutons, dikes, and sills of more than one age. The Fredericksburg complex, in part, includes schists of the Quantico Slate of early Paleozoic (Ordovician?) age. The boundary separating the

[1] Present address: Department of Geology, University of Idaho, Moscow, ID 83843.

[2] Deceased.

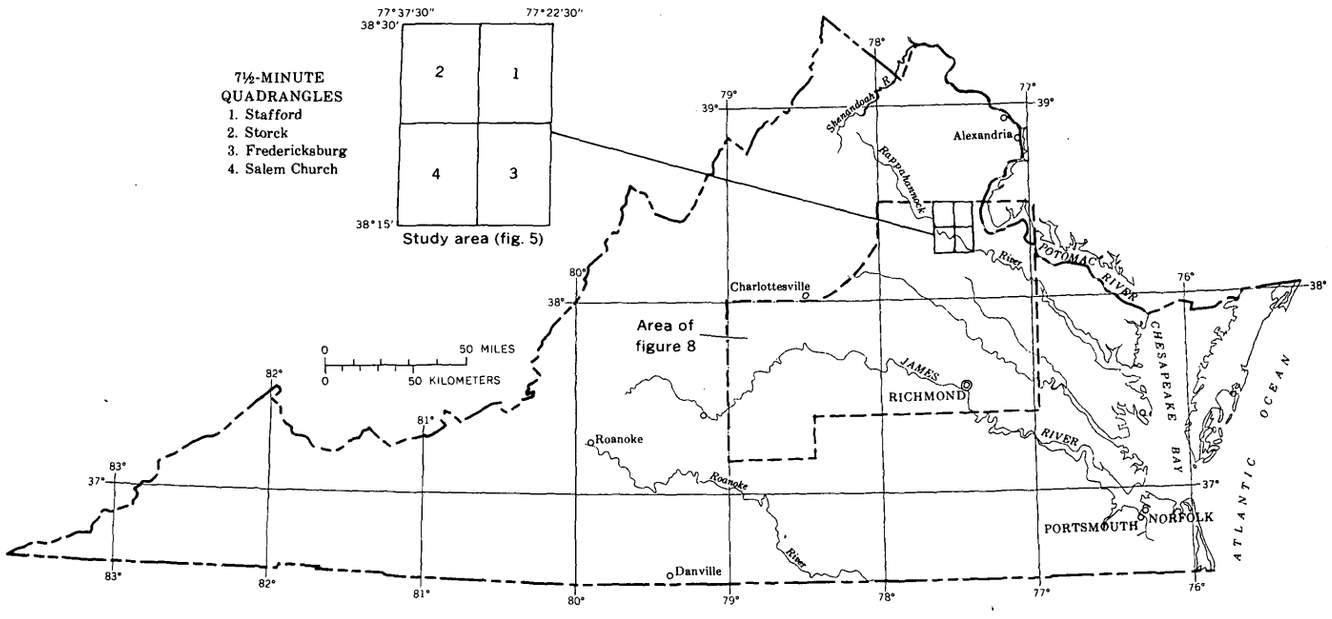

Figure 1.—Index map showing location of quadrangles discussed in this report and general area covered by figure 8.

Age	Formation and map symbol	
Holocene through Cretaceous	Coastal Plain sediments, terraces and alluvium (QKcp)	
	Unconformity	
Early Paleozoic (Ordovician?)	Quantico Slate (Pzq)	
	Unconformity(?)	
Cambrian, Cambrian(?), and Early Cambrian(?)	Chopawamsic Formation (Cc) / Diamictite (d)	Schist and slate (s)
Paleozoic and (or) Precambrian(?)	Fredericksburg complex, undivided (fc); microcline gneissic granite member (fg); granodioritic gneiss member (fgd)	

Figure 2.—Provisional stratigraphic sequence of the rocks in southern Stafford County, Va.

Fredericksburg complex from the stratigraphic sequence on its northwest side is arbitrarily placed approximately where abundant granitic and pegmatitic sills and dikes are first recognized in the host rocks of schist. Two gneissic members of the Fredericksburg complex (fig. 2) are shown in figures 3 and 4. The microcline gneissic granite member (fg) is a coarse-grained pale-pink granite with large phenocrysts of microcline and a foliation imparted by streaks of biotite. The granodioritic gneiss (fgd) is generally a gray fine- to medium-grained well-foliated and highly lineated rock composed chiefly of plagioclase, quartz, and biotite and may range from granodiorite to diorite in composition.

The "Geologic Map of Virginia" compiled by Stose (1928) shows patches of Baltimore Gneiss, Petersburg Granite, and undifferentiated granites, all assigned to the Precambrian, as underlying much of the area mapped as Fredericksburg complex in this report. However, the more recent State map (Milici and others, 1963) shows this same general terrane as underlain by schist, granite, and Petersburg Granite, all of which are considered as of uncertain Paleozoic or Precambrian age. The microcline gneissic granite member of the Fredericksburg complex is probably, in part, the unit shown as Petersburg Granite on these earlier maps. One isotopic age of zircons from a sample of quartz-plagioclase-biotite-hornblende gneiss from within the eastern part of the Fredericksburg complex has yielded a Pb^{207}/Pb^{206} age of late Precambrian (606 m.y.). This is considered to be a minimum age, as recent lead loss or loss of lead at an earlier time would make this age still older (Louis Pavlides and T. W. Stern in U.S. Geological Survey, 1973, p. 38).

Therefore, the tectonic unit designated as the Fredericksburg complex contains rocks of both Precambrian and Paleozoic age.

Diamictite unit, Chopawamsic Formation, and schist and slate unit.—Granitelike rocks that are massive, dark gray, nonstratified and characterized by quartz lumps and schist clasts randomly scattered in a micaceous quartz- and plagioclase-rich matrix, make up the diamictite unit shown in the northern

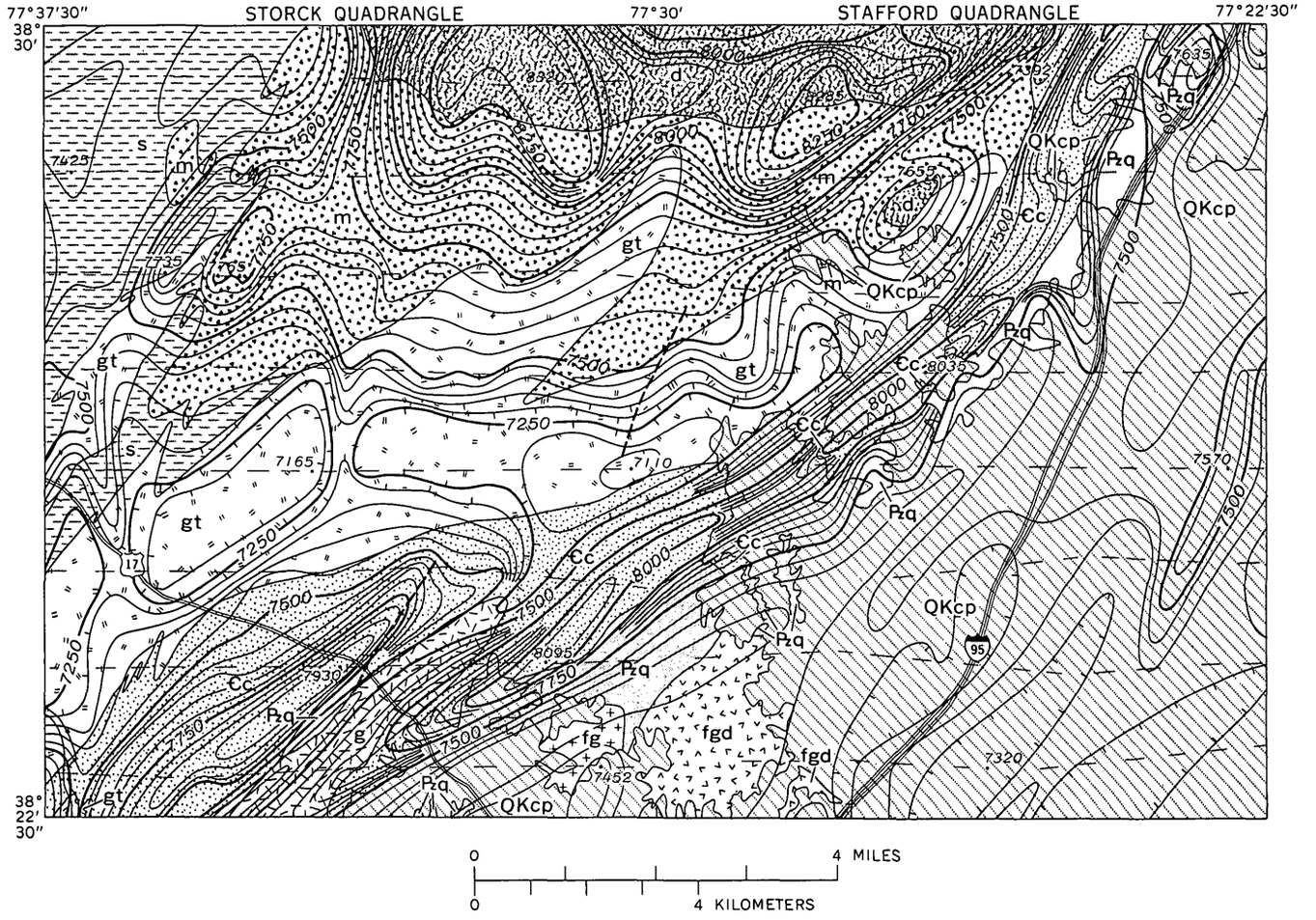

Figure 3.—Preliminary generalized geologic sketch map and superposed aeromagnetic map of the Stafford and Storck quadrangles; d, diamictite; s, schist and slate; m, mafic rocks; gt, granitoid rocks; g, granitic rocks; fg, microcline gneissic granite of the Fredericksburg complex; fgd, granodioritic gneiss of the Fredericksburg complex; Cc, Chopawamsic Formation; Pzq, Quantico Slate; and QKcp, Coastal Plain sediments and alluvium, undivided. Contact lines (solid) include arbitrary boundary separating Fredericksburg complex from stratigraphic units to the west; faults are dashed. Contour interval is 50 gammas; hachures indicate areas of relatively lower magnetic intensity.

part of figures 3 and 4. This diamictite had earlier been recognized and mapped as pebble gneiss by Southwick, Reed, and Mixon (1971) in the area immediately north of that shown in figures 3 and 4. Milici, Spiker, and Wilson (1963), following the earlier work of Lonsdale (1927), have shown this unit and its continuation to the north as part of a granite pluton. This was a reasonable assignment because the sedimentary nature of this rock type was recognized only relatively recently in Maryland by Cloos and Cooke (1953), Fisher (1963), and Hopson (1964). Before then, this rock type had been mapped by others as the Skyesville Granite in Maryland. Higgins (1972, fig. 1) extended the diamictite unit too far to the south (Pavlides, 1974; Higgins, 1974) of the limits shown in figures 3 and 4.

The Chopawamsic Formation consists of metamorphosed mafic volcaniclastic and volcanic rocks and felsic volcanic rocks, as well as minor beds of clastic metasedimentary rocks. At the southwest margin of the Stafford quadrangle and within the Chopawamsic Formation is a small area of massive metagabbroic and metabasaltic rock whose relationship to the clearly volcanic and volcaniclastic rocks is at present uncertain. These rocks have been included as part of the Chopawamsic in this report. However, they may be part of a small mafic intrusion, genetically related to the mafic unit (m) rather than to the Chopawamsic Formation.

The schist and slate unit(s) exposed in the western part of the Storck quadrangle consists mostly of fine-grained micaceous schists, green slate, slaty siltstone, and a gritty to granule-schist characterized by elongate quartz grains. The mutual stratigraphic relationship of the schist and slate unit, the diamictite unit, and the Chopawamsic Formation is not clear within the Storck and Stafford quadrangles (figs. 3, 4). However, immediately to the northeast, Southwick, Reed, and Mixon (1971) assigned a pelitic schist and a pebble gneiss unit, that appear to be coextensive respectively with the schist and slate unit and the diamictite unit of this report, as the more or

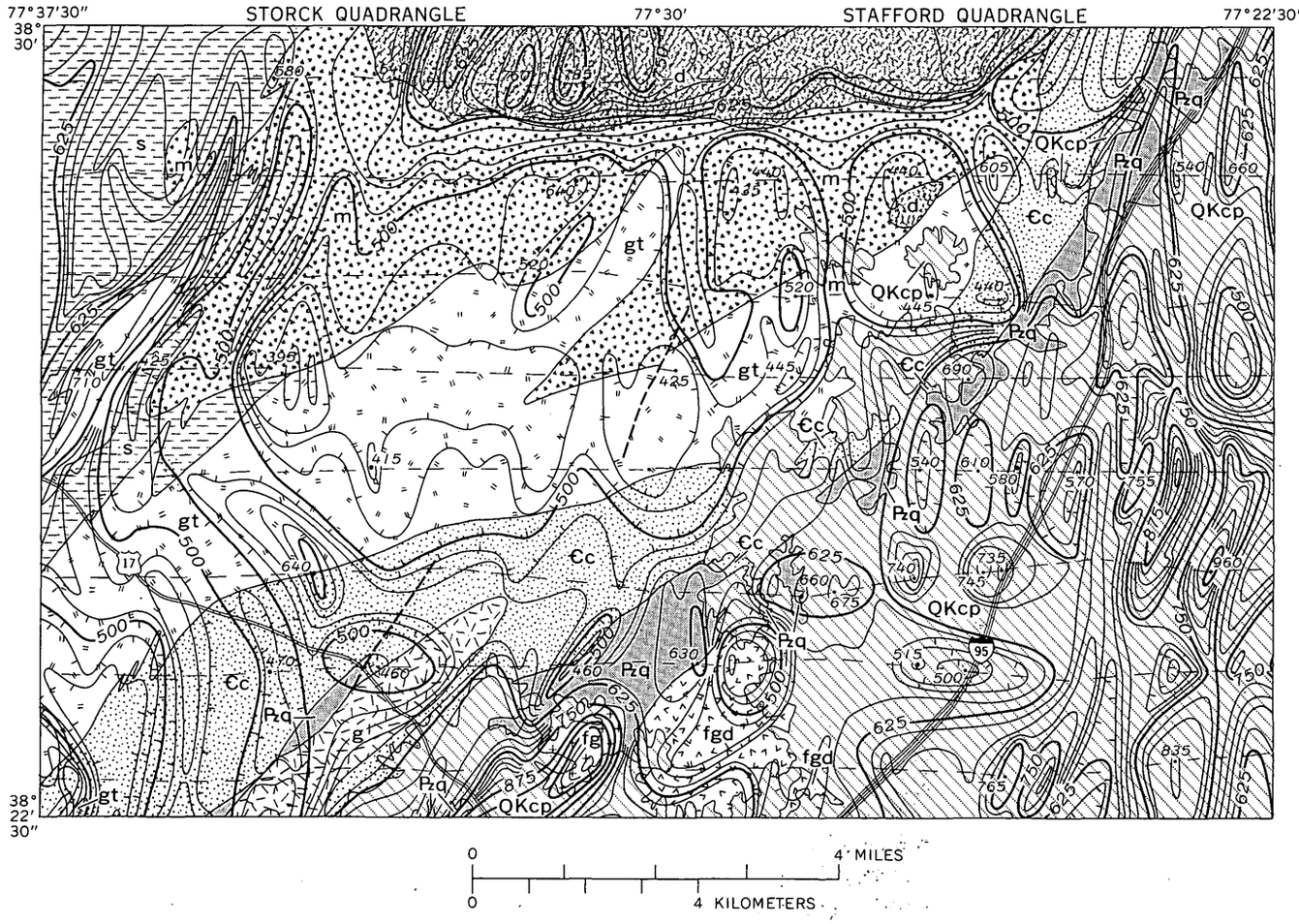

Figure 4.—Preliminary generalized geologic sketch map and superposed aeroradioactivity map of the Stafford and Storck quadrangles. See figure 3 for explanation of geologic units. Contour interval is 25 units of gamma radiation in counts per second; hachures indicate areas of relatively lower gamma radiation.

less laterally equivalent units of the Wissahickon Formation of Virginia, which they considered to be of Precambrian (?) age. Higgins (1972) assigned most of the Wissahickon Formation of Maryland and Virginia to the Cambrian. The Chopawamsic Formation is considered to overlie conformably and also to interfinger locally with the diamictite (pebble gneiss) unit (Southwick and others, 1971). The Chopawamsic is considered correlative with the James Run Formation of Maryland (Southwick and others, 1971; Higgins, 1972, p. 1001–1002) and of Lower Cambrian age.

Quantico Slate.—Sulfidic carbonaceous slate that locally contains layers of metagraywacke as much as a few feet thick characterizes the Quantico Slate in its northern part (figs. 3, 4). Along strike to the southwest, in the vicinity of the Fredericksburg complex, it changes to a muscovite-garnet-biotite schist that locally contains staurolite. A thin mylonitic quartzite unit locally separates the schist of the Quantico from the underlying metavolcanic rocks of the Chopawamsic Formation. For purposes of this report, the quartzite is not shown separately in figures 3 and 4 but is included with the Quantico. The Quantico Slate is dated as early Paleozoic (Ordovician?) and is considered coeval with the Arvonia Slate of the central Virginia Piedmont (Watson and Powell, 1911). The contact between the Quantico Slate and Chopawamsic Formation has been described as gradational (Southwick and others, 1971, p. D3–D6; Higgins, 1972). The local presence of quartzite at the base of the Quantico and its early Paleozoic (Ordovician?) age as contrasted with the Cambrian age of the Chopawamsic, however, suggest that an unconformity separates the two formations (Pavlides, in U.S. Geological Survey, 1973, p. 38). A disconformity is also reported to separate Arvonia Slate from granitic rocks on which it locally lies in Fluvanna and Buckingham Counties, Va. (Taber, 1913, p. 41–42; Brown, 1969, p. 32).

Coastal Plain sediments.—Sedimentary sandy and clay-bearing units of Cretaceous (Potomac Group) and Paleocene (Aquia Formation) age and lesser amounts of gravel deposits and stream alluvium make up the unit designated as Coastal

Plain in figures 3 and 4. The Potomac Group and Aquia Formation unconformably overlie the Piedmont rocks along the eastern margin of the Piedmont terrane.

Intrusive rocks.—The mafic unit of figures 3 and 4 consists mostly of massive hornblende-rich metagabbro and metabasalt as well as massive hornblendite and relatively fresh to altered massive pyroxenite and noritic gabbro. Sparse talc schist has been found locally along the northwest margin of the unit. Granitic and aplitic dikes locally crosscut the mafic rocks, and in some places irregular granitic dikes resemble a net vein system. The intrusive nature of the mafic unit is deduced from the presence of mafic dikes in the schist and slate unit on its northwest side. Also, the presence in thin section of poikilitic muscovite porphyroblasts in the diamictitic rocks on the north side of the mafic unit may be a contact metamorphic effect related to the emplacement of the mafic unit.

The granitoid unit south of the mafic rocks is made up, for the most part, of metamorphosed and cataclastically deformed tonalitic, dioritic, and granodioritic rocks. In the east-central part of the Stafford quadrangle (figs. 3, 4), a narrow belt of mylonitic and metamorphosed granitic rocks is present along the southern margin of the granitoid unit. Rocks of the granitoid unit are locally intrusive into the Chopawamsic Formation. Whether the granitoid unit crosscuts or is itself crosscut by the mafic unit on its north side is uncertain, as are relative ages of these two units. The elongate granitic pluton in the south-central part of the Storck quadrangle (figs. 3, 4) is poorly exposed but is intrusive into the Chopawamsic and Quantico Formations.

The smaller granitoid unit in the west-central part of the Storck quadrangle (figs. 3, 4) is lithologically more complex than the larger granitoid mass and also has more muscovitic altered granitic rocks associated with it.

RELATIONSHIP BETWEEN GEOLOGY AND GEOPHYSICAL DATA

In general, magnetic anomalies are caused by differences in the content of disseminated magnetic minerals in the rocks. The mineral content is commonly not in excess of a few percent and is normally magnetite. Aeroradioactivity anomalies are caused by the total gamma-ray flux recorded along the flightpath at a fixed distance above ground; this is the cumulative flux of cosmic radiation, radionuclides in the air, and radionuclides from the upper few inches of the ground. The cosmic radiation is measured daily during the survey and is subtracted from the radiometric data, whereas the radionuclides in air cannot be measured directly and are incorporated as presumably uniform background noise in the survey data. The ground component of radioactivity is derived from gamma rays of natural radionuclides from the soil and bedrock exposures and results from the decay of K^{40} and members of the uranium and thorium radioactive-decay series.

The order in which the lithologic units are described below is for convenience in discussing the related geophysical data; it bears no relationship to stratigraphic or chronologic order. Table 1 lists the minerals in the rock units that are believed to cause the aeromagnetic and aeroradioactivity anomalies.

Aeromagnetic and geologic correlations.—The diamictite and mafic units in the northern part of the area both contain magnetite (table 1), and they compose a single magnetic unit (fig. 3) not resolvable aeromagnetically into the two distinctive lithologic units that underlie the broad positive anomaly of this region. The diamictite is generally more magnetite-rich than the mafic unit, however, and underlies the highest amplitude part of the positive aeromagnetic anomaly common to these two rock units. Locally therefore, the higher volume magnetic susceptibility of diamictite does magnetically resolve diamictite from mafic rocks, as reflected by the positive magnetic anomaly with a maximum amplitude of 7,655 gammas that occurs over the small mass of diamictite in the north-central part of the Stafford quadrangle (fig. 3).

The metamorphosed felsic and mafic volcanic rocks of the Chopawamsic Formation contain appreciable accessory magnetite and have marked magnetic intensity. Their northeast trend is clearly reflected by the associated superposed linear positive magnetic anomalies. The Chopawamsic Formation widens to the southwest in the Storck quadrangle (fig. 3) and is there intruded by a small linear granitic mass (g) containing considerably less magnetite than the enclosing metavolcanic rocks of the Chopawamsic. This has resulted in a saddle within the magnetic anomaly associated with the Chopawamsic (fig. 3) here, that reflects the lower magnetic susceptibility of the granitic pluton.

The granitic pluton was apparently emplaced, in part, within a fault complex (figs. 3, 5). The fault on the north side of the pluton has a right-lateral displacement, which also coincides with the displacement deduced from the two parallel magnetic anomalies in this area. The extension of this fault northeastward coincides with the southeast margin of the northeast-trending prong of granitoid rocks in the east-central part of the Storck quadrangle. If this fault indeed does extend northeastward and cuts the granitoid unit, the granitoid unit on the east side of the fault may underlie part of the terrane now mapped as Chopawamsic Formation in the south-central part of the Storck quadrangle. Such an interpretation is suggested by the nature of the magnetic pattern in this area. However, a southward extension of the granitoid contact would require an assumption that the scattered volcanic rocks found east of the northeast-trending fault in this poorly exposed terrane are inclusions or roof pendants within the granitoid unit.

The small magnetic anomaly over the microcline gneissic granite mass (fg) of the Fredericksburg complex in the southeast corner of the Storck quadrangle reflects the greater magnetite content of this unit with respect to the enclosing and nearby Quantico Slate and granodioritic gneiss of the Fredericksburg complex.

Magnetite is generally a sparse accessory constituent in the granitoid unit that lies between the mafic unit and the

Table 1.—*Qualitative partial mineralogy and* K_2O *content of Piedmont and Coastal Plain formations*
[1, abundant; 2, common; 3, accessory;–, scarce or absent; H, high correlation; B, background values; NA, not available]

Formations and lithologic units with map designations in parentheses	Qualitative partial mineralogy							K_2O content (percent)			Anomaly correlation with formations	
	Glauconite	K-feldspar	Plagioclase	Muscovite	Biotite	Magnetite	U- and Th-bearing minerals	Average	Range	Number of analyses	Magnetic	Radioactivity
Aquia (QKcp)	1	–	–	3	–	–	–	2.30	NA	[a]1	B	H
Quantico (Pzq)	–	–	2,3	[b]2	[b]2	–	–	2.59	0.98–3.5	3	B	B
Chopawamsic (Cc)	–	–	2,3	–	–	3	–	0.14	0.12–0.15	5	H	B
Diamictite unit (d)	–	–	1	1	3	3	–	2.77	2.4–3.3	3	H	H
Fredericksburg complex												
Microcline gneissic granite (fg)	–	1	3	3	2	–	[c]3	4.78	[d]4.40–[e]5.15	2	B	H
Granodioritic gneiss (fgd)	–	–	1	3	2	3	–	1.53	1.00–1.90	3	B	B
Mafic unit (m)	–	–	2,3	–	–	3	–	0.23	0.60–0.68	12	H	B
Granitoid unit (gt)	–	–	1	1–3	–	–	–	0.32	0.26–0.38	2	B	H
Granitic unit (g)	–	1–3	1	–	–	–	–	NA	NA	.....	B	B

[a]Analyses taken from Glaser (1971, table 8, p. 47).
[b]Common in southern part of strike belt where Quantico is also staurolitic.
[c]Based on data published by Neuschel, Bunker, and Bush (1971) for this unit in the Salem Church quadrangle.
[d]Analysis of fresh rock in Salem Church quadrangle (Neuschel and others, 1971, table 1, p. 304); rock also contains about 6.74 ppm equivalent uranium and 39.04 ppm thorium.
[e]Analysis of fresh rock in Salem Church quadrangle (Neuschel and others, 1971, table 1, p. 304); rock also contains about 3.55 ppm equivalent uranium and 42.80 ppm thorium.

Chopawamsic Formation in figure 3. This contrasts with the greater abundance of magnetite in the bounding mafic unit and Chopawamsic Formation. Thus, the granitoid rock terrane is characterized by a magnetic low in figure 3 that closely delineates the regional trend of much of this unit.

The northeast-trending linear positive magnetic anomaly in the east-central part of the Stafford quadrangle is believed to reflect magnetite-bearing crystalline rocks of the Piedmont basement rather than any magnetite-rich sedimentary rocks within the Coastal Plain sequence.

Aeroradiometric and geologic correlations.—The radiometric background of the various rock units of the area is, in almost all places, apparently directly related to K_2O content of the rocks (table 1) and results from the decay of K^{40}; except for one unit that has a greater than normal uranium and thorium content.

Although the diamictite and mafic units are generally not resolvable by their magnetic properties, except locally (fig. 3), they are sharply delineated by their radioactivity differences, as indicated in figure 4. The diamictite here is clearly characterized by higher levels of radioactivity because of its more potassic composition. This is accounted for by the high mica content of this unit in contrast to the absence or very minor content of mica locally present in some of the rocks of the mafic unit. Feldspar is not believed to contribute significantly to the radioactivity features of these rocks because, except for the presence locally of small amounts of potassic feldspar in diamictite, the characteristic feldspar of both rock units is plagioclase. Apparently the granitic and aplitic dikes that crosscut the mafic unit do not contribute significantly to its radioactive expression.

A ground check of the microcline gneissic granite unit of the Fredericksburg complex, using a portable Mount Sopris scintillometer, indicated that the host gneissic granite emits considerably more radioactivity than the crosscutting granitic dikes and pegmatites. Thus, the radioactivity high in the southeast corner of the Storck quadrangle results from the microcline gneissic granite and not from the crosscutting dikes.

The microcline gneissic granite is more extensively exposed to the south in the Salem Church quadrangle (fig. 1), where it has been described as quartz monzonite (Neuschel, 1970). Here also the unit is characterized by a higher radioactivity than the enclosing rock, and this radioactivity has been shown to be directly related to the contained potassium, thorium, and, particularly, uranium of the rock (Neuschel and others, 1971).

The southern part of the northeast-trending linear positive radioactivity anomaly in the northwest part of the Storck quadrangle may be related to the muscovite content of some of the altered granitic rocks within the granitoid unit. The northern segment of this anomaly is not as readily relatable to bedrock geology because of the extensive weathering of the

schist and slate unit across which this anomaly trends. The anomaly also may indicate a relatively local high K_2O content in the metasedimentary rocks.

The granitoid mass in the central part of the area shown in figure 4 contains mostly plagioclase and is low in potassic feldspar as well as in micas; hence, its volumetric radioactive response related to its K^{40} radioactivity is low, similar to the potassium-poor mafic unit on its north side and the Chopawamsic Formation on its south side. The above mineralogy is reflected in the low K_2O content of these units (table 1).

The Quantico Slate has micaceous rocks with about the same K_2O content as the diamictite unit (see table 1) and would normally be expected to give an aeroradioactivity response similar to that of the diamictite unit. However, the Quantico Slate occurs along the east edge of the Piedmont where it is irregularly overlapped by the Coastal Plain sediments. The resulting patchy outcrop pattern of the Quantico and the rather wide spacing of the flightpaths used in surveying the area have resulted in a dispersed low-amplitude aeroradioactivity pattern that is difficult to discern in figure 4. This contrasts with the well-exposed terrane of the diamictite with its well-developed aeroradioactivity pattern.

The north-trending linear aeroradiometric anomalies over the Coastal Plain sediments in the eastern part of the Stafford quadrangle are apparently related to glauconite-rich and locally muscovitic sediments. Ground checking of these anomalies indicates that the glauconitic Aquia Formation is the unit primarily responsible for them. Chemical analyses of the glauconitic sands associated with the aeroradiometric anomalies of the Stafford quadrangle (fig. 4) are not available. However, chemical analyses of Aquia Formation greensands from Maryland indicate a K_2O content of 2.30 percent, whereas the glauconite separates from the Aquia contain 6.22 percent K_2O (Glaser, 1971, table 8, p. 47). According to Mixon (in U.S. Geological Survey, 1970, p. 28–29), glauconite is more abundant in that part of the Aquia deposited in a more offshore environment than in the part deposited closer to shore. The absence of any radiometric anomalies over patches of Aquia Formation known to exist near the Coastal Plain–Piedmont contact may reflect this facies distribution of glauconite in the Aquia.

Gravity and geologic correlations.—Gravity anomalies are directly related to density contrasts between rock masses. The Bouguer gravity map (fig. 5) is divisible, on the basis of distinctive northeast-trending gravity levels, into three segments: a northwest, a central, and a southeast part. The northwest part of the gravity map consists of an east- to northeast-trending positive anomaly centered over the mafic unit that characteristically contains high-density rocks in comparison with the adjoining diamictite and granitoid unit (fig 5). This anomaly has a southeastward regional gradient whose slope changes markedly at about the 2- or 4-mGal contours, a break that closely coincides with the northwest boundary of the Fredericksburg complex (fig. 5). This southeastward regional gradient northwest of the Fredericksburg complex appears to be related to the southeast-sloping surface of the mafic unit.

Gravity modeling based upon measured average densities (fig. 6) can approximate the measured gravity field with a relatively simple and reasonable shape. A gravity profile $A-A'$ (fig. 5) through the 22-mGal maximum was selected for modeling and treated as a two-dimensional problem. The simplest shape that fits the data is a sphenolithlike mafic body, 8,000 ft (2,438 m) thick, with a gentle southeast-dipping upper surface (fig. 7). This body would truncate the Chopawamsic Formation and floor the granitoid unit at shallow depths. Density contrasts with the country rock of 0.3 g/cm^3 for the mafic unit and 0.1 g/cm^3 for the Chopawamsic Formation limit the depth extent of the mafic body. Lack of data on the northwest edge of the mafic unit prevents modeling this contact. Here, because of deep weathering, samples of the schists and slates could not be used to obtain meaningful specific gravity measurements. Lithologic similarities, however, suggest that these rocks have a range of specific gravity similar to that of the rocks of the Quantico Slate. A more refined model than that of figure 7 is not warranted because of the spacing of the stations.

The marked rise of the gravity field southeast of Fredericksburg (fig. 5) is the edge of a large northeast-trending linear anomaly (fig. 8) which extends over a distance of 50 mi (80 km) (Johnson, 1973) and which is discussed below. A northwest-trending gravity lineament that protrudes from this gradient south of Fredericksburg is assumed to be a subsurface dike of mafic material intruded into the Fredericksburg complex. There is no surface evidence of this northwest lineament, as the rocks of the Fredericksburg complex in this region uniformly trend northward.

The central low part of the gravity map is inferred from the specific gravity data in figure 6 to result from the less dense Fredericksburg complex bounded on both sides by more dense rocks. If the densities for the Fredericksburg complex (fig. 6) contain sample bias, whereby more of the country rock rather than the felsic intrusions influences the histogram weighting, the gravity low over the Fredericksburg complex may represent an effective lowering of the average volumetric density of the Fredericksburg complex by the many felsic intrusions that characterize it. The contour closure to the northeast (fig. 5) may indicate the termination of the Fredericksburg terrane in that area.

REGIONAL RELATIONSHIPS

On the basis of the correlations between the geologic and geophysical surveys described above, certain geologic extrapolations and interpretations into other areas of the Virginia Piedmont are now possible. Figure 8 summarizes some of these extrapolations.

The northeast-trending positive magnetic anomaly centered over the Chopawamsic (fig. 3) can be traced reliably south-

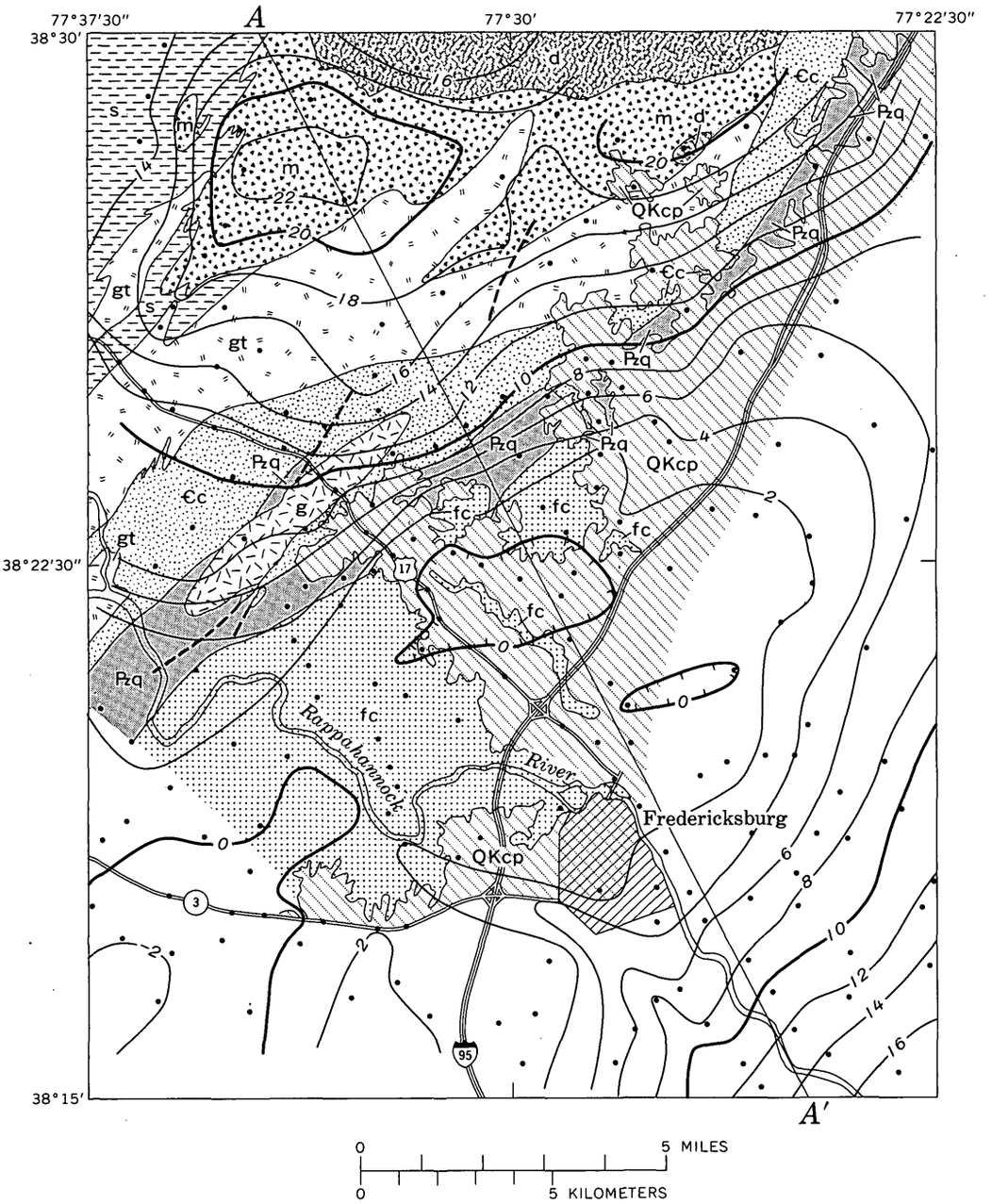

Figure 5.—Preliminary generalized geologic sketch map and superposed Bouguer gravity map of the Stafford, Storck, Fredericksburg, and Salem Church quadrangles, which respectively compose the northeast, northwest, southeast, and southwest parts of the map: fc, Fredericksburg complex, undivided; all other rock units as described in figure 3. Contour interval is 2 mGal; hachures indicate areas of closed depressions; •, gravity station.

westward into a contiguous similarly trending positive magnetic anomaly shown by Neuschel (1970, fig. 2) as being underlain by a linear belt of chlorite-actinolite schist (Neuschel, 1970, fig. 4). This belt, which extends about 40 mi (64 km) southwestward from the southern limits of the Storck quadrangle (figs. 3 and 8), is a continuation of the Chopawamsic Formation. If projected southwest of the aeromagnetic map of Neuschel (1970, fig. 2), this linear belt of magnetic anomalies trends into the northwest limb of the Columbia syncline (fig. 8), which contians magnetic metavolcanic and metasedimentary rocks of early Paleozoic age stratigraphically below the Arvonia Slate (Smith and others, 1964, pls. 1 and 3). To the west, these volcanic rocks also underlie the nearby Arvonia syncline (fig. 8), but the Columbia and Arvonia synclines are separated mostly by granodiorite. This granodiorite is considered intrusive into the lower Paleozoic

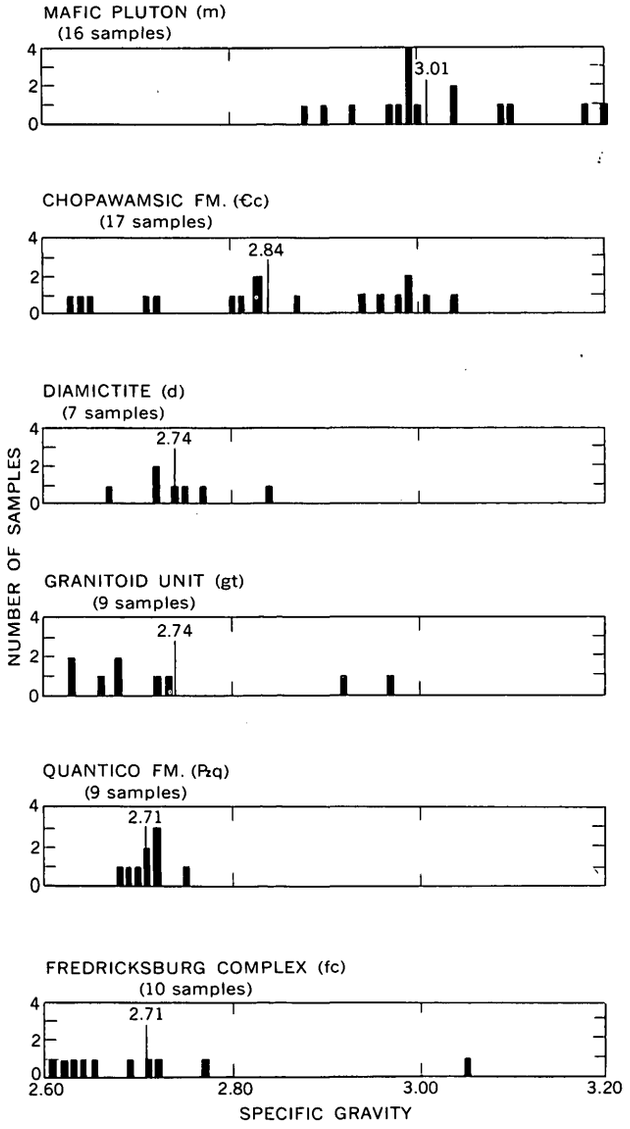

Figure 6.—Frequency distribution of specific gravity measurements of Piedmont rock samples and their mean values (indicated by vertical line).

rocks by Smith, Milici, and Greenberg (1964, p. 21 and pl. 1). However, Brown (1969, p. 15, 33) has assigned this granodiorite to the Hatcher Complex, upon which he believes the Arvonia Slate rests with unconformity. Brown (1969, p. 9) also has assigned the metavolcanic rocks below the Arvonia Slate to the Evington Group which he considers, in part, to be coeval with his Hatcher Complex and also unconformably below the Arvonia Slate. Although problems in stratigraphy exist in the area of the Columbia and Arvonia synclines, there seems little doubt that the volcanic rocks beneath the Arvonia Slate can be traced by their magnetic characteristics into the Chopawamsic Formation belt with which they are considered coeval.

The continuation of the Chopawamsic volcanic belt southwestward, as interpreted from Neuschel's (1970, figs. 2, 4) geologic and aeromagnetic data south of the Rappahannock River, has also been concluded by Higgins, Fisher, Johnson, and Zietz (1973), on the basis of a regional aeromagnetic compilation that as yet is unpublished. However, this southwestward projection of the Chopawamsic may not occur in as linear a fashion as the aeromagnetic data suggest. Reconnaissance mapping immediately south of the Rappahannock by two of the writers (Pavlides and Sylvester) suggests that folds and intrusions may locally disrupt this volcanic belt from the strict linear trend indicated in figure 8. Farther south, however, this belt of volcanic rocks may again continue in an overall southwest trend.

Small, irregularly elliptical mafic and ultramafic rock masses extend from Appomattox to Poindexter in a belt which also includes the mafic pluton near Garrisonville (fig. 8), described earlier. The oval mass near Diana Mills (fig. 8) is composed of hornblende metadiorite, hornblende-quartz metadiorite, hornblendite, amphibolite, metaperidotite, orbicular serpentinite, pegmatite, and aplite (Brown, 1969, p. 20). The two bodies near Buckingham (fig. 8) were described by Ern (1968, p. 20–23) as containing metapyroxenite and metapyroxenite that grades upward into metagabbro; all these rocks are locally cut by dikes that range in composition from quartz monzonite to felsic diorite. Although Ern (1968, p. 20) described these mafic rocks as "tabular concordant intrusions," his geologic cross sections (Ern, 1968, pl. 1) clearly show them as intrusions crosscutting folded metasedimentary rocks of the Candler Formation of the Evington Group. More detailed mapping in the Appomattox area (fig. 8) may also result in a stocklike configuration for the tabular mafic rocks there.

In addition to the petrographic similarity of the mafic and ultramafic bodies along the Appomattox-Garrisonville trend, these bodies also are characterized by similarities in the gravity anomalies associated with them. The mafic bodies are typically associated with small positive gravity highs with suboval to irregular circular closures of about 4 or 8 mGal (fig. 8; also compare Johnson, 1973, pl. 1, and Johnson, 1971, sheets 7 and 8). This contrasts with the broad elongate positive gravity anomalies to the southeast, chiefly under Coastal Plain sediments (fig. 8; Johnson, 1973, pl. 1; Johnson, 1971, sheets 7 and 8).

The analysis of the gravity anomaly of the mafic intrusion near Garrisonville indicates that the intrusive body is a rootless pluton (fig. 7). The similarity of the gravity anomaly of the Garrisonville pluton with the gravity anomalies associated with the other mafic and ultramafic intrusions along the Garrisonville-Appomattox belt suggests that these intrusions also are small rootless plutons. S. S. Johnson of the Virginia Division of Mineral Resources also has concluded independently, on the basis of his preliminary studies, that several of the mafic and ultramafic intrusive bodies south of Garrisonville are small rootless plutons (S.S. Johnson, written commun., 1973).

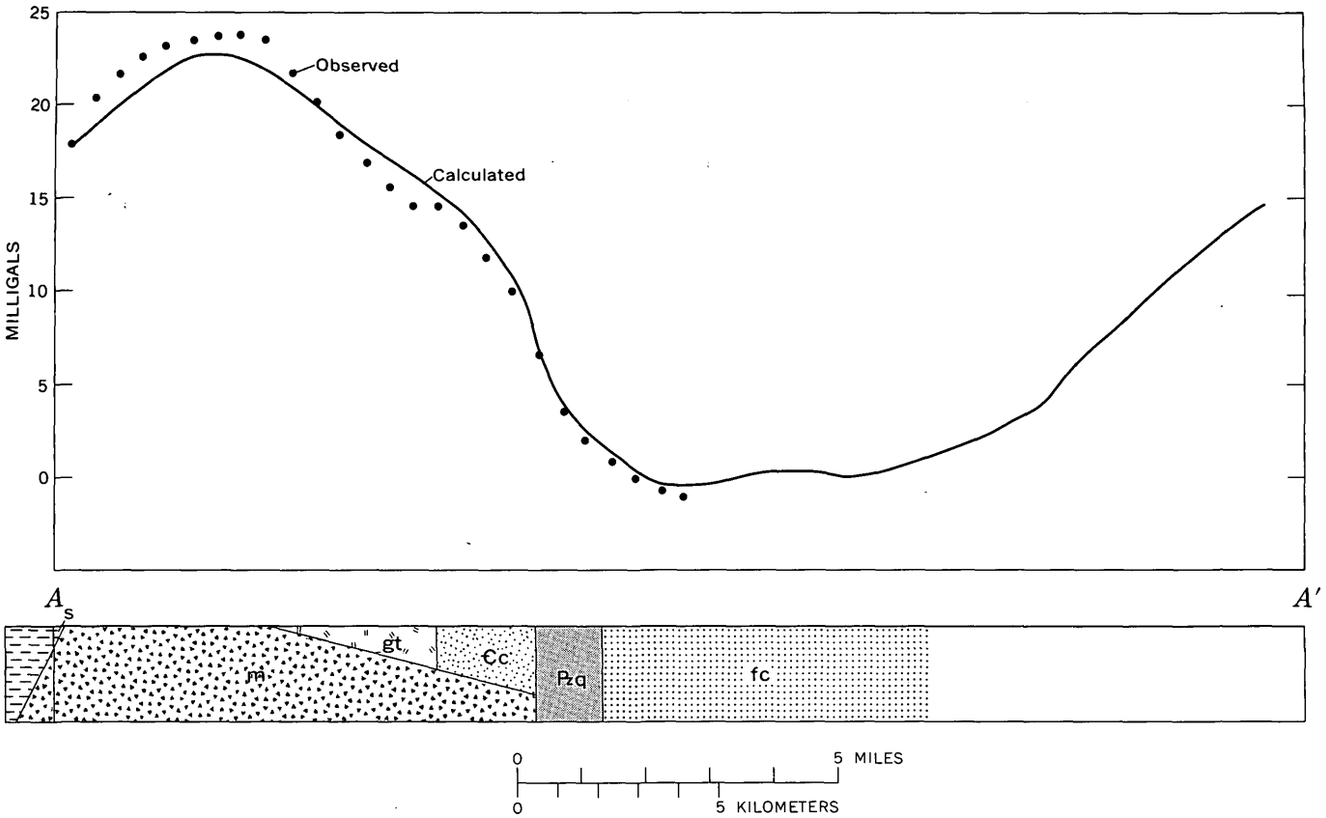

Figure 7.—Analysis of gravity profile A–A' (fig. 5) over the mafic pluton near Garrisonville, Va. Density contrast of +0.3 is used for the mafic body and +0.1 for the Chopawamsic Formation.

The time of emplacement of the mafic and ultramafic plutons along the Appomattox-Garrisonville axis is not closely established. In the Garrisonville area, these mafic and ultramafic rocks intrude schists and slates of Cambrian(?) age but not the Quantico Slate of early Paleozoic (Ordovician ?) age. The plutons near Buckingham intrude the Candler Formation of the Evington Group (Ern, 1968, p. 20 and pl. 1), which is pre-Arvonia (Middle and Late Ordovician) and post-Catoctin (Precambrian) in age. Similarly, the oval mafic-ultramafic pluton and the sill-like ultramafic body near Diana Mills also intrude rocks of the Evington Group of Paleozoic(?) age but not rocks of the Ordovician Arvonia Slate (Brown, 1969, p. 20 and pl. 1). A general penecontemporaneous post-Cambrian to pre-Late Ordovician age for the emplacement of the plutons of the Appomattox-Garrisonville belt, therefore, is suggested by the above field relationships.

A gravity high approximately 12 mi (19 km) east of Buckingham (fig. 8) is centered along the axis of the Whispering Creek anticline where hornblende gneiss and granitic rocks of the Hatcher Complex occur (Brown, 1969, pl. 1). This gravity high is not in the same lithotectonic belt as those of the Appomattox-Garrisonville belt, and although it resembles the gravity highs in this belt, it is caused by a different suite of rocks.

The axis of the large linear northeast-trending positive gravity anomaly about 30 mi (48 km) southeast of Appomattox and a similar positive gravity anomaly along strike farther northeast (Johnson, 1971, sheet 8; 1973) is schematically shown in figure 8. These large eastern gravity highs of the Virginia Piedmont are on the trend along which lies the positive gravity gradient southeast of Fredericksburg (fig. 5). Positive anomalies of this magnitude must represent dense mafic rocks either at or relatively close to the Earth's surface (Johnson, 1973). It is of interest, however, that this belt of presumed buried mafic rocks has a magnetic low centered over it (Zietz and others, 1968), indicating that it lacks magnetite. This may be related to a regional metamorphic effect or to the original chemical composition of these rocks and their igneous history. A block of Triassic rocks may underlie part of the area of the large gravity high southeast of Fredericksburg (fig. 8), as suggested by the compilation of De Buchananne (1968, sheet 1). Triassic rock has been identified in well cuttings from within this area (G. D. DeBuchananne, oral commun., July 1973). It is possible but not probable that basaltic rocks of Triassic age

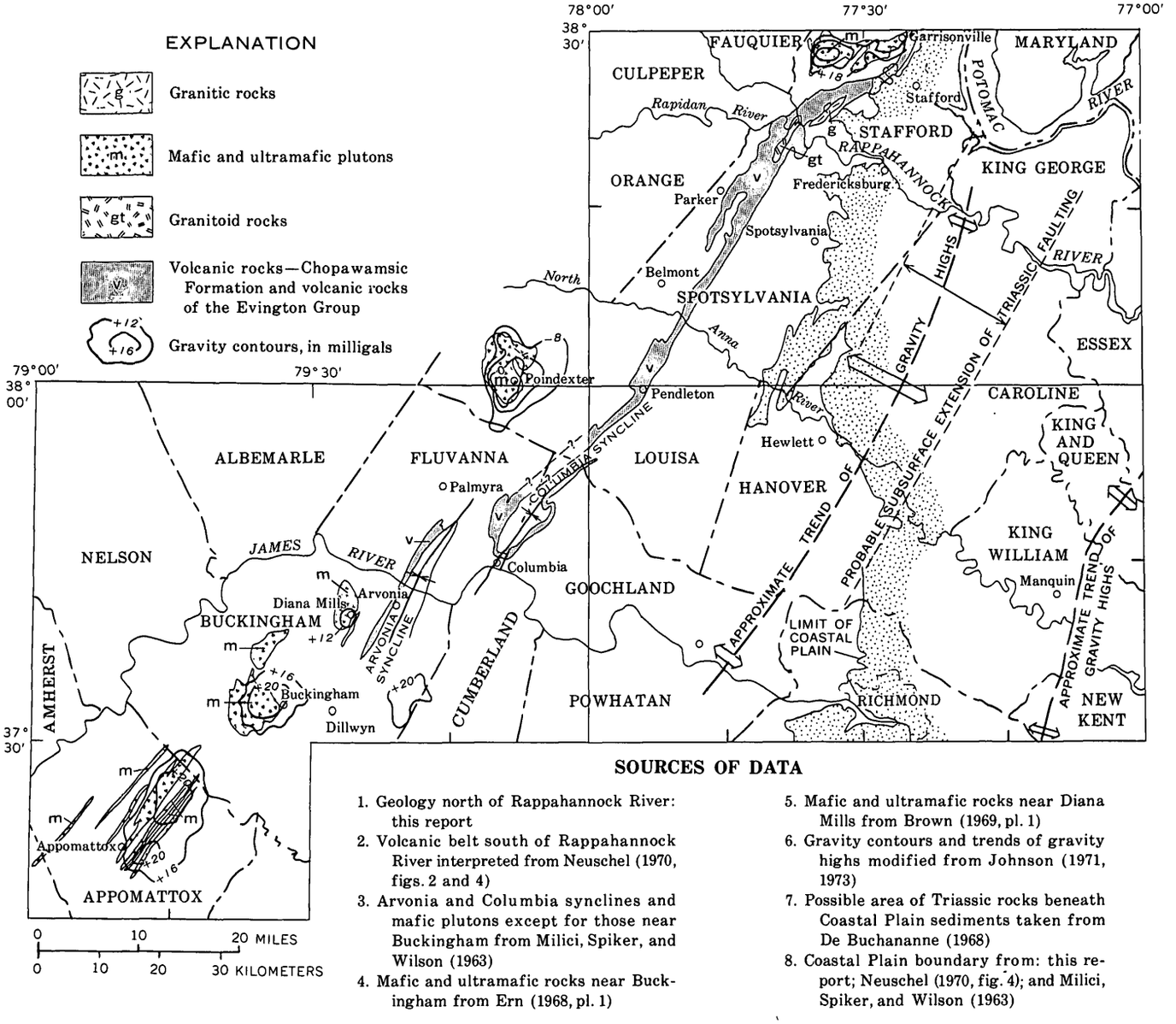

SOURCES OF DATA

1. Geology north of Rappahannock River: this report
2. Volcanic belt south of Rappahannock River interpreted from Neuschel (1970, figs. 2 and 4)
3. Arvonia and Columbia synclines and mafic plutons except for those near Buckingham from Milici, Spiker, and Wilson (1963)
4. Mafic and ultramafic rocks near Buckingham from Ern (1968, pl. 1)
5. Mafic and ultramafic rocks near Diana Mills from Brown (1969, pl. 1)
6. Gravity contours and trends of gravity highs modified from Johnson (1971, 1973)
7. Possible area of Triassic rocks beneath Coastal Plain sediments taken from De Buchananne (1968)
8. Coastal Plain boundary from: this report; Neuschel (1970, fig. 4); and Milici, Spiker, and Wilson (1963)

Figure 8.—Generalized geologic sketch map of northeastern Virginia showing selected lithologic, structural, and gravity features. Dotted lines show approximate position of Triassic faulting beneath the Coastal Plain cover.

present in this fault-block may help cause the gravity high in this general area. Triassic rocks of the Richmond Basin, approximately on strike southwest of the buried Triassic rocks southeast of Fredericksburg, however, do not have any positive gravity anomalies associated with them. The magnitude of the anomaly southeast of Fredericksburg as well as the regional extent of this and related anomalies, therefore, seem to result from rocks other than those of the Triassic blocks.

Along this same anomaly axis in Virginia a northeast-trending mass of granite gneiss is present from about the latitude of Crozier to just north of Spotsylvania (Milici and others, 1963). This granite gneiss unit was mapped as Baltimore Gneiss on the 1928 edition of the "Geologic Map of Virginia" (Stose, 1928). Neuschel (1970, fig. 4) indicated, however, that part of this terrane near Hewlett is underlain by diorite and gabbro, rock types that may reflect the general composition of the buried dense rock mass producing the gravity anomaly elsewhere along strike. Johnson (1973, pl. 1) showed this anomaly as having a steep gradient on its southeast side and a gentler gradient on its northwest side. This suggests to us that the anomaly-producing rock mass dips northwest.

REFERENCES CITED

Brown, W. R., 1969, Geology of the Dillwyn quadrangle, Virginia: Virginia Div. Mineral Resources Rept. Inv. 10, 77 p.

Cloos, Ernst, and Cooke, C. W., 1953, Geologic map of Montgomery County and the District of Columbia: Maryland Dept. Geology, Mines and Water Resources, scale 1:62,500.

De Buchananne, G. D., 1968 Ground-water resources of the James, York, and Rappahannock River basins of Virginia west of the Fall Line: U.S. Geol. Survey Hydrol. Inv. Atlas HA-283.

Ern, E. H., 1968, Geology of the Buckingham quadrangle, Virginia: Virginia Div. Mineral Resources Rept. Inv. 15, 45 p.

Fisher, G. W., 1963, The Petrology and structure of the crystalline rocks along the Potomac River, near Washington, D.C.: Baltimore, Md., Johns Hopkins Univ., Ph.D. dissert.

Glaser, J. D., 1971, Geology and mineral resources of southern Maryland: Maryland Geol. Survey Rept. Inv. 15, 85 p.

Higgins, M. W., 1972, Age, origin, regional relations, and nomenclature of the Glenarm Series, central Appalachian Piedmont—A reinterpretation: Geol. Soc. America Bull., v. 83, no. 4, p. 989–1026.

——1974, Age, origin, regional relations, and nomenclature of the Glenarm Series, central Appalachian Piedmont—A reinterpretation: Reply: Geol. Soc. America Bull., v. 85, p. 156.

Higgins, M. W., Fisher, G. W., Johnson, S. S., and Zietz, Isidore, 1973, Preliminary interpretation of an aeromagnetic map of the crystalline rocks of Virginia: Geol. Soc. America Abs. with Programs, v. 5, no. 2 p. 178.

Hopson, C. A., 1964, The crystalline rocks of Howard and Montgomery Counties, *in* The geology of Howard and Montgomery Counties: Baltimore, Maryland Geol. Survey, p. 27–215.

Johnson, S. S., 1971, Bouguer gravity in Virginia, 36°30′ to 39°30′N.; 78°00′ to 79°00′W.: Virginia Div. Mineral Resources Rept. Inv. 27, 40 p.

——1973, Bouguer gravity in northeastern Virginia and the Eastern Shore peninsula: Virginia Div. Mineral Resources Rept. Inv. 32, 48 p.

Lonsdale, J. T., 1927, Geology of the gold-pyrite belt of the northeastern Piedmont, Virginia: Virginia Geol. Survey Bull. 30, 110 p.

Milici, R. C., Spiker, C. T., Jr., and Wilson, J. M., compilers, 1963, Geologic map of Virginia: Charlottesville, Virginia Div. Mineral Resources, scale 1:500,000.

Neuschel, S. K., 1965, Natural gamma aeroradioactivity of the District of Columbia and parts of Maryland, Virginia, and West Virginia: U.S. Geol. Survey Geophys. Inv. Map GP-475.

——1970, Correlation of aeromagnetics and aeroradioactivity with lithology in the Spotsylvania area, Virginia: Geol. Soc. America Bull., v. 81, no. 12, p. 3573–3582.

Neuschel, S. K., Bunker, C. M., and Bush, C. A., 1971, Correlation of uranium, thorium, and potassium with aeroradioactivity in the Berea area, Virginia: Econ. Geology, v. 66, no. 2, p. 302–308.

Pavlides, Louis, 1974, Age, origin, regional relations and, nomenclature of the Glenarm Series, central Appalachian Piedmont—A reinterpretation: Discussion: Geol. Soc. America Bull., v. 85, p. 153–155.

Smith, J. W., Milici, R. C., and Greenberg, S. S., 1964, Geology and mineral resources of Fluvanna County: Virginia Div. Mineral Resources Bull. 79, 62 p.

Southwick, D. L., Reed, J. C., Jr., and Mixon, R. B., 1971, The Chopawamsic Formation—A new stratigraphic unit in the Piedmont of northeastern Virginia: U.S. Geol. Survey Bull. 1324-D, p. D1-D11.

Stose, G. W., compiler, 1928, Geologic map of Virginia: Charlottesville, Virginia Geol. Survey.

Taber, Stephen, 1913, Geology of the gold belt in the James River basin, Virginia: Virginia Geol. Survey Bull. 7, 271 p.

U.S. Geological Survey, 1970, Geological Survey research 1970: U.S. Geol. Survey Prof. Paper 700-A, 426 p.

——1973, Geological Survey research 1973: U.S. Geol. Survey Prof. Paper 850, 366 p. [1974].

Watson, T. L., and Powell, S. L., 1911, Fossil evidence of the age of the Virginia Piedmont slates: Am. Jour. Sci., 4th ser., v. 31, p. 33–44.

Zietz, Isidore, Stockard, H. P., and Kirby, J. R., 1968, Transcontinental geophysical survey (35°–39° N.), magnetic and bathymetric map from 74° to 87° W. longitude: U.S. Geol. Survey Misc. Geol. Inv. Map I-535-A.

Jour. Research U.S. Geol. Survey
Vol. 2, No. 5, Sept.-Oct. 1974, p. 581–592

THE ASSOCIATION OF GEOCHEMICAL ANOMALIES WITH A NEGATIVE GRAVITY ANOMALY IN THE CHIEF MOUNTAIN–SODA CREEK AREA, CLEAR CREEK COUNTY, COLORADO

By G. C. CURTIN and H. D. KING, Denver, Colo.

Abstract.—Geochemical studies in the Chief Mountain–Soda Creek area, Clear Creek County, Colo., show that anomalously high amounts of Au, Ag, Pb, Zn, Cd, and Bi in mull ash, and Cu and Hg in soil, correspond to a negative gravity anomaly in the Front Range mineral belt. The correspondence of the geochemical anomalies to the negative gravity anomaly suggests the presence of altered and mineralized rock and a Tertiary intrusive body at depth. This gravity anomaly and other similar gravity anomalies in the Front Range mineral belt merit further investigation for possible ore deposits.

The Chief Mountain–Soda Creek area is located at an altitude of 2,530–3,350 m (8,300–11,000 ft) in the Front Range mineral belt about 5 km (3 mi) south of Idaho Springs, Clear Creek County, Colo. (fig. 1). Although the area has been prospected from time to time, only one vein system of economic interest has been found. This vein, developed as the Lexington mine (fig. 2), has not been extensively worked.

Geochemical investigations were made within a 10-km^2 (6-mi^2) area, including the Lexington mine and Soda Creek on the north and Chief Mountain on the south (fig. 2), as part of the development of geochemical exploration techniques for use in alpine and subalpine environments. The investigations were done to determine if geochemical anomalies are associated with one of about 25 conspicuous negative gravity anomalies found by Brinkworth (1970) in the Front Range mineral belt. The selected anomaly (fig. 2) is similar in size and intensity to several gravity anomalies that are associated with ore deposits and Tertiary porphyritic rocks which occur as dikes and small irregular stocks. These anomalies probably reflect both the density contrast of 0.1 g/cm^3 between the Tertiary porphyries and the Precambrian rocks (Case, 1967) and zones of alteration resulting from the ore-forming processes. The close spatial and genetic relationships between Tertiary porphyries and Tertiary ore deposits in the Front Range mineral belt have been described by Lovering and Goddard (1950), Sims, Drake, and Tooker (1963), Moench and Drake (1966), and Hawley and Moore (1967), who inferred that both the ore deposits and the Tertiary porphyries were derived from the same source. Although no large bodies of Tertiary rocks are exposed in this area, the negative gravity anomaly suggests the presence of a subjacent Tertiary pluton. Correspondence of positive geochemical anomalies to the negative gravity anomaly would further support the inferred presence of both a Tertiary pluton and mineralized rock beneath the surface at the site of this anomaly.

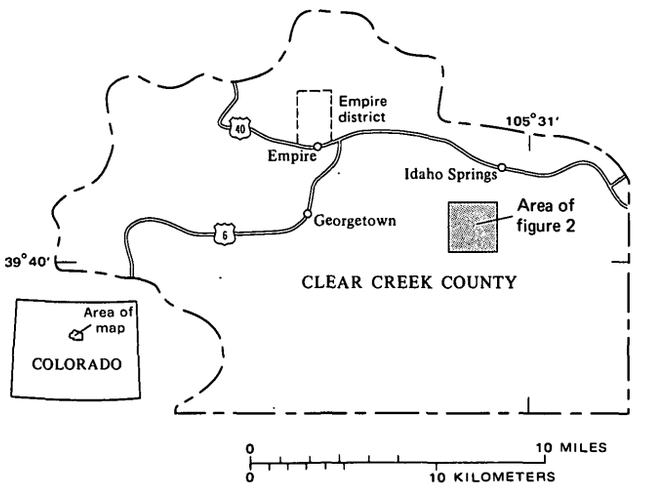

Figure 1.—Index maps showing location of Clear Creek County and the Chief Mountain-Soda Creek area, Colorado.

GEOLOGIC SETTING

The geology of the area has been described by S. H. Ball (in Spurr and Garrey, 1908) and Lovering and Goddard (1950). The Chief Mountain–Soda Creek area is underlain mainly by units of Precambrian biotite schist and biotite gneiss of the Idaho Springs Formation (fig. 2) and by units of Swandyke Hornblende Gneiss. All these units have been intruded by small, partly concordant bodies of Precambrian Boulder Creek Granite, Silver Plume Granite, and granite pegmatite in the central and southern parts of the area, and by a large mass of

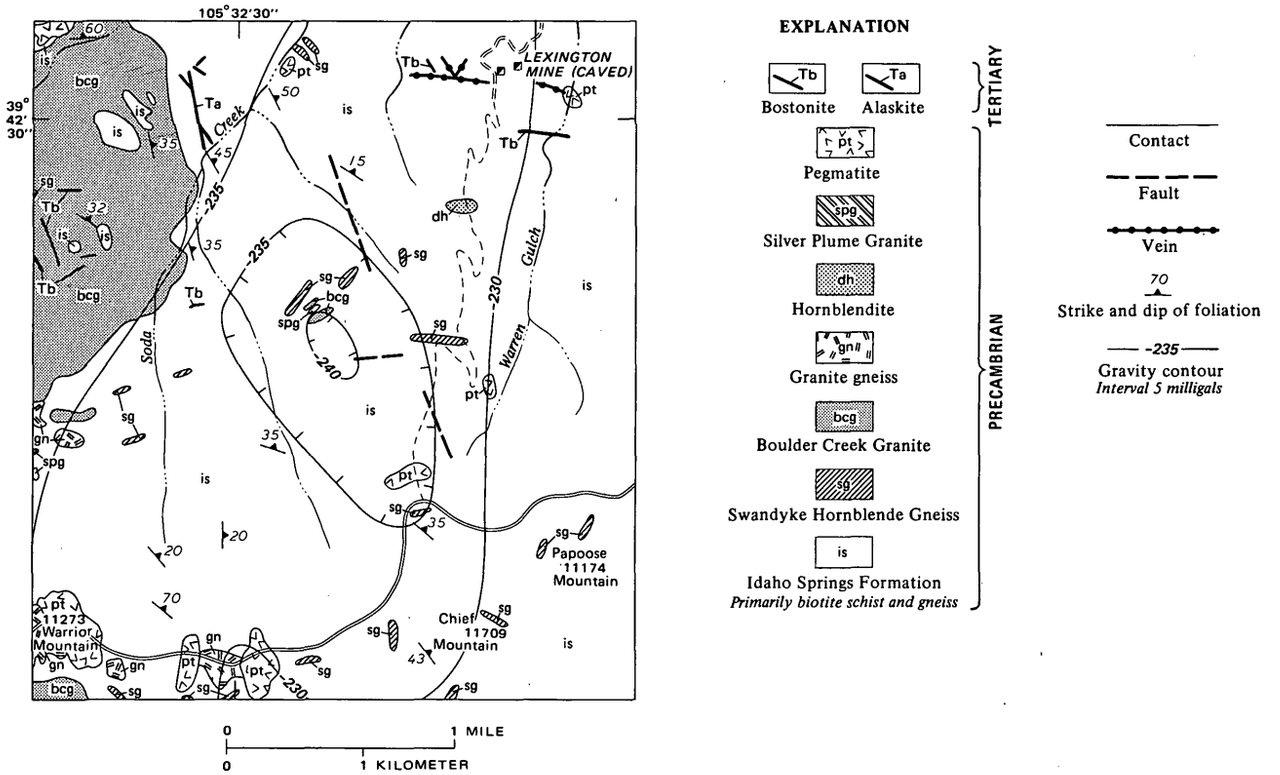

Figure 2.–Geologic map of the Chief Mountain–Soda Creek area, Colorado. Modified from Lovering and Goddard (1950).

Boulder Creek Granite in the west. Small dikes of bostonite and alaskite porphyry of Tertiary age intrude the older rocks. Several small fault zones in the area are characterized by veinlets of iron and manganese oxide separated by moderately to strongly argillized and sheared country rock. The Precambrian rocks are unaltered within most of the area, but in the central part they have been affected by weak argillic alteration.

Because Quaternary colluvium on the hillsides and Quaternary alluvium in the stream bottoms cover much of the bedrock, outcrops are sparse. The Quaternary deposits are not shown in figure 2.

The only economically important vein in the area is that explored by the Lexington mine. The shaft of this mine was caved when visited by us, but vein material on the dump consisted primarily of pyrite and massive to vuggy gray quartz.

This shaft was also caved when Spurr and Garrey visited it more than six decades ago, but they described the vein as striking N. 75° W. and dipping 48° N. at the shaft (Spurr and Garrey, 1908, p. 381). They reported that about 105 m (350 ft) northwest of the shaft the vein split into small branches. Spurr and Garrey considered nearly all the mines along the valley of Soda Creek and its tributaries to be merely prospects, because production from them had been rather small.

GEOCHEMICAL INVESTIGATIONS

Material sampled

The samples of mull, soil, and rock used for geochemical analyses were collected at 165 sites (figs. 3–13). The mixed forest cover from which the mull is derived is primarily lodgepole pine (*Pinus contorta*), Engelmann spruce (*Picea engelmannii*), alpine fir (*Abies lasiocarpa*), and Douglas-fir (*Pseudotsuga mensiesii*); thus the mull can be classed as coniferous mull.

The mull is present as pads, 2.5–7.5 cm (1–3 in.) thick, beneath individual trees. The burrowing of rodents and the action of downslope wash have resulted in the addition of different quantities of mineral matter to these pads. Coniferous mull was collected at every sample site; at several sites, however, a part of the mull was derived from aspen, groves of which are present locally.

A layer of gray to gray-brown ash-textured soil, 2.5–7.5 (1–3 in.) thick, that contains abundant small roots is present beneath the mull layer. This layer is defined as the A horizon. Below this layer is a mixture of weathered cobbles and yellow to yellow-brown coarse to fine sand of colluvial origin and defined as the B horizon. At each site a sample was collected

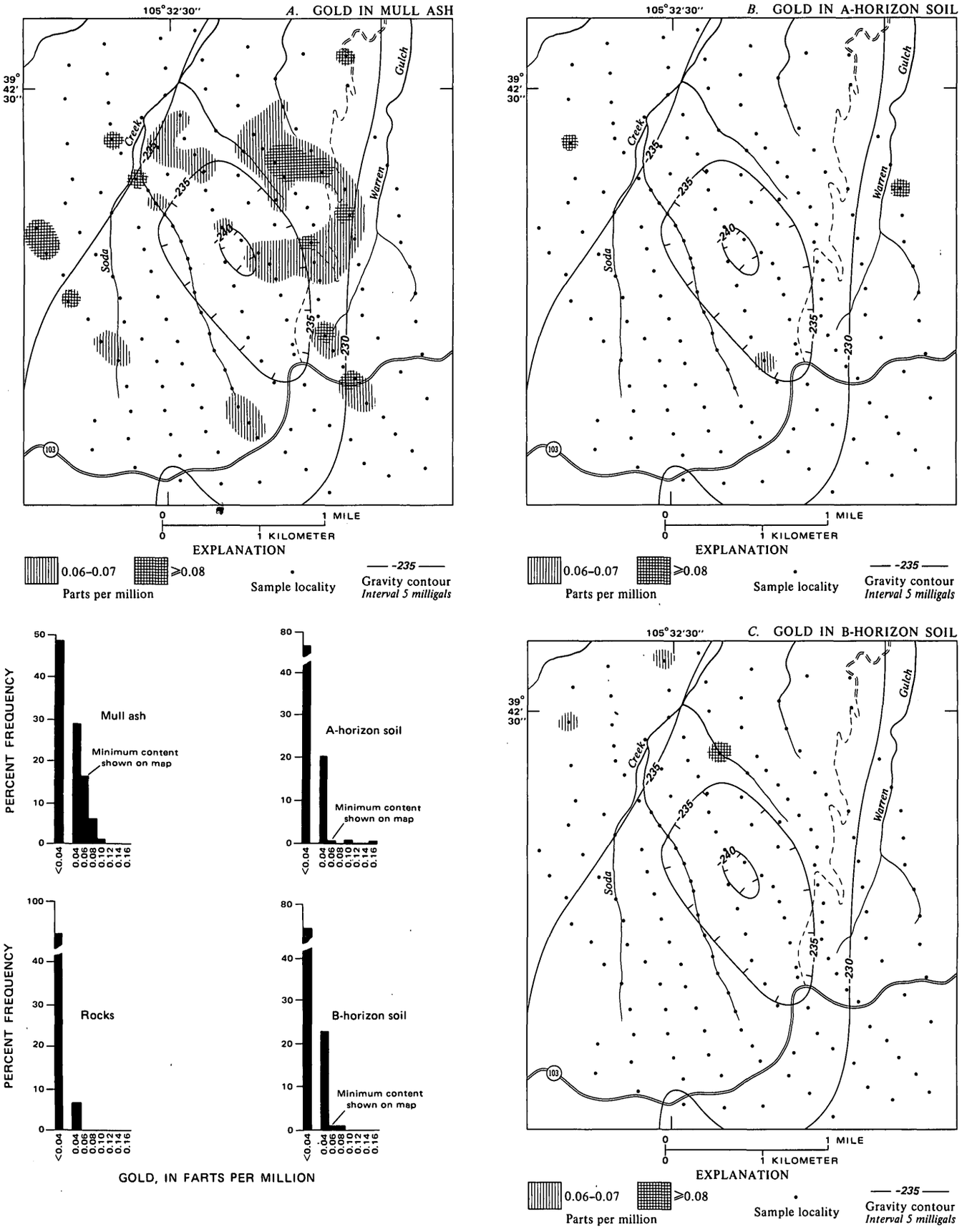

Figure 3.—Geochemical maps and histograms of Au distribution in mull ash and soil and histogram of Au distribution in rocks. Analyses by R. L. Turner, J. R. Watterson, and M. S. Erickson.

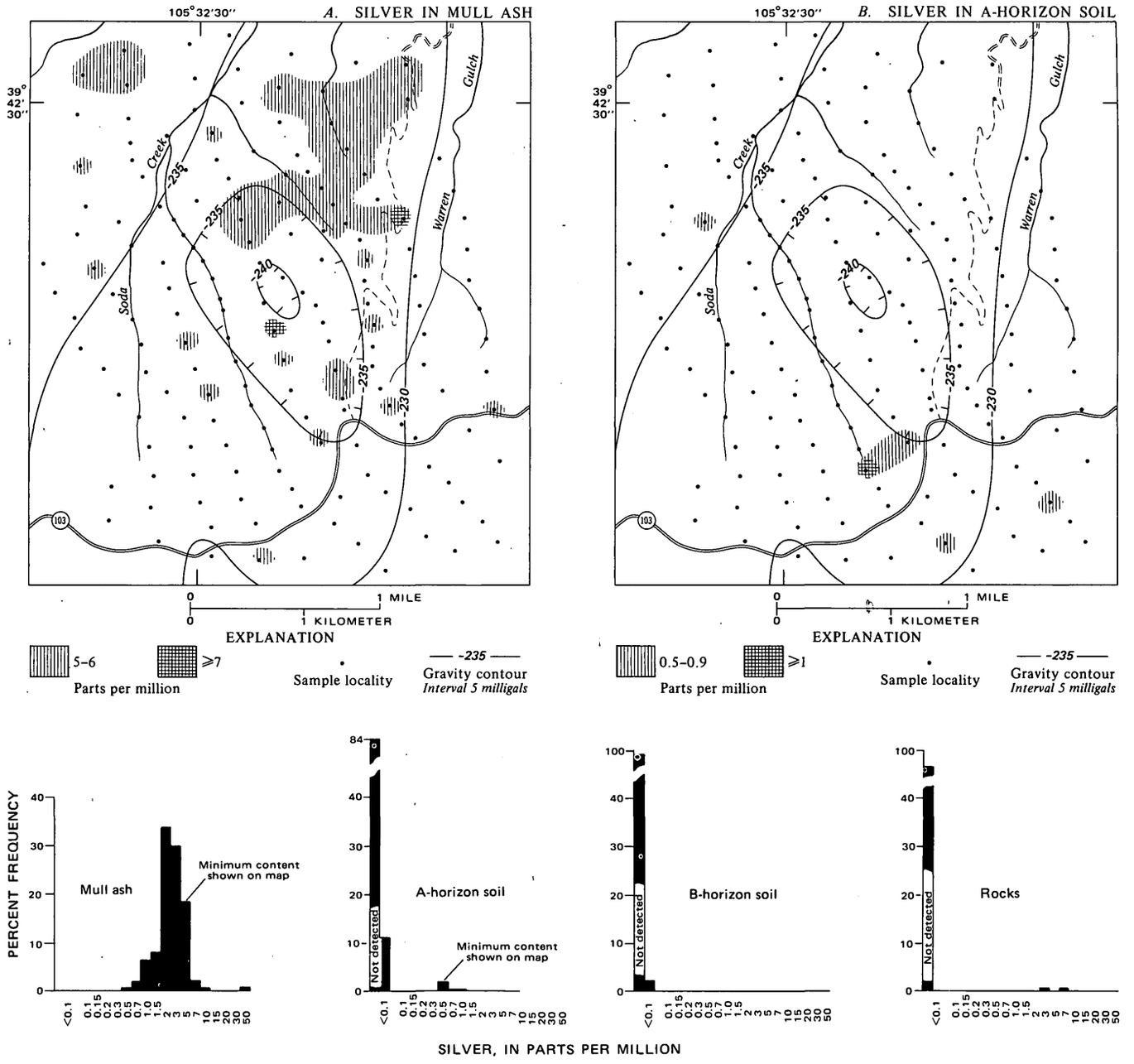

Figure 4.–Geochemical maps and histograms of Ag distribution in mull ash and soil and histogram of Ag distribution in rocks. Analyses by E. L. Mosier, J. M. Nishi, J. A. Domenico, and R. T. Hopkins, Jr.

from the A horizon, and another from the B horizon. The B horizon was sampled to an average depth of 30 cm (12 in.).

Float was collected at most of the sites, but bedrock was collected wherever possible.

Analytical procedures

Several analytical procedures were used. Au and Hg were determined by atomic absorption methods (Thompson and others, 1968; Vaughn and McCarthy, 1964). The other metals were determined by semiquantitative spectrographic methods for mull ash (Mosier, 1972) and for soil (Grimes and Marranzino, 1968).

Soil samples were sieved and the minus 2-mm fraction was ground and pulverized for analysis. Mull samples were sieved to remove rock fragments and large pieces of vegetal litter, and the minus 2-mm fraction was ashed and analyzed for Au. A split of the mull ash was sieved to remove sand-size grains, and

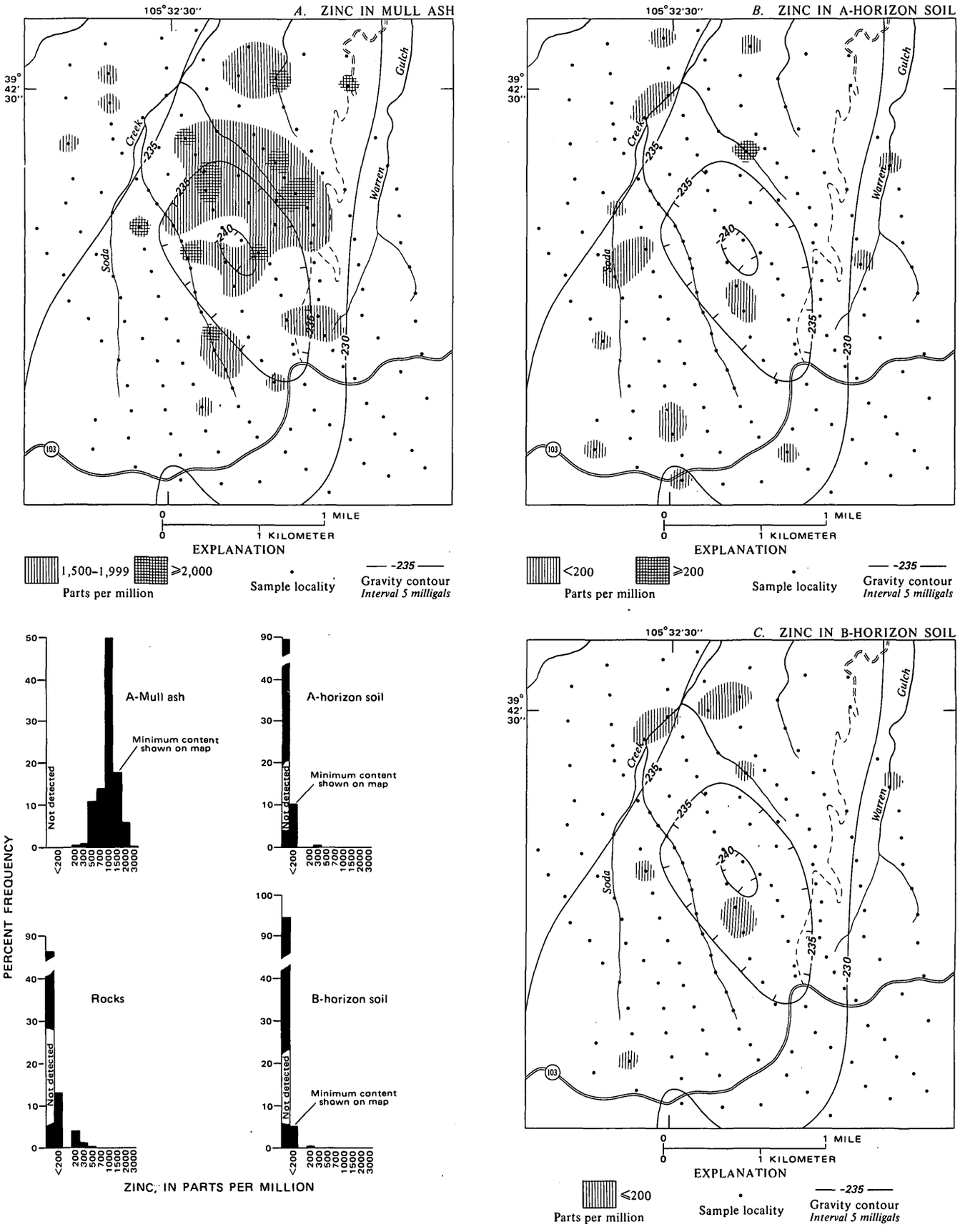

Figure 5.—Geochemical maps and histograms of Zn distribution in mull ash and soil and histogram of Zn distribution in rocks. Analyses by E. L. Mosier, J. M. Nishi, J. A. Domenico, R. T. Hopkins, Jr., and C. L. Forn.

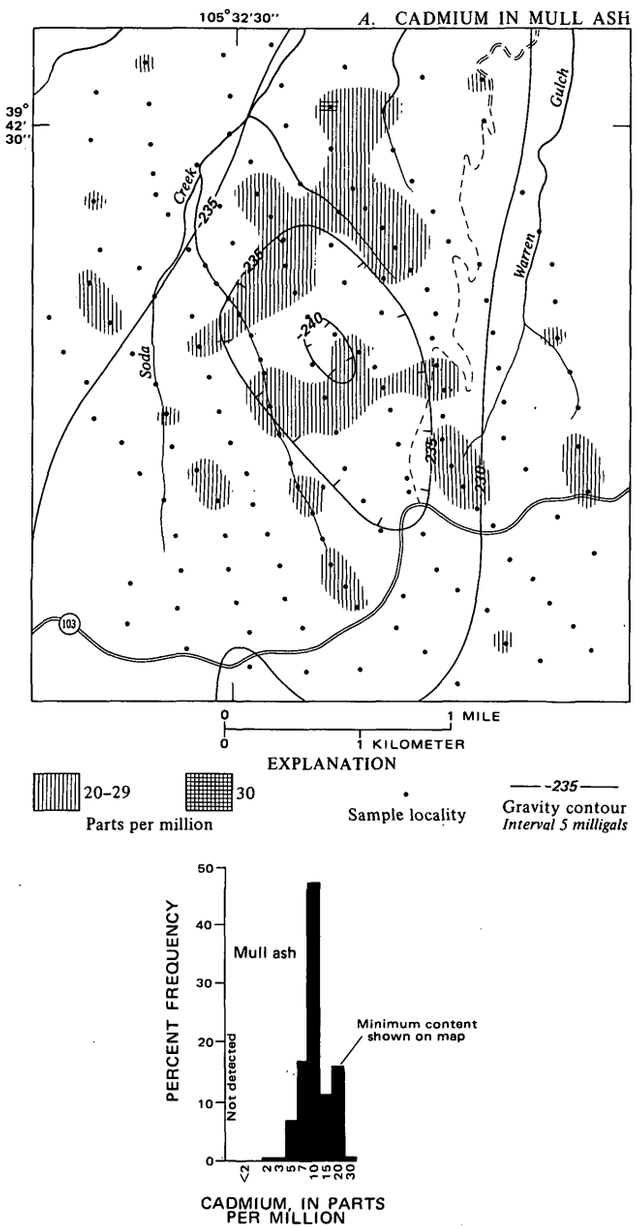

Figure 6.–Geochemical map and histogram of Cd distribution in mull ash. Analyses by E. L. Mosier and J. M. Nishi.

the minus 0.25-mm fraction was analyzed for the other metals by the semiquantitative spectrographic method for organic materials. The ash of the mull, as the term is used in this report, is the sum of the admixed mineral matter and the ash of the organic matter. The metal content of the mull samples is reported on an ashed-weight basis.

Distribution and nature of the geochemical anomalies

The areas of anomalous concentrations of Au, Ag, Zn, Cd, Pb, Bi, Cu, Sn, Mo, Hg, and Mn are shown in figures 3–13. The analytical data are summarized in the accompanying histograms which show the percentage frequency distributions of these elements. Histograms of Au, Ag, Zn, Pb, Cu, and Hg in rocks are shown to allow comparison of element concentration in rocks with that in soil and mull ash. Cd, Bi, Sn, and Mo were not detected in rocks.

Anomalous values for individual elements were determined after considering the percentage frequency distributions and patterns of areal distribution. The minimum element content in the anomalous areas on each of the maps is shown on the histograms (figs. 3–13).

Positive anomalies of Au, Ag, Zn, Cd, Pb, and Bi in mull ash are widespread and coextensive. Anomalies of Au, Ag, Pb, Zn, and Cd roughly correlate with each other in the north-central part of the area (figs. 3*A*, 4*A*, 5*A*, 6*A*, 7*A*); high concentrations of Pb and Bi outline an anomalous zone in the south and west (figs. 7*A*, 8*A*). These anomalies form an encircling pattern which correlates with that of the negative gravity anomaly.

In contrast to the distribution of the above elements, positive anomalies of Cu, Sn, and Mo in the mull ash are small and discontinuous. The anomalies of these elements do not correlate with each other or with the anomalies of the elements discussed above.

Anomalies in soil, with the exception of Cu and Hg, are also small and discontinuous. The scattered anomalies of Au, Ag, Zn, Pb, and Bi in soil do not show good correlations with each other and contrast noticeably with the widespread anomalies of these elements in mull ash. Cd, Sn, and Mo were not detected in the soil.

Cu and Hg, on the other hand, form more continuous patterns in soil than do the other elements. The pattern of Cu anomalies in the B horizon and, to a lesser extent, in the A horizon of the soil (figs. 9*B*, 9*C*) indicates Cu enrichment in the central part of the area. High Hg anomalies in soil (figs. 12*A*, 12*B*) roughly correspond to the anomalies of Pb and Bi in mull ash. Mull was not analyzed for Hg because an adequate rapid method for the analysis of Hg in mull is not available.

Biotite schist and gneiss and hornblende gneiss are the principal rocks that underlie the anomalies in mull ash. With few exceptions, either very small amounts, or none, of the elements Au, Ag, Zn, Cd, Pb, Bi, Cu, Sn, Mo, and Hg were detected in the samples of the rock, which were mostly float, within these anomalous areas. The exceptions were samples from three prospect pits in small shear zones and one sample from the Lexington vein where it crops out. These samples contained anomalous amounts of Au, Ag, Zn, Pb, Bi, Cu, and Hg.

The significance of anomalies in the ash of mull and in the soil can be better understood when these anomalies are compared to similar anomalies in the Empire district in the Front Range mineral belt (Curtin and others, 1971). In the Empire district, positive anomalies of Au, Ag, Cu, Pb, Zn, Bi, and Mo in the ash of mull outline the known ore deposits and

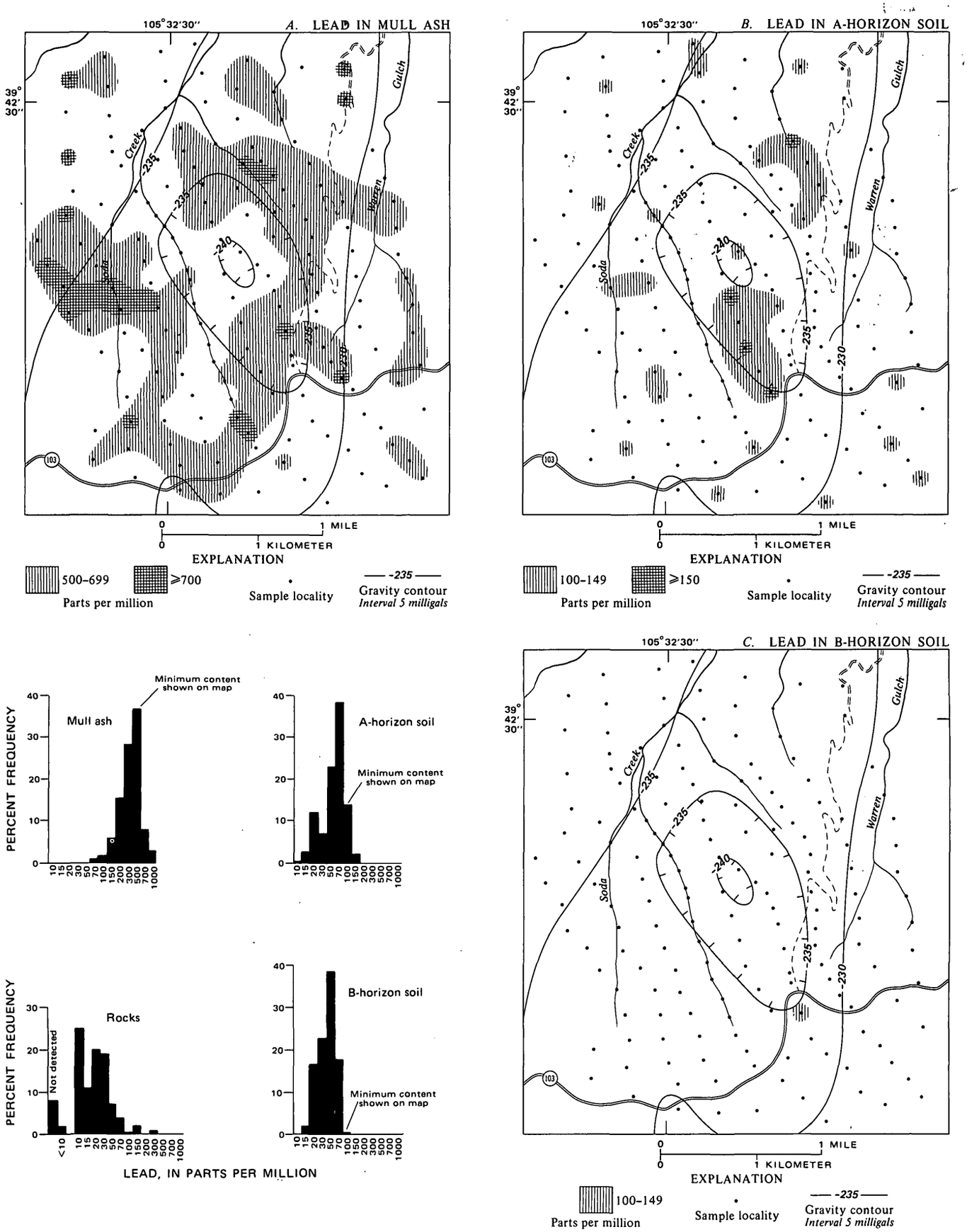

Figure 7.—Geochemical maps and histograms of Pb distribution in mull ash and soil and histogram of Pb distribution in rocks. Analyses by E. L. Mosier, J. M. Nishi, J. A. Domenico, R. T. Hopkins, Jr., and C. L. Forn.

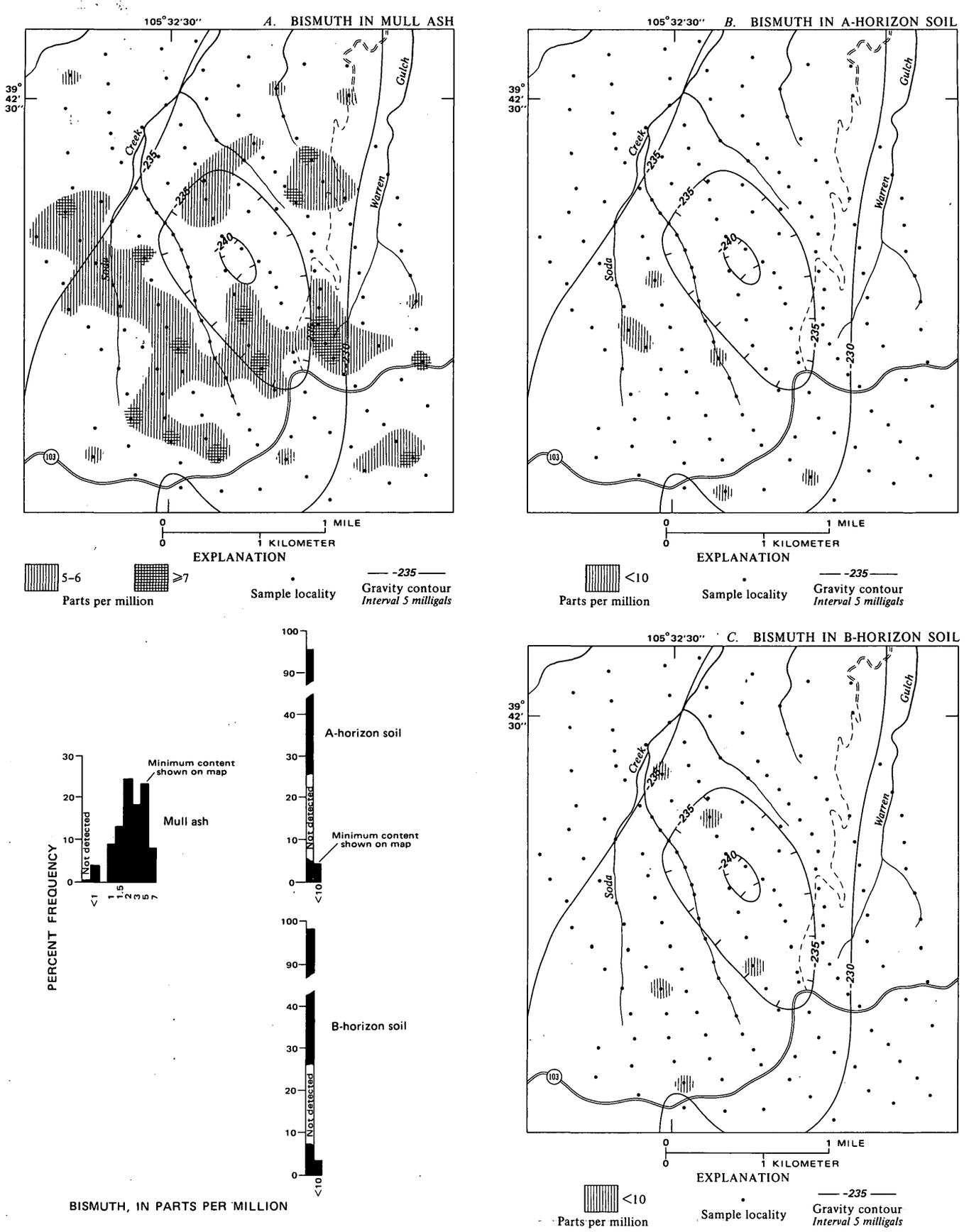

Figure 8.–Geochemical maps and histograms of Bi distribution in mull ash and soil. Analyses by E. L. Mosier, J. M. Nishi, J. A. Domenico, and R. T. Hopkins, Jr.

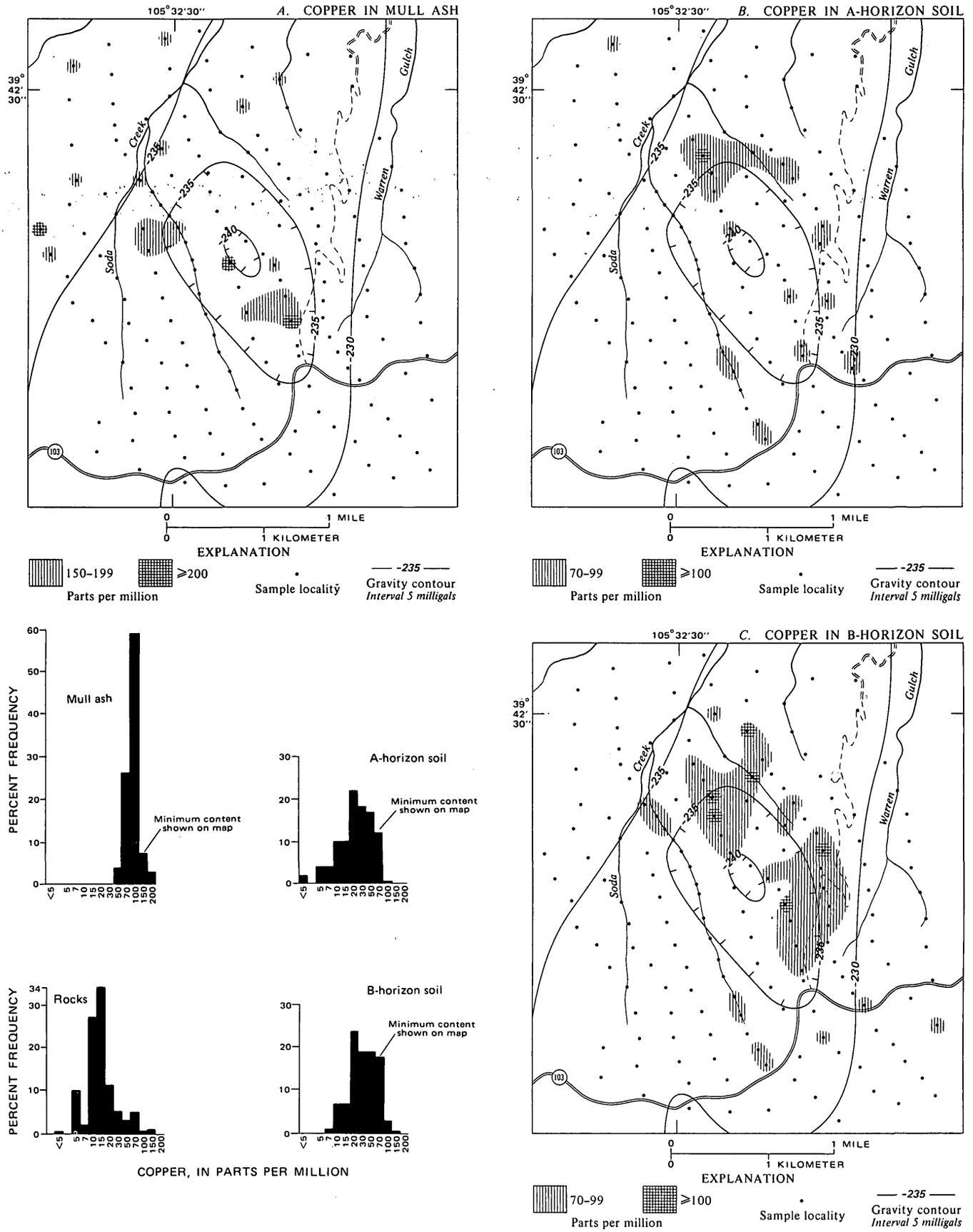

Figure 9.—Geochemical maps and histograms of Cu distribution in mull ash and soil and histogram of Cu distribution in rocks. Analyses by E. L. Mosier, J. M. Nishi, J. A. Domenico, R. T. Hopkins, Jr., and C. L. Forn.

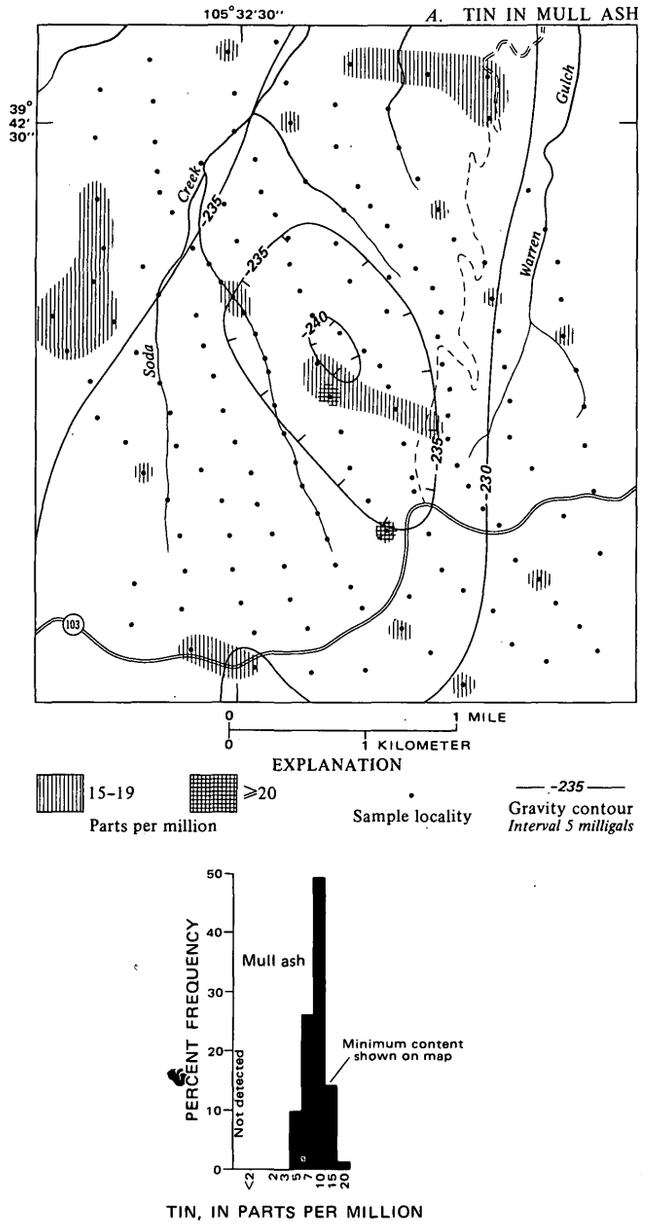

Figure 10.–Geochemical map and histogram of Sn distribution in mull ash. Analyses by E. L. Mosier and J. M. Nishi.

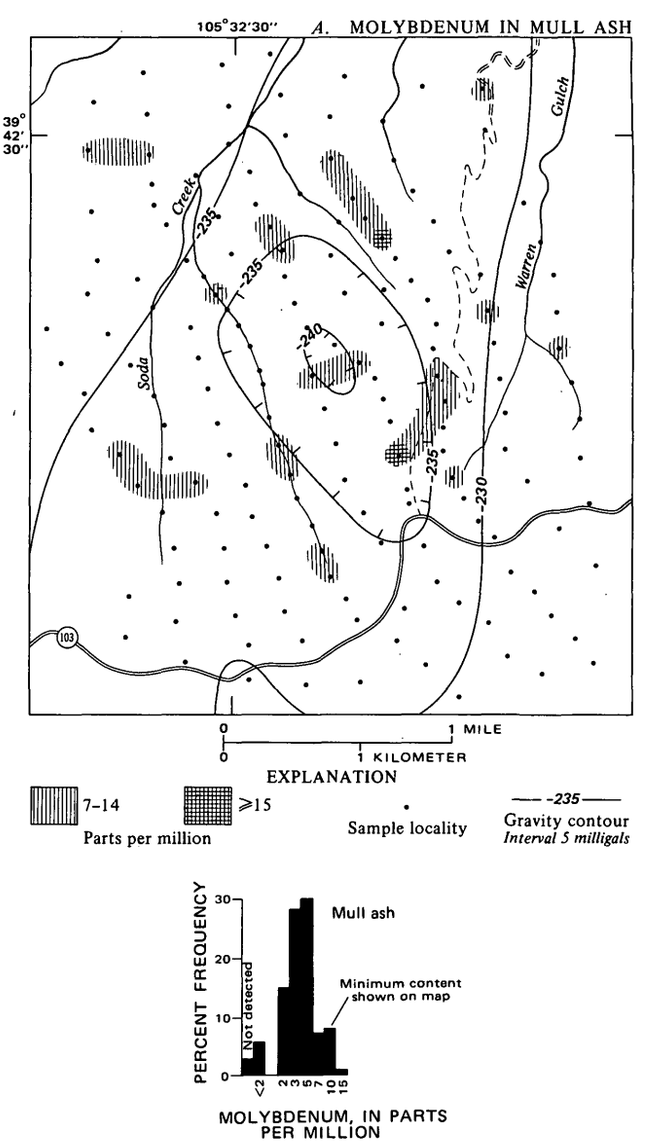

Figure 11.–Geochemical map and histogram of Mo distribution in mull ash. Analyses by E. L. Mosier and J. M. Nishi.

indicate extensions of these deposits, whereas the small, discontinuous anomalies of these elements in the soil correlate with ore deposits in only a few places. Comparisons of metal values in the ash of mull in this area with those in the Empire district show that (1) the concentrations of Ag and Zn in this area are noticeably higher than those in the Empire district, (2) the concentration of Pb is about the same in both areas, and (3) the concentration of Au, Cu, Bi, Mo, and Sn are noticeably lower in this area than in the Empire district. The difference in concentrations of Au, Cu, and Bi is to be expected, however, because auriferous pyrite and chalcopyrite were principal minerals of the near-surface ore deposits in the Empire district and metallic Bi was reported as having occurred in one of the major ore zones (Spurr and Garrey, 1908, p. 399). Moreover, results of our sampling in the Empire district and in other places in the Front Range mineral belt (unpub. data, 1971) show that Au and Bi are detected in mull ash only over mineralized areas.

The concentration of Hg in the soil is noticeably higher here than in the Empire district and the Hg anomalies are larger in area than those which correspond to the ore deposits in the Empire district.

Mn depletion in the Chief Mountain–Soda Creek area is indicated by Mn anomalies in mull ash where areas of Mn

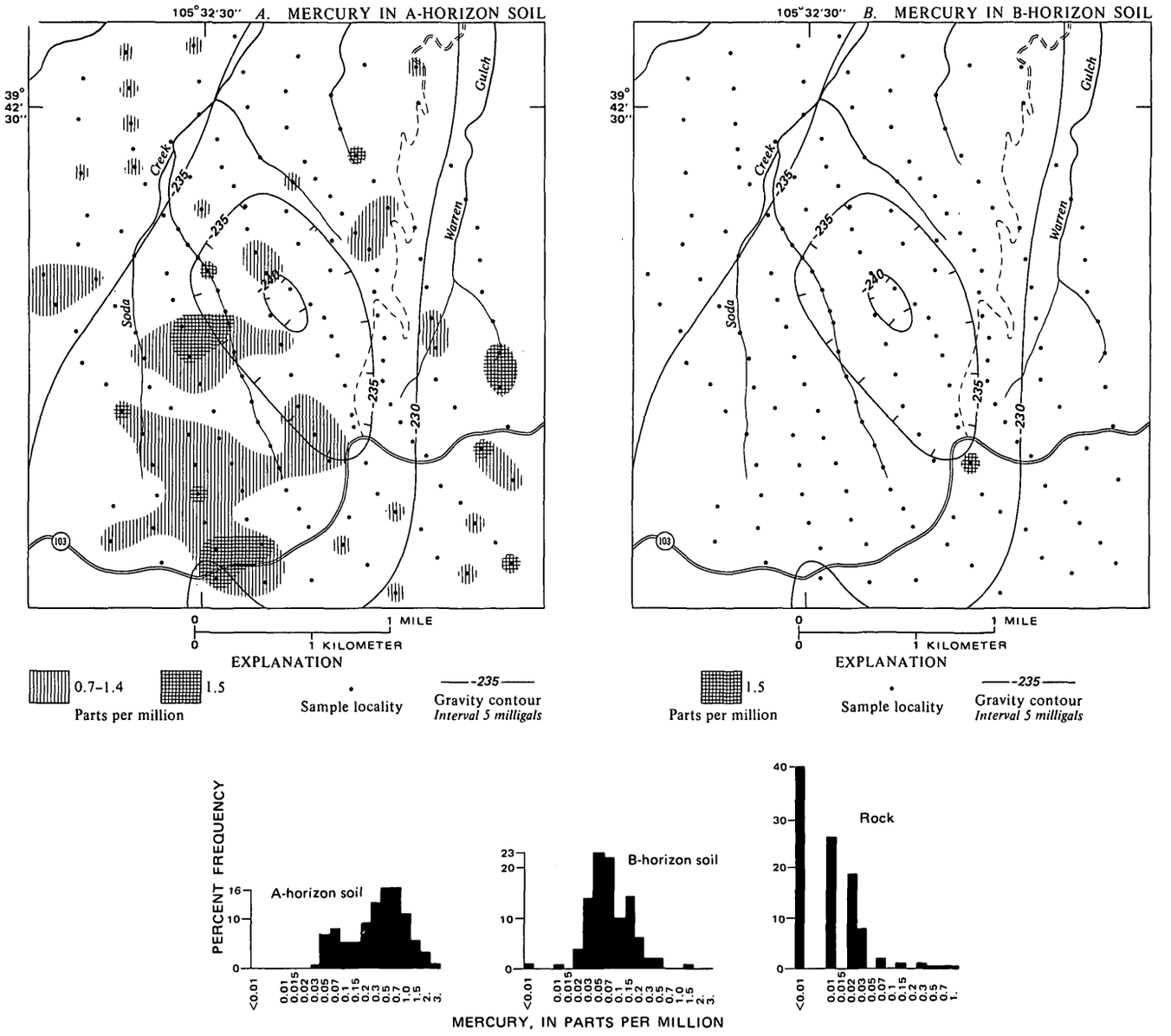

Figure 12.—Geochemical maps and histograms of Hg distribution in soil, and histogram of Hg distribution in rocks. Analyses by R. L. Turner.

concentration of 7,000 p/m or more (fig. 13) partly encircle areas of Mn concentration of 2,000 p/m or less. The areas of low Mn values roughly correlate with areas of positive anomalies of Au, Ag, Zn, and Cd in the ash of mull and with areas of Cu anomalies in the soil. Similar patterns were described in the Empire district (Curtin and others, 1971, p. B36, fig. 22; Chaffee, 1972, p. C7) wherein areas of Mn depletion correspond to areas of ore deposits and alteration.

Enrichment of elements in the mull ash

The distribution and abundance of metals shown on the geochemical maps together with the histograms of metal content in mull ash, in soil, and in float and surface bedrock (figs. 3–8, 10, 11, 13) demonstrate the enrichment of Au, Ag, Zn, Cd, Pb, Bi, Cu, Sn, Mo, and Mn in mull ash relative to soil and rock. The minimum values shown on the maps for Ag, Zn, Pb, and Cu in mull ash are greater by a factor of 10 for Ag, 7½ for Zn, 5 for Pb, and 2 for Cu than the minimum values shown on the maps for these elements in soil.

The enrichment of elements in mull ash is a result of the biogeochemical cycling process, first described by Goldschmidt (1937, p. 670), by which elements are dissolved by soil water, enter plants through the roots, accumulate in the leaves and other plant parts, and are preferentially concentra-

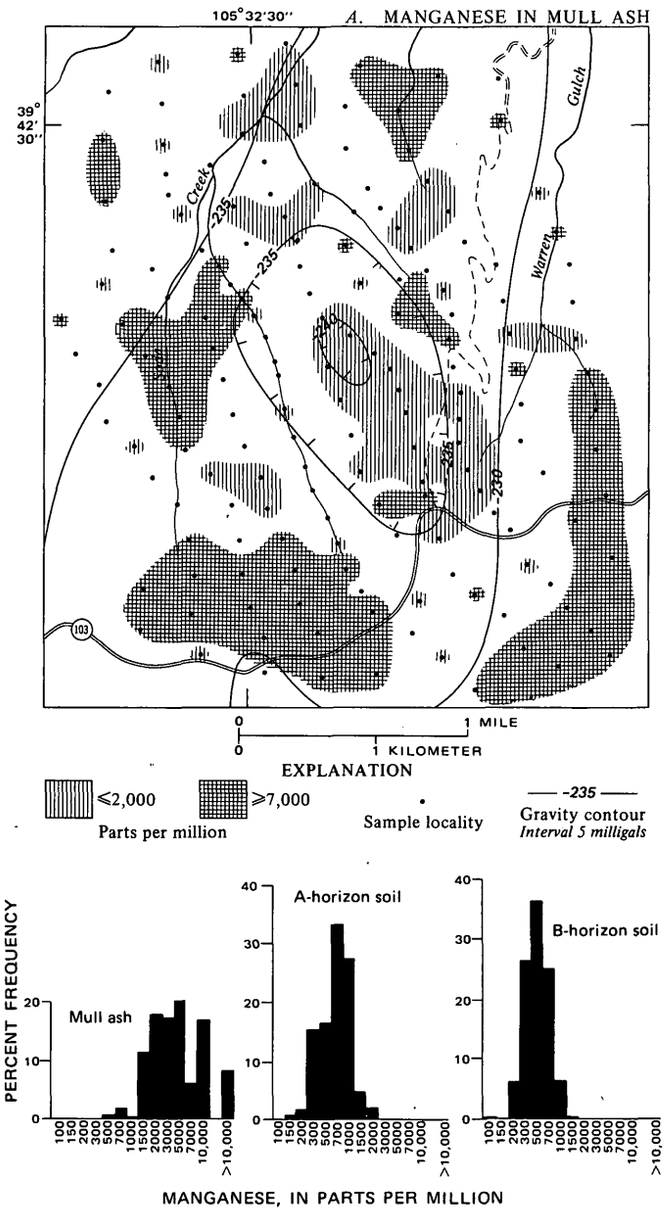

Figure 13.–Geochemical map and histogram of Mn distribution in mull ash and histograms of Mn distribution in soil. Analyses by E. L. Mosier, J. M. Nishi, J. A. Domenico, and R. T. Hopkins, Jr.

ted in the mull layer as the other products of plant decay are leached away.

CONCLUSIONS

The geochemical anomalies are not directly related to surface exposures of bedrock, as shown by the facts that the metal values in the bedrock are comparatively low and that the anomalies do not correspond to particular geologic features such as rock types or fault zones. Likewise, the vein of the Lexington mine and the several small fault zones do not appear to be sufficiently mineralized or to be sufficiently large to provide a source for these anomalies.

A source at some unknown depth below the surface seems most likely to satisfy the geophysical and geochemical data. The negative gravity anomaly indicates the presence of a mass of rock less dense than the Precambrian rocks exposed at the surface. The distribution of geochemical anomalies, particularly with reference to the similarity to the distribution of anomalies in the Empire district (Curtin and others, 1971, figs. 4 and 8), suggests that the anomalies reflect leakage from a concealed Tertiary pluton.

Further exploration will be required to determine whether the elements which formed the geochemical anomalies came from sizable metal deposits. This and other negative gravity anomalies in the Front Range mineral belt should be explored in more detail with the aim of detecting concealed ore deposits associated with Tertiary intrusive rocks.

REFERENCES CITED

Brinkworth, G. L., 1970, Complete Bouguer anomaly gravity map and generalized geology of an area west of Denver, Colorado: U.S. Geol. Survey open-file map, 1 sheet, scale 1:125,000.

Case, J. E., 1967, Geophysical ore guides along the Colorado mineral belt: U.S. Geol. Survey open-file rept., 13 p.

Chaffee, M. A., 1972, Distribution and abundance of gold and other selected elements in altered bedrock, Empire mining district, Clear Creek County, Colorado: U.S. Geol. Survey Bull. 1278-C, 23 p.

Curtin, G. C., Lakin, H. W., Hubert, A. E., Mosier, E. L., and Watts, K. C., 1971, Utilization of mull (forest humus layer) in geochemical exploration in the Empire district, Clear Creek County, Colorado: U.S. Geol. Survey Bull. 1278-B, 39 p.

Goldschmidt, V. M., 1937, The principles of distribution of chemical elements in minerals and rocks: Chem. Soc. [London] Jour., January-June, p. 665–673.

Grimes, D. J., and Marranzino, A. P., 1968, Direct-current arc and alternating-current spark emission spectrographic field methods for the semiquantitative analysis of geologic materials: U.S. Geol. Survey Circ. 591, 6 p.

Hawley, C. C., and Moore, F. B., 1967, Geology and ore deposits of the Lawson-Dumont–Fall River district, Clear Creek County, Colorado: U.S. Geol. Survey Bull. 1231, 92 p.

Lovering, T. S., and Goddard, E. N., 1950, Geology and ore deposits of the Front Range, Colorado: U.S. Geol. Survey Prof. Paper 223, 319 p. (1951).

Moench, R. H., and Drake, A. A., Jr., 1966, Economic geology of the Idaho Springs district, Clear Creek and Gilpin Counties, Colorado: U.S. Geol. Survey Bull. 1208, 91 p.

Mosier, E. L., 1972, A method for semiquantitative spectrographic analysis of plant ash for use in biogeochemical and environmental studies: Appl. Spectroscopy, v. 26, no. 6, p. 636–641.

Sims, P. K., Drake, A. A., Jr., and Tooker, E. W., 1963, Economic geology of the Central City district, Gilpin County, Colorado: U.S. Geol. Survey Prof. Paper 359, 231 p.

Spurr, J. E., and Garrey, G. H., 1908, Economic geology of the Georgetown quadrangle (together with the Empire district), Colorado, *with* General geology, by S. H. Ball: U.S. Geol. Survey Prof. Paper 63, 422 p.

Thompson, C. E., Nakagawa, H. M., and Van Sickle, G. H., 1968, Rapid analysis for gold in geologic materials, *in* Geological Survey research 1968: U.S. Geol. Survey Prof. Paper 600-B, p. B130–B132.

Vaughn, W. W., and McCarthy, J. H., 1964, An instrumental technique for the determination of submicrogram concentrations of mercury in soils, rocks, and gas, *in* Geological Survey research 1964: U.S. Geol. Survey Prof. Paper 501-D, p. D123–D127.

Jour. Research U.S. Geol. Survey
Vol. 2, No. 5, Sept.-Oct. 1974, p. 593–598

THE SARGENT-BERROCAL FAULT ZONE AND ITS RELATION TO THE SAN ANDREAS FAULT SYSTEM IN THE SOUTHERN SAN FRANCISCO BAY REGION AND SANTA CLARA VALLEY, CALIFORNIA

By ROBERT J. McLAUGHLIN, Menlo Park, Calif.

Abstract.—The Sargent-Berrocal fault zone is a belt of thrust faults extending for about 58 mi (94 km) southeastward from the vicinity of Los Altos to San Juan Bautista, Calif. The fault zone generally dips southwestward toward the adjacent San Andreas fault at low to steep angles, and the southwest block has moved upward and northeastward. Thrusting across the fault zone has produced large-scale offset, which may increase to the southeast. If strike-slip movement has occurred, it has probably been minor. Offset Quaternary strata, physiographic features, and recent seismic activity all indicate that the Sargent-Berrocal fault zone has been active in the last one million years and that some elastic strain is currently being released along the northwest and southeast parts of the fault zone.

Recent joint U.S. Geological Survey–Department of Housing and Urban Development investigations have been directed toward recognition of active faults in the San Francisco Bay region, California. These investigations indicate that discontinuous thrust faults near Los Altos suspected as active by Dibblee (1966) are, in fact, active and are part of a continuous zone of thrusts extending for 58 mi (94 km) to the southeast of Los Altos (fig. 1). This paper briefly describes the activity of this fault zone and discusses its structural and environmental implications.

STRUCTURE AND STRATIGRAPHY

The fault zone will be referred to in this paper as the Sargent-Berrocal fault zone. The Sargent segment, named by J. E. Allen (1946), lies a few miles southeast of Hecker Pass near San Juan Bautista (fig. 1). Allen considered the Sargent fault to be largely vertical, with the north side up. McLaughlin (1971) and McLaughlin, Simoni, Osbun, and Bauer (1971), however, considered it a thrust fault with the south side up and they extended it northwestward to the Mount Madonna area.

North of Mount Madonna, the Sargent fault joins the Berrocal fault along a zone of complex imbricate structures (fig. 1). The Berrocal fault was named in the New Almaden area by Bailey and Everhart (1964) and was extended to the southeast by McLaughlin, Simoni, Osbun, and Bauer (1971). Bailey and Everhart (1964) have mapped the Berrocal fault zone northwestward to the vicinity of Los Gatos. In this report the Berrocal fault zone has been extended beyond Los Gatos to the Stevens Creek Reservoir area, where in many places it is obscured by landslide deposits of Holocene age. It is also extended north of Stevens Creek where it comprises two parallel strands. The northern strand lies along the northeastern base of the foothills of the Santa Cruz Mountains between Saratoga and Los Altos Hills, and the southern strand trends northwestward along the northeast side of the steep ridges between Los Altos Hills and Los Gatos.

Geologic mapping southeast of Highway 17 (McLaughlin and others, 1971; Bailey and Everhart, 1964) suggests that the dip of the fault zone ranges from 20° SW to vertical. In the vicinity of Los Altos, southwestward dips of 32°–61° have been inferred from geologic mapping (Dibblee, 1966), and dips of 5°–75° SW have been interpreted from a gravity study (Fleck, 1967).

The block southwest of the Sargent-Berrocal fault zone has moved up and northeastward, relative to the northeast block. North of Black Mountain (Dibblee, 1966), Miocene, Pliocene, and Pleistocene strata are overlain at a low angle along the fault zone by late Mesozoic rocks of the Franciscan assemblage (section A–A', fig. 2), indicating a thrust fault. Farther to the southeast, between Loma Prieta and Mount Madonna, non-Franciscan Mesozoic rocks are thrust over Miocene strata (section C–C', fig. 2). Folds in the Miocene strata are subparallel to the fault zone, and many are tightly appressed or overturned northeastward, suggesting southwest-northeast compression. Locally, southwest-dipping diapirs or small-scale thrusts present along the northeast limbs of the anticlinal folds also suggest southwest-northeast compression.

Several lines of evidence indicate large-scale offset across the Sargent-Berrocal fault zone. Northeast of Black Mountain, strata of similar age are present northeast and southwest of the fault zone (fig. 2), but gravity data in this area (Fleck, 1967, p. 29) indicate that Cenozoic strata may be overridden hori-

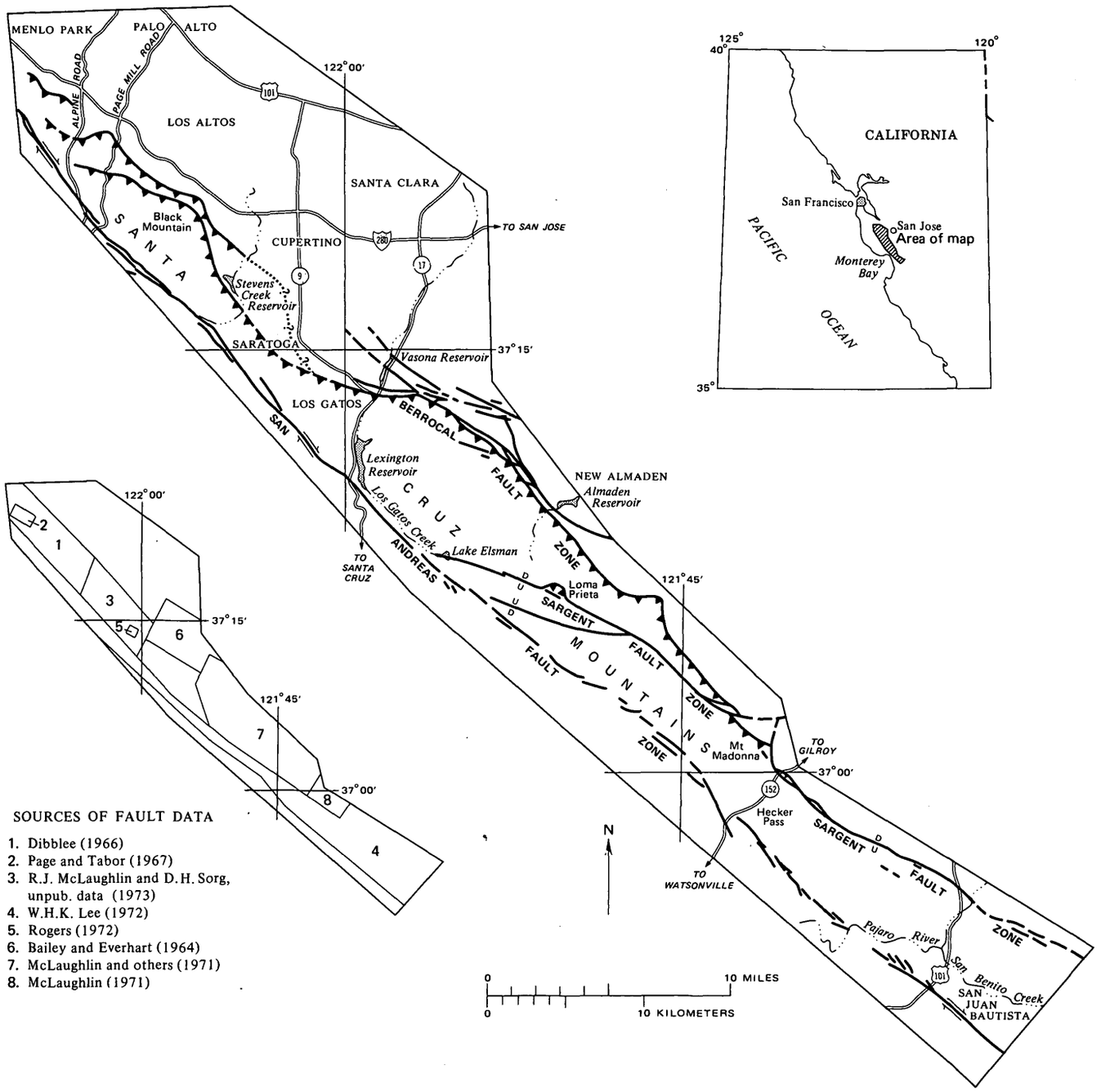

Figure 1.—Location of the Sargent-Berrocal fault zone.

zontally for at least 7,500 ft (2.3 km) by rocks of the Franciscan assemblage. Farther southeast, between Highways 17 and 152, prominent differences in stratigraphy across the fault zone suggest large-scale offset. In that area a thick section of late Cretaceous and Tertiary marine strata is present in the southwest fault block (fig. 2), whereas only early and middle Miocene strata are present in the northeast fault block, in unconformable contact with a basement composed largely of Franciscan rocks. Some of this stratigraphic contrast may be due to strike slip, but there is no evidence of large-scale offsets of this type, and field observations indicate thrusting. The stratigraphic differences observed across the Sargent-Berrocal fault zone between Highways 17 and 152 may be the result of either greater crustal shortening in that area than farther to the northwest, or decreased discordance of the fault zone trace with the regional strike of strata southeast of Highway 17.

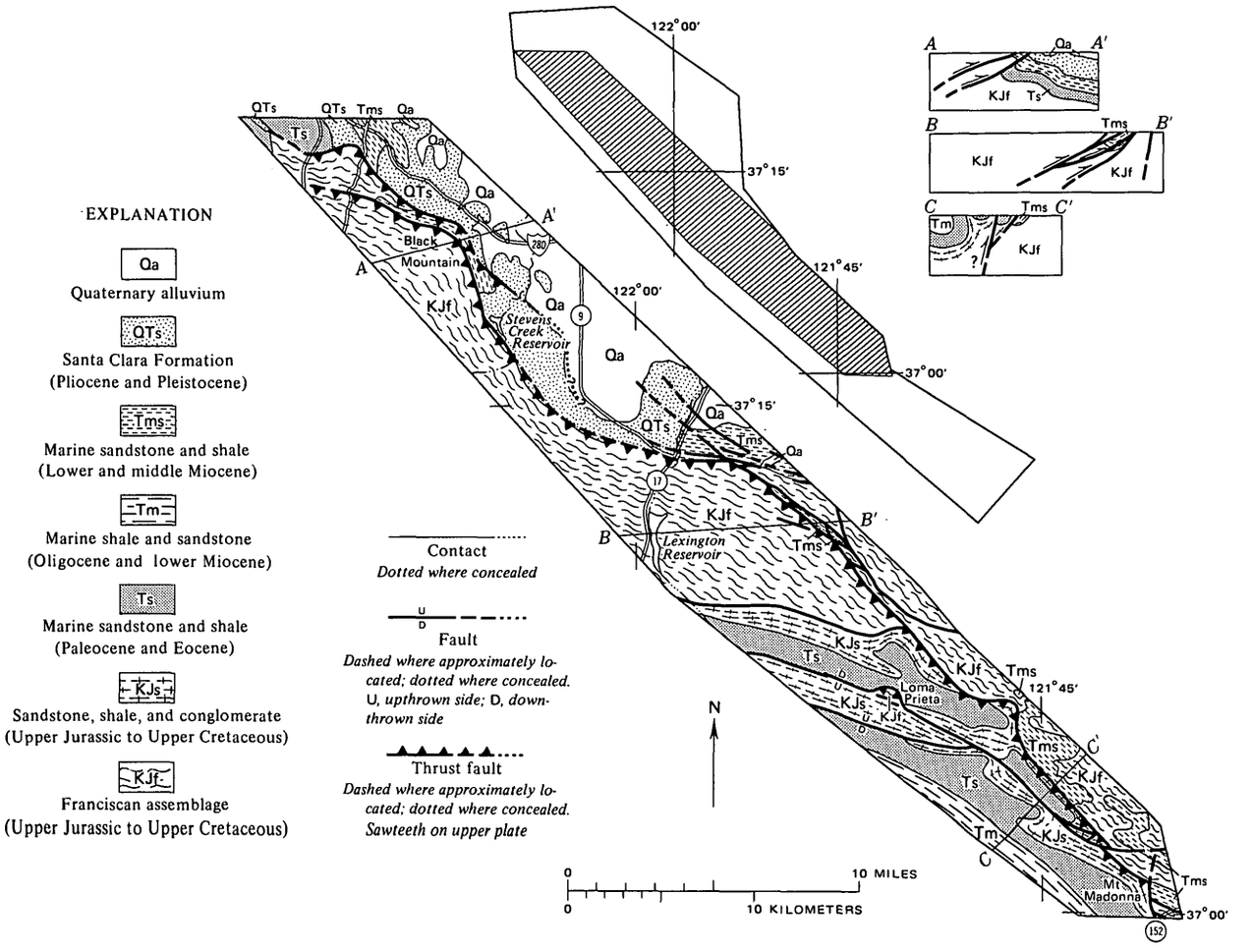

Figure 2.—Generalized geologic map and structure sections along the Sargent-Berrocal fault zone. Screened area on index map shows location of geologic map in figure 1.

EVIDENCE FOR RECENT ACTIVITY

The fault zone southeast of Highway 152 is nearly vertical and is marked along its course by linear troughs, benches, notches, sag ponds, and alined drainages. Holocene offset is indicated near the intersection of the fault zone with Whitehurst Road (fig. 3), where the bed of a northeast-flowing stream is vertically offset 1.3 ft (0.4 m), with the southwest side of the fault up. Many earthquakes of magnitude 5.0 or less have occurred southeast of Highway 152, and their epicenters are coincident or very nearly coincident with the Sargent segment of the fault zone (fig. 3).

Between Highways 152 and 17, the Sargent-Berrocal fault zone is within a late Mesozoic to middle Miocene terrane, and the age of offsets is therefore post-middle Miocene. Recent activity in this area is suggested in places by such features as captured drainages and linear troughs, but seismic activity here is much lower than along the segment to the southeast. Only a few scattered epicenters of earthquakes with magnitudes less than 2.0 have been recorded in this area.

Northwest of Highway 17 the Sargent-Berrocal fault zone offsets steeply tilted and folded gravels of the Santa Clara Formation, which ranges in age from 1 to 3 m.y. (Cummings, 1968). Since there is no evidence to indicate that folding accompanied deposition, these offsets are probably no more than one million years old. Recent activity is also suggested by reports (Lawson, 1908, p. 107) that surface ruptures occurred during the earthquake of 1906 at the intersections of the fault zone with Page Mill and Alpine Roads, near Palo Alto. An earthquake that occurred along this segment in the Stevens Creek area on April 28, 1967 (Bolt and others, 1968) had a hypocentral depth of 4.3 mi (7 km) and magnitude of 2.8. Fault-plane solutions for this earthquake suggest either down-to-the-southwest movement across a near-vertical fault or low-angle thrusting from the south. More recent earthquakes with magnitudes of 3.7 and less have occurred in the vicinity

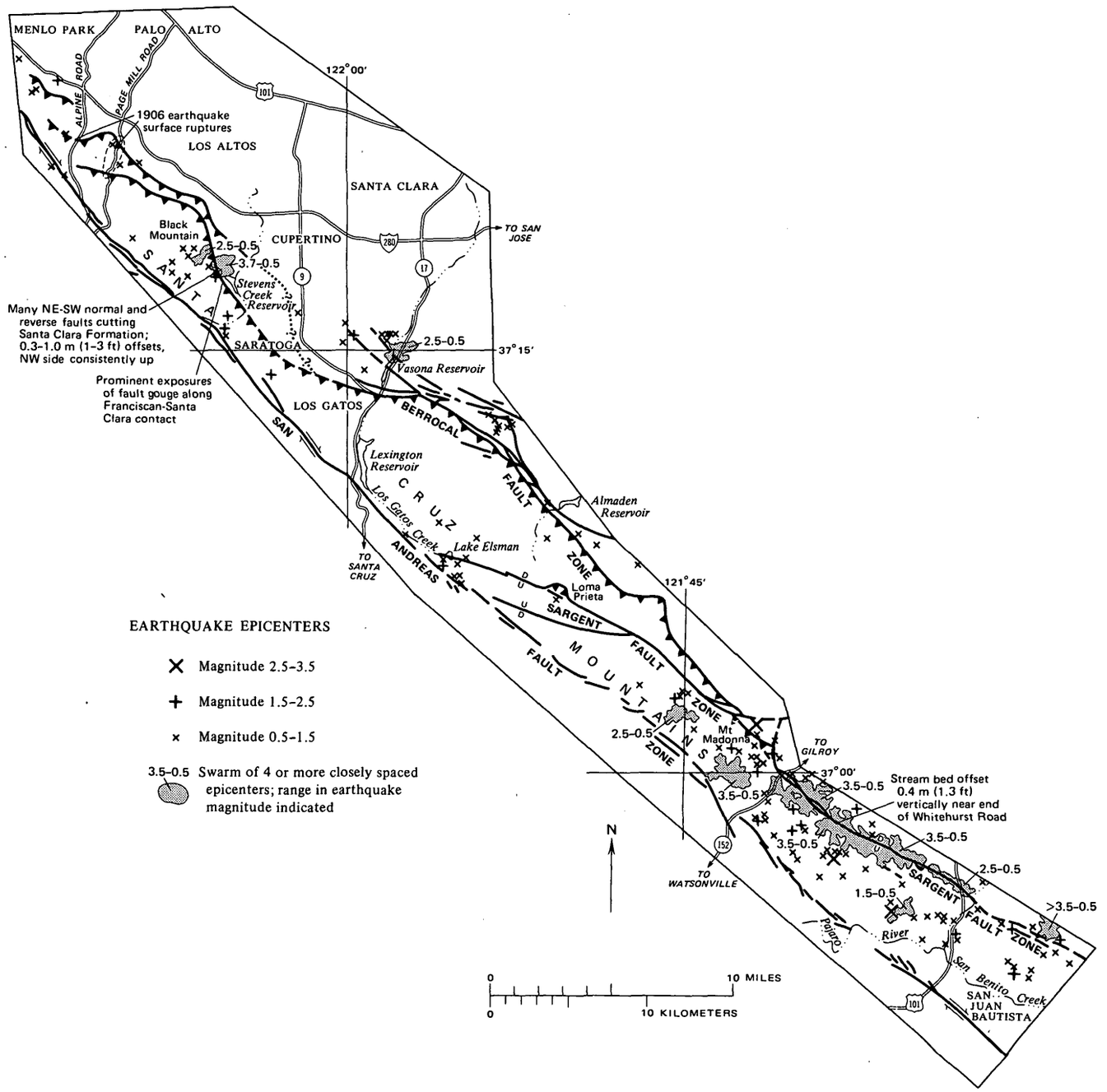

Figure 3.—Epicenters of earthquakes and evidence of offsets along the Sargent-Berrocal fault zone from 1969 to 1971 (compiled from Lee, 1972). Notes along the fault traces indicate areas where evidence of fault activity is especially clear.

of Stevens Creek, and they also appear to have been associated with the Sargent-Berrocal fault zone (fig. 3).

RELATION OF STRUCTURE AND SEISMICITY TO THE SAN ANDREAS STRESS SYSTEM

The Sargent-Berrocal and San Andreas fault zones are within the same regional stress system, so that regional strain accumulation in the system is relieved during earthquakes along either fault. However, the San Andreas fault zone is "locked" in the area northwest of San Juan Bautista (Healy and others, 1972; Farrington and Meyers, 1973), so that elastic strain accumulating in this area is released largely during earthquakes along the Sargent-Berrocal fault zone. In southern California, recent major earthquakes that occurred along thrust faults near Bakersfield (magnitude 7.7 earthquake along

the White Wolf fault, 1952) and San Fernando (magnitude 6.4 earthquake along the San Fernando fault, 1971) were thought by Allen (1972, p. 7) to have relieved elastic strain adjacent to locked segments of the San Andreas fault zone. The occurrence of these active thrust faults in southern California adjacent to locked segments of the San Andreas fault is insufficient grounds for concluding that a major earthquake will occur along the Sargent-Berrocal fault zone, but it does indicate that major earthquakes can occur along faults that have similar geometric relationships to locked segments of the San Andreas fault.

Although earthquakes along the Sargent-Berrocal fault zone occur in response to the present San Andreas stress system, the orientation of the fault zone trace appears unrelated to this stress pattern. This is apparent from Mohr's principles of brittle failure (Allen, 1957), according to which the Sargent-Berrocal fault zone must be oriented perpendicular to the maximum principal stress for thrusting to occur, and the San Andreas fault must be oriented oblique to the maximum principal stress for strike slip to occur. When these requirements are applied to the known surface traces of the Sargent-Berrocal and San Andreas fault zones, the inferred orientations of maximum principal stress for the two fault zones are not equivalent (fig. 4). These differences may be accounted for by the fact that the Sargent-Berrocal fault zone is at least in part alined with zones of weakness that formed prior to the San Andreas stress system. The basement rocks in this area consist of the late Mesozoic Franciscan assemblage, which is thought to have been complexly deformed and thrust beneath coeval strata of the Great Valley sequence before the San Andreas fault formed (Bailey and others, 1970; Atwater, 1970). The Sargent-Berrocal fault zone is alined along its course with this older thrust contact between Franciscan and non-Franciscan Mesozoic rocks, and with shear zones that also predate the San Andreas fault zone, suggesting that renewed movement along these older zones of weakness has had considerable influence on the present orientation of the Sargent-Berrocal fault zone.

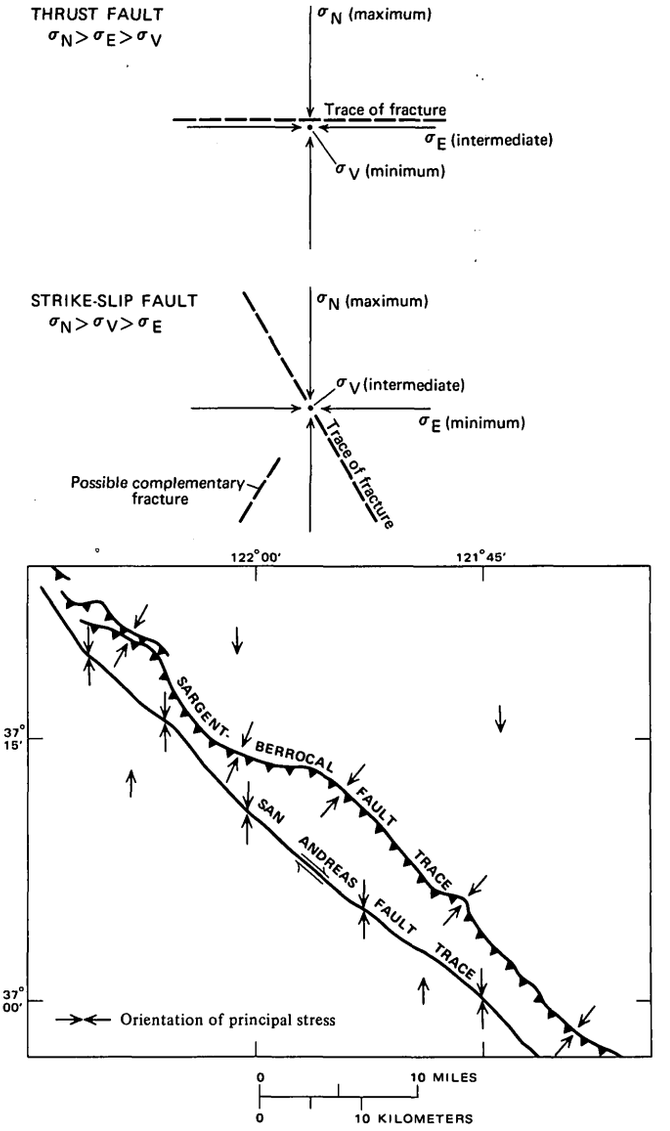

Figure 4.—Hypothetical relations between principal stress axes in strike-slip and thrust fault systems (from Allen, 1957), and orientation of maximum principal stress in the area studied. The change in orientation of maximum principal stress across the San Andreas fault system near the Sargent-Berrocal fault zone may have been caused by failure along zones of deformation that formed in Franciscan basement rocks before the San Andreas fault system developed.

ENVIRONMENTAL IMPLICATIONS

At present, criteria for predicting the potential maximum magnitude of earthquakes along active faults are very limited (Wallace, 1970), but predictions have been attempted on the basis of fault-break length. The data of Bonilla and Buchanan (1970) suggest that slip along a fault break as long as the Sargent-Berrocal fault zone (58 mi or 94 km) could generate an earthquake greater than magnitude 7.0. However, this estimate is made without regard to present seismic activity, which presumably relieves some accumulated elastic strain and reduces the potential maximum magnitude. For example, seismic activity northwest of Highway 17 and southeast of Mount Madonna relieves elastic strain at least along those segments of the Sargent-Berrocal fault zone (fig. 3). On the other hand, low seismic activity along the fault zone between Highway 17 and Mount Madonna may indicate that elastic strain is presently accumulating in that area, although it is also possible that all strain is relieved in the areas of concentrated seismic activity.

In some areas along the Sargent-Berrocal fault zone, active landslides are as potentially hazardous as active faulting. Many of the landslides, such as those near Stevens Creek Reservoir, appear to be fault related, suggesting the probability of extensive slide damage along some populated segments of the fault zone in the event of a major earthquake.

CONCLUSION

Available evidence indicates that large-scale offset has occurred within the last one million years along the Sargent-Berrocal fault zone. Although current seismic activity is concentrated in areas northwest of Highway 17 and southeast of Mount Madonna, physiographic expression of the fault zone along the intervening segment suggests relatively recent fault activity, and there is no reason to believe that the locus of seismic activity cannot change with time.

REFERENCES CITED

Allen, C. R., 1957, San Andreas fault zone in San Gorgonio Pass, southern California: Geol. Soc. America Bull., v. 68, p. 315–350.

——1972, The San Fernando earthquake of February 9, 1971, and public policy: Special Subcommittee of the Joint Committee on Seismic Safety, California Legislature, p. 1–11.

Allen, J. E., 1946, Geology of the San Juan Bautista quadrangle, California: California Div. Mines and Geology Bull. 133, 111 p.

Atwater, Tanya, 1970, Implications of plate tectonics for the Cenozoic tectonic evolution of western North America: Geol. Soc. America Bull., v. 81, p. 3513–3536.

Bailey, E. H., Blake, M. C., Jr., and Jones, D. L., 1970, On-land Mesozoic oceanic crust in California Coast Ranges, *in* Geological Survey research 1970: U.S. Geol. Survey Prof. Paper 700-C, p. 70–81.

Bailey, E. H., and Everhart, D. L., 1964, Geology and quicksilver deposits of the New Almaden district, Santa Clara County, California: U.S. Geol. Survey Prof. Paper 360, 206 p.

Bolt, B. A., Lomnitz, C., and McEvilly, T. V., 1968, Seismological evidence on the tectonics of central and northern California and the Mendocino escarpment: Seismol. Soc. America Bull., v. 58, p. 1725–1767.

Bonilla, M. G., and Buchanan, J. M., 1970, Interim report on worldwide historic surface faulting: U.S. Geol. Survey open-file rept., 32 p.

Cummings, J. C., 1968, The Santa Clara Formation and possible post-Pliocene slip on the San Andreas fault in central California, *in* Dickinson, W. R., and Grantz, Arthur, eds., Proceedings of the conference on geologic problems of the San Andreas fault system: Stanford Univ. Pubs. Geol. Sci., v. 11, p. 191–207.

Dibblee, T. W., Jr., 1966, Geology of the Palo Alto quadrangle, Santa Clara and San Mateo counties, California: California Div. Mines and Geology map sheet 8, scale 1:62,500.

Farrington, R. L., and Meyers, C. W., 1973, A major bend in the San Andreas fault, central California—A possible mechanism for locking the fault: Geol. Soc. America Abs. with Programs v. 5, no. 1.

Fleck, R. J., 1967, Structural significance of the contact between Franciscan and Cenozoic rocks, southern San Francisco Peninsula, California: Stanford Univ., M.S. thesis.

Healy, J. H., Lee, W. H. K., Pakiser, L. C., Raleigh, C. B., and Wood, M. D., 1972, Prospects of earthquake prediction and control: Tectonophysics, v. 14, p. 319–332.

Lawson, A. C., ed., 1908, The California earthquake of April 18, 1906: Carnegie Inst. Washington Pub. 87, v. 1, 451 p.

Lee, W. H. K., 1972, Seismicity map of greater San Francisco Bay Area, California, 1969–1971: U.S. Geol. Survey open-file map, scale 1:250,000.

McLaughlin, R. J., 1971, Geologic map of the Sargent fault zone in the vicinity of Mount Madonna, Santa Clara County, California, U.S. Geol. Survey open-file map, scale 1:12,000.

McLaughlin, R. J., Simoni, T. R., Osbun, E. G., and Bauer, P. G., 1971, Preliminary geologic map of the Loma Prieta-Mount Madonna area, Santa Clara and Santa Cruz Counties, California: U.S. Geol. Survey open-file map, scale 1:24,000.

Wallace, R. E., 1970, Earthquake recurrence intervals on the San Andreas fault: Geol. Soc. America Bull., v. 81, p. 2875–2890.

Jour. Research U.S. Geol. Survey
Vol. 2, No. 5, Sept.-Oct. 1974, p. 599—608

STRATIGRAPHY, STRUCTURE, AND GEOLOGIC HISTORY OF THE LUNAR LAKE CALDERA OF NORTHERN NYE COUNTY, NEVADA

By E. B. EKREN, W. D. QUINLIVAN, R. P. SNYDER; and F. J. KLEINHAMPL;
Denver, Colo.; Menlo Park, Calif.

Prepared in cooperation with the U.S. Atomic Energy Commission

Abstract.—The Lunar Lake caldera is in northern Nye County, Nev., about 70 mi (110 km) east-northeast of Tonopah. It is the youngest caldera in the central Nevada multiple-caldron complex and the source of the tuff of Lunar Cuesta, a multiple-flow simple cooling unit of quartz latitic welded tuff that is about 25 m.y. old. The tuff was distributed over an area of nearly 3,000 mi² (7,770 km²) and has a volume of approximately 90 mi³(375 km³). The Lunar Lake caldera is the site of the Lunar Crater basalt field which contains basalts of Pleistocene and probably Holocene age. These basalts were fed from northeast-trending fissures that had much earlier served as vents for ash-flow tuffs and lavas, possibly including the tuff of Lunar Cuesta.

U.S. Geological Survey investigations in central Nevada on behalf of the U.S. Atomic Energy Commission have led to the recognition of a multiple-caldron complex (U.S. Geological Survey, 1970, p. A39–A40). The boundaries of this caldron complex have been delineated by a combination of geological and geophysical (gravity, aeromagnetic, reflection seismograph) techniques and information from several deep drill holes. Ash-flow tuffs that can reasonably be inferred to have been extruded from the caldron complex include the Windous Butte Formation (Cook, 1965), which is the most widespread and possibly the oldest (30.7 m.y., according to Grommé and others, 1972), and the tuff of Lunar Cuesta, which is about 25 m.y. old and one of the youngest. This report is concerned primarily with the tuff of Lunar Cuesta, whose extrusion resulted in the formation of the present-day topographically expressed Lunar Lake caldera. Rock units that are closely related to the tuff of Lunar Cuesta in time and space are also discussed.

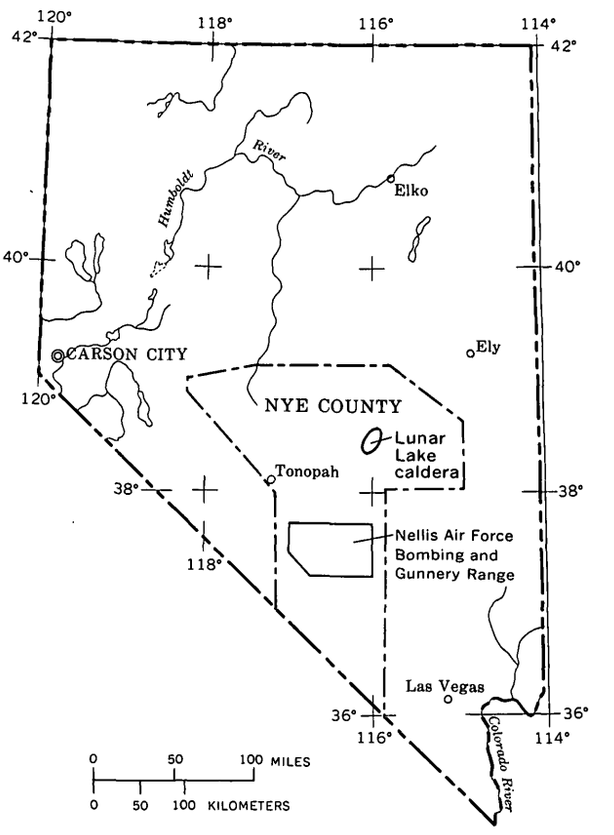

Figure 1.—Map of Nevada showing location of Lunar Lake caldera.

GEOLOGIC SETTING

The Lunar Lake caldera (fig. 1) is in northern Nye County, Nev., approximately 70 mi (110 km) east-northeast of Tonopah. It lies in the southeastern part of the central Nevada multiple-caldron complex (fig. 2), within which ash-flow tuffs and genetically related lavas probably average at least 7,000 ft (2,130 m) in thickness. Drill hole HTH-3, for example, in the central part of the complex (fig. 2) collared in the tuff of Williams Ridge and Morey Peak (Ekren, Hinrichs, and others, 1974) and bottomed in the same unit at a depth of 6,000 ft (1,830 m). We have inferred (U.S. Geological Survey, 1970, p. A39–A40) that this tuff is genetically related to the Windous Butte Formation, and recent paleomagnetic studies suggest that it may be coextensive with the upper part of the Windous Butte.

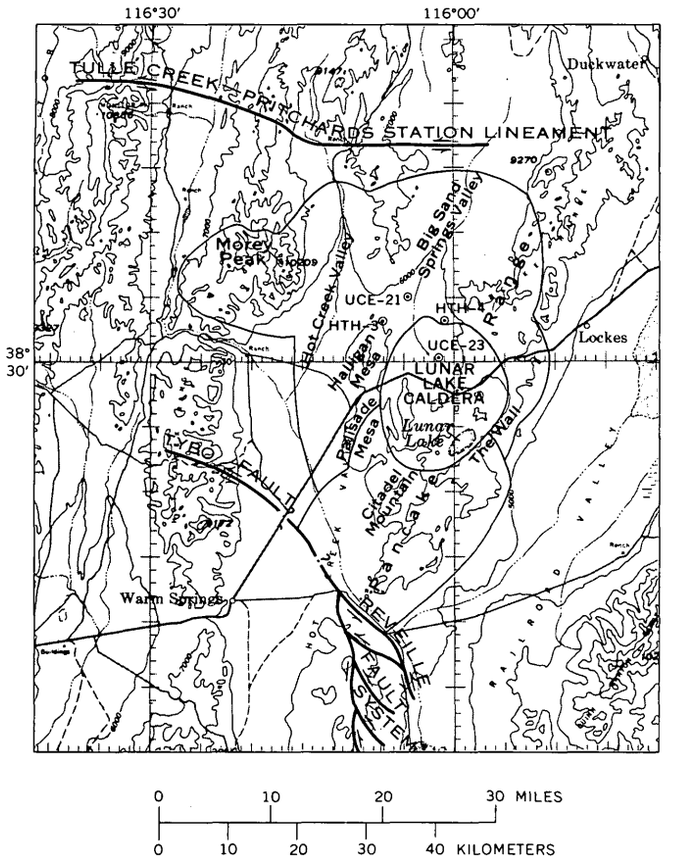

Figure 2.—Map showing location of Lunar Lake caldera with respect to the central Nevada caldron complex, the Tybo and Reveille strike-slip faults, and the Tulle Creek-Pritchards Station lineament, ⊙, Drill hole. Base from U.S. Coast and Geodetic Survey Reno Sectional Aeronautical Chart, 1:500,000, 1958–65.

Except for the strata exposed in the southern Pancake Range in and adjacent to the Lunar Lake caldera, all rocks in the area of the multiple-caldron complex are intensely faulted and fractured, and every drill hole within the complex (see geologic map of the Moores Station quadrangle, by Ekren, Hinrichs, and others, 1974) penetrated highly fractured and faulted rocks. The complex is bounded on the north by the east-trending Tulle Creek–Pritchards Station aeromagnetic lineament along which some left-lateral strike-slip movement has been inferred by Ekren, Bath, Dixon, Healey, and Quinlivan (1974). The complex is inferred to have been cut on the south and southwest by the northwest-trending left-lateral Tybo and Reveille strike-slip faults (Quinlivan and Rogers, 1974; Ekren, Rogers, and Dixon, 1974).

The Lunar Lake caldera is the site of the Lunar Crater basalt field. According to Scott and Trask (1971) the basaltic rocks include subalkaline, alkaline, and basanitoid types and contain a variety of xenoliths, some of which are inferred to have been derived from the upper mantle. The basalt lavas and pyroclastic ejecta were vented from a series of northeast-trending fissures (fig. 3). Chains of cinder cones that overlie the fissure zones are confined to the larger caldron complex but breach the Lunar Lake caldera on the northeast and southwest sides. The northeast-trending fissure zones were also the vents for several of the pre-basalt volcanic units, possibly including the tuff of Lunar Cuesta.

STRATIGRAPHY

The Tertiary volcanic units of the Lunar Lake caldera area (fig. 3) have been described in detail on the geologic maps of the Lunar Crater quadrangle (Snyder and others, 1972) and The Wall quadrangle (Ekren, Hinrichs, and Dixon, 1973). All units will be very briefly described herein. With the exception of the Shingle Pass Tuff whose source is inferred to have been outside the central Nevada caldron complex (Sargent and Houser, 1970), the units are typically calc-alkaline and are petrographically and chemically extremely similar.

Rocks older than the tuff of Lunar Cuesta

Rocks older than the tuff of Lunar Cuesta form the layer-cake stratigraphy of Palisade and Halligan Mesas (fig. 3), and the beautiful stratiform exposures of these rocks are primarily responsible for the name "Pancake Range." They include at the base of the exposure the tuff of Williams Ridge and Morey Peak, which consists of two lithologically identical cooling units in drill hole HTH-3 and in the vicinity of Black Rock Summit (figs. 3, 5). Both are multiple-flow compound cooling units of phenocryst-rich quartz latite (table 1, samples 12, 13). This tuff apparently underlies much of the central Nevada caldron complex (fig. 2), where it has great thickness, and is inferred to have been erupted concurrently with caldera subsidence after the main extrusions of the Windous Butte Formation (table 1, samples 14, 15) had ceased.

The tuff of Williams Ridge and Morey Peak is overlain on Halligan and Palisade Mesas (fig. 3) by the tuff of Halligan Mesa and in the vicinity of Black Rock Summit by the tuff of Black Rock Summit. The tuff of Halligan Mesa is 500–600 ft (150–180 m) thick; it is a multiple-flow compound cooling unit of moderately phenocryst-rich rhyolite which is characterized by a high percentage of quartz that is amethyst to dark smoky, bipyramidal in habit, and as much as 5 mm in diameter (table 1, sample 10). The unit is nearly completely free of lithic fragments. The tuff of Black Rock Summit, on the other hand, contains only 12–25 percent phenocrysts of plagioclase, biotite, and pseudomorphs after hornblende and pyroxene. Despite its basic suite of phenocrysts the tuff is rhyolitic in composition (table 1, sample 11). In exposures south of U.S. Highway 6 the tuff of Black Rock Summit is conspicuously flow layered and laminated. The laminar flowage structures are so well developed that the rock is unrecognizable as a tuff except in the basal 50–100 ft (15–30 m). The tuff at the top of the exposures has ramp structures similar in all respects to

structures at the top of lava flows. The tuff is overlain without an obvious cooling break by flow breccia and lava having the same phenocryst mineralogy as the tuff. These features strongly suggest extrusion of both lava and tuff from the general vicinity of Black Rock Summit, and it is inferred that the laminar flowage structures developed as a result of faulting that probably occurred concurrently with tuff eruption. This inference is made because the tuff of Black Rock Summit does not seem to be the type of tuff that would flow under stable conditions. The tuff is chemically unlike ash-flow tuffs that flow on very gentle slopes under small static load conditions, such as the Grouse Canyon Member of Belted Range Tuff in southern Nevada (Hoover, 1964), the tuff of Wagontire Mountain in Oregon (Walker and Swanson, 1968), and the Precambrian tuffs of southeastern Missouri (Anderson, 1970). All these tuffs are characterized by low Al_2O_3 and by high Na_2O and total-iron contents, unlike the tuff of Black Rock Summit (table 1, sample 11).

Overlying the tuff of Halligan Mesa is the tuff of Palisade Mesa, a multiple-flow compound cooling unit of phenocryst-rich rhyolite and quartz latite (table 1, sample 9). This unit is conspicuously columnar jointed where it is 400–500 ft (122–152 m) thick on Palisade Mesa and it is overlain by the Monotony Tuff (Ekren and others, 1971). The tuff of Williams Ridge and Morey Peak and the tuffs of Halligan and Palisade Mesas appear to have been erupted in rapid succession without long erosional intervals between eruptions; at least, we know of no unconformities or pronounced disconformities between these units, all of which are thought to be genetically related. The Monotony Tuff (Ekren and others, 1971), in contrast, has a pronounced angular unconformity in places at its base, and locally it is separated from older units by coarse gravels. The Monotony, however, on the basis of similarity with older and younger units (table 1, sample 8) and its areal distribution, is inferred to have its source in the central Nevada multiple-caldron complex, and its caldera, as will be discussed later in this report, is overlapped and truncated by the Lunar Lake caldera.

The tuff of Big Round Valley (Quinlivan and others, 1974) crops out over several square miles north of Black Rock Summit and northeast of the Lunar Lake caldera. The tuff consists of two cogenetic multiple-flow compound cooling units that have an aggregate thickness of 700 ft (210 m), both of which resemble the tuffs of Halligan and Palisade Mesas in composition and phenocryst mineralogy. The tuff of Big Round Valley is not believed correlative with them, however, as it is nearly everywhere separated from the tuff of Williams Ridge and Morey Peak by the tuff of Black Rock Summit, which was faulted before emplacement of the tuff of Big Round Valley and is overlain conformably by the Monotony Tuff. An eruptive center for the tuff of Big Round Valley has not been identified.

Rocks younger than the tuff of Lunar Cuesta

Rocks younger than the tuff of Lunar Cuesta from oldest to youngest are the rhyolite of Big Sand Springs Valley, the tuff of Buckskin Point, quartz latite and andesite lavas, tuff of Buckwheat Rim, tuff of Black Beauty Mesa, and a tuff referred to informally as "granite-weathering tuff." With the exception of the last named, all units were extruded from the Lunar Lake area, but these extrusions did not give rise to calderas. All but the rhyolite lavas are thickest in the vicinity of Citadel Mountain, and they are inferred to have been extruded from a southwestward extension of the same northeast-trending faults that later served as conduits for the rising basalts. The rhyolite lavas (rhyolite of Big Sand Springs Valley, fig. 3) were erupted from multiple vents in caldron ring-fracture zones along the southeastern and northern sides of the caldera. At localities A and B (fig. 3) the rhyolite filled two sharp scallops that formed during collapse of the caldera. The rhyolite in these scallops obviously was erupted very shortly after the tuff of Lunar Cuesta was extruded, as indicated by the preservation of the vapor-phase top of the tuff of Lunar Cuesta in these areas. Along the northern flank, however, the rhyolite lavas rest on older strata. Either this northern area underwent extremely rapid erosion after the eruption of the tuff of Lunar Cuesta or the tuff was never deposited there because of high paleotopography. The rhyolite is nearly aphyric and contains no more than 4 percent tiny phenocrysts of quartz, feldspar, and biotite (table 1, sample 1).

South of the Lunar Lake caldera, the tuff of Lunar Cuesta is overlain by the tuff of Buckskin Point, a multiple-flow compound cooling unit as much as 250 ft (75 m) thick that consists of phenocryst-poor dark-gray rhyodacite (table 1, sample 4) at the base and phenocryst-rich light-gray quartz latite at the top. On the south flank of Citadel Mountain the tuff of Buckskin Point is overlain, without a cooling break, by quartz latitic vent breccia that grades upward into lithic-free, coarse-grained, phenocryst-rich quartz latite lava (fig. 3). The tuff of Buckskin Point is magnetically reversed.

The tuff of Buckskin Point and the local quartz latite lava are overlain by andesite lavas and flow breccias that are dark brownish-gray to black and contain 8–30 percent phenocrysts of plagioclase and clinopyroxene and orthopyroxene (table 1, sample 3). These lavas are 1,200 ft (366 m) thick on Citadel Mountain, and, like the tuffs, they thin abruptly to the northwest and southeast. In the vicinity of Buckskin Point (fig. 3), lavas and flow breccias cropping out between the quartz latite and andesite are dacitic and rhyodacitic in composition, indicative of a gradual change in composition from quartz latite to andesite as lava eruptions proceeded.

The andesite lavas are overlain by the tuff of Buckwheat Rim, a multiple-flow compound cooling unit (possibly two

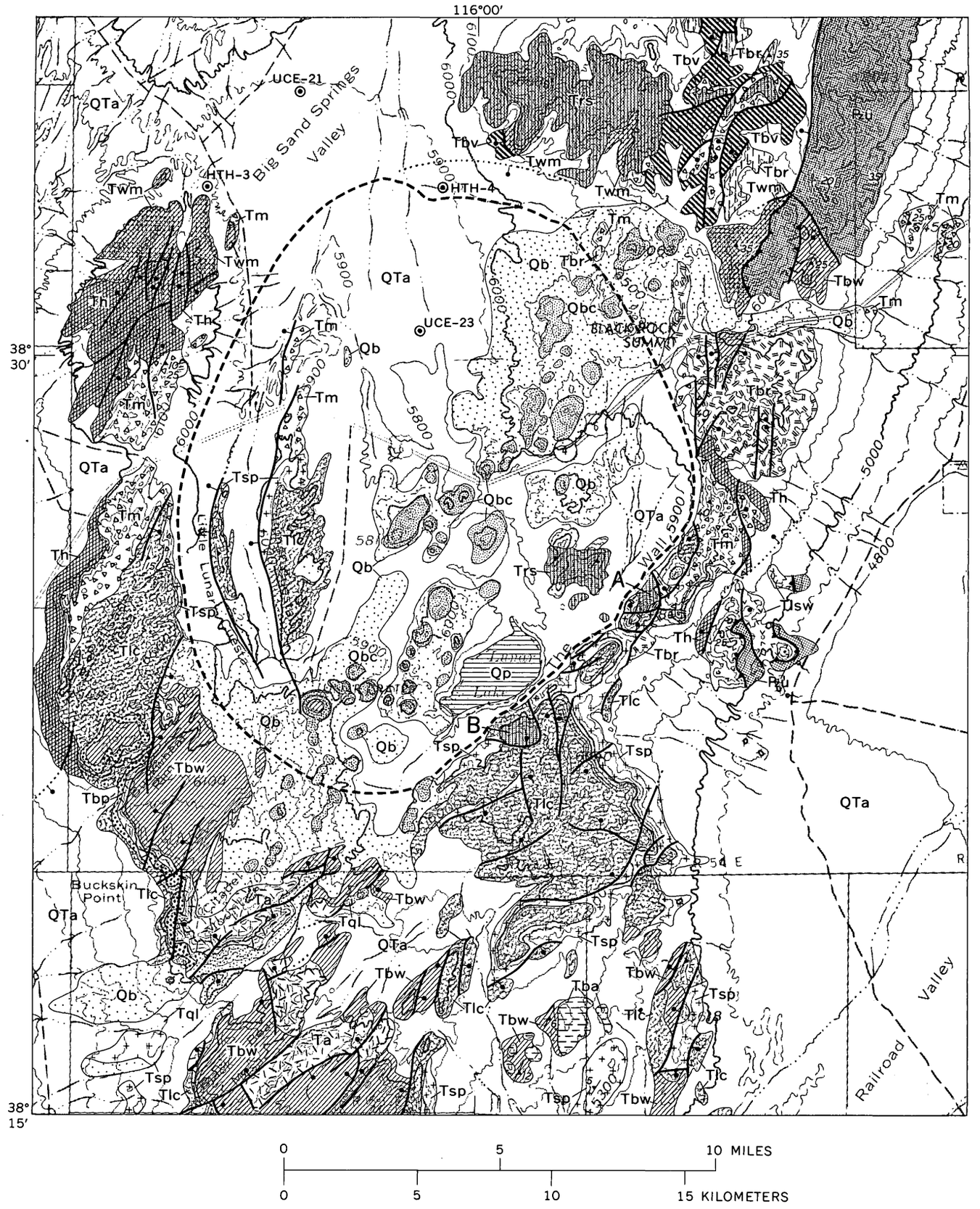

Figure 3.—Geologic map of the Lunar Lake area. Base from U.S. Geological Survey quadrangle maps, 1:250,000 (Tonopah, 1956–62, and Lund, 1956–70).

CORRELATION OF MAP UNITS

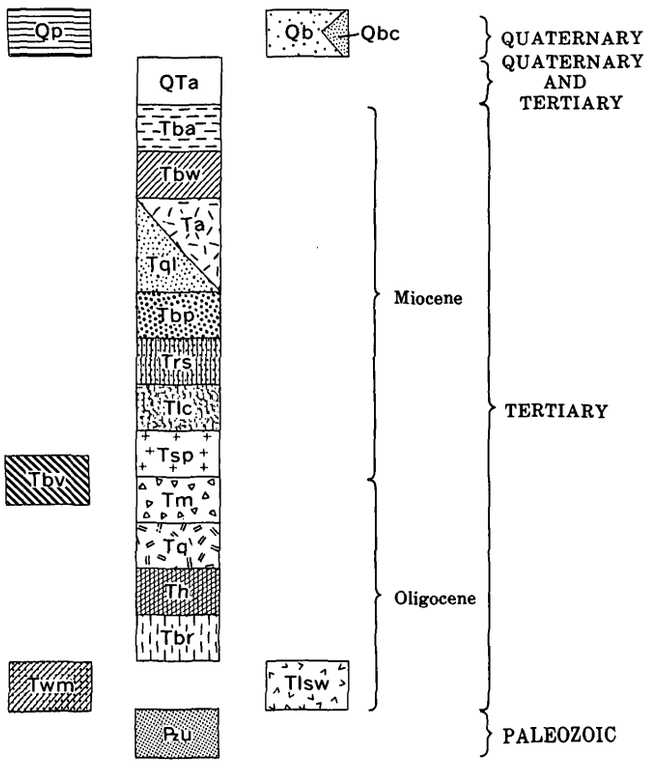

LIST OF MAP UNITS

Qp — Playa deposits (Quaternary)

Basalt (Quaternary)

Qb — Lava flows

Qbc — Cinder cones

QTa — Alluvium and colluvium (Quaternary and Tertiary)

Tba — Basaltic andesite (Miocene)

Tbw — "Granite-weathering tuff," tuff of Black Beauty Mesa, and tuff of Buckwheat Rim (Miocene)

Intermediate lavas (Miocene)

Ta — Andesite

Tql — Quartz latite

Tbp — Tuff of Buckskin Point (Miocene)

Trs — Rhyolite of Big Sand Springs Valley (Miocene)

Tlc — Tuff of Lunar Cuesta (Miocene)

Tsp — Shingle Pass Tuff (Miocene)

Tm — Monotony Tuff (Oligocene)

Tbv — Tuff of Big Round Valley (Miocene and Oligocene) —Age relations uncertain

Tq — Quartz latite lava (Oligocene)

Th — Tuffs of Palisade and Halligan Mesas (Oligocene)

Tbr — Tuff of Black Rock Summit (Oligocene)

Tlsw — Landslipped welded tuff (Oligocene)

Twm — Tuff of Williams Ridge and Morey Peak (Oligocene)

Pzu — Paleozoic rocks

Contact

Fault—Dotted where concealed. Bar and ball on downthrown side

Gravity slide fault—Sawteeth on upper plate

20 — Strike and dip of beds

20 — Strike and dip of compaction foliation

Buried boundary of Lunar Lake caldera

UCE-23 — Drill hole

cooling units) as much as 500 ft (150 m) thick that consists of cliff-forming, moderately welded, mafic-poor rhyolite at the base (one-third of unit) and slope-forming, partially welded mafic-rich quartz latite and rhyodacite (table 1, sample 2) at the top (two-thirds of unit). The tuff of Buckwheat Rim is magnetically reversed. On the southwest flank of Citadel Mountain and on Black Beauty Mesa the tuff of Buckwheat Rim is overlain, without an obvious cooling break, by stratified quartz latitic vent breccia having the same phenocryst mineralogy as the underlying welded tuff.

On Black Beauty Mesa (fig. 3) and on local areas to the south and east, the tuff of Buckwheat Rim is overlain by two thin simple cooling units of rhyodacitic densely welded tuff called the tuff of Black Beauty Mesa. These units are indistinguishable in outcrop and in thin section from the basal rhyodacitic tuff of Buckskin Point, but the tuff of Black Beauty Mesa is magnetically normal.

The "granite-weathering tuff" disconformably overlies the tuff of Black Beauty Mesa and other units in the Lunar Lake area. It is quartz-rich rhyolite and everywhere is characterized by chatoyant alkali feldspar. It is very similar to the tuff of White Blotch Spring in the northern Nellis Air Force Base Bombing and Gunnery Range (Ekren and others, 1971) and we presume that it was vented from a center in or near the bombing and gunnery range.

The tuff of Lunar Cuesta

The tuff of Lunar Cuesta is a multiple-flow simple cooling unit of quartz latite; it is typically densely welded, devitrified,

Table 1.—*Chemical analyses, in percent, of selected volcanic rocks in and around the Lunar Lake caldera*

[Values for sample 11, for SiO_2 and Al_2O_3 by X-ray fluorescence, analyst, J. S. Wahlberg; total Fe, MgO, and CaO by atomic absorption, analyst Wayne Mountjoy; Na_2O and K_2O by flame photometer, analyst Wayne Mountjoy; TiO_2 by Tiron colorimetry, analyst Claude Huffman, Jr.; P_2O_5 obtained colorimetrically, analyst G. D. Shipley. Values for all other samples by rapid rock analysis; analysts S. D. Botts, P. L. D. Elmore, G. W. Chloe, J. Kelsey, H. Smith, Lowell Artis, and J. L. Glenn]

Sample	1	2	3	4	5	6	7	8	9	10	11	12	13	14	15
Laboratory No.	W178-668	W172-306	W172-302	W172-305	W178-672	W178-676	W178-678	W178-671	W172-139	W172-140	D159-546	W172-143	W172-145	W175-163	W175-164
Field No.	W-68-BE-18	RS-5E	RS-6	RS-5A	WPC-5	SPC-8	RC-9	RC-3	NPC-33	NPC-26	BE-281-66	NPC-2	NPC-15	70FB-83	70FB-84
SiO_2	75.0	65.2	50.00	65.5	69.8	72.2	69.2	68.0	73.2	74.7	75.1	64.6	71.4	77.6	67.8
Al_2O_3	12.9	15.7	17.70	14.4	14.3	12.8	15.3	15.3	13.9	12.2	13.5	15.4	14.1	12.5	15.2
Fe_2O_3	.70	3.9	7.80	3.2	1.6	1.1	1.7	3.2	1.1	.84	1.25	3.7	1.5	.72	1.5
FeO	.78	.60	2.50	2.0	.40	.48	.70	.50	.44	.24		.44	.28	.16	1.9
MgO	.17	1.1	4.00	1.1	.55	.48	1.0	1.1	.37	.37	.37	1.4	.54	.25	1.2
CaO	.82	4.0	8.80	3.3	2.0	2.6	3.1	3.7	1.6	1.6	1.44	3.7	2.0	1.3	3.3
Na_2O	3.5	2.6	2.50	3.2	2.9	3.1	3.2	3.0	3.3	3.0	2.88	2.4	2.8	2.9	2.6
K_2O	5.1	3.6	1.40	3.9	4.6	4.8	4.2	3.5	4.7	4.5	4.41	3.2	4.7	4.6	4.1
H_2O+	.49	.80	2.22	1.5	2.9	.43	1.0	1.2	.84	1.0	.....	1.3	1.3	.38	1.9
H_2O-	.19	1.2		.50	.88	.38	.78	1.0	.15	.36	.....	2.2	.84	.17	.22
TiO_2	.04	.62	1.90	.93	.20	.15	.26	.42	.20	.13	.21	.64	.27	.06	.55
P_2O_5	.....	.22	.69	.38	.08	.06	.10	.14	.08	.08	.19	.15	.08	.02	.13
MnO	.04	.04	.16	.12	.09	.06	.05	.10	.03	.04	.....	.03	.03	.00	.00
Co_2	.08	.22	.31	<.05	.02	.49	.08	.04	<.05	.28	.....	<.05	<.05	.00	.00
Total	99.81	99.80	99.80	100.03	100.32	99.13	100.07	101.20	99.96	99.34	99.35	99.16	99.84	100.66	100.40

1. Rhyolite of Big Sand Springs Valley at lat 38°27′ N., long 115°57′ W. 3.8 percent phenocrysts: quartz 30.9, alkali feldspar 49.1, plagioclase 18.2, biotite 1.8, hornblende tr.
2. Tuff of Buckwheat Rim at lat 38°19′ N., long 116°7 1/2′ W. 49.8 percent phenocrysts: quartz 16.8, alkali feldspar 0.7, plagioclase 49.9, biotite 6.8, opaque minerals 2.1.
3. Andesite lava at lat 38°19′ N., long 116°7 1/2′ W. 25.1 percent phenocrysts: plagioclase 75.7, biotite 1.8, opaque minerals 5.5, clinopyroxene 16.4, hornblende 0.5.
4. Tuff of Buckskin Point at lat 38°19′ N., long 116°7 1/2′ W. 13.5 percent phenocrysts: quartz 4.2, alkali feldspar 6.3, plagioclase 62.1, biotite 8.4, opaque minerals 1.1, hornblende 8.4, pyroxene 1.1, altered mafic minerals 2.1, holes in thin section 6.3.
5. Tuff of Lunar Cuesta at lat 38°23′ N., long 116°11′ W. Modes not counted for samples 5, 6, and 7. Modes of tuff of Lunar Cuesta sampled elsewhere in central Nevada give the following ranges or averages: 20–35 percent phenocrysts: quartz 12–20, alkali feldspar 7–15, plagioclase 45–75, biotite 10–15, hornblende 3, opaque minerals 2.
6. Tuff of Lunar Cuesta at lat 38°14′ N., long 116°3′ W.
7. Tuff of Lunar Cuesta at lat 38°27 1/2′ N., long 116°5′ W.
8. Monotony Tuff at lat 38°28′ N., long 116°5′ W. Mode count for several samples: 25–55 percent phenocrysts: quartz 10–22, alkali feldspar 5–12, plagioclase 46–63, biotite 10–22, hornblende tr–7, clinopyroxene 1–5, orthopyroxene tr, opaque minerals 1–2.
9. Tuff of Palisade Mesa at lat 38°29 1/2′ N., long 116°8′ W. 36.3 percent phenocrysts: quartz 31.4, alkali feldspar 28.1, plagioclase 32.6, biotite 5.1, opaque minerals 1.7, hornblende 1.1.
10. Tuff of Halligan Mesa at lat 38°31′ N., long 116°8′ W. 28.0 percent phenocrysts: quartz 21.1, alkali feldspar 26.5, plagioclase 41.2, biotite 8.0, opaque minerals 0.8, hornblende 2.1.
11. Tuff of Black Rock Summit at lat 38°29 1/2′ N., long 115°54′ W. Mode count for several samples: 12–25 percent phenocrysts: quartz 8–25, alkali feldspar 0–3, plagioclase 65–70, biotite 7–16, hornblende 0–3, clinopyroxene tr., opaque minerals tr–3.
12. Tuff of Williams Ridge and Mount Grey Peak at lat 38°33′ N., long 116°8′ W. 51.4 percent phenocrysts: quartz 27.3, alkali feldspar 1.5, plagioclase 53.4, biotite 6.5, opaque minerals 0.7, hornblende 2.4, altered mafic minerals 7.8, holes in thin section 0.4.
13. Tuff of Williams Ridge and Mount Grey Peak at lat 38°32′ N., long 116°8′ W. 26.2 percent phenocrysts: quartz 27.9, alkali feldspar 21.8, plagioclase 40.1, biotite 4.7, opaque minerals 0.3, hornblende 3.3, holes within section 1.9.
14. Windous Butte Formation (tuff) at lat 38°45′ N., long 116°20′ W. 38.0 percent phenocrysts: quartz 40.8, alkali feldspar 38.9, plagioclase 19.0, biotite 1.1, opaque minerals 1.3.
15. Windous Butte Formation (tuff) at lat 38°45′ N., long 116° 20′ W. 29.0 percent phenocrysts: quartz 19.1, plagioclase 52.9, biotite 15.2, hornblende 12.2, orthopyroxene 0.7.

and bluish gray, and weathers to brown and buff. In most localities it contains abundant red lithic fragments of Shingle Pass Tuff in its nonwelded to partially welded basal part. It contains 20–35 percent phenocrysts of which quartz constitutes 12–20 percent, alkali feldspar 7–15 percent, plagioclase 45–75 percent, biotite 10–15 percent, hornblende 3 percent, and opaques 2 percent (table 1, samples 5–7). The tuff is everywhere magnetically reversed.

The conclusion that the tuff of Lunar Cuesta was erupted from the Lunar Lake area and that its eruption gave rise to the Lunar Lake caldera is based on three lines of evidence: (1) The thickest known sections of the tuff are adjacent to the Lunar Lake caldera, (2) rhyolite of Big Sand Springs Valley, which is chemically similar to the tuff (fig. 4), rest directly on the tuff of Lunar Cuesta in two sharp scallops (locs. A and B, fig. 3) along the southeastern wall (these rhyolite-scallop-tuff relationships would be extremely unlikely if the caldera formed as a result of either earlier or later tuff eruptions), and (3) the Lunar Lake caldera lies near the center of the area of distribution of the tuff (fig. 5).

The "inferred original" distribution shown in figure 5 encompasses all areas where the tuff is preserved in situ or where its former presence is indicated by erosional rubble. The inferred distribution includes areas that have been either deeply eroded or deeply buried but can reasonably be inferred to have been covered by the tuff. For example, the extension of the tuff eastward into Railroad Valley is recognized on the basis of the large thickness preserved along the west flank of the valley. The extension south of the southern Pancake Range beyond the southernmost outcrops is recognized on the basis of evidence there of extensive removal by erosion prior to the eruption of younger tuffs. Such removal is indicated along the east flank of the Pancake Range in the Reveille quadrangle (Ekren, Rogers, and Dixon,

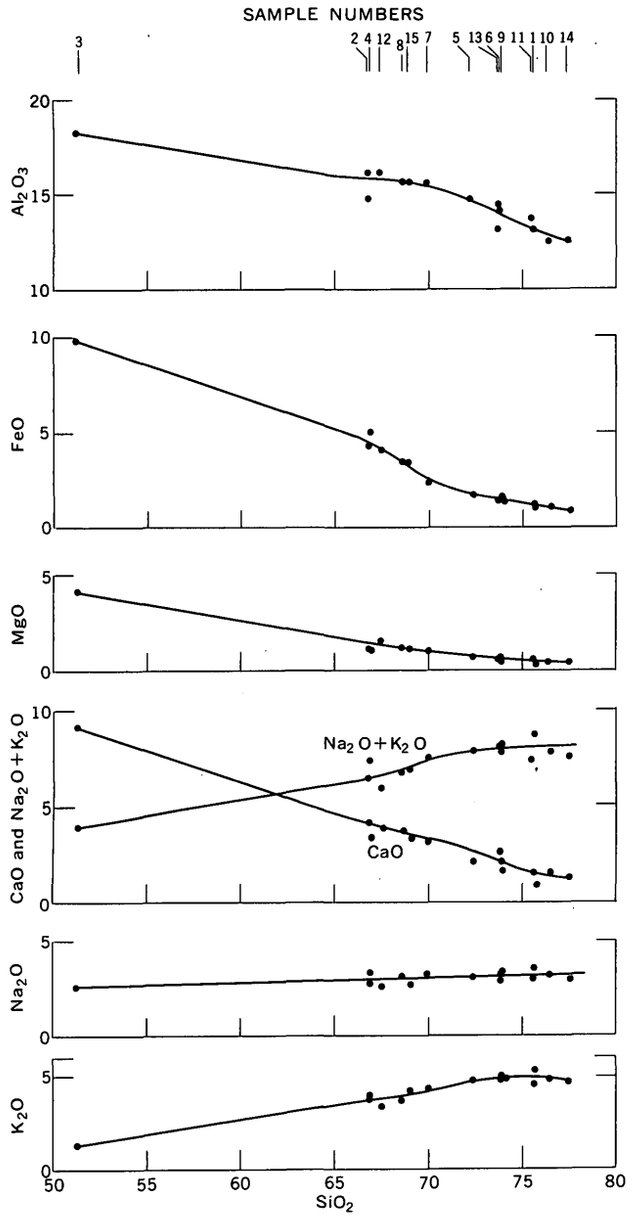

Figure 4.—Variation diagrams for samples listed in table 1. All analyses in weight percent recalculated (minus H_2O and CO_2) to 100 percent.

1974) where the tuff thins from 200+ ft (61+ m) to 0 in a distance of less than 3 mi (4.8 km), and there is no indication of a "lap out" against old topography nor a decrease in the degree of welding. If we use the inferred boundaries shown in figure 5 and assume an average thickness of 200 ft (61 m), the tuff had a volume of approximately 90 mi^3 (370 km^3) and covered nearly 3,000 mi^2 (7,770 km^2).

The tuff of Lunar Cuesta is about 25 m.y. old, on the basis of K-Ar analyses of the tuff itself and of samples from overlying and underlying strata. Samples of tuff of Lunar Cuesta exposed on the wall east of Lunar Lake were analyzed by R. F. Marvin, who reported (written commun., 1970) dates of 25.5±0.8 m.y. on biotite and 22.5±0.7 m.y. on sanidine. The Shingle Pass Tuff, exposed beneath the tuff of Lunar Cuesta on Palisade Mesa, also yielded dates of 25.5±0.8 m.y. on biotite and 22.5±0.7 m.y. on sanidine. The rhyolite of Big Sand Springs Valley above the tuff of Lunar Cuesta yielded a date of 25.8±3 m.y. on a whole-rock sample; and the tuff of Buckskin Point gave a date of 25.4±1.3 m.y. on biotite.

Chemical variations

Chemical analyses of the principal rocks in the Lunar Lake caldera and the central Nevada caldron complex are shown in table 1, and plots of major oxides against percentage of silica are shown in figure 4. These analyses indicate that no systematic chemical variations took place as eruptions proceeded, starting about 30.5 m.y. ago (approximate age of the Windous Butte) and ending about 25 m.y. ago (approximate age of the tuff of Buckskin Point). The youngest rocks are the most basic as well as the most silicic of the suite (fig. 4). The available analyses indicate that the Windous Butte shows more extreme chemical variations within a single cooling unit than any of the other principal units in the area (compare samples 14 and 15, table 1 and fig. 4). The major oxides of the contrasting lithologies in the Windous Butte, however, all plot neatly along the curves defined by the major oxides of the younger rocks (fig. 4). The Windous Butte is characterized by a mafic-poor rhyolitic base (sample 15) and a mafic-rich quartz latitic top (sample 14). This trend is, in fact, shown by most of the ash-flow tuff cooling units in the Lunar Lake area.

The alkali-lime index for the tuffs and lavas of the Lunar Lake area is approximately 62 (fig. 4). This index is well within the calc-alkalic field of Peacock (1931).

Noble (1972) indicated that most of the lower Miocene volcanic rocks of the Great Basin, particularly those 25–22 m.y. in age, closely resemble the highly differentiated rhyolites found in bimodal basalt-rhyolite provinces. The Shingle Pass Tuff, which separates the younger rocks associated with the Lunar Lake caldera from older rocks of the central Nevada caldron complex, was cited as an example of this type of volcanism. We concur in recognition of the distinctive features of the Shingle Pass Tuff, as well as of the Bates Mountain Tuff and New Pass Tuff, also cited by Noble as examples of "early Miocene silicic volcanic rocks that represent a new pulse of magmatism rather than a continuation of Oligocene calc-alkalic volcanism * * *." Of interest is the close bracketing of the Shingle Pass Tuff in the report area by calc-alkalic volcanism that displays no obvious changes in chemistry or mineralogy.

STRUCTURE AND GEOLOGIC HISTORY OF THE LUNAR LAKE CALDERA

The Lunar Lake caldera is expressed as a partially enclosed topographic basin bounded on the east by an arcuate ridge, The Wall (fig. 2), on the west by Palisade and Halligan Mesas,

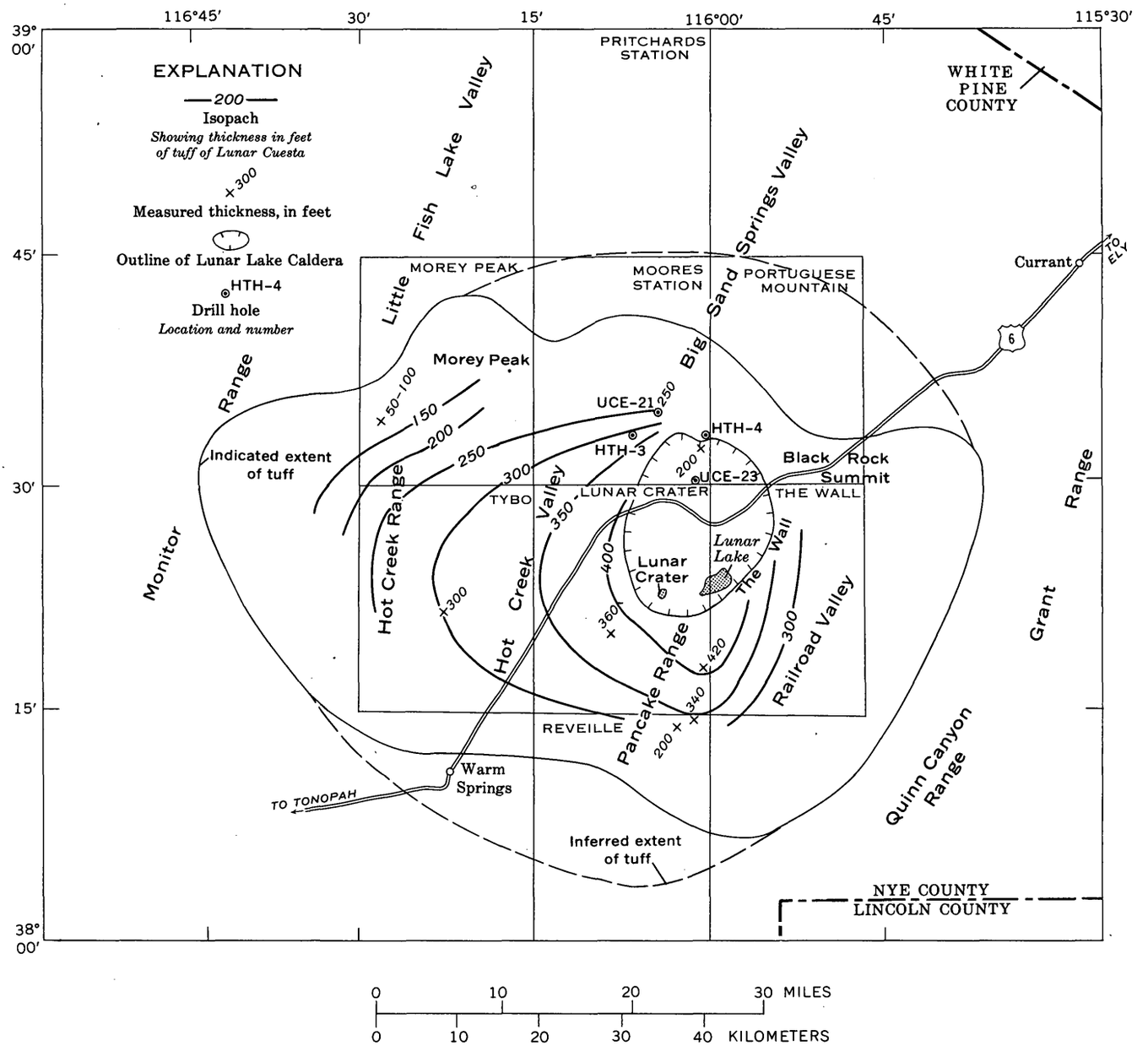

Figure 5.—Sketch map showing quadrangles mapped in central Nevada and showing indicated and inferred original extent of tuff of Lunar Cuesta.

and on the south by Citadel Mountain. On the north side the basin is contiguous with Big Sand Springs Valley. The caldera is best observed from high points along The Wall where a view to the west gives the impression of peering into an enormous kettle filled with bubbling (numerous extinct cinder cones) viscous black liquid (basalt lavas). The boundary of the caldera is well defined only on the eastern and southeastern sides along The Wall. The location of the northern boundary is based on drill-hole and reflection seismic data. The northern boundary was placed south of drill hole HTH-4 (fig. 3) because this drill hole did not penetrate either the tuff of Lunar Cuesta or the Monotony Tuff, which was nearly 1,000 ft (305 m) thick in drill hole UCE-23. Drill hole HTH-4, however, cut several fault zones; drilling operations were extremely difficult and there was a trememdous loss of drilling fluid. Only two cores were obtained, one from 1,166 ft (355 m) and the other from 6,030 ft (1,840 m). Lithologic correlations (Ekren, Hinrichs, and others, 1974) were made principally on the basis of cuttings and geophysical logs. The possibility exists, therefore, that both the tuff of Lunar Cuesta and the Monotony Tuff were faulted out in this drill hole, and it is problematic whether the caldera wall lies north or south of or, perhaps,

within the drill-hole location. The occurrence of rhyolite of Big Sand Springs Valley between depths of about 200 and 800 ft (60 and 240 m) indicates that a major fault, probably east-trending, lies between the drill hole and the large rhyolite mass exposed to the northeast (fig. 3). This fault, if it is east-trending as postulated in figure 3, could mark the main caldera boundary or a relatively minor secondary ring-fracture zone.

The presumed location of the caldera boundary between drill holes UCE-21 and UCE-23 is inferred from a reflection seismic survey run on a traverse line southeastward from UCE-21 toward UCE-23. The boundary was placed at a point on the traverse about 2.5 mi (4 km) southeast of UCE-21 at the southeast edge of a zone of no reflections, which was interpreted as a structural high between the Lunar Lake caldera and a deeper, older caldron—the "outer Hot Creek Valley caldron" (Ekren, Hinrichs, and others, 1974). The boundaries of this older caldron are not shown in figure 2.

There is no present-day indication of western and southwestern boundaries to the caldera. This could be due to an original lack of caldera boundary faults along the western half of the Lunar Lake depression. Initially, the western half of the "caldera" simply sagged toward the center of the structure. P. P. Orkild, who mapped part of the Lunar Lake area in 1966, suggested that this type of volcanic depression be termed a "trapdoor caldron" (written commun., 1972). On the other hand, the lack of a discernible boundary today may have resulted from basin-range faulting which effectively lowered the outer rim of the caldera (Palisade Mesa) and raised the interior (Little Lunar Cuesta). We favor the "trapdoor" interpretation. That a structural break of some kind exists in this area is clearly indicated by the marked contrast between the nearly flat-lying broad mesas west of Little Lunar Cuesta and the broad depression broken only by the subdued east-tilted cuestas and the abundant cinder cones east of Palisade Mesa. That this structural break may be arcuate in form is suggested by the curvilinear nature of the Little Lunar Cuesta fault block (fig. 3).

The caldera, as just defined, is semicircular in plan, measuring about 11 mi (18 km) east to west, and 13 mi (21 km) north to south. Owing to the effect of postcaldera basin-and-range faulting, the amount of vertical displacement is difficult to determine in the caldera. Drill hole UCE-23, for example, penetrated the tuff of Lunar Cuesta at a depth of 1,200 ft (365 m) and an elevation of 4,600 ft (1,400 m), which is nearly 2,000 ft (610 m) lower than the top of the tuff in the nearest outcrop outside the caldera. This 2,000 ft (610 m) of structural relief may be due partly to caldera displacement and partly to basin-and-range faulting, or it may constitute the structural relief remaining after the drill-hole area was relatively uplifted by basin-and-range faulting. The first possibility seems more plausible, however, and a minimum of about 1,000 ft (305 m) and a maximum of about 2,000 ft (610 m) of displacement for the central part of the Lunar Lake caldera probably are a reasonable estimate.

Drill hole UCE-23 cut a basalt flow intercalated in alluvium at a depth of 140–175 ft (43–53 m), continued in alluvium to a depth of about 1,100 ft (335 m); from 1,100 ft (335 m) to 1,200 ft (365 m) it cut 100 ft (30 m) of bedded tuff and debris; it penetrated intensely fractured (probably faulted) tuff of Lunar Cuesta between 1,200 and 1,240 ft (365 and 380 m). The total thickness of the tuff of Lunar Cuesta cut by the drill hole, determined from cuttings and geophysical logs, is 200–350 ft (61–105 m), which indicates that the tuff is no thicker in the caldera than outside; conceivably it is thinner. Eruption of the tuff of Lunar Cuesta, therefore, apparently was completed before caldera subsidence began. In this regard, the Lunar Lake caldera is similar to the Valles caldera of New Mexico where the last erupted tuff is no thicker inside the caldera than outside (Smith and Bailey, 1968), and it differs from the Timber Mountain caldera in southern Nevada (Byers and others, 1969) and many other calderas where subsidence and tuff eruptions occurred concurrently.

The relationship of the Lunar Lake caldera with older caldrons within the large multiple-caldron complex (fig. 2) indicates that it was the last caldera to form and, although nested within the central complex, its boundaries overlap and partly coincide with boundaries of older caldrons. The proximity of the buried northern wall to the wall of the "outer Hot Creek Valley caldron" (Ekren, Hinrichs, and others, 1974), as indicated by a reflection seismic survey, has been previously described. That an earlier caldron wall existed approximately at the present-day well-defined eastern wall of the Lunar Lake caldera is strongly suggested by the unconformable relationships of the Monotony Tuff where it rides up against a northeast-trending topographic high formed of pre-Monotony quartz latite lava (loc. A, fig. 3) and against the tuff of Black Rock Summit and the tuff of Palisade Mesa (figs. 3, 5) in exposures south of Black Rock Summit. This older wall could have formed during a period of subsidence related to the extrusion of the tuff of Palisade Mesa or the tuff of Halligan Mesa, or both. If this is so, the data from drill hole UCE-23 indicate that younger rocks, principally the voluminous Monotony Tuff, filled the caldera prior to the eruption of the tuff of Lunar Cuesta. The possibility also exists that the drill hole lies within the caldera which formed as a result of Monotony Tuff eruptions.

On Palisade Mesa, the northeast-trending fault that extends through the mesa (against which the Shingle Pass Tuff was deposited and over which the tuff of Lunar Cuesta was deposited) is inferred to be the western wall or boundary of the caldera that formed as a result of the extrusions of the widespread Monotony Tuff. This caldera is truncated by the Lunar Lake caldera in the vicinity of Lunar Cuesta, and its northern boundary is concealed within the Lunar Lake caldera. Farther south, in the Reveille quadrangle (Ekren, Rogers, and Dixon, 1974), the caldera is cut by a system of northwest-trending left-lateral faults, and the southwestern part of the caldera is strung out as a series of fault slices along splays of the left-lateral system (Ekren, Rogers, and Dixon, 1974).

CHRONOLOGY OF VOLCANIC EVENTS

1. Tuff eruptions and the development of a multiple-caldera complex started in central Nevada about 30–31 m.y. ago with the eruption of the Windous Butte Formation and related rocks.
2. For a period of 3–4 m.y. tuff eruptions continued and numerous calderas were formed within the caldron complex. About 25 m.y. ago the tuff of Lunar Cuesta was erupted from vents located in the southeastern part of the caldron complex. The eruption of this tuff, having a volume of about 90 mi^3 (375 km^3), resulted in the collapse of a semicircular area about 12 mi (19 km) in diameter and possibly 1,000–2,000 ft (305–610 m) deep—the herein-named Lunar Lake caldera.
3. Rhyolite lavas were erupted from the northern and southeastern ring-fracture zones of the Lunar Lake caldera.
4. The tuff of Buckskin Point, quartz latite and andesitic lavas, and the tuffs of Buckwheat Rim and Black Beauty Mesa were erupted from fissures in the vicinity of Citadel Mountain. These eruptions did not result in caldera development.
5. The caldera was broken by basin-and-range faults, and two fault blocks were uplifted relative to the remainder of the caldera to form Lunar and Little Lunar Cuestas.
6. In Quaternary time basalt lavas and pyroclastic debris were erupted from a northeast-trending fissure system that extends through the Lunar Lake caldera and coincides, in part, with the old fissure system that extends through the Citadel Mountain area.

REFERENCES CITED

Anderson, R. E., 1970, Ash-flow tuffs of Precambrian age in southeast Missouri: Missouri Div. Geol. Survey and Water Resources Rept. Inv. 46, 50 p.

Byers, F. M., Jr., Carr, W. J., and Orkild, P. P., 1969, Volcano-tectonic history of southwestern Nevada caldera complex, U.S.A. [abs.] *in* Symposium on volcanoes and their roots: Oxford, England, Internat. Assoc. Volcanology and Chemistry of the Earth's Interior, v. abs., p. 84–86.

Cook, E. F., 1965, Stratigraphy of Tertiary volcanic rocks in eastern Nevada: Nevada Bur. Mines Rept. 11, 61 p.

Ekren, E. B., Anderson, R. E., Rogers, C. L., and Noble, D. C., 1971, Geology of northern Nellis Air Force Base Bombing and Gunnery Range, Nye County, Nevada: U.S. Geol. Survey Prof. Paper 651, 91 p.

Ekren, E. B., Bath, G. D., Dixon, G. L., Healey, D. L. and Quinlivan, W. D., 1974, Tertiary history of Little Fish Lake Valley, Nye County, Nevada, and implications as to the origin of the Great Basin: U.S. Geol. Survey Jour. Research, v. 2, no. 1, p. 105–118.

Ekren, E. B., Hinrichs, E. N., and Dixon, G. L., 1973, Geologic map of The Wall quadrangle, Nye County, Nevada: U.S. Geol. Survey Misc. Geol. Inv. Map I-719, scale 1:48,000.

Ekren, E. B., Hinrichs, E. N., Quinlivan, W. D., and Hoover, D. L., 1974, Geologic map of the Moores Station quadrangle, Nye County, Nevada: U.S. Geol. Survey Misc. Geol. Inv. Map I-756, scale 1:48,000.

Ekren, E. B., Rogers, C. L., and Dixon, G. L., 1974, Geologic and Bouguer gravity map of the Reveille quadrangle, Nye County, Nevada: U.S. Geol. Survey Misc. Geol. Inv. Map I-806, scale 1:48,000. (In press.)

Grommé, C. S., McKee, E. H., and Blake, M. C., Jr., 1972, Paleomagnetic correlations and potassium-argon dating of middle Tertiary ash-flow sheets in the eastern Great Basin, Nevada and Utah: Geol. Soc. America Bull., v. 83, p. 1619–1638.

Hoover, D. L., 1964, Flow structures in a welded tuff, Nye County, Nevada [abs.], *in* Abstracts for 1963: Geol. Soc. America Spec. Paper 76, p. 83.

Noble, D. C., 1972, Some observations on the Cenozoic volcano-tectonic evolution of the Great Basin, western United States: Earth and Planetary Sci. Letters, v. 17, p. 142–150.

Peacock, M. A., 1931, Classification of igneous rock series: Jour. Geology, v. 39, no. 1, p. 54–67.

Quinlivan, W. D., and Rogers, C. L., 1974, Geologic map of the Tybo quadrangle, Nye County, Nevada: U.S. Geol. Survey Misc. Geol Inv. Map I-821, scale 1:48,000. (In press.)

Quinlivan, W. D., Rogers, C. L., and Dodge, H. W., Jr., 1974, Geologic map of the Portuguese Mountain quadrangle, Nye County, Nevada: U.S. Geol. Survey Misc. Geol. Inv. Map I-804, scale 1:48,000. (In press.)

Sargent, K. A., and Houser, F. N., 1970, The Shingle Pass Tuff of central Nevada: Geol. Soc. America Abs. with Programs (Cordilleran sec.), v. 2 no. 2, p. 140–141.

Scott, D. H., and Trask, N. J., 1971, Geology of the Lunar Crater volcanic field, Nye County, Nevada: U.S. Geol. Survey Prof. Paper 599-I, 22 p.

Smith, R. L., and Bailey, R. A., 1968, Resurgent caldrons, *in* Coats, R. R., Hay, R. L., and Anderson, C. A., eds., Studies in volcanology—A memoir in honor of Howel Williams: Geol. Soc. America Mem. 116, p. 613–662.

Snyder, R. P., Ekren, E. B., and Dixon, G. L., 1972, Geologic map of the Lunar Crater quadrangle, Nye County, Nevada: U.S. Geol. Survey Misc. Geol. Inv. Map I-700, scale 1:48,000.

U.S. Geological Survey, 1970, Geological Survey research 1970: U.S. Geol. Survey Prof. Paper 700-A, 426 p.

Walker, G. W., and Swanson, D. A., 1968, Laminar flowage in a Pliocene soda rhyolite ash-flow tuff, Lake and Harney Counties, Oregon, *in* Geological Survey research 1968: U.S. Geol. Survey Prof. Paper 600-B, p. B37–B47.

Jour. Research U.S. Geol. Survey
Vol. 2, No. 5, Sept.-Oct. 1974, p. 609-618

CORRELATION OF UPPERMOST PRECAMBRIAN AND LOWER CAMBRIAN STRATA FROM SOUTHERN TO EAST-CENTRAL NEVADA

By JOHN H. STEWART, Menlo Park, Calif.

Abstract.—Study of exposed uppermost Precambrian and Lower Cambrian strata in southern and east-central Nevada and intervening areas indicates that the Johnnie Formation of southern Nevada and the McCoy Creek Group (restricted) are correlative. In detail, the uppermost units of both sequences, the Rainstorm Member of the Johnnie Formation and the Osceola Argillite (and the equivalent unit G) of the McCoy Creek Group, are lithologically similar and also considered correlative. Both are characterized by pale-red or purplish-medium-gray siltstone with abundant bedding-surface markings, and both contain scarce to abundant amounts of evenly or lenticularly laminated limestone or silty limestone. Both units are lithologically unique in their respective areas of occurrence, and both are known to be widely distributed. Several thousand feet of dominantly detrital rocks occur above the Johnnie Formation in southern Nevada and the McCoy Creek Group in east-central Nevada. These detrital rocks consist of quartzite and siltstone in southern Nevada (the Stirling Quartzite, Wood Canyon Formation, and Zabriskie Quartzite) and dominantly quartzite (the Prospect Mountain Quartzite) in east-central Nevada. Study in areas between southern and east-central Nevada indicates that the Stirling, Wood Canyon, and Zabriskie Formations change facies to the north and become lithologically similar to one another. The Prospect Mountain Quartzite of east-central Nevada is believed to be the final result of the facies change. It is equivalent to the combined Stirling, Wood Canyon, and Zabriskie of southern Nevada.

More than 10,000–15,000 ft (3,050–4,570 m) of uppermost Precambrian and Lower Cambrian quartzite, conglomerate, siltstone, and carbonate rock is exposed in parts of southern and east-central Nevada (fig. 1). One set of stratigraphic nomenclature has been developed for southern Nevada (Barnes and Christiansen, 1967; Stewart and Barnes, 1966; Stewart, 1970) and another set for east-central Nevada (Misch and Hazzard, 1962; Woodward, 1963), and little attempt has been made to establish regional correlations between the two nomenclatural domains. This paper describes the stratigraphy of uppermost Precambrian and Lower Cambrian rocks in parts of eastern Nevada and reports apparently established correlations between the two nomenclatural areas.

The stratigraphic summary in both southern and east-central Nevada is based largely on published reports, whereas that of intervening areas is based largely on the author's fieldwork during parts of 1969 and 1970. Detailed stratigraphic sections were measured near Delamar, Caliente, and Patterson Mountain, and outcrops were examined at Pioche and Chief Mountain.

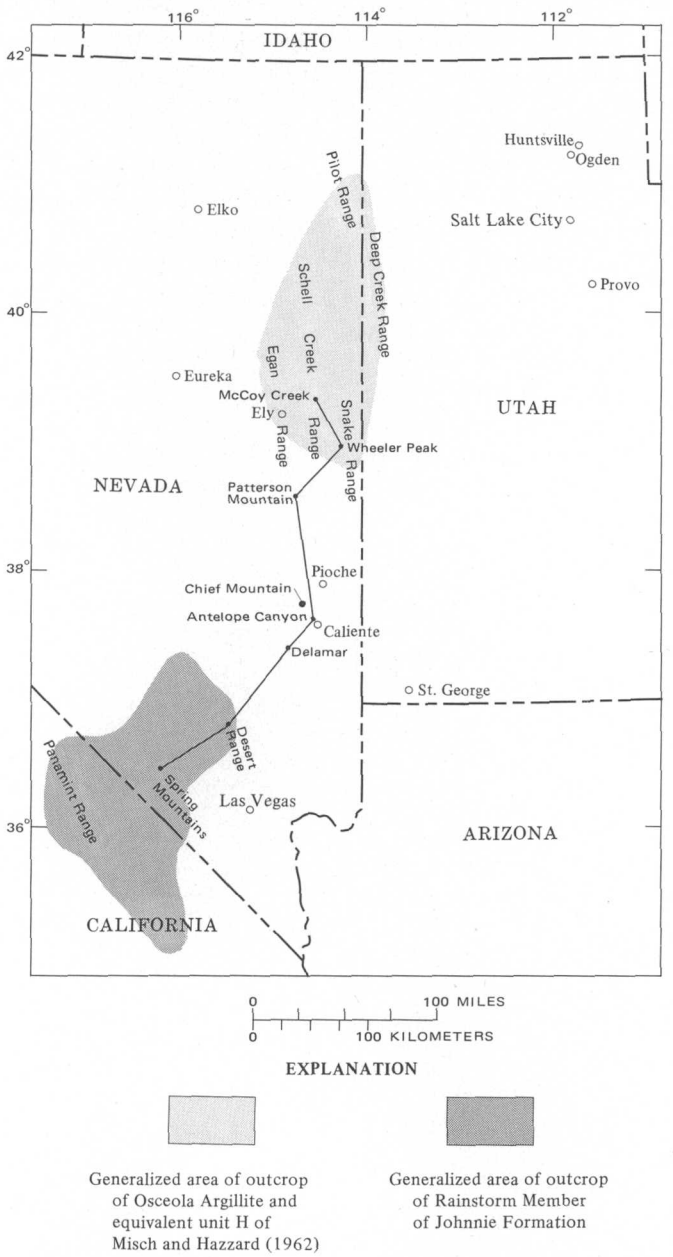

Figure 1.—Map of southern and east-central Nevada showing location of stratigraphic sections shown in figures 3 and 5.

Acknowledgments.—I thank M. D. Crittenden, Jr., R. K. Hose, and D. H. Whitebread for helpful discussions during the course of the study and for constructive criticism of the manuscript. R. K. Hose kindly supplied unpublished data concerning the McCoy Creek section.

SOUTHERN NEVADA

Uppermost Precambrian and Lower Cambrian strata in southern Nevada (Stewart, 1970; Stewart and Barnes, 1966; Barnes and Christiansen, 1967) include strata of five formations consisting, in ascending order, of the Johnnie Formation, Stirling Quartzite, Wood Canyon Formation, Zabriskie Quartzite, and the lower part of the Carrara Formation (fig. 2). The Johnnie, the Stirling, and the lower part of the Wood Canyon are generally considered to be Precambrian in age, whereas the upper part of the Wood Canyon Formation contains metazoan fossils of definite Early Cambrian age (Barnes and Christiansen, 1967; Stewart, 1970). The Zabriskie is unfossiliferous but lies between units containing identifiable Lower Cambrian fossils and must, therefore, also be Early Cambrian in age. The Carrara, on the basis of its fauna, is Early Cambrian in the lower part and Middle Cambrian in the upper part (Palmer, 1971).

The Johnnie Formation consists of fine- to coarse-grained quartzite, conglomeratic quartzite, siltstone, shale, and lesser amounts of limestone and dolomite. The lower part of the formation is divided into various local stratigraphic units, none of which can be correlated with certainty across southern Nevada (figs. 1 and 3). The upper part of the formation, however, consists of the regionally persistent Rainstorm Member made up of three units: (1) A thin basal siltstone unit composed of greenish-gray, medium-gray, moderate-yellowish-brown, and grayish-red siltstone and shale and a thin very distinctive grayish-orange oolitic dolomite (the so-called Johnnie oolite), (2) a middle carbonate unit composed of pale-red to grayish-red siltstone and limy siltstone and also of pale-red limestone, all characteristically having a purplish cast, and (3) an upper siltstone and quartzite unit composed of greenish-gray and light-olive-gray siltstone and very fine grained micaceous sandstone or quartzite. Bedding-surface markings such as ripple marks, possible flute casts, and drag marks are abundant in the siltstone of the middle carbonate unit (fig. 4). The Rainstorm Member has been traced for 130 mi (209 km) in a north-northeast direction in southern Nevada and adjacent parts of California and throughout this distance has fairly uniform lithologic characteristics. The distinctive oolitic dolomite bed, which is generally 6–12 ft (1.8–3.7 m) thick, occurs near the base of the member almost continuously throughout the area of distribution. Locally, the Rainstorm Member, or possible lateral equivalents, contain fine- to medium-grained quartzite and granule conglomerate (Stewart, 1970, p. 29), some of which contain graded bedding (Stewart, 1970, p. 103, 115). The Rainstorm Member has many lithologic characteristics in common with the Osceola Argillite (and equivalent unit G) of Misch and Hazzard (1962) in east-central Nevada, and the two units are considered correlative (fig. 3).

<table>
<tr><th rowspan="2">Series</th><th colspan="2" rowspan="2">Southern Nevada</th><th colspan="4">East-central Nevada</th></tr>
<tr><th colspan="2">Wheeler Peak area</th><th colspan="2">McCoy Creek area</th></tr>
<tr><td>Lower and Middle Cambrian</td><td colspan="2">Lower part of Carrara Formation</td><td colspan="2">Pioche Shale</td><td colspan="2">Pioche Shale</td></tr>
<tr><td rowspan="2">Lower Cambrian</td><td colspan="2">Zabriskie Quartzite</td><td colspan="2" rowspan="3">Prospect Mountain Quartzite</td><td colspan="2" rowspan="3">Prospect Mountain Quartzite</td></tr>
<tr><td rowspan="2">Uppermost Precambrian (Precambrian Z)</td><td colspan="2">Wood Canyon Formation</td></tr>
<tr><td colspan="2">Stirling Quartzite</td></tr>
<tr><td rowspan="5">Uppermost Precambrian (Precambrian Z)</td><td rowspan="5">Johnnie Formation</td><td>Rainstorm Member</td><td rowspan="5">McCoy Creek Group*</td><td>Osceola Argillite*</td><td rowspan="5">McCoy Creek Group*</td><td>Unit G*</td></tr>
<tr><td rowspan="4">Various local informal members or units</td><td>Shingle Creek Quartzite</td><td>Unit F*</td></tr>
<tr><td>Strawberry Creek Formation*</td><td>Unit E*</td></tr>
<tr><td>Willard Creek Quartzite*</td><td>Unit D*</td></tr>
<tr><td>(base not exposed)</td><td>Unnamed rocks (base not exposed)</td><td>Unit A–C* (base not exposed)</td></tr>
</table>

Figure 2.—Stratigraphic nomenclature of Lower and Middle Cambrian and uppermost Precambrian units in southern and east-central Nevada. Asterisk indicates nomenclature of Misch and Hazzard (1962). The McCoy Creek Group as used here excludes the Stella Lake Quartzite and the equivalent unit H, which were originally included in the McCoy Creek Group by Misch and Hazzard.

The Stirling Quartzite overlies the Johnnie Formation and consists of cliff-forming, medium- to coarse-grained vitreous quartzite and minor amounts of siltstone and carbonate. It is divided into five regionally extensive members (fig. 3), two of which are composed mostly of quartzite, two mostly of mixtures of siltstone and quartzite, and one of carbonate and quartzite.

The overlying Wood Canyon Formation is divided into three members (fig. 3). The lower and upper members are similar and composed of siltstone, fine-grained quartzite, and thin but persistent carbonate layers. The middle member is composed of medium- to coarse-grained, locally conglomeratic, quartzite.

The thin Zabriskie Quartzite overlies the Wood Canyon Formation and consists of quartz-rich, medium- to coarse-grained vitreous quartzite.

The Carrara Formation, at the top of the sequence considered here, overlies the Zabriskie and consists largely of siltstone and carbonate. The lowermost part of the Carrara contains minor amounts of quartzite.

DELAMAR

At least 3,000 ft (914 m) of dominantly quartzitic strata is exposed in the Delamar area (fig. 5) and has been assigned to the Prospect Mountain Quartzite (Wheeler, 1948; Callaghan, 1937; Tschanz and Pampeyan, 1970). The strata can be divided into several units that can be correlated confidently with the Stirling Quartzite, Wood Canyon Formation, and Zabriskie Quartzite of southern Nevada, and these formational names are used here, replacing the name Prospect Mountain Quartzite. Although the Stirling Quartzite is faulted and incompletely exposed in the Delamar district, about 1,400 ft (427 m) of the upper part of the formation appears to be structurally intact in a section about 1.9 mi (3.1 km) south-southwest of Delamar. Here the Stirling Quartzite is composed of light-gray to yellow-gray, fine- to coarse-grained quartzite and conglomeratic quartzite. None of the members of the Stirling recognized in southern Nevada were recognized at Delamar, but these members are difficult to distinguish in some areas in southern Nevada such as the Desert Range (figs. 1 and 3).

An 80- to 90-ft (24- to 27-m) unit of basalt in the upper part of the Stirling in the Delamar district was mapped by Callaghan (1937) as a Tertiary basalt sill, but it is highly vesicular and is here considered to be a Precambrian flow within the quartzitic sequence. Similar flows near Caliente at Chief Mountain and on Patterson Mountain (Kellogg, 1963) occupy the same stratigraphic position with respect to the top of the Stirling Quartzite (figs. 3 and 5) and are considered to be related flows, although they probably do not represent one single flow unit.

The Wood Canyon Formation is about 1,300 ft (396 m) thick in a section measured 3.3 mi (5.3 km) south-southwest of Delamar. The contact with the Stirling is at a sharp color break between yellow-gray vitreous quartzite below and greenish-gray to dark-greenish-gray quartzite and sandstone above. Abundant siltstone occurs in the lower 30 ft (9.1 m) of the Wood Canyon, and this siltstone-rich sequence may be correlative with the lower member of the Wood Canyon Formation in southern Nevada. Units equivalent to the middle and upper members of the Wood Canyon Formation are well defined in the Delamar area. The middle member, about 1,000 ft (305 m) thick is composed of yellow-gray and greenish-gray, fine- to medium-grained quartzite and minor amounts of grayish-red or greenish-gray siltstone containing *Scolithus* tubes in the uppermost part. The upper member 300 ft (91 m) thick, is composed of very fine to fine-grained, olive-gray quartzite or sandstone and greenish-gray micaceous siltstone containing locally abundant animal tracks, trails, and borings. The Wood Canyon Formation forms a slope between the ledge-forming Stirling below and the ledge-forming Zabriskie above.

The Zabriskie Quartzite is a 260-ft (79-m) unit of pinkish-gray to white vitreous quartzite. It forms a conspicuous ledge marked "Q" on the right-hand side of figure 5 of Callaghan (1937). The unit marked "Q" in the center of the picture, however, is Stirling. *Scolithus* tubes are abundant in the lower part of the Zabriskie at Delamar, as they are in the southern Great Basin (Stewart, 1970, fig. 28).

The Pioche Shale overlies the Zabriskie and consists mostly of shale and limestone nearly 900 ft (274 m) thick (Callaghan, 1937). It is equivalent to the lower part of the Carrara Formation of southern Nevada.

CALIENTE

About 2,200 ft (671 m) of quartzitic strata exposed near Caliente (figs. 1, 3, and 5) that previously has been assigned to the Prospect Mountain Quartzite (Callaghan, 1936; Tschanz and Pampeyan, 1970) is here assigned to the Stirling Quartzite, Wood Canyon Formation, and Zabriskie Quartzite. The stratigraphic units recognized are similar to those at Delamar. The best exposures are in Antelope Canyon about 1–2 mi (1.6–3.2 km) northwest of Caliente, where all three formations are present. The exposed part of the Stirling, about 900 ft, (274 m) thick, consists dominantly of ledge-forming, yellow-gray to pinkish-gray, cross-stratified, fine- to medium-grained quartzite or conglomeratic quartzite. A 120 ft (37-m)-thick vesicular basalt flow occurs about 300 ft (91 m) below the top of the Stirling. This flow also crops out on Chief Mountain, 6 mi (9.7 km) north-northwest of Antelope Canyon. The Wood Canyon Formation, about 1,055 ft (322 m) thick, consists of a lower 65-ft (19.8-m) member of greenish-gray siltstone, silty sandstone, and quartzite, a middle 720-ft (219-m) member of pale-red, grayish-red, and pinkish-gray, fine- to coarse-grained, locally conglomeratic sandstone and quartzite, containing thin layers of grayish-red siltstone, and an upper 270-ft (82-m) member of greenish-gray to olive-gray siltstone and medium-gray to yellow-gray, silty, fine-

grained quartzite. The Zabriskie Quartzite exposed in Antelope Canyon is a ledge-forming, white, fine- to medium-grained quartzite that is quarried for railroad ballast and for local construction material (Tschanz and Pampeyan, 1970, p. 125). The Zabriskie is at least 200 ft (61 m) thick, although it is too badly crushed and contorted for an accurate measurement of thickness. It contains *Scolithus* tubes in the lower part.

PIOCHE

Poorly exposed quartzitic strata near Pioche that have previously been assigned to the Prospect Mountain Quartzite (Wheeler, 1948; Park and others, 1958; Merriam, 1964; Tschanz and Pampeyan, 1970) are here assigned to the Wood Canyon Formation and Zabriskie Quartzite. Only the middle and upper members of the Wood Canyon Formation are exposed. The middle member, which consists of grayish-red, fine- to medium-grained quartzite and scarce red siltstone, is best exposed about 2 mi (3.2 km) southeast of Pioche on Red Hill and on a ridge extending northwest from there for several thousand feet. The upper member of the Wood Canyon Formation is poorly exposed to the east of the outcrops of the middle member and consists of siltstone and fine-grained quartzite. The overlying Zabriskie Quartzite is best exposed on Treasure Hill, half a mile south of Pioche, and on a ridge extending south from there for about 4,000 ft (1,219 m). It is a resistant unit of pinkish-gray quartzite, about 195 ft (59 m) thick, containing *Scolithus* tubes in the lower part. The Zabriskie grades upward through about 40 ft (12 m) into shale, siltstone, sandstone, and limestone of the Pioche Shale of Early and Middle Cambrian age.

PATTERSON MOUNTAIN

At least 3,600 ft (1,097) m) of quartzitic strata is exposed on the west side of Patterson Mountain in the Schell Creek Range. These strata have been assigned to the Prospect Mountain Quartzite (Kellogg, 1963; Tschanz and Pampeyan, 1970), and this usage is retained here. The Patterson Mountain section is midway in the lateral transition from the Stirling, Wood Canyon, and Zabriskie Formations on the south to the Prospect Mountain Quartzite on the north. The Stirling, Wood Canyon, and Zabriskie apparently become similar in lithology toward the north and at Patterson Mountain are difficult to distinguish from one another.

The Prospect Mountain Quartzite on the west side of Patterson Mountain can be divided into six units (fig. 5). Unit 1, the basal part of the exposed section, is 850 ft (259 m) thick and composed of pinkish-gray to yellow-gray quartzite containing a poorly exposed basalt (Kellogg, 1963) from 260 to 350 ft (79 to 107 m) below the top. Unit 2 is 1,775 ft (541 m) of quartzite similar to unit 1, but of a somewhat redder color and containing a small amount of siltstone. *Scolithus* tubes were found in the upper part. Unit 3 is 375 ft (114 m) of olive-gray siltstone and very fine to fine-grained quartzite and contains

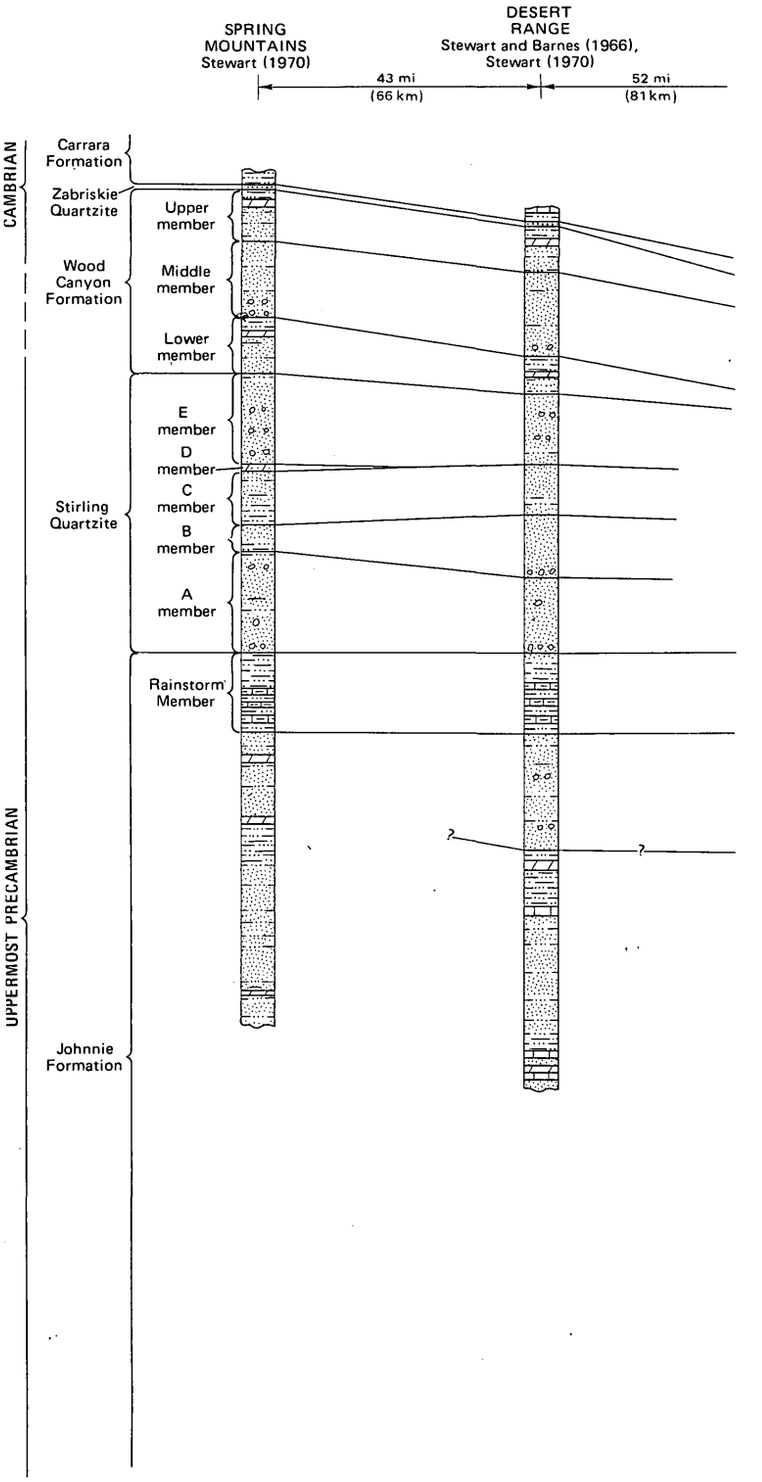

Figure 3.—Correlation

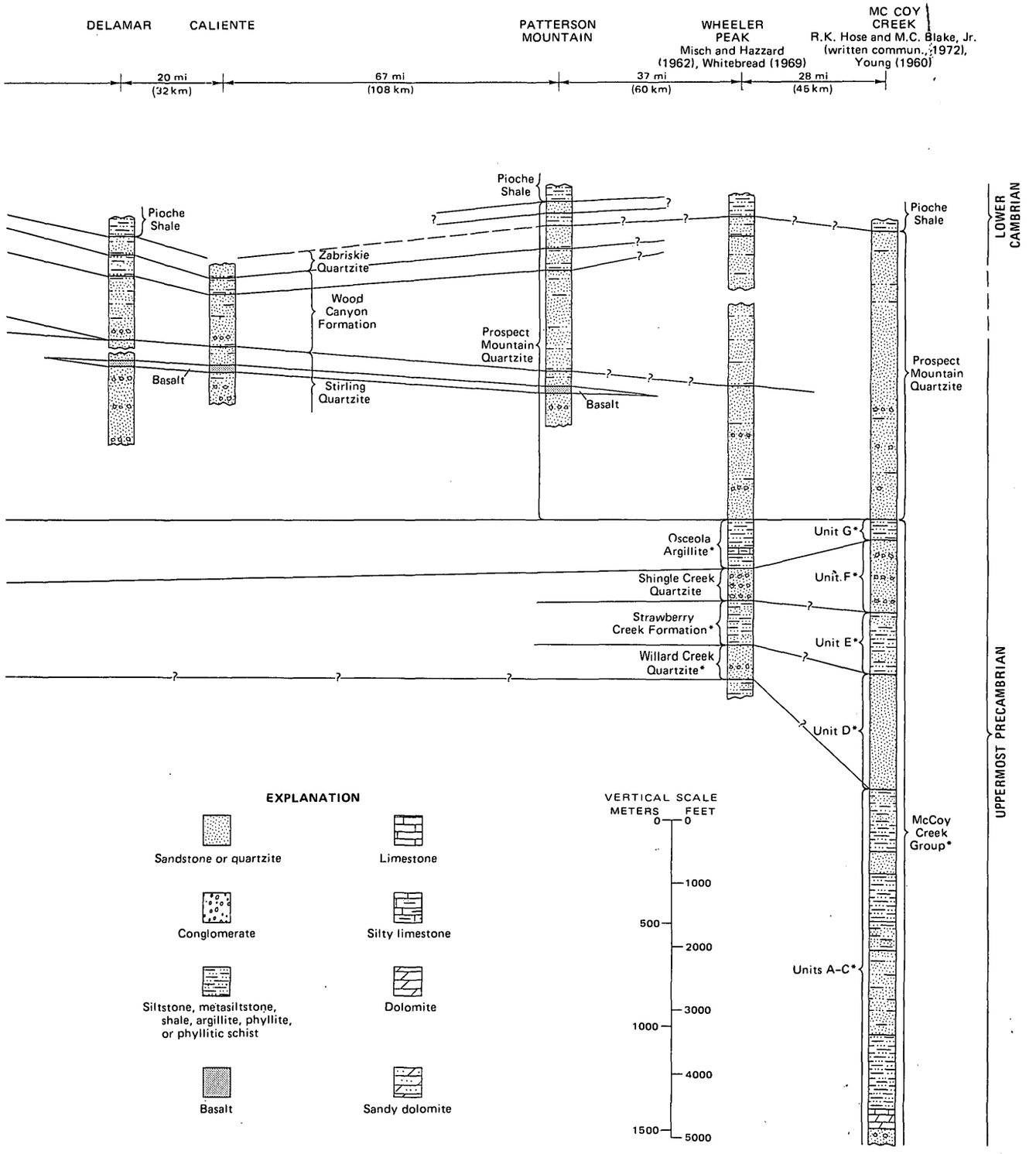

of units from southern to east-central Nevada. Asterisk indicates nomenclature of Misch and Hazzard (1962).

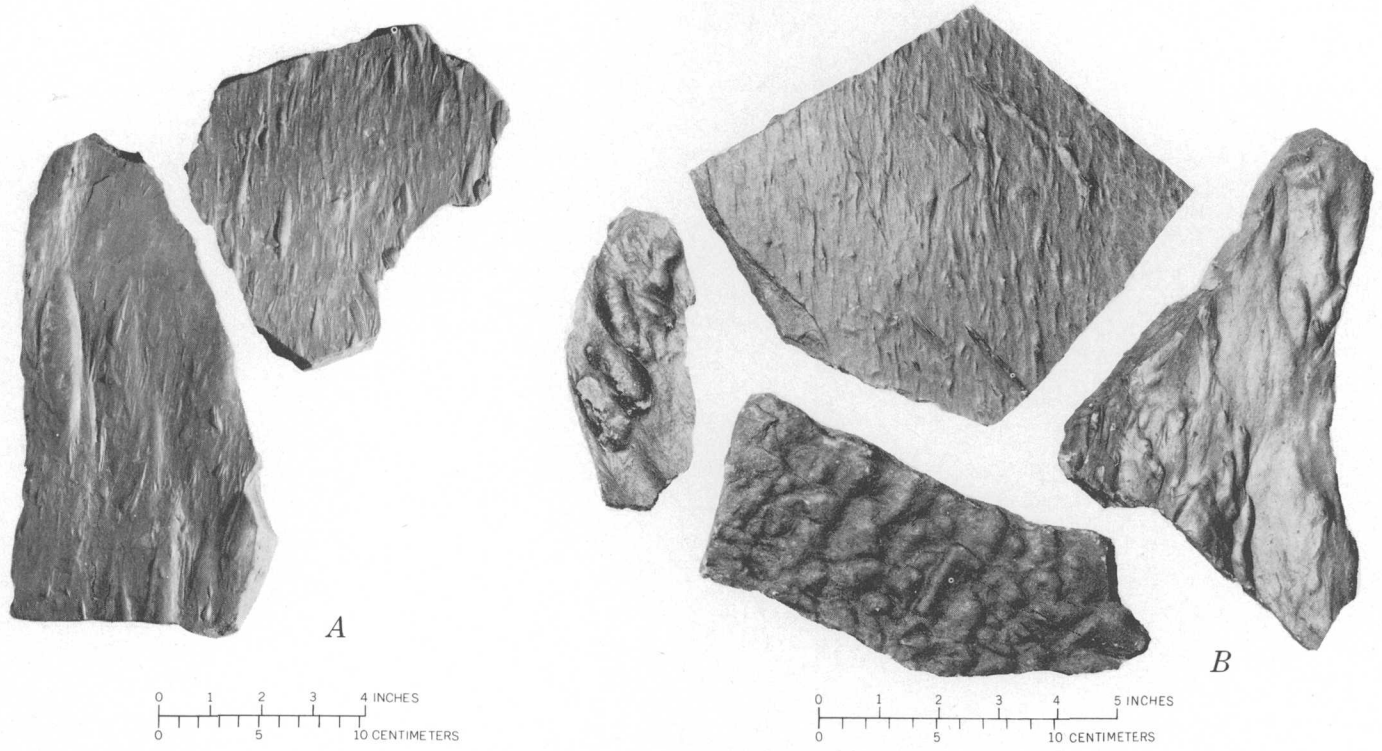

Figure 4.—Bedding-plane markings in (*A*) Rainstorm Member of Johnnie Formation in Panamint Range, Calif., and (*B*) Osceola Argillite of Misch and Hazzard (1962) in Wheeler Peak area.

abundant trace fossils in the lower part. Unit 4 is 370 ft (113 m) of white and very pale orange, fine- to medium-grained quartzite containing *Scolithus* tubes in the lower part. Unit 5 contains abundant trace fossils and is 260 ft (79 m) of greenish-gray siltstone to silty, fine- to medium-grained quartzite containing one 20-ft (6-m) unit of siltstone and silty sandstone in the lower part. Unit 6 forms a conspicious 95 ft (59-m)-thick white ledge of fine- to medium-grained quartzite at the top of the Prospect Mountain Quartzite and is overlain by argillite, sandstone, and limestone of the Pioche Shale.

Unit 1 is lithologically similar to the Stirling Quartzite and appears to be a lateral continuation of that unit. The position of the basalt on Patterson Mountain is similar to that of the basalt in the Stirling at Delamar and Caliente, which further supports this correlation (figs. 3 and 5). Unit 2 probably is equivalent to the middle member of the Wood Canyon Formation, although the amount of siltstone is considerably less than in typical Wood Canyon and the quartzite is not as red. Unit 3 is lithologically similar to the upper member of the Wood Canyon and is considered correlative. Unit 4 is probably correlative to the Zabriskie; the units are lithologically similar, and both contain *Scolithus* in the lower part. Unit 5 may be equivalent to the lower part of the Pioche Shale exposed at Delamar, Caliente, and Pioche, although at Patterson Mountain it is included in the Prospect Mountain Quartzite. Unit 6 is apparently unrelated to any units exposed in southern Nevada or at Delamar, Caliente, or Pioche.

EAST-CENTRAL NEVADA

Uppermost Precambrian and Lower Cambrian strata in east-central Nevada include, in ascending order, the McCoy Creek Group of Misch and Hazzard (1962), the Prospect Mountain Quartzite, and the lower part of the Pioche Shale.

The McCoy Creek Group is more than 10,000 ft (3,048 m) thick in the McCoy Creek area, Schell Creek Range, where it has been divided into eight major units by Misch and Hazzard (1962). They refer to these units by letters, with unit A at the base and unit H at the top. Units A, B, and C are dominantly fine-textured rocks—phyllite, phyllitic schist, and metasiltstone—in places with minor amounts of quartzite and a marble unit near the base. Unit D is cliff-forming, locally conglomeratic, quartzite; unit E is phyllite, argillite, and metasiltstone; unit F is cliff-forming conglomeratic quartzite; and unit G is gray and purple metasiltstone. Unit H has been included by Hose and Blake (1970) in the Prospect Mountain Quartzite, and I have adopted that usage because, as those workers recognized, it cannot readily be mapped as a separate unit.

Woodward (1963, 1965, 1967, 1968) has indicated correlations of these lettered units throughout east-central and northeastern Nevada and parts of western Utah. Recently, R. K.

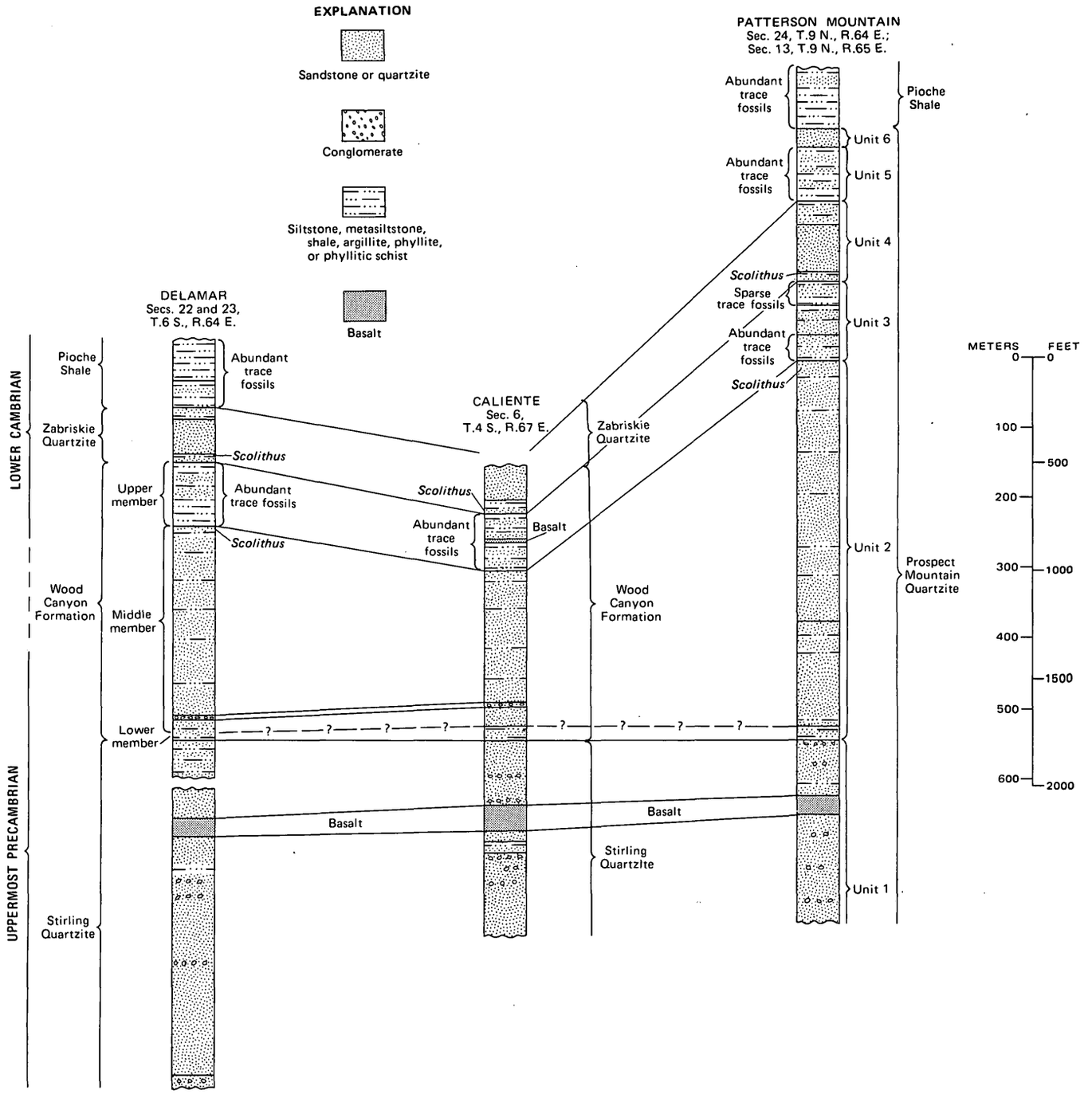

Figure 5.—Detailed correlations from Delamar to Patterson Mountain, Nev. Lithologic symbols same as in figure 3.

Hose and M. C. Blake, Jr. (written commun., 1972) have restudied the McCoy Creek section and have revised some of Misch and Hazzard's (1962) stratigraphic assignments. In figure 3, I have used Hose and Blake's stratigraphic column and have indicated corresponding units, where possible, in Misch and Hazzard's lettered system.

In the Wheeler Peak area, only the top few thousand feet of the McCoy Creek Group of Misch and Hazzard (1962) is exposed. Here Misch and Hazzard (1962) recognized six units, which are, in ascending order, (1) a poorly exposed 300-ft (914-m)-thick unit of fine- to medium-grained clastic rock, (2) the Willard Creek Quartzite, a unit of cliff-forming, locally conglomeratic quartzite about 500 ft (152 m) thick, (3) the Strawberry Creek Formation, a unit of schist and fine-grained quartzite about 750 ft (229 m) thick, (4) the Shingle Creek Conglomeratic Quartzite (called Shingle Creek Quartzite by

Whitebread, 1969), a unit of cliff-forming quartzite and conglomeratic quartzite about 500 ft (152 m) thick, and (5) the Osceola Argillite, a unit of siltstone and sparse silty limestone about 800 ft (244 m) thick (Whitebread, 1969, indicates a thickness of 600–750 ft, or 183–229 m), and (6) the Stella Lake Quartzite, which Misch and Hazzard (1962) considered to be the top unit of their McCoy Creek Group in the Wheeler Peak area. The Stella Lake Quartzite has been included by Whitebread (1969) and Hose and Blake (1970) in the Prospect Mountain Quartzite, and I have adopted that usage here. As indicated by Misch and Hazzard (1962) and by Woodward (1963, 1965, 1967), the most likely correlations (fig. 3) between the Wheeler Peak area and McCoy Creek are as follows: Willard Creek Quartzite with unit D, Strawberry Creek Formation with unit E, Shingle Creek Quartzite with unit F, and Osceola Argillite with unit G.

The Osceola Argillite of Misch and Hazzard (1962) and the equivalent unit G are of particular importance for regional correlations because, as will be described later, they closely resemble the Rainstorm Member of the Johnnie Formation in southern Nevada, and the Osceola, unit G, and Rainstrom are each lithologically unique in their respective areas of occurrence. The Osceola Argillite or unit G has been recognized in the Wheeler Peak area (Misch and Hazzard, 1962), the McCoy Creek area (Misch and Hazzard, 1962), the central and northern Egan Range (Woodward, 1963; unit H of Fritz, 1968), and the Pilot Range (Woodward, 1967), all in Nevada, and in the Deep Creek Range in Utah (Woodward, 1965). The Osceola Argillite and unit G consist mostly of medium-gray, even or irregularly laminated siltstone that has a distinct bluish or purplish cast. Thin discontinuous light-greenish-gray laminae and lenses commonly give the rock an irregularly banded appearance. Markings (fig. 4) are common on surfaces of laminae and have a variety of shapes. Such markings include irregular cusp-shaped or linear ripples, microripples, irregular lobes vaguely similar to flute casts, and drag marks. Light-gray and light-brownish-gray limestone and silty limestone, in places with a pinkish cast, occur in the Osceola Argillite in the Wheeler Peak area and in the equivalent unit G in the Pilot Range. The limestone and silty limestone occur as thin lenticular laminae and, to a lesser extent, as more regularly laminated units from less than an inch to several inches thick. All gradations from limestone to siltstone occur.

Locally, greenish-gray, evenly laminated, platy, micaceous siltstone, with few, if any, bedding-plane markings, and interbedded very fine to fine-grained quartzite constitute most of the Osceola Argillite or unit G. Such rock constitutes the lower 270 ft (82 m) of the unit G in the Egan Range, 11 mi (17.7 km) north of Ely, and almost all of the unit in the northern Schell Creek Range (secs. 11 and 13, T. 21 S., R. 65 E., 23 mi or 37 km, north of McCoy Creek) and in the northern Egan Range (secs. 33 and 34, T. 22 N., R. 63 E., 33 mi or 53 km, north of Ely).

Fine- to coarse-grained, locally conglomeratic quartzite units have been observed in the Osceola Argillite or unit G at three localities: (1) northern Egan Range, mentioned above, 33 mi (53 km) north of Ely, (2) Egan Range, also mentioned above, 11 mi (17.7 km) north of Ely, and (3) northern Deep Creek Range (Woodward, 1965). In the Deep Creek Range, the quartzite unit is considered to be a local channel fill (Woodward, 1965); small scour surfaces occur at the base of the quartzite unit at the locality 33 mi (53 km) north of Ely. Conspicuously graded bedding occurs in fine to conglomeratic quartzite at the locality 11 mi (17.7 km) north of Ely.

The Prospect Mountain Quartzite consists of a thick sequence of yellow-gray, fine- to medium-grained, cross-stratified and thin-bedded, locally conglomeratic quartzite and scarce thin beds of grayish-red siltstone. As used here, the name Prospect Mountain Quartzite includes the Stella Lake Quartzite and the laterally equivalent unit H of Misch and Hazzard (1962). The lowermost 3,400 ft (1,036 m) of the Prospect Mountain Quartzite is exposed on the north side of Wheeler Peak. Here the lower 2,100 ft (640 m) is lighter colored and more massive and contains less siltstone than the upper 1,300 ft (396 m) exposed. The uppermost 800 ft (244 m), or more, of the Prospect Mountain Quartzite is well exposed about 5 mi (8 km) south-southwest of Wheeler Peak. Here the upper 150 ft (46 m) contains about equal amounts of siltstone and quartzite and is transitional into the overlying Pioche Shale. Overall, the Prospect Mountain Quartzite is a monotonous sequence of quartzite and scarce siltstone within which no thick units of siltstone or carbonate occur. No regionally persistent subdivisions are recognized. The Prospect Mountain Quartzite may be approximately 5,000 ft (1,524 m) thick in the Wheeler Peak area (Whitebread, 1969), 4,000–5,000 ft (1,219–1,524 m) in the Schell Creek Range about 15 mi (24 km) south of McCoy Creek (Drewes, 1967, p. 7), and 4,500 ft (1,372 m) in the Schell Creek Range about 10 mi (16 km) north of McCoy Creek (Young, 1960). The 4,500-ft estimate includes 2,300 ft (701 m) of Young's "unit D of the Piermont group," which is considered here to be also part of the Prospect Mountain Quartzite.

The McCoy Creek Group of Misch and Hazzard (1962), excluding the Stella Lake Quarzite and the laterally equivalent unit H, is here considered to be correlative to the Johnnie Formation of southern Nevada, and the Propect Mountain Quartzite is considered to be correlative to the combined Stirling Quartzite, Wood Canyon Formation, and Zabriskie Quartzite of southern Nevada.

Units A through F of Misch and Hazzard's McCoy Creek Group correlate with strata in the Johnnie Formation below the Rainstorm Member (fig. 3). In southern Nevada, this part of the stratigraphic section is laterally variable in lithology (Stewart and Barnes, 1966; Stewart, 1970), and correlation of pre-Rainstorm units between the Spring Mountains and Desert Range (fig. 3) is uncertain; similar correlations are even more tenuous between the Desert Range and the Wheeler Peak area, a distance of 160 mi (257 km) within which no outcrops of the Johnnie Formation or McCoy Creek Group are known. The Johnnie Formation and McCoy Creek Group are nonethe-

less lithologically similar. They contain, in general, approximately equal amounts of quartzite and siltstone (or phyllite). Carbonate units occur in both, particularly near the base, and quartzite, particularly in thick units, is most abundant in the upper half (compare the Desert Range and McCoy Creek sections, fig. 3).

The Osceola Argillite (and equivalent unit G) of Misch and Hazzard (1962) and the Rainstorm Member of the Johnnie Formation are highly similar lithologically and are considered here to be correlative. Both are characterized by pale-red or purplish-medium-gray siltstone with abundant bedding-plane markings (fig. 4), and both contain abundant to scarce amounts of evenly or lenticularly laminated limestone or silty limestone.

Other similarities between the Rainstorm and Osceola (and equivalent unit G) are the local abundance of greenish-gray micaceous siltstone and very fine to fine-grained sandstone and the sparse occurrence of lenticular (possibly channel-fill) quartzite and conglomerate, some of which contain graded bedding.

Both the Osceola and Rainstorm are lithologically unique in their respective areas of occurrence, and both are known to be widely distributed. The Rainstorm Member can be traced for a distance of 130 mi (209 km) in a north-northeast direction in southern Nevada and adjacent parts of California. The Osceola Argillite (and equivalent unit G) can be identified at places from the Pilot Range to the Wheeler Peak area, a distance of 140 mi (225 km). In addition, unit G in the Pilot Range is similar lithologically to the gray to lavender-gray argillite and pinkish-gray silty limestone in the middle part of the Kelley Canyon Formation (Crittenden and others, 1971) in the Huntsville area of Utah, 130 mi (209 km) to the east, indicating the possibility that rocks like those of unit G are even more widespread than presently recognized. However, unit G appears to occupy a much higher stratigraphic position than the Kelley Canyon, perhaps indicating that the two units are not correlative.

The general correlation of the Prospect Mountain Quartzite with the combined Stirling, Wood Canyon, and Zabriskie formations seems assured by the stratigraphic studies at Delamar, Caliente, and Patterson Mountain (fig. 5). This series of sections indicates that the Stirling, Wood Canyon, and Zabriskie change facies to the north and become lithologically similar. At Patterson Mountain they are so similar that they probably could not be mapped separately. As a result, the Patterson Mountain section is assigned entirely to the Prospect Mountain Quartzite.

Detailed work might establish that units equivalent to the Stirling, Wood Canyon, and Zabriskie could be recognized in the Prospect Mountain Quartzite in areas other than Patterson Mountain. For example, the lower 2,100 ft (640 m) of the Prospect Mountain Quartzite on Wheeler Peak may be equivalent to the Stirling, whereas the upper 1,300 ft (396 m) (an incomplete section and not the upper 1,300 ft (396 m) of the formation), which contains more siltstone and is redder than the lower 2,100 ft (640 m), may be equivalent to the lower and middle parts of the Wood Canyon Formation (fig. 3).

Detailed correlations of units at the top of the Prospect Mountain Quartzite have not been established, and two interpretations are plausible. As shown in figures 3 and 5, the topmost units (units 5 and 6) of the Prospect Mountain Quartzite at Patterson Mountain are above what is called Prospect Mountain Quartzite at Wheeler Peak and McCoy Creek. If this correlation is correct, unit 5 might be correlative with the Cabin Shale and unit 6 with the Middle Cambrian Busby Quartzite (Nolan, 1935; Bick, 1966; Palmer, 1971) of the Deep Creek Range in Utah. An alternate possibility is that units 5 and 6 of the Patterson Mountain section grade into the top part of the Prospect Mountain Quartzite as mapped at Wheeler Peak and McCoy Creek. Which of these two possible correlations, or whether some other one, is correct can be resolved only by further work.

AGE ASSIGNMENTS

The correlations presented here have led to an inconsistency in the age assignments of uppermost Precambrian and Lower Cambrian rocks in east-central Nevada as compared with southern Nevada. In southern Nevada, the Precambrian-Cambrian boundary is placed, on the basis of the lowest occurrence of olenellid trilobites or archeocyathids, within the Wood Canyon Formation or the partly correlative Campito Formation (Nelson, 1962; McKee and Moiola, 1962; Taylor, 1966; Stewart, 1966, 1970; Barnes and Christiansen, 1967), although Cloud and Nelson (1966) have placed the boundary below the Campito Formation, within rocks correlative with the upper part of the Stirling Quartzite. In east-central Nevada, the Prospect Mountain Quartzite is generally considered to be entirely Early Cambrian in age (Kellogg, 1963; Drewes, 1967; Fritz, 1968; Whitebread, 1969; Hose and Blake, 1970), although the Stella Lake Quartzite (or unit H), which is here included in the Prospect Mountain Quartzite, was considered to be Precambrian in age by Misch and Hazzard (1962) and Woodward (1963). On the basis of the correlation presented here, only the upper part of the Prospect Mountain Quartzite, that part equivalent to the upper part of the Wood Canyon Formation, should be Early Cambrian in age; the remainder should be Precambrian. The Prospect Mountain Quartzite, therefore, is hereby assigned a Precambrian Z and Early Cambrian age.

REFERENCES CITED

Barnes, Harley, and Christiansen, R. L., 1967, Cambrian and Precambrian rocks of the Groom district, Nevada, southern Great Basin: U.S. Geol. Survey Bull. 1244-G, p. G1–G34.

Bick, K. F., 1966, Geology of the Deep Creek Mountains, Tooele and Juab Counties, Utah: Utah Geol. and Mineralog. Survey Bull. 77, 120 p.

Callaghan, Eugene, 1936, Geology of the Chief district, Lincoln County, Nevada: Nevada Univ. Bull., v. 30. no. 2, 32 p.

——1937, Geology of the Delamar district, Lincoln County, Nevada: Nevada Univ. Bull., v. 31, no. 5, 69 p.

Cloud, P. E., Jr., and Nelson, C. A., 1966, Phanerozoic-Cryptozoic and related transitions—new evidence: Science, v. 154, no. 3750, p. 766–770.

Crittenden, M. D., Jr., Schaeffer, F. E., Trimble, D. E., and Woodward, L. A., 1971, Nomenclature and correlation of some upper Precambrian and basal Cambrian sequences in western Utah and southeastern Idaho: Geol. Soc. America Bull., v. 82, no. 3, p. 581–602.

Drewes, Harald, 1967, Geology of the Connors Pass quadrangle, Schell Creek Range, east-central Nevada: U.S. Geol. Survey Prof. Paper 557, 93 p.

Fritz, W. H., 1968, Geologic map and sections of the southern Cherry Creek and northern Egan Ranges, White Pine County, Nevada: Nevada Bur. Mines Map 35, scale 1:62,500.

Hose, R. K., and Blake, M. C., Jr., 1970, Geologic map of White Pine County, Nevada: U.S. Geol. Survey open-file map.

Kellogg, H. E., 1963, Paleozoic stratigraphy of the southern Egan Range, Nevada: Geol. Soc. America Bull., v. 74, p. 685–708.

McKee, E. H., and Moiola, R. J., 1962, Precambrian and Cambrian rocks of south-central Esmeralda County, Nevada: Am. Jour. Sci., v. 260, no. 7, p. 530–538.

Merriam, C. W., 1964, Cambrian rocks of the Pioche mining district, Nevada, *with a section on* Pioche shale faunules *by* A. R. Palmer: U.S. Geol. Survey Prof. Paper 469, 59 p.

Misch, Peter, and Hazzard, J. C., 1962, Stratigraphy and metamorphism of Late Precambrian rocks in central northeastern Nevada and adjacent Utah: Am. Assoc. Petroleum Geologists Bull., v. 46, no. 3, p. 289–343.

Nelson, C. A., 1962, Lower Cambrian-Precambrian succession, White-Inyo Mountains, California: Geol. Soc. America Bull., v. 73, no. 1, p. 139–144.

Nolan, T. B., 1935, The Gold Hill mining district, Utah: U.S. Geol. Survey Prof. Paper 177, 172 p.

Palmer, A. R., 1971, The Cambrian of the Great Basin and adjoining areas, western United States, *in* Holland, C. H., ed., Cambrian of the New World: New York, Wiley-Interscience, p. 1–78.

Park, C. F., Jr., Gemmill, Paul, and Tschanz, C. M., 1958, Geologic map and sections of the Pioche Hills, Lincoln County, Nevada: U.S. Geol. Survey Mineral Inv. Field Studies Map MF-136.

Stewart, J. H., 1966, Correlation of Lower Cambrian and some Precambrian strata in the southern Great Basin, California and Nevada, *in* Geological Survey research 1966: U.S. Geol. Survey Prof. Paper 550-C, p. C66–C72.

——1970, Upper Precambrian and Lower Cambrian strata in the southern Great Basin, California and Nevada: U.S. Geol. Survey Prof. Paper 620, 206 p.

Stewart, J. H., and Barnes, Harley, 1966, Precambrian and Lower Cambrian formations in the Desert Range, Clark County, Nevada, *in* Cohee, G. V., and West, W. S., Changes in stratigraphic nomenclature by U.S. Geological Survey, 1965: U.S. Geol. Survey Bull. 1244-A, p. A35–A42.

Taylor, M. E., 1966, Precambrian mollusc-like fossils from Inyo County, California: Science, v. 153, no. 3732, p. 198–201.

Tschanz, C. M., and Pampeyan, E. H., 1970, Geology and mineral deposits of Lincoln County, Nevada: Nevada Bur. Mines Bull. 73, 188 p.

Wheeler, H. E., 1948, Late Precambrian-Cambrian stratigraphic cross section through southern Nevada: Nevada Univ. Bull., Geology and Mining Ser. 47, 58 p.

Whitebread, D. H., 1969, Geologic map of the Wheeler Peak and Garrison quadrangles, Nevada and Utah: U.S. Geol. Survey Misc. Geol. Inv. Map I-578.

Woodward, L. A., 1963, Late Precambrian metasedimentary rocks of Egan Range, Nevada: Am. Assoc. Petroleum Geologists Bull., v. 47, no. 5, p. 814–822.

——1965, Late Precambrian stratigraphy of northern Deep Creek Range, Utah: Am. Assoc. Petroleum Geologists Bull., v. 49, no. 3, p. 310–316.

——1967, Stratigraphy and correlation of late Precambrian rocks of Pilot Range, Elko County, Nevada, and Box Elder County, Utah: Am. Assoc. Petroleum Geologists Bull., v. 51, no. 2, p. 235–243.

——1968, Lower Cambrian and Upper Precambrian strata of Beaver Mountains, Utah: Am. Assoc. Petroleum Geologists Bull., v. 52, no. 7, p. 1279–1290.

Young, J. C., 1960, Structure and stratigraphy in north-central Schell Creek Range, *in* Geology of east-central Nevada: Intermountain Assoc. Petroleum Geologists, 11th Ann. Field Conf., 1960, Guidebook, p. 158–172.

Jour. Research U.S. Geol. Survey
Vol. 2, No. 5, Sept.-Oct. 1974, p. 619—624

NEW EVIDENCE ON THE AGE OF THE TOP OF THE MADISON LIMESTONE (MISSISSIPPIAN), BIGHORN MOUNTAINS, WYOMING AND MONTANA

By WILLIAM J. SANDO and BERNARD L. MAMET,[1]
Washington, D.C., Montreal, Canada

Abstract.—The youngest strata recognized in the Madison Limestone are dated by foraminifers and corals at two localities on the west flank of the Bighorn Mountains in Wyoming and Montana. Fossils collected in situ from the Madison at Shell Canyon represent Zone 12 of Mamet and Skipp of late Salem age (middle Viséan), previously thought to be unrepresented by strata in the northern Cordilleran region of the United States. A block of residual chert found at Devils Canyon contains fossils with a possible age range of microfaunal Zones 12–15 (late Salem to Ste. Genevieve, middle to late Viséan), providing further evidence of an extended age range for Madison strata prior to post-Madison, pre-Amsden erosion.

The Madison Limestone, a widespread sequence of Mississippian carbonate rocks in Montana, Idaho, Wyoming, and Utah, has long been known to be separated from superjacent formations by a widespread regional unconformity, but the time span of the hiatus represented by this discontinuity has been evaluated only recently. Zonation of the Madison and superjacent beds by means of foraminifers, corals, and brachiopods (Sando, Mamet, and Dutro, 1969; Sando, Gordon, and Dutro, 1975) led to the conclusion that the time interval not represented by sedimentary deposits varies considerably in magnitude in different parts of the northern Cordilleran region and has a maximum span of nearly three provincial series of the Mississippian (fig. 1).

The youngest fossils previously found in the Madison are foraminifers of Zone 11 of Mamet and Skipp (1970a, b), which is of early Meramecian (middle Salem) age. The oldest fossils overlying the post-Madison unconformity are foraminifers of Zone 13 of Mamet and Skipp (1970a, b), which is of middle Meramecian (early St. Louis) age. Thus, the minimum time lost from the Madison sedimentary record is the interval represented by Zone 12 (late Salem equivalent) (fig. 1), an interval of about one million years duration (Sando and others 1969, p. E20). Five zones are missing from the Mississippian sequence of southeast Idaho (fig. 1). A combination of biostratigraphic and lithostratigraphic evidence suggests that strata representing 3 to 4 zones are missing from the western Wyoming sequence and that strata representing 4 to 11 zones are missing from the sedimentary record in central Wyoming (fig. 1).

Prior to the present study, no conclusive evidence of the missing intervals had been found anywhere in the northern Cordilleran region of the United States. A presumed transition between the Charles Formation and the overlying Kibbey Formation in the subsurface of the Williston basin in northeast Montana (Nordquist, 1953, p. 81) led many geologists (for example, Roberts, 1966, fig. 2) to conclude that all Meramecian time is represented in the upper part of the Madison Group in the Williston basin area. However, the youngest fossils reported from the Charles Formation (Sando, 1960) are corals now known to be of early Meramecian age (Zone D of Sando and others 1969), which suggests that the widespread hiatus is also present in the Williston basin. Brindle (1960, p. 28, 29) reported fossils of the same age in the upper part of the Charles in the subsurface of southeastern Saskatchewan, where the Madison Group is truncated by Mesozoic strata. In Montana, the inferred paleogeography of the Kibbey Formation, which represents an eastward transgression of the Cordilleran sea and was not deposited in the Williston basin until middle Chesterian (Zone 17) time, would seem to preclude continuous sedimentation through Meramecian time (Sando and others, 1975).

The first verified occurrences of rocks younger than Zone 11 in the Madison Limestone of the northern Cordilleran region are reported here. These occurrences are at two localities on the west flank of the Bighorn Mountains (fig. 2).

SHELL CANYON LOCALITY

The Shell Canyon locality is in NW¼SE¼NE¼ sec. 17, T. 53 N., R. 90 W., Bighorn County, Wyo., where the Bull Ridge Member (Sando, 1968) of the Madison Limestone crops out in the northwest slope of the canyon along U.S. Highway 14 (fig. 2). The member consists of a lower unit of silty fine-grained dolomite and dolomitic siltstone overlain by

[1] Université de Montréal.

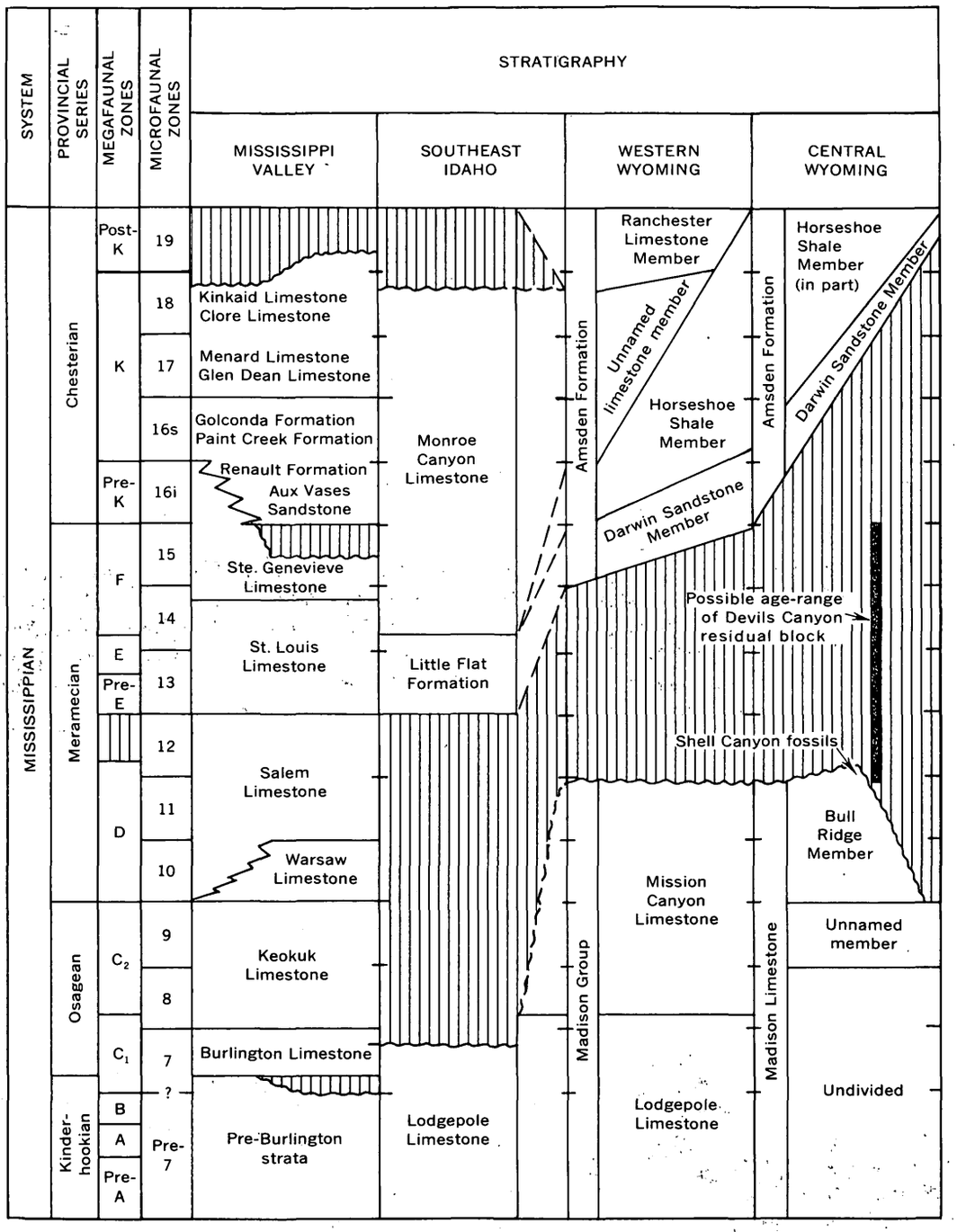

Figure 1.—Temporal relations of Mississippian stratigraphic units in the Mississippi Valley, southeast Idaho, western Wyoming, and central Wyoming. Data from Sando, Mamet and Dutro (1969) and Sando, Gordon, and Dutro (1975).

a solution-riddled limestone sequence containing two stromatolite beds (fig. 3). The entire member was invaded by sandstone of the Darwin Sandstone Member which normally is present at the base of the overlying Amsden Formation; the standstone occurs here only in joint fillings and in an ancient sinkhole that extends from the unconformity at the top of the Bull Ridge downward to and below its base. The Bull Ridge Member is overlain by the Horseshoe Shale Member of the Amsden.

Foraminifers, associated with Zone D corals and brachiopods, were collected from limestone 24 ft (7.3 m) below the top of the Bull Ridge Member. The faunal assemblage (USGS loc. 22593-PC) is as follows:

Brunsia sp.

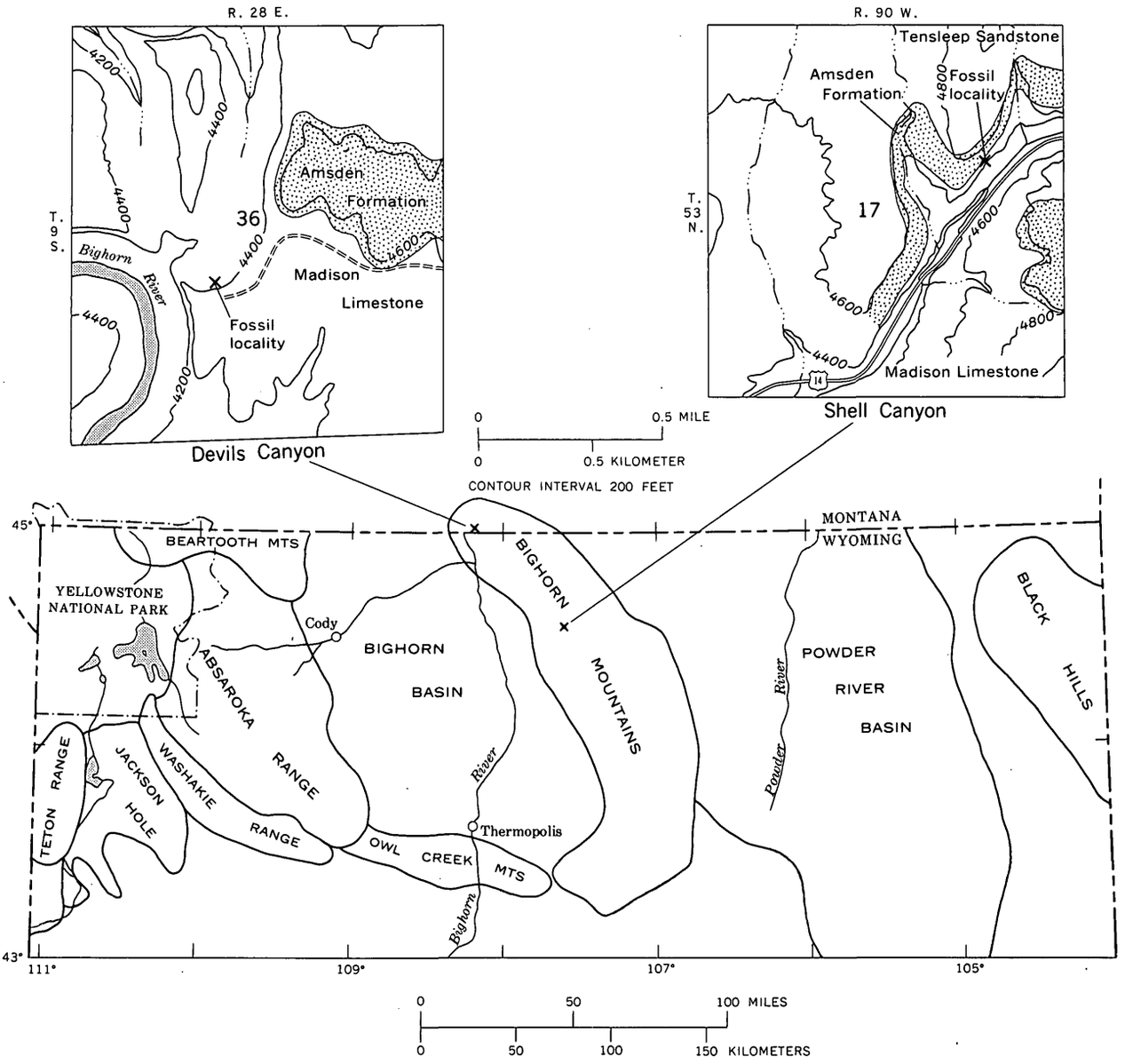

Figure 2.—Geologic sketch maps and index to location of Shell Canyon and Devils Canyon fossil localities. Base from Black Mountain, Wyo., 1960, and Mystery Cave, Mont., 1964, 7-½–minute quadrangles.

Calcisphaera sp.
Dainella sp.
D. chomatica Brazhnikova
Earlandia of the group *E. clavatula* (Howchin)
E. of the group *E. vulgaris* (Rauzer-Chernoussova and Reitlinger)
Endothyra sp.
Eoendothyranopsis of the the group *E. spiroides* (Zeller)
E. spiroides (Zeller)
E. hinduensis (Skipp in Mckee and Gutschick)
Globoendothyra sp.
G. of the group *G. baileyi* (Hall)
G. aff. *G. paula* (Vissarionova)
Kamaena sp.
Koninckopora sp.
K. inflata (de Koninck)
K. tenuiramosa Wood
Palaeotextularia sp.
Priscella prisca (Rauzer-Chernoussova and Reitlinger)
Skippella sp. nom. nud.
Tetrataxis sp.
Vicinesphaera sp.
Vesiculophyllum sp.
Spirifer shoshonensis Branson and Greger?

A Salem age equivalent is clearly indicated by the proliferation of *Globoendothyra* of the group *G. baileyi* (Hall)

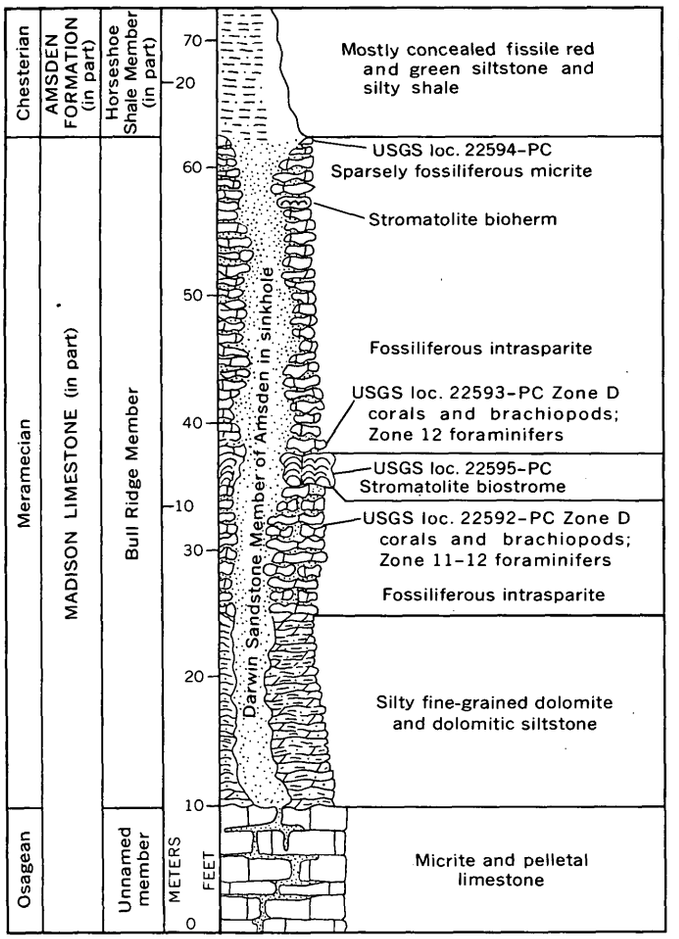

Figure 3.—Diagrammatic representation of the Shell Canyon section showing stratigraphic positions of fossil collections.

associated with abundant *Eoendothyranopsis* of the group *E. spiroides* (Zeller). The Salem fauna spans the early to early middle Viséan and is well known in association with magafaunal Zone D (Sando and others, 1969).

The presence of *Koninckopora* thalli (notably well preserved *Koninckopora inflata* (de Koninck)), of *Globoendothyra* aff. *G. paula* (Vissarionova), and of *Palaeotextularia* is indicative of Zone 12. This association has only been observed in the upper part of the Salem Limestone and equivalent strata and is reported here from the Madison Limestone for the first time. A similar fauna is known in the middle Viséan part of the Mount Head Formation in nearby Alberta (Petryk and others, 1970).

DEVILS CANYON LOCALITY

The Devils Canyon locality is near the center of NE¼SW¼ sec. 36, T. 9 S., R. 28 E., Bighorn County, Mont., at the southern bend of a cutoff meander of the Bighorn River about a half mile (0.8 km) south of Devils Canyon (fig. 2). Here the Bull Ridge Member of the Madison is truncated by the post-Madison, pre-Amsden erosion surface so that only the lower silty dolomitic unit is preserved above the underlying unnamed member of the Madison, which consists of cliff-forming limestone and dolomite (fig. 4).

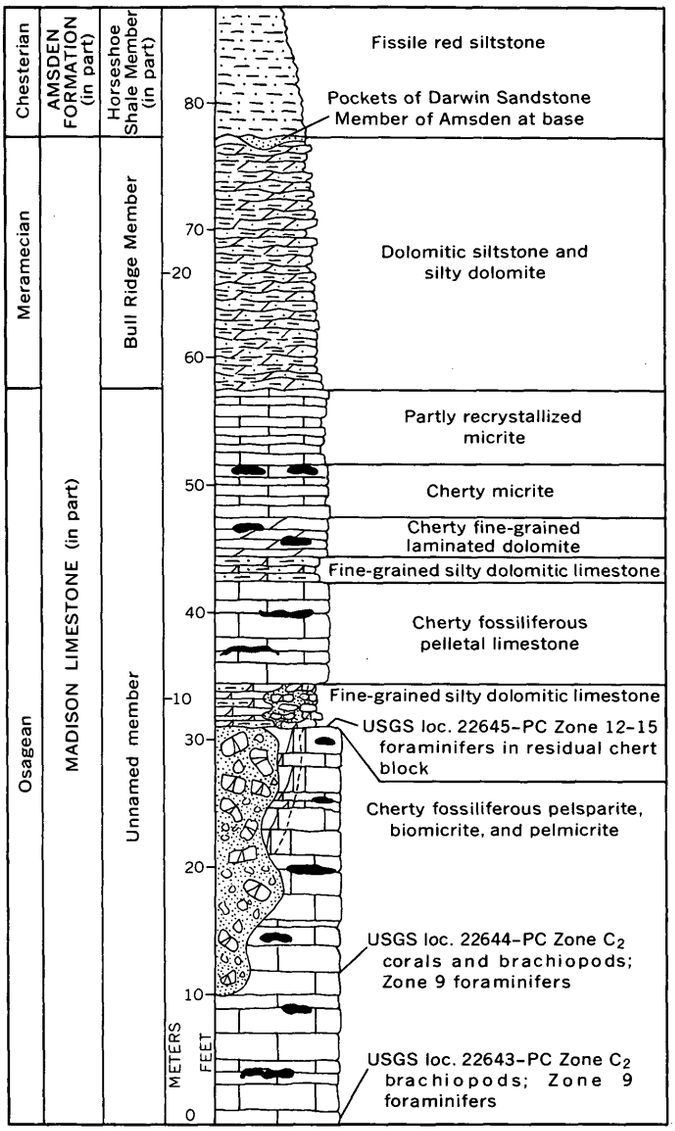

Figure 4.—Diagrammatic representation of the Devils Canyon section showing stratigraphic positions of fossil collections.

A loose, angular, caliche-coated block of silicified biomicrite about 20 by 13 cm containing ostracode and coral debris was found resting on a ledge 46 ft (14.0 m) below the top of the Madison. Identifiable megafossils in this block (USGS loc. 22645-PC) are *Syringopora*? sp. and *Lithostrotionella* cf. *L. banffensis* (Warren).

The tabulate coral in this assemblage is too poorly preserved for certain identification, even to the generic level. The key element in the faunule is a species of the cerioid rugose coral *Lithostrotionella*. Although this specimen is so fragmentary

and poorly preserved that specific identification is uncertain, the species is clearly unlike any ever found in the Madison or in any of the beds overlying the Madison in Montana and Wyoming. Its morphology is suggestive of one of the Meramecian species such as *Lithostrotionella banffensis* (Warren), which was described from the Mount Head Formation in western Canada (Bamber, 1966, p. 17). The Mount Head Formation includes Zones 10–15 of the foraminiferal scheme (Petryk, Mamet, and Macqueen, 1970, fig. 7). Mamet and Armstrong (1972, fig. 10) and Armstrong (1973, fig. 2) report a range of foraminiferal Zones 12–16_i for the species in the Lisburne Group of arctic Alaska.

Microfossils are scarce and difficult to identify due to widespread chertification. The microfauna is as follows:

Calcisphaera sp.
Earlandia sp.
cf. *Endothyra* of the group *E. bowmani* Phillips emend. Brady
Eoendothyranopsis sp.
Eoforschia sp.
Eovolutina sp.
Globoendothyra paula (Vissarionova)
Globoendothyra of the group *G. tomiliensis* (Grozdilova in Lebedeva)
Kamaena sp.
Palaeotextularia sp.
Priscella sp. nom. nud.
Skippella sp. nom. nud.

The known range of such an assemblage is Zone 12 to Zone 15. Unless better preserved material is found, and specific identification of the *Eoendothyranopsis* fauna is feasible, a more precise age cannot be estimated.

INTERPRETATION

Inasmuch as the Madison Limestone is truncated by an unconformity throughout its outcrop area, estimates of the time range of Madison sedimentation are difficult. The new microfaunal evidence at Shell Canyon increases the known timespan of the Madison to include part of Zone 12 of the foraminiferal zonation scheme. Megafossils found with the foraminifers at Shell Canyon extend the range of Zone D of the megafossil zonation into Zone 12. Elsewhere in North America, Zone 12 is represented in the upper part of the Salem Limestone of the Mississippi Valley area, the upper part of the Redwall Limestone of northern Arizona, the upper part of Mamet and Skipp's "Bullion Limestone" of southeastern Nevada, the Mount Head and Livingstone Formations of southwestern Alberta, the Lower Debolt and Prophet Formations of British Columbia, the Flett Formation of the Northwest Territories, and the Lisburne Group of arctic Alaska (Mamet and Skipp, 1970a, fig. 3).

The limestone sequence in the Bull Ridge Member at Shell Canyon was strongly affected by solution associated with post-Madison, pre-Amsden karst formation. Reduction of the sequence by solution and consequent compaction may account for preservation of the Zone 12 remnant below the unconformity.

The aberrant fragment of silicified fossiliferous limestone found below the unconformity at Devils Canyon is probably also a remnant of strata of Zone 12 age. The angular character of the fragment and its occurrence near a breccia-filled solution cavity suggests that it is a residual block that was washed into a nearby sinkhole during erosion of the Madison. This occurrence is reminiscent of the residual fossiliferous chert fragments overlying the Redwall Limestone and in solution cavities in the upper part of the Redwall in northern Arizona (Sando, 1963, 1969), where the chert fragments contain some corals that do not occur in the main body of the Redwall and represent strata that were removed during post-Redwall erosion.

REFERENCES CITED

Armstrong, A. K, 1973, *Lithostrotion reiseri* n. sp., a cerioid colonial coral from Meramec-age beds, Lisburne Group, arctic Alaska: U.S. Geol. Survey Jour. Research, v. 1, no. 2, p. 137–145, 10 figs.

Bamber, E. W., 1966, Type lithostrotionid corals from the Mississippian of western Canada: Canada Geol. Survey Bull. 135, 28 p., 4 pls.

Brindle, J. E., 1960, Mississippian megafaunas in southeastern Saskatchewan: Saskatchewan Dept. Mineral Resources Rept. 45, 107 p., 4 figs., 29 pls.

Mamet, B. L., and Armstrong, A. K., 1972, Lisburne Group, Franklin and Romanzof Mountains, northeastern Alaska, *in* Geological Survey research 1972: U.S. Geol. Survey Prof. Paper 800-C, p. C127–C144, 10 figs.

Mamet, B. L., and Skipp, B. A., 1970a, Preliminary foraminiferal correlations of early Carboniferous strata in the North American Cordillera, *in* Colloques sur la stratigraphie du Carbonifére: Liège Univ. Cong. et Colloques, v. 55, p. 327–347, 3 figs.

——1970b, Lower Carboniferous calcareous Foraminifera—preliminary zonation and stratigraphic implications for the Mississippian of North America [with discussion]: Internat. Cong. Carboniferous stratigraphy and geology, 6th, Sheffield 1967, Comptes rendus, v. 3, p. 1129–1146, 10 figs.

Nordquist, J. W. 1953, Mississippian stratigraphy of northern Montana, *in* Billings Geol. Soc. 4th Ann. Field Conf. Guidebook: p. 68–82, 8 figs.

Petryk, A. A., Mamet, B. L., and Macqueen, R. W., 1970, Preliminary foraminiferal zonation, Rundle Group and uppermost Banff Formation (Lower Carboniferous), southwestern Alberta: Bull. Canadian Petroleum Geology, v. 18, no. 1, p. 84–103, 7 figs.

Roberts, A. E., 1966, Stratigraphy of Madison Group near Livingston, Montana, and discussion of karst and solution-breccia features: U.S. Geol. Survey Prof. Paper 526-B, p. B1–B23, 10 figs.

Sando, W. J., 1970, Corals from well cores of Madison Group, Williston basin. U.S. Geol. Survey Bull. 1071-F: p. 157–190, pls. 13–20, figs., 16, 17 [1961].

——1963, New species of colonial rugose corals from the Mississippian of northern Arizona: Jour. Paleontology, v. 37, no. 5, p. 1074–1079, 1 fig., pls. 145, 146.

——1968, A new member of the Madison Limestone (Mississippian) in Wyoming: Geol. Soc. America Bull., v. 79, no. 12, p. 1855–1858, 2 figs.

——1969, Corals, *in* McKee, E. D., and Gutschick, R. C., eds., History of the Redwall Limestone of northern Arizona: Geol. Soc. America Mem. 114, p. 257–344, pls. 29–40.

Sando, W. J., Gordon, Mackenzie, Jr., and Dutro, J. T., Jr., 1975, Stratigraphy and geologic history of the Amsden Formation (Mississippian and Pennsylvanian) of Wyoming: U.S. Geol. Survey Prof. Paper 848-A. (In press.)

Sando, W. J., Mamet, B. L., and Dutro, J. T., Jr., 1969, Carboniferous megafaunal and microfaunal zonation in the northern Cordillera of the United States: U.S. Geol. Survey Prof. Paper 613-E, p. E1–E29, 7 figs., 1 table.

Jour. Research U.S. Geol. Survey
Vol. 2, No. 5, Sept.-Oct. 1974, p. 625—630

CHERT DERIVED FROM MAGADIITE IN A LACUSTRINE DEPOSIT NEAR ROME, MALHEUR COUNTY, OREGON

By RICHARD A. SHEPPARD and ARTHUR J. GUDE 3d, Denver, Colo.

Abstract.—Nodules and thin beds of chert occur in the upper part of the informally named Rome beds, about 8–11 km southwest of Rome, Oreg. The chert is in green to gray mudstone, about 8 m beneath a conspicuous gray and yellow zeolitic tuff. The bedded chert contains molds of saline minerals and it grades southward and marginward into nodular chert. The nodular chert is of two varieties: relatively large lobate nodules that have greenish-brown interiors and abundant saline crystal molds, and relatively small lobate nodules that have gray interiors and a surface reticulation. The latter variety is the so-called snakeskin agate prized by lapidaries. Both nodular varieties characteristically have a thin white rind. The cherts are similar, if not identical, to cherts reported from Quaternary lacustrine deposits in eastern Africa and from Pleistocene to Jurassic lacustrine deposits in Wyoming. The Rome chert probably formed from a hydrous sodium silicate precursor such as magadiite during diagenesis. Magadiite is generally a primary precipitate from a highly alkaline lake which is capable of attaining a high concentration of silica in solution.

Chert in sedimentary deposits is relatively common throughout the geologic record. Much of the chert occurs in marine rocks, and much of it was derived from siliceous organisms. Recently, however. Eugster (1967) documented the transformation of magadiite ($NaSi_7O_{13}(OH)_3 \cdot 3H_2O$) to chert in Quaternary lacustrine strata of Lake Magadi, Kenya. Since then, the formation of chert from magadiite or other hydrous sodium silicate precursors has been reported from other Quaternary lacustrine deposits in eastern Africa (Hay, 1968; 1970) and from Pleistocene to Jurassic lacustrine deposits in Wyoming (Surdam and others, 1972).

This report describes the occurrence and nature of chert in a Pliocene lacustrine deposit near Rome, Oreg. The Pliocene deposit, known informally as the Rome beds, crops out in an area about 160 km southwest of Boise, Idaho. Figure 1 is a generalized geologic map of the area and is modified from the reconnaissance map of Walker and Repenning (1966). All the rocks are flat lying or dip only slightly. The oldest rocks that crop out are Miocene and Pliocene sedimentary and volcanic rocks. The Rome beds unconformably overlie these older rocks and are unconformably overlain by Pliocene and Quaternary sedimentary and volcanic rocks.

The Rome beds are lacustrine and fluviatile and are at least 100 m thick (Wolf and Ellison, 1971). The lithology of the Rome beds is variable and consists chiefly of conglomerate, sandstone, siltstone, mudstone, and tuff. Most of the clastic rocks are tuffaceous. Our study was restricted to the upper lacustrine part of the Rome beds which consist chiefly of green and gray mudstone that is capped by a conspicuous gray and yellow zeolitic tuff unit. This tuff is the youngest unit of the Rome beds and is informally called the marker tuff (Sheppard and Gude, 1969).

Acknowledgments.—We thank Gary Mackintosh and D. M. Dennis for supplying unpublished information on the cherts near Rome, Oreg., and Buckhorn, N. Mex., respectively. Louise S. Hedricks photographed hand specimens and thin sections of the Rome chert, and her results are greatly appreciated.

OCCURRENCE AND DESCRIPTION OF CHERT

Cherts from the Rome beds were collected at the three localities shown in figure 1. All three localities are in the same stratigraphic horizon which is about 8 m beneath the marker tuff. Three kinds of chert were recognized: small lobate nodules, large lobate nodules, and thin beds.

Small lobate nodules

The small lobate nodules were collected from locality 1 (fig. 1). Figure 2 shows some representative nodules which are characterized by a surface reticulation. The nodules occur in a discontinuous layer that is as much as 10 cm thick, and most nodules are less than 5 cm in their longest dimension. These nodules are prized by rockhounds and lapidaries and are appropriately called snakeskin agates. Gary Mackintosh (McDermitt, Nev.) brought the Rome snakeskin agates to our attention in 1972, but the locality and the nodules were described earlier by Rodgers (1969).

The small lobate nodules typically consist of light- to dark-gray, dense, homogeneous chert with a thin white coating. The coating is relatively soft and is generally less than 1 mm thick. Examination of thin sections of the chert shows that it consists of irregular, fine-grained patches of chalcedony (fig. 3). The largest patches are about 10 μm in size, and all the patches exhibit anomalous extinction. The coating is milky in

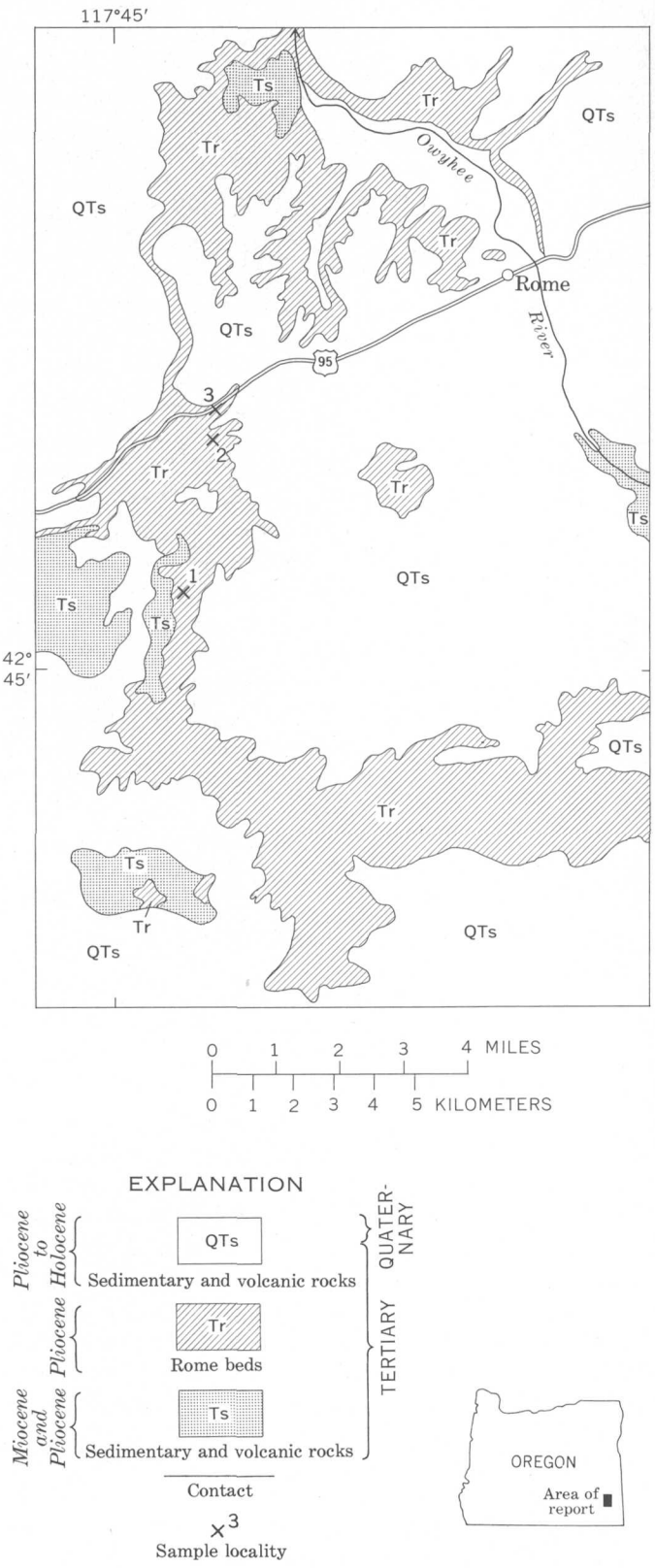

Figure 1.—Generalized geologic map of the Rome area, modified from the reconnaissance map of Walker and Repenning (1966), showing sample localities.

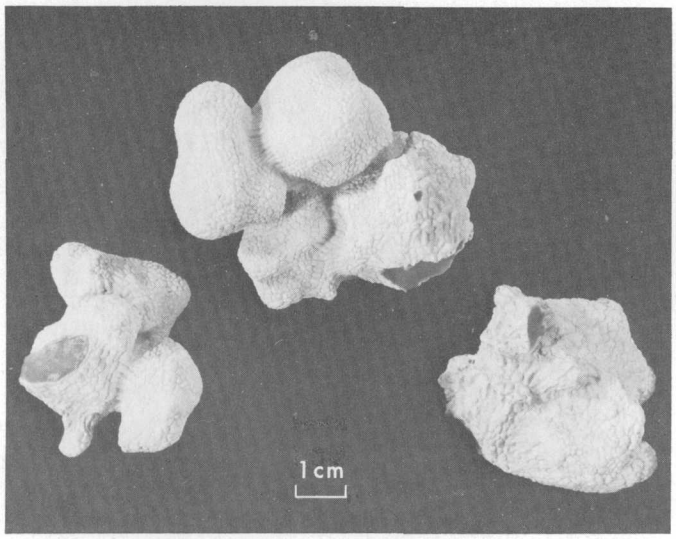

Figure 2.—Small lobate nodules of chert (snakeskin agate) showing characteristic surface reticulation and thin white coating.

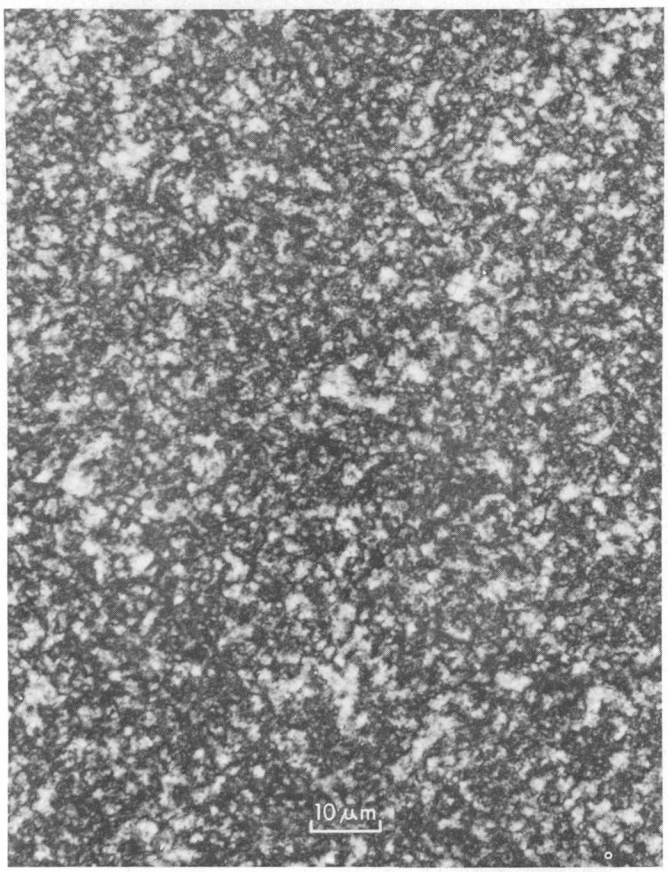

Figure 3.—Photomicrograph of a small lobate nodule of chert showing aggregate of irregular patches of chalcedony.

reflected light and is finer grained than the dense chert. X-ray powder diffractometer patterns of both the dense chert and the white coating are identical with that of quartz. The megascopic and microscopic characteristics of these small lobate

nodules are very similar to those of chert nodules from Pleistocene lacustrine deposits at Olduvai Gorge, Tanzania, described by Hay (1968, p. 265–268).

Large lobate nodules

The large lobate nodules were collected from locality 2 (fig. 1), where the chert caps a small butte. The chert nodules occur in a layer that is about 30 cm thick, and most of the nodules are less than 15 cm in their longest dimension. Figure 4 shows the large lobate nodules that characteristically have a thin white coating over a greenish-brown interior. In

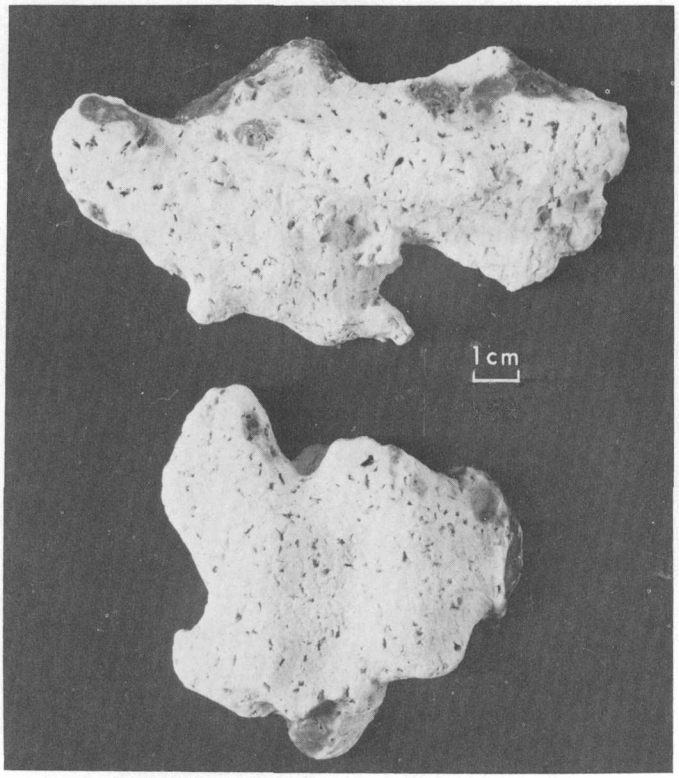

Figure 4.—Large lobate nodules of chert showing characteristic crystal molds and thin white coating.

contrast with the small nodules, these large ones have numerous crystal molds, both on the surface and in the interior of the nodules. Some of the crystal molds are deformed, but others resemble euhedral gaylussite or pirssonite. Similar crystal molds have been reported in cherts that formed from hydrous sodium silicate precursors in Quaternary lacustrine deposits from Lake Magadi, Kenya (Eugster, 1969, p. 16), and from the Pliocene Moonstone Formation of Wyoming (Surdam and others, 1972, p. 2264).

Thin section studies of the large lobate nodules show that they consist chiefly of finely crystalline chalcedony, most of which is less than 2 μm in size. These large nodules also contain about 2–3 percent fine-grained iron oxides, calcite, and detrital clay minerals. The iron oxides and clay minerals probably are responsible for the color of the nodules. Vague spherulites of chalcedony are recognizable, especially under crossed nicols (fig. 5). The spherulites are ellipsoidal and 50–250 μm in their longest dimension. Fibrous chalcedony of

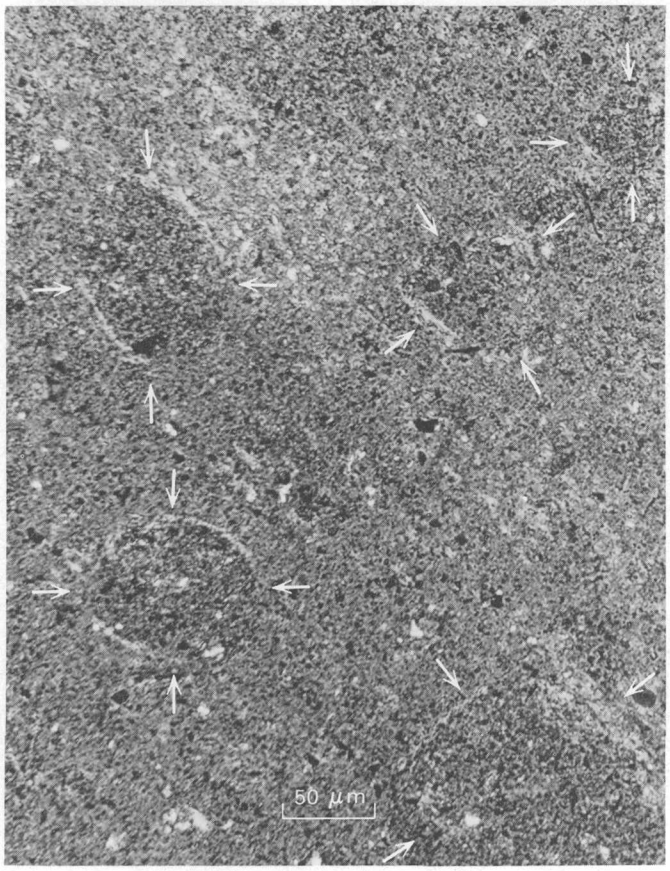

Figure 5.—Photomicrograph of a large lobate nodule of chert; arrows indicate vague spherulites of chalcedony after magadiite(?). Nicols crossed 85°.

the spherulites is length fast. Inasmuch as most of the magadiite in lacustrine deposits is spherulitic, the chalcedonic spherulites are interpreted as relicts of the original magadiite. Many of the crystal molds, particularly those in the interior of the nodules, are filled or partly filled with quartz or quartz and calcite. Three varieties of quartz occur in most of the mold fillings. A thin layer of length-slow chalcedony lines the cavities and is followed by finely crystalline, granular quartz, and then by coarsely crystalline quartz (fig. 6). Some of the coarse quartz shows crystal faces where it projects into a previously unfilled cavity. This sequence is the same in all cavities; and calcite, where present, postdates the coarse quartz.

Thin beds

Chert from thin beds was collected at locality 3 (fig. 1) where a unit about 1 m thick consists of three thin chert beds separated by green mudstone. The chert beds are about 15 cm

Figure 6.—Photomicrograph of a large lobate nodule of chert showing part of a crystal mold that is filled with quartz. The mold filling consists of three varieties of quartz: a thin layer of fibrous chalcedony followed by finely crystalline, granular quartz, and then coarsely crystalline quartz. Nicols crossed 85°.

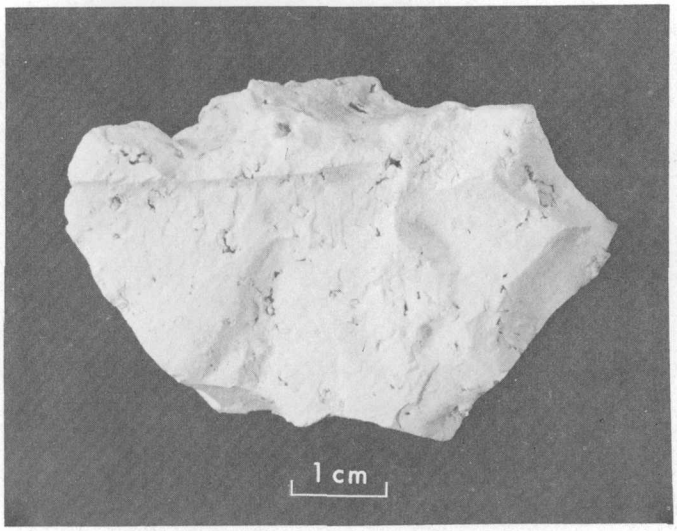

Figure 7.—Fragment of a thin chert bed showing subconchoidal fracture and crystal molds.

thick, white to dark gray, and break with a typical conchoidal or subconchoidal fracture (fig. 7). Like the large lobate nodules, the thin beds of chert contain numerous crystal molds that resemble gaylussite or pirssonite.

Thin section studies of the bedded chert show that the chert is chiefly chalcedony which is 4 µm or less in size. Detrital fine-grained plagioclase, biotite, and clay minerals comprise about 2–4 percent of the chert. Minor amounts of potassium feldspar, clinoptilolite, and fluorite were also detected in some samples by X-ray powder diffraction. All these minor constituents are probably authigenic.

CHEMICAL COMPOSITION

Standard chemical analyses were not performed on any of the cherts, but semiquantitative spectrographic analyses of the two nodular varieties are given in table 1. The analyses indicate that the cherts contain only minor constituents other than SiO_2. Aluminum and calcium are the most abundant impurities, and these elements are probably in clay minerals

Table 1.—*Semiquantitative spectrographic analyses of chert nodules*

[Analyst: M. W. Solt. Results are to be identified with geometric brackets whose boundaries are 1.2, 0.83, 0.56, 0.38, 0.26, 0.18, 0.12, and so forth, but are reported arbitrarily as midpoints of these brackets, 1, 0.7, 0.5, 0.3, 0.2, 0.15, 0.1, and so forth. The precision of a reported value is approximately plus or minus one bracket at 68-percent confidence, or two brackets at 95-percent confidence. G, greater than 10 percent; L, detected but below limit of determination; N, not detected. The following elements were looked for but not detected: Ag, As, Au, Be, Bi, Cd, Ce, Co, Eu, Ga, Ge, Hf, In, K, La, Li, Nb, Ni, P, Pb, Pd, Pt, Re, Sb, Sc, Sn, Ta, Te, Th, Tl, U, W, Y, and Zn]

	Small lobate nodule	Large lobate nodule
	Weight percent	
Si	G	G
Al	.2	.7
Fe	.05	.3
Mg	.03	.07
Ca	.3	.3
Na	.15	.2
Ti	.003	.05
	Parts per million	
B	200	70
Ba	70	1,500
Cr	N	3
Cu	3	7
Mn	50	20
Mo	N	3
Sr	L	30
V	N	30
Yb	N	1
Zr	15	30

and calcite, respectively. Iron and sodium are also relatively high in the large lobate nodule.

GENESIS OF THE CHERT

Magadiite, the presumed precursor for the Rome cherts, is known to precipitate in alkaline lakes, particularly those of the sodium carbonate-bicarbonate variety (Eugster, 1967). Jones, Rettig, and Eugster (1967) found that these brines from closed basins in volcanic terranes of Oregon and Kenya have a pH as high as 11 and SiO_2 contents as high as 2,700 ppm. These alkaline brines are capable of storing large amounts of silica in solution. Freshwater flooding of the silica-rich, alkaline lake water may cause a stratified condition. Magadiite could then precipitate at the interface between the freshwater and the saline, alkaline water because of lowering of the pH. The magadiite, because it is soft and plastic, is very susceptible to deformation under slight loads.

Although magadiite was not recognized in the Rome beds, there is much evidence to indicate that the uppermost lacustrine beds were deposited in a saline, alkaline environment. The obvious evidence, bedded saline minerals, was not observed; however, molds of presumed gaylussite and pirssonite in the chert and in the associated tuffs and mudstones (Sheppard and Gude, 1969) indicate saline, alkaline conditions. The abundance of zeolites, potassium feldspar, and fluorite—all of diagenetic origin—also suggests a saline, alkaline depositional environment for the upper lacustrine part of the Rome beds. The diagenetic potassium feldspar in the Rome beds has a relatively high boron content and anomalous cell parameters which seem unique to feldspar that formed in saline, alkaline lacustrine deposits (Sheppard and Gude, 1973).

The conversion of magadiite to chert during diagenesis involves a loss of sodium and water as well as a decrease in the volume of the solid phase. Two possible equations for the conversion are

$$\underset{\text{magadiite}}{NaSi_7O_{13}(OH)_3} \cdot 3H_2O + H^+ \rightarrow \underset{\text{chert}}{7SiO_2} + 5H_2O + Na^+$$

and

$$\underset{\text{magadiite}}{NaSi_7O_{13}(OH)_3} \cdot 3H_2O \rightarrow \underset{\text{chert}}{7SiO_2} + 4H_2O + Na^+ + OH^-$$

The chemical parameters of the interstitial fluids that may control the transformation of magadiite to chert are suggested by the above equations and include (1) a reduction of the pH, (2) a reduction of the activity of sodium, (3) a reduction of the activity of silica, and (4) a reduction of the activity of water—caused perhaps by an increase in the salinity of the interstitial fluids. Eugster (1969) favored a lowering of the pH and the activity of sodium to account for the transformation at Lake Magadi. These decreases could be accomplished simultaneously by leaching of the magadiite by percolating meteoric water. However, the conversion of magadiite to chert at Lake Magadi and Olduvai Gorge was attributed by Hay (1970) to a decrease in the activity of silica. More recently, O'Neil and Hay (1973) concluded on the basis of oxygen-isotope studies that chert had formed from magadiite and other hydrous sodium silicate precursors in fluids of widely varying salinities and chemical activity ($aNa^+ : aH^+$) ratios.

Our study did not allow us to determine which parameter or combination of parameters was the driving force for the conversion of magadiite to chert. Eugster (1969) suggested that kenyaite or amorphous silica may be an intermediate product in the conversion. We observed neither field nor petrographic evidence to confirm an intermediate step for the Rome chert. We, therefore, assume that the chert formed directly from magadiite by a solution-precipitation mechanism. The conversion apparently takes place in a relatively short time. The minimum time necessary for the formation of the cherts in the East African lacustrine deposits was probably a few hundred to a few thousand years (Hay, 1968; Eugster, 1969).

The chert in the Rome beds inherited several features from the original magadiite. These features include (1) the lobate form of the nodular chert that was produced by plastic deformation of the magadiite prior to conversion to chert, (2) the relicts of magadiite spherulites, and (3) the molds of saline minerals. The characteristic surface reticulation of the small lobate nodules is apparently due to the volume reduction in the conversion of magadiite to chert. These features are identical with those of chert known to have formed from magadiite, and they seem to be unique to chert of this derivation (Hay, 1968; Surdam and others, 1972).

This occurrence of "Magadi-type" chert in the Rome beds confirms the prediction of Surdam, Eugster, and Mariner (1972) that chert of similar derivation will be found in many continental deposits of the Western United States. C. L. Pillmore of the U.S. Geological Survey recently showed us numerous specimens of chert that are identical with the small lobate nodules (snakeskin agate) from the Rome beds. According to D. M. Dennis (oral commun., 1973), the chert was collected about 8 km northwest of Buckhorn, Grant County, N. Mex. Unfortunately, we were unable to obtain additional information about the locality. Other occurrences of Magadi-type chert will undoubtedly be found, particularly in Cenozoic lacustrine deposits of the southwestern United States. As emphasized by Surdam, Eugster, and Mariner (1972), recognition of Magadi-type chert in a deposit is evidence that the depositional environment was alkaline with a pH of at least 9.5.

REFERENCES CITED

Eugster, H. P., 1967, Hydrous sodium silicates from Lake Magadi, Kenya—precursors of bedded chert: Science, v. 157, p. 1177–1180.

——1969, Inorganic bedded cherts from the Magadi area, Kenya: Contr. Mineralogy and Petrology, v. 22, p. 1–31.

Hay, R. L., 1968, Chert and its sodium-silicate precursors in sodium-carbonate lakes of East Africa: Contr. Mineralogy and Petrology, v. 17, p. 255–274.

——1970, Silicate reactions in three lithofacies of a semi-arid basin, Olduvai Gorge, Tanzania: Mineralog. Soc. America Spec. Paper 3, p. 237–255.

Jones, B. F., Rettig, S. L., and Eugster, H. P., 1967, Silica in alkaline brines: Science, v. 158, no. 3806, p. 1310–1314.

O'Neil, J. R., and Hay, R. L., 1973, $^{18}O/^{16}O$ ratios in cherts associated with the saline lake deposits of East Africa: Earth and Planetary Sci. Letters, v. 19, p. 257–266.

Rodgers, J. R., 1969, The snakeskin agate area, Oregon: Lapidary Jour., v. 23, no. 7, p. 960–962.

Sheppard, R. A., and Gude, A. J., 3d, 1969, Authigenic fluorite in Pliocene lacustrine rocks near Rome, Malheur County, Oregon, *in* Geological Survey research 1969: U.S. Geol. Survey Prof. Paper 650-D, p. D69–D74.

——1973, Boron-bearing potassium feldspar of authigenic origin in closed-basin deposits: U.S. Geol. Survey Jour. Research, v. 1, no. 4, p. 377–382.

Surdam, R. C., Eugster, H. P., and Mariner, R. H., 1972, Magadi-type chert in Jurassic and Eocene to Pleistocene rocks, Wyoming: Geol. Soc. America Bull., v. 83, p. 2261–2266.

Walker, G. W., and Repenning, C. A., 1966, Reconnaissance geologic map of the west half of the Jordan Valley quadrangle, Malheur County, Oregon: U.S. Geol. Survey Misc. Geol. Inv. Map I-457.

Wolf, K. H., and Ellison, Bruce, 1971, Sedimentary geology of the zeolitic volcanic lacustrine Pliocene Rome beds, Oregon, 1: Sed. Geology, v. 6, p. 271–302.

Jour. Research U.S. Geol. Survey
Vol. 2, No. 5, Sept.-Oct. 1974, p. 631—636

SPECTROFLUORIMETRIC PROCEDURE USING 2,3-NAPHTHALENEDIAMINE FOR DETERMINING SELENIUM IN ROCKS

By MARIAN M. SCHNEPFE, Washington, D.C.

Abstract.—A spectrofluorimetric procedure using 2,3-naphthalenediamine is given for determining submicrogram and microgram quantities of selenium in mineralized rocks. Conditions for the satisfactory isolation and concentration of the selenium are investigated and tested on six USGS standard rocks of various types. Selenium contents of samples treated by an alkaline sinter and leach are compared with those obtained by acid decomposition and with published values determined by neutron-activation analyses. In pure solutions, 0.01 μg of selenium can be determined with a relative standard deviation of 25 percent, thus setting the determination limit at approximately 0.01 ppm Se in a 1.0-g sample. When the amount of selenium is ⩾0.1 ppm, a relative standard deviation of 10 percent or less is obtained.

Geochemical studies of the selenium content of rocks require accurate and reasonably rapid determinations of submicrogram and microgram quantities of selenium. Although neutron-activation methods are sufficiently sensitive (Brunfelt and Steinnes, 1967, 1971), they require expensive instrumentation; spectrographic procedures necessitate preconcentration to attain the required sensitivity and to ensure representative sampling (Waring and others, 1958). Atomic-absorption spectrophotometric procedures have been applied to the determination of selenium, but at present they are not sufficiently sensitive for most rocks (Chakrabarti, 1968; Lau and Lott, 1971; Severne and Brooks, 1972); higher sensitivity may be obtained by atomic-fluorescence spectrometry (Cresser and West, 1969; Dagnall and others, 1967), but this method is not yet directly applicable to geologic materials.

Spectrofluorimetric procedures using 2,3-naphthalenediamine have been widely investigated and found to possess the requisite sensitivity (Allaway and Cary, 1964; Clarke, 1970; Cousins, 1960; Cukor and others, 1964; Hall and Gupta, 1969; Hemsted and others, 1972; Lane, 1966; Levesque and Vendette, 1971; Lott and others, 1963; Nazarenko and others, 1970; Olson, 1969; Parker and Harvey, 1962; Watkinson, 1966; Wiersma and Lee, 1971; Wilkie and Young, 1970), but problems of selenium losses persist, most notably during the sample decomposition and the separation of selenium. Rock samples, especially those containing high concentrations of organic matter, lose selenium by volatilization during sample decomposition.

In this work, acid and alkaline decomposition are applied to six standards representing a variety of rock types that have selenium contents ranging from 0.031 to 3.7 ppm. Conditions for the decomposition and separation of selenium giving nearly quantitative recovery are described.

Acknowledgment.—The author wishes to express her appreciation to J. I. Dinnin for assistance in the literature search.

REAGENTS AND APPARATUS

Sintering mixture: Zinc oxide, 80 percent (w/w); magnesium oxide, 10 percent (w/w); and sodium carbonate, 10 percent (w/w).

Arsenic-tellurium solution: A solution is prepared that contains 4 mg/ml of arsenic and 1 mg/ml of tellurium in 20 percent (v/v) hydrochloric acid. Dissolve 2.64 g of spectrographic grade arsenic trioxide in 2 g of sodium hydroxide and 10 ml of water. After solution of the oxide, dilute to ≈50 ml with water and add 50 ml of hydrochloric acid. Transfer to a 500-ml flask. Dissolve 0.50 g of spectrographic-grade tellurium metal in 5 ml of nitric acid. Evaporate several times with 3-ml portions of hydrochloric acid and transfer the contents with the aid of 50 ml of hydrochloric acid to the 500-ml flask containing the arsenic. Dilute to 500-ml volume with water and mix.

Selenium standard solutions: To prepare a 100-ppm Se(IV) solution dissolve 0.1000 g of selenium metal with 5 ml of nitric acid in a porcelain evaporating dish. Evaporate to dryness on a steam bath. Evaporate several times with 3 ml of water, transfer to a l-liter volumetric flask and dilute to volume with 4 *N* hydrochloric acid. More dilute selenium standards are made by successive dilutions with 4 *N* hydrochloric acid.

Hypophosphorus acid 50 percent (w/v) (purified): Available commercially.

Stabilizing solution: (Ethylenedinitrilo)tetraacetic acid disodium salt (sodium salt of EDTA), 1 percent (w/v), and hydroxylamine hydrochloride, 2.5 percent (w/v).

Naphthalenediamine solution: A solution containing 0.1 percent (w/v) of a purified grade of 2,3-naphthalenediamine, 0.5 percent (w/v) hydroxylamine hydrochloride, and 0.06 *N* hydrochloric acid. To a separatory funnel add appropriate quantities of the 2,3-naphthalenediamine, hydroxylamine hydrochloride, and 0.5 percent (v/v) hydrochloric acid.

Shake the funnel to dissolve the constituents just minutes before addition to sample solutions previously adjusted to pH 2. If the 2,3-napthalenediamine reagent crystals are yellow or brown, high blank values may result. If this is so, the naphthalenediamine solution should be extracted with several 10-ml portions of cyclohexane. Exposure of the reagent crystals and the solution to strong light is avoided.

Quinine sulfate in 0.1 *N* sulfuric acid: Prepare solutions with quinine sulfate ranging from 0.1 to 50 ppm.

Ammonium hydroxide, 7*N*.

Formic acid, 88 percent.

Cyclohexane.

Spectrofluorimeter: A Baird Atomic Fluorispec, Model Sf-1,[1] with a xenon arc source was used for all fluorescence measurements. Fluorescence curves were obtained with an auxiliary Varian x-y recorder as well as by manual adjustments of the exciting and emitting wavelength controls. All measurements were made in 1-cm rectangular quartz cuvettes.

Alumina crucibles, 25 ml.

Separatory funnels, 60 ml, equipped with Teflon stopcocks.

PROCEDURE

In a small beaker mix 1.000 g of the sample with 9 g of the sintering mixture. Transfer to an alumina crucible and cover with an additional gram of the sintering mixture. Process two sintering mixture blanks along with the samples. Sinter in a muffle furnace gradually raising the temperature to 900°C and hold at this temperature for 2 h. Cool the crucibles and transfer the contents of each to a 250-ml beaker. The bulk of each sintered mass is poured into a beaker. The small amount remaining in the crucible is easily washed and transferred to the beaker with the aid of 225 ml of water used for the subsequent leaching step. Cover the beakers and place on a steambath. Leach the sinters for 4 h or overnight, stirring them occasionally. Centrifuge to separate the leachates or cool and filter the solutions through 9-cm medium-porosity filter paper. No washing of the residues is necessary. Evaporate the alkaline leachates to approximately 50-ml volumes. To each add 50 ml of concentrated hydrochloric acid and 1 ml of the arsenic-tellurium reagent. Cover, and after heating the solution on the steam bath, add 5 ml of hypophosphorus acid solution. Keep the beakers containing the solutions covered and continue to heat on the steam bath for a minimum of 4 h to coagulate the precipitated metals. Allow solutions to stand overnight either on the steam bath or at room temperature. Then by gravity, filter each solution through a 15-ml coarse glass filter crucible supported over a 250-ml beaker on a Teflon disk. Wash precipitates with approximately 50 ml of water. Remove the crucible and disk, rinsing the bottoms with a stream of water. Place the filter crucible supported by the Teflon disk on a clean 100-ml beaker. Using a pipet, slowly "leak" 5 ml of concentrated nitric acid down the filter crucible walls to dissolve the metallic precipitate. Cover the crucible with a watchglass and proceed to the next sample. Using a pipet, wash the filter crucibles with three 5-ml quantities of water. Add 12 ml of 7 *N* ammonium hydroxide and, after complete drainage, remove the crucible and the disk. Stir the solutions with a Teflon-covered rod and add to each, while stirring, 10 ml of stabilizing solution followed by 3 ml of formic acid. Cool the solutions to room temperature and adjust the pH to 2.0 with a pH meter, using ammonium hydroxide (7*N*) or hydrochloric acid (6 *N*). Then add 5 ml of the naphthalenediamine solution to each while stirring. Cover the beakers and immediately place them in a dark cabinet for 2 to 3 h. After this reaction period, pour the reaction mixture into a separatory funnel containing 10.0 ml of cyclohexane. Extract the selenium complex by shaking the funnel for 3 min. Drain and discard the aqueous phase. Collect the cyclohexane extract into a small Pyrex beaker and then transfer to a 15-ml centrifuge tube, retaining the water droplets in the beaker. Centrifuge approximately 3 min and then place the covered tube in a dark cabinet until all extractions are completed. Pour each extract into a 1-cm cuvette and measure the fluorescence at 520 nm with the excitation set at 382 nm. Corrections should be made for the reagent blanks and the net fluorescence related to a calibration curve prepared from selenium coprecipitated with arsenic and tellurium and then extracted by the same procedures used for the samples. Solutions of quinine sulfate in 0.1 *N* sulfuric acid can be used as reference standards for daily use in retaining the instrument settings.

RESULTS AND DISCUSSION

Sample decomposition

Some procedures for determining selenium utilize perchloric acid to decompose the sample (Clarke, 1970; Hall and Gupta, 1969; Lane, 1966; Levesque and Vendette, 1971; Nazarenko and others, 1970; Olson, 1969; Severne and Brooks, 1972; Watkinson, 1966; Wiersma and Lee, 1971). Several investigators have cautioned against protracted fuming with perchloric acid, which results in selenium volatilization (Bock and Jacob, 1964; Stanton and McDonald, 1965; Wilkie and Young, 1970). By using a perchloric acid solution containing selenium spiked with ^{75}Se, we confirmed that severe losses of selenium occur during the evaporation of perchloric acid in either platinum or Teflon vessels.

Selenium can also be lost by deposition on platinum. In a platinum dish, 0.1 μg of selenium(IV) spiked with ^{75}Se was evaporated to dryness from 1 ml of 1 percent (v/v) hydrochloric acid and then fumed with 1 ml of perchloric acid; 50 percent of the selenium remained attached to the platinum

[1] Use of trade names is for descriptive purposes only and does not constitute an endorsement of the products by the U.S. Geological Survey.

dish in a form insoluble in 6 *N* hydrochloric acid. When 0.1 μg of selenium in a solution containing 10 ml each of hydrofluoric acid and nitric acid and 1 ml of perchloric acid was evaporated to perchloric acid fumes, then 13 percent of the selenium adhered to the platinum; when orthophosphoric acid was substituted for the perchloric acid, approximately 50 percent of the selenium remained on the platinum dish. Similar evaporations in Teflon vessels resulted in no acid-insoluble deposits. As a result of these findings, Teflon vessels were used in the acid-dissolution procedure.

Because of volatilization losses of selenium during the evaporation of perchloric acid solutions, other acids were considered. Hemsted, Sina, and Çekiçer (1972) recommended orthophosphoric acid with nitric acid for the decomposition of soils and sediments preparatory to the determination of selenium. Combining hydrofluoric acid with the acids recommended by the above authors and spiking the solution with ^{75}Se, we checked for volatilization losses of selenium during the overnight evaporation of the acidic mixture on a steam bath. No selenium losses were noted. In this mixture of acids, the nitric acid oxidizes reduced forms of selenium; the hydrofluoric and orthophosphoric acids effectively decompose a variety of minerals. Further tests using this acid mixture were made on actual samples.

Selenium was determined in six USGS standard rocks that have a variety of compositions: peridotite (PCC-1), granodiorite (GSP-1), basalt (BCR-1), marine mud (MAG-1), and two shales (SCo-1 and SGR-1). Before the concentration and isolation of selenium by its coprecipitation with tellurium and the final measurement of the fluorescence of the cyclohexane-extracted piazselenol, 1.000-g samples were decomposed with 10 ml each of hydrofluoric and nitric acids and 5 ml of orthophosphoric acid. The acid decomposition procedure for six samples (duplicate runs on three splits) resulted in selenium values agreeing reasonably well with those obtained by neutron-activation analysis (Brunfelt and Steinnes, 1967, 1971) for the three standard rocks for which data are available (table 1). The first four samples listed above yielded metallic precipitates that were well coagulated and easily filtered. Acid decomposition of the two shale samples was incomplete, and the reduction of selenium in the filtered solution was slow, especially for SGR-1. The wide range of selenium values for SGR-1, which has a very high organic content, was so great as to be meaningless (values ranging from 0.4 to 3.0 ppm).

Acid decomposition, in which the total sample is dissolved, results in the presence of large amounts of iron and other sample constituents which complicate the reduction of selenium with its coprecipitant and which lead to possible interferences in the determination of selenium as the piazselenol. A decomposition using an alkaline sinter followed by an aqueous leach was considered as a means of obtaining more consistent results because of the retention of possible interferences in the sinter.

Nazarenko and Kislova (1971), although recommending an acid decomposition for reasons of simplicity, acknowledged that higher selenium values were obtained with an alkaline sinter. Belopol'skaya (1960) used Eschka mixture ($2MgO:1Na_2CO_3$) for the decomposition of many sulfur-containing minerals. Belopol'skaya also noted that determination of selenium in these samples gave results that were 5 to 10 percent higher than those decomposed by acids. A decomposition using Eschka mixture was tried. Silica gel led to

Table 1.—*Estimate of selenium content, in parts per million, in six USGS standard rocks*
[*C*, coefficient of variation]

Sample	Acid decomposition				Alkaline sinter				Neutron activation	
	Run 1	Run 2	Mean	*C* error (percent)	Run 1	Run 2	Mean	*C* error (percent)	Value	Source
PCC-1	0.020	0.017	0.022	34.4	0.034	0.034	0.031	19.4	0.022	Brunfelt and Steinnes, 1967.
	.017	.025			.035	.020				
	.017	.033			.034	.029				
GSP-1	.065	.074	.073	20.2	.090	.072	.088	13.6	.059	
	.071	.060			.079	.100				
	.100	.067			.089	.100				
BCR-1	.083	.078	.079	7.2	.120	.120	.118	3.4	[1].103	
	.080	.080			.120	.130				
	.083	.070			.110	.110				
SCo-1	.58	.90	.882	16.2	1.04	.88	.907	8.4	.....	
	1.05	1.06			.93	.90				
	.78	.92			.89	.80				
MAG-1	1.35	.94	1.23	16.4	1.29	1.28	1.31	2.0	.....	
	1.06	1.32			1.36	1.30				
	1.31	1.39			1.30	1.32				
SGR-1	....	....	....	....	3.75	3.80	3.69	7.8	.....	
					3.70	3.60				
					3.30	4.00				

[1] The more recent neutron-activation value for sample BCR-1 is 0.121 ppm (Brunfelt and Steinnes, 1971).

problems in filtering the selenium-tellurium precipitate from the acidified leachate. Six 1-g portions of each of the six standard rock samples were then decomposed by sintering with 10 g of another mixture, also recommended by Belopol'skaya (1960), consisting of zinc oxide, magnesium oxide, and sodium carbonate in the ratio of 4:1:1. The resulting selenium values given in table 1, together with those obtained by an acid decomposition, confirm that higher selenium values and lower coefficients of variance result from an alkaline sinter.

Because filtration problems from silica gel persisted for several of the samples, various combinations of the flux consitutents were tested. Ten g of a mixture composed of sodium carbonate and magnesium and zinc oxides was applied to 1-g samples of the standard rocks. Of the three sintering constituents, the sodium carbonate proved to be the most reactive in the sample decomposition. When the sodium carbonate exceeded 15 percent, the silica tended to be solubilized. The zinc oxide to magnesium oxide ratio was of little significance other than to affect the bulk of the sintered product. However, higher ratios of zinc oxide produced a much more easily leached and filtered sinter. Further investigations showed that the ratio of the constituents of the sinter mixture can be varied considerably with acceptable results. However, the least problem with silica and the best agreement with the selenium values given in table 1 resulted when the zinc oxide to magnesium oxide to sodium carbonate ratio was 8:1:1. With this mixture very little acid is required for the neutralization of the leachate.

Higher and more consistent selenium values resulted from sintering samples at 900°C rather than 700°C. Extending the sintering period from 1.5 to 4 h at 900°C resulted in no measurable effect on the selenium values.

Separation of selenium by coprecipitation

Many references cite the reduction of arsenic to the metal in order to concentrate and to separate selenium (Allaway and Cary, 1964; Cousins, 1960; Lane, 1966; Severne and Brooks, 1972; Stanton and McDonald, 1965; Wiersma and Lee, 1971). Bock and Jacob (1964) experimented with both arsenic and tellurium and concluded that tellurium was preferred, as a smaller amount of tellurium was required for the quantitative collection of selenium. In initial tests during this investigation, arsenic, despite its demonstrated effectiveness in the isolation of submicrograms of selenium, was abandoned in favor of tellurium. When sample solutions resulted from acid decomposition in which large amounts of iron were present, as much as 10 min was required for the reduction of the arsenic by the hypophosphorus acid, whereas the tellurium was reduced within a minute. More significantly, the tellurium, according to radiotracer and spectrofluorimetric data, proved to be equally effective in the quantitative separation of 0.1 μg of selenium, and the tellurium precipitate was much better coagulated and more readily filtered.

In subsequent experiments conducted to determine the concentration range for which a linear response of fluorescence could be obtained, the fluorescences of cyclohexane extracts of selenium solutions subjected initially to tellurium coprecipitation were compared with those in which the selenium was reacted with 2,3-naphthalenediamine only. In the latter experiment, the fluorescence showed a linear relation for selenium concentrations up to 7 μg per 10 ml in cyclohexane, whereas the fluorescence of solutions resulting from selenium initially isolated by coprecipitation with tellurium showed a negative departure from linearity above a concentration of 1 μg per 10 ml. The actual recovery of selenium by tellurium precipitation fell from 97 to 85 to 80 and to 41 percent for 1,2,3 and 10 μg of selenium, respectively. Varying the mode of heating the solution before or after the addition of the hypophosphorus acid did not change the results significantly. Increasing the tellurium from 4 to 8 mg for the isolation of 10 μg of selenium from 100 ml of 6 *N* hydrochloric acid increased the selenium recovery from approximately 41 to 69 percent. A parallel experiment in which 4 and 8 mg of arsenic were used as the coprecipitant resulted in 79 and 91 percent recoveries of 10 μg of selenium. Large amounts of coprecipitant were shown to result in higher blanks. To capitalize on the greater coprecipitating ability of the arsenic and the better coagulability of the tellurium precipitates, various combinations of the two elements were investigated. Best results were obtained for the isolation of 10 μg of selenium with the combination of 1 mg of tellurium and 4 mg of arsenic. This combination coagulated almost as well as pure tellurium, and the separation of as much as 10 μg of selenium was essentially quantitative, as indicated by the superposability of the concentration-fluorescence curves obtained for preconcentrated selenium and for selenium added directly to 2,3-naphthalenediamine solution.

Effect of hydrochloric acid on coagulation of As-Se-Te precipitate

Solutions containing 1 mg of tellurium and 4 mg of arsenic in 100-ml volumes were made with the hydrochloric acid concentration ranging from 1 *N* to 6 *N*. Aside from the different colors produced in the metallic precipitates after the addition of the hypophosphorus acid, at 1 *N* and 2 *N* the metallic precipitate tended to float and creep up the beaker walls. At 5 *N* and 6 *N* the precipitate settled to the bottom of the beakers in well-coagulated form. The results were intermediate for the other solutions. After 4 h, a Tyndall beam was observed in all supernatant solutions except those at 5 *N* and 6 *N*. On the basis of these observations, it is recommended that the solutions be digested on the steam bath for a minimum of 4 h. To ensure complete coagulation of the precipitates, solutions should be allowed to stand overnight before filtering.

Variables affecting fluorescence of selenium complex

No detailed study was made of the variables that might affect the fluorescence of the selenium complex. In general,

the reagents and their concentrations are about the same as those found by others to give satisfactory results (Allaway and Cary, 1964; Clarke, 1970; Cukor and others, 1964; Hall and Gupta, 1969; Hemsted and others, 1972; Lane, 1966; Levesque and Vendette, 1971; Lott and others, 1963; Nazarenko and others, 1970; Olson, 1969; Parker and Harvey, 1962; Watkinson, 1966; Wiersma and Lee, 1971; Wilkie and Young, 1970).

It is selenium(IV) that reacts with the 2,3-naphthalenediamine to form the fluorescent complex. In some sample decomposition procedures, hexavalent selenium is produced, and if selenium is not isolated by its coprecipitation with another metal, an extra step is necessary to insure the reduction of the selenium(VI) to selenium(IV). In the procedure described in this paper, no additional step is necessary to insure the tetravalency of selenium, as the nitric acid reaction with the arsenic-selenium-tellurium precipitate produces only tetravalent selenium.

Spectral characteristics

Scans of the excitation and fluorescence spectra of the cyclohexane extracts of the piazselenol confirmed the general spectral character given in the literature (Cukor and others, 1964; Levesque and Vendette, 1971; Parker and Harvey, 1962). Excitation at 382 nm gave a maximum fluorescence at the 520-nm peak. The fluorescence contributed by a 2,3-naphthalenediamine blank was negligible.

Calibration curve and sensitivity

A calibration curve was prepared for 0 to 10 μg of selenium extracted into 10 ml of cyclohexane. A linear relation between fluorescence and selenium concentration was obtained for selenium levels up to approximately 0.7 ppm. A negative departure from linearity was observed for concentration greater than 0.7 ppm Se. A detailed examination of the calibration curve for selenium in the 0 to 0.01 ppm range showed it to be linear.

Instrument settings were made so as to give a full-scale deflection for 0.1 *N* sulfuric acid solutions of quinine sulfate of various concentrations. A quinine sulfate concentration of 0.5 μg/ml gives the fluorescence equivalent to a selenium concentration of approximately 0.01 μg/ml of selenium as reported earlier by Watkinson (1966). Other concentrations of quinine sulfate and selenium solutions showed the same equivalence when their ratios were 50:1.

The presence of 0.01 μg of selenium in pure solution is determinable within a relative standard deviation of 25 percent, thus setting the determination limit at approximately 0.01 ppm Se in a 1-g sample. When the amount of selenium being determined is greater than 0.1 μg, a relative standard deviation of 10 percent or less can be expected.

Recovery of ^{75}Se

A solution containing 1 μg of selenium was spiked with ^{75}Se to give approximately 10^5 counts/min and carried through the procedure. After adjustment of all fractions to a fixed volume, the activity of each was measured and compared with a counting standard. The recovery of the selenium was approximately 84 percent. Approximate selenium losses accounted for are as follows: 1 percent in the sinter residue, 2 percent on the sintered glass filter crucible after the nitric acid dissolution of the As-Se-Te precipitate, 3 percent in the combined filtrate and washings from the As-Se-Te precipitate, and 6 percent in the aqueous phase after the cyclohexane extraction. Similar results were obtained with 0.1 μg of selenium spiked with ^{75}Se.

Test of procedure

Selenium was determined in duplicate portions from each of three randomly selected bottles of six USGS standard rocks. The results by the recommended alkaline sintering procedure are given in table 1 together with the results by the acid-decomposition procedure and the published values determined by neutron-activation analysis.

The coefficient of variation generally decreases as the amount of the selenium determined increases. The coefficients for the two shales, SCo-1 and SGR-1, are exceptions to this trend, perhaps attributable to volatilization losses. For samples known to have a relatively high organic content, the rate of temperature increase during the sinter should be decreased.

CONCLUSION

Several advantages are offered by the alkaline-sinter procedure for determining small amounts of selenium: (1) Compared with the acid-decomposition procedure, the danger of losing selenium by volatilization during the sample decomposition is negligible, (2) elements that complicate the As-Se-Te reduction remain almost completely in the sinter residue, and (3) interfering elements are separated by the As-Se-Te precipitation. Because the selenium is isolated from most of the sample constituents, the sample and standard solutions treated with the 2,3-naphthalenediamine are practically similar in composition and therefore more conducive to producing consistent results.

REFERENCES CITED

Allaway, W. H., and Cary, E. E., 1964, Determination of submicrogram amounts of selenium in biological materials: Anal. Chemistry, v. 36, p. 1359–1362.

Belopol'skaya, T. L., 1960 [original pub. in Russian]; 1962 [abs. in Russian]; 1963, Use of sintering for the determination of selenium and tellurium in mineral raw materials: Anal. Abs., 1963, v. 10, No. 1401.

Bock, R., and Jacob, D., 1964, Die bestimmung von selenspuren: Zeitschrift Anal. Chemie, v. 200, p. 81–134.

Brunfelt, A. O., and Steinnes, Eiliv, 1967, Determination of selenium in standard rocks by neutron activation analysis: Geochim. et. Cosmochim. Acta, v. 31, p. 283–285.

——1971, A neutron-activation scheme developed for the determination of 42 elements in lunar material: Talanta, v. 18, no. 12, p. 1197–1208.

Chakrabarti, C. L., 1968, The atomic absorption spectroscopy of selenium: Anal. Chim. Acta, v. 42, p. 379–387.

Clarke, W. E., 1970, Fluorimetric determination of selenium in cast iron with naphthalene-2,3-diamine: Analyst, v. 95, p. 65–69.

Cousins, F. B., 1960, A fluorimetric microdetermination of selenium in biological material; Australian Jour. Experimental Biology and Med. Sci., v. 38, p. 11–16.

Cresser, M. S., and West, T. S., 1969, Determination of selenium by atomic fluorescence in an air-acetylene flame with an integrating atomic emission spectrophotometer using automatic background correction: Spectroscopy Letters, v. 2, p. 9–12.

Cukor, P., Walzcyk, J., and Lott, P. F., 1964, The application of isotope dilution analysis to the fluorimetric determination of selenium in plant material: Anal. Chim. Acta, v. 30, p. 473–482.

Dagnall, R. M., Thompson, K. C., and West, T. S., 1967, The atomic-fluorescence spectroscopic determination of selenium and tellurium: Talanta, v. 14, p. 557–563.

Hall, R. J., and Gupta, P. L., 1969, The determination of very small amounts of selenium in plant samples: Analyst, v. 94, p. 292–299.

Hemsted, W. R. T., Sina, M., and Çekiçer, S., 1972, A simplified method for the determination of selenium in soils and sediments: Analyst, v. 97, no. 1154, p. 383–387.

Lane, J. C., 1966, Determination of selenium in soil and biological materials: Irish Jour. Agr. Research, v. 5, p. 177–183.

Lau, H. K. Y., and Lott, P. F., 1971, An indirect atomic-absorption method for the determination of selenium: Talanta, v. 18, p. 303–310.

Levesque, M., and Vendette, E. D., 1971, Selenium determination in soil and plant materials: Canadian Jour. Soil Sci., v. 51, p. 85–93.

Lott, P. F., Cukor, P., Moriber, G., and Solga, J., 1963, 2,3-diaminonaphthalene as a reagent for the determination of milligram to submicrogram amounts of selenium: Anal. Chemistry, v. 35, p. 1159–1163.

Nazarenko, I. I., Kislov, A. M., Kislova, I. V., and Malevskii, A. Yu., 1970, [2,3-diaminonaphthalene as a reagent for determining submicrogram amounts of selenium]: Zhur. Anal. Khimii, v. 25, p. 1135–1139 (in Russian).

Nazarenko, I. I., and Kislova, I. V., 1971, [Determination of selenium in silicate materials]: Zavodskaya Laboratoriya, v. 37, p. 414 (in Russian).

Olson, O. E., 1969, Fluorimetric analysis of selenium in plants: Assoc. Official Anal. Chemistry Jour., v. 52, p. 627–634.

Parker, C. A., and Harvey, L. G., 1962, Luminescence of some piazselenols: Analyst, v. 87, p. 558–565.

Severne, B. C., and Brooks, R. R., 1972, Rapid determination of selenium and tellurium by atomic-absorption spectrophotometry: Talanta, v. 19, p. 1467–1470.

Stanton, R. E., and McDonald, A. J., 1965, The determination of selenium in soils and sediments with 3,3′-diaminobenzidine: Analyst, v. 90, p. 497–499.

Waring, C. L., Worthing, H. W., and Hazel, K. V., 1958, Spectrochemical method for the determination of selenium: Anal. Chemistry, v. 30, no. 9, p. 1504–1506.

Watkinson, J. H., 1966, Fluorometric determination of selenium in biological material with 2,3-diaminonaphthalene: Anal. Chemistry, v. 38, p. 92–97.

Wiersma, J. H., and Lee, G. F., 1971, Selenium in lake sediments—analytical procedure and preliminary results: Environmental Sci. and Technology, v. 5, p. 1203–1206.

Wilkie, J. B., and Young, M., 1970, Improvement in the 2,3-diaminonaphthalene reagent for micro-fluorescent determination of selenium in biological materials: Jour. Agr. and Food Chemistry, v. 18, p. 944–945.

☆ U.S. GOVERNMENT PRINTING OFFICE: 1974—585-402/1

RECENT PUBLICATIONS OF THE U.S. GEOLOGICAL SURVEY

(The following books may be ordered from the Superintendent of Documents, Government Printing Office, Washington, DC 20402, to whom remittances should be sent by check or money order. Give series number, title, stock number shown in parentheses in this list, and catalog number shown in brackets. Prices of Government publications are subject to change. Increases in costs make it necessary for the Superintendent of Documents to increase the selling prices of many publications offered. As it is not feasible for the Superintendent of Documents to correct the prices manually in all of the publications stocked, the prices charged on your order may differ from the prices printed in the publications and in this list.)

Professional Papers

384-C. The disintegration of the Wolf Creek meteorite and the formation of pecoraite, the nickel analog of clinochrysotile, by G. T. Faust, J. J. Fahey, B. H. Mason, and E. J. Dwornik. 1973 (1974). p. 107–135. $1.30. (2401-02392) [I 19:16:384-C]

731. Geology of the Pulga and Bucks Lake quadrangles, Butte and Plumas Counties, Calif., by Anna Hietanen. 1973 (1974). 66 p.; plates in pocket. $3.45. (2401-00309) [I 19:16:731]

768. Lithostratigraphy and depositional environments of the Lexington Limestone (Ordovician) of central Kentucky, by E. R. Cressman. 1973 (1974). 61 p.; text and plates in case. $8.25. (2401-00362) [I 19:16:768]

Bulletins

1386. Silurian, Devonian, and Mississippian formations of the Funeral Mountains in the Ryan quadrangle, Death Valley region, California, by J. F. McAllister. 1974. 35 p.; plates in pocket. $1.60. (2401-02476) [I 19:3:1386]

1394-G. Revision of nomenclature of the upper part of the Green River Formation Piceance Creek basin, Colorado, and eastern Uinta Basin, Utah, by W. B. Cashion and J. R. Donnell. 1974. p. G1–G9. 25¢. (2401-02473) [I 19:3:1394-G]

Water-Supply Papers

1757-L. Aquifers in the Sokoto Basin, northwestern Nigeria, with a description of the general hydrogeology of the region, by H. R. Anderson and William Ogilbee. 1973 (1974). p. L1–L79; plates in separate case. $6.75. (2401-02389) [I 19:13:1757-L]

1939-E. Geohydrology and water resources of the Tucson basin, Arizona, by E. S. Davidson. 1973 (1974). p. E1–E81; plates in separate case. $6.40. (2401-02390) [I 19:13:1939-E]

1969. Water-supply development and management alternatives for Clinton, Eaton, and Ingham Counties, Mich., by K. E. Vanlier, W. W. Wood, and J. O. Brunett, 1973 (1974). 111 p.; plates in pocket. $3.20. (2401-02422) [I 19:13:1969]

1989. Water resources of the Little River basin, Louisiana, by M. W. Gaydos, J. E. Rogers, and R. P. Smith. 1973 (1974). 74 p.; plates in pocket. $3.15. (2401-02416) [I 19:13:1989]

2006. The Pine-Popple River basin—Hydrology of a wild river area, northeastern Wisconsin, by Edward Oakes, S. J. Field, and L. P. Seeger. 1973 (1974). 57 p.; plates in pocket. $3.20. (2401-02388) [I 19:13:2006]

2027. Analog model study of the ground-water basin of the upper Coachella Valley, Calif., by S. J. Tyley. 1974. 77 p. $1.05. (2401-02486) [I 19:13:2027]